



NAGRA	NTB 90 - 20
SKB	TR 90 - 11
UK-DOE	WR 90 - 042

Poços de Caldas Report No. 2

**Mineralogy, petrology and
geochemistry of the Poços de
Caldas analogue study sites,
Minas Gerais, Brazil.**

I. Osamu Utsumi uranium mine

JANUARY 1991

An international project with the participation of Brazil, Sweden (SKB),
Switzerland (NAGRA), United Kingdom (UK DOE) and USA (US DOE).
The project is managed by SKB, Swedish Nuclear Fuel and
Waste Management Co.



**NAGRA
SKB
UK-DOE**

**NTB 90 - 20
TR 90 - 11
WR 90 - 042**

Poços de Caldas Report No. 2

**Mineralogy, petrology and
geochemistry of the Poços de
Caldas analogue study sites,
Minas Gerais, Brazil.**

I. Osamu Utsumi uranium mine

JANUARY 1991

An international project with the participation of Brazil, Sweden (SKB), Switzerland (NAGRA), United Kingdom (UK DOE) and USA (US DOE). The project is managed by SKB, Swedish Nuclear Fuel and Waste Management Co.

Mineralogy, petrology and geochemistry of the Poços de Caldas analogue study sites, Minas Gerais, Brazil.

I. Osamu Utsumi uranium mine

N. WABER¹, H.D. SCHORSCHER², T. PETERS¹

¹Mineralogisch-Petrographisches Institut, Universität Bern, Baltzerstrasse 1, 3012 Bern (Switzerland).

²Universidade de São Paulo, Instituto de Geociências-DMP, C.P. 20.899, 01498 São Paulo (Brazil).

Abstract

The lithology of the Osamu Utsumi mine is composed mainly of a sequence of volcanic and subvolcanic phonolites and nepheline syenite intrusions similar to those of the Poços de Caldas caldera complex; volcanic breccia pipes about 80 m in diameter also occur, characterised by U-Th-Zr-REE mineralisation concentrated in the matrix. A strong hydrothermal alteration, related to the formation of the breccias, has resulted in the potassic alteration and pyritisation of the phonolites and syenites, with a low-grade mineralisation of disseminated pitchblende. The potassic alteration has transformed all feldspars into pure potash feldspars, nepheline into illite and kaolinite, and clinopyroxenes, which are the primary REE-bearers, into mixtures of TiO₂-rich minerals, clay minerals and pyrite. The enrichment of K, S, U, Th, Pb, Rb, Ba and Mo was accompanied by a strong depletion in Ca, Na, Mg and Sr. Fluid inclusion data indicate temperatures around 250°C and a KCl-H₂O mixture with approximately 7 wt.% KCl for the hydrothermal fluids. For fluids in the breccia pipes that transported additional Zr, Hf and F, the inclusions indicate boiling and give temperatures of 210°C with 40-45 wt.% KCl for a KCl-NaCl-H₂O brine containing FeSO₄ and KF. Ultramafic dykes (dated to 76 Ma) with carbonatitic affiliation put a younger age limit on the hydrothermal event.

As a result of supergene weathering below a lateritic soil cover 20 to 40 m thick and a saprolite zone 15 to 60 m thick, the pyrites in the rocks have been oxidised to varying depths of 80 to 140 m below surface, resulting in a redox front marked by a contrasting colour change in the rock from oxidised (yellow/buff) to reduced (grey/green) rock. In the vicinity of water-bearing fissures these redox fronts have penetrated to greater depths. Due to mobilisation in the oxidised zone and precipitation immediately below the redox front, a secondary pitchblende mineralisation, partly occurring as nodules associated with

secondary pyrite, has been developed. This secondary pyrite is sometimes related with CdS and has a δS of -13‰ compared to δS values of -3.63 to $+1.24\text{‰}$ for hydrothermal pyrites; the low δS values of the former are attributed to bacterial action. In the immediate vicinity of the redox front, dissolution of the potash feldspar becomes apparent and the kaolinite content begins to increase. The marked colour change at the redox front is caused by the presence of hydrous ferric oxides that, with time, evolve from amorphous Fe-hydroxides to goethite and hematite. On the oxidised side alunite-jarosite minerals are frequent. The porosity increases by 5 to 8% (almost doubled) at the redox front.

Gibbsite is present when potash feldspar has been removed at the saprolite-laterite contact. Many of the REEs are associated with phosphate-rich clays (including the crandallite group minerals) and seem to be hardly mobilised by the oxidising weathering fluids. Only a slight general loss of REEs was observed between oxidised and reduced rock, with the degree of loss being greater for the light REEs. Certain indications of a fractionation of Ce and Eu from the other REEs are present.

Zusammenfassung

Die Lithologie der Osamu Utsumi Mine ist im wesentlichen bestimmt durch eine Folge von vulkanischen und subvulkanischen Phonoliten und Nephelin-Syenit-Intrusionen, ähnlich wie diejenigen im übrigen Poços-de-Caldas-Caldera-Komplex. Es existieren auch vulkanische Brekzien-Schlote von etwa 80 m Durchmesser, die durch U-Th-Zv-SEE-Mineralisationen in der Matrix charakterisiert sind. Eine starke hydrothermale Umwandlung, die mit der Bildung der Brekzien zusammenhängt, führte zu einer K-Umwandlung und Pyritisierung der Phonolite und Syenite sowie zu einer schwachen Mineralisierung mit feinverteilter Pechblende. Die K-Umwandlung führte alle Feldspäte in reine K-Feldspäte über, desgleichen Nephelin in Illit und Kaolinit sowie Klinopyroxene (als primäre Träger der SEE) in Mischungen von TiO_2 -reichen Mineralien, Tonmineralien und Pyrit. Die Anreicherung von K, S, U, Th, Pb, Rb, Ba und Mo war gekoppelt mit einer Verarmung an Na, Ca, Mg und Sr. Flüssigkeitseinschlüsse deuten auf Temperaturen um 250°C und KCl- H_2O -Mischungen mit etwa 7 Gew.% KCl für die hydrothermalen Lösungen. Für die Fluide in den Brekzien-Schlotten, die zusätzlich Zr, Hf und F transportierten, deuten die Einschlüsse auf Sieden bei 210°C und KCl-Gehalte von 40-45 Gew.% in einer KCl-NaCl- H_2O -Lösung, die auch FeSO_4 und KF enthält. Ultrabasische, karbonatitische Gänge (datiert auf 76 Ma) liefern eine untere Altersgrenze für die hydrothermale Phase.

Als Ergebnis einer deszendenden Verwitterung unter einer tonigen Erdschicht von 20-40 m und einer Saprolitzzone von 15-60 m wurde der Pyrit in den Gesteinen bis zu variablen Tiefen von 80-140 m unter der Oberfläche oxidiert. So entstand eine Redoxfront, die durch einen auffälligen Farbwechsel von oxidiertem (gelb/ocker) zu reduziertem (grau/grün) Gestein gekennzeichnet ist. Im Bereich wasserführender Klüfte drangen diese Redoxfronten in grössere Tiefen vor. Durch Auflösung in der oxidierten Zone und Abscheidung unmittelbar unter der Redoxfront entstand eine sekundäre Pechblende-Mineralisation, z.T. als Knollen in Verbindung mit sekundärem Pyrit. Dieser sekundäre Pyrit ist manchmal vergesellschaftet mit CdS und hat ein δS von -13 ‰ verglichen mit δS -Werten von -3.63 bis +1.24 ‰ für hydrothermale Pyrite. Der niedrige δS -Wert von -13 ‰ deutet auf bakterielle Prozesse. In unmittelbarer Nähe der Redoxfront wird die Auflösung von K-Feldspat und die Zunahme des Kaolinitgehaltes beobachtet. Der auffällige Farbwechsel an der Redoxfront wird durch amorphe, hydratisierte Ferrihydroxide erzeugt, die mit der Zeit zu Goethit und Hämatit umgewandelt werden. Auf der oxidierten Seite sind Alunit-Jarosit-Mineralien häufig. Die Porosität steigt von 5 auf 8 % an der Redoxfront.

Gibbsit ist vorhanden, wenn der K-Feldspat am Saprolit-Laterit-Kontakt verschwunden ist. Eine Anzahl der SEE sind an phosphatreiche Tone (einschliesslich der Crandallit-Mineralien) gebunden und werden durch die oxidierenden Lösungen kaum mobilisiert. Nur ein geringer allgemeiner Verlust an SEE zwischen oxidiertem und reduziertem Gestein wurde beobachtet, wobei der Verlust für die leichten SEE grösser ist. Es existieren einige Hinweise auf eine Fraktionierung von Ce und Eu von den anderen SEE.

Résumé

Les roches de la mine d'uranium de Osamu Utsumi sont constituées principalement de la même séquence volcanique et subvolcanique que celle du complexe de caldera de Poços de Caldas, caractérisée par des intrusions de phonolites et syénites néphélitiques. On y trouve aussi des brèches de cheminée volcanique d'environ 80 m de diamètre, dont la matrice est concentrée en minéraux U-Th-Zr-TRs (Terres rares). Une forte phase hydrothermale, liée à la formation des brèches, a produit une altération potassique et une pyritisation des phonolites et syénites, ainsi qu'une minéralisation de faible degré de pechblende disséminée. L'altération potassique a transformé tous les feldspaths en purs feldspaths potassiques, la néphéline en illite et kaolinite, et les clinopyroxènes, qui sont les supports primaires des TRs, en mélanges riches en TiO_2 , minéraux argileux et pyrite. L'enrichissement en K, S, U, Th, Pb, Rb, Ba et Mo a été accompagné d'un fort appauvrissement en Ca, Na, Mg et Sr. Les données des inclusions fluides indiquent que les fluides hydrothermaux possédaient une température d'environ 250°C et se composaient d'une mixture d'eau et d'environ 7 % de KCl, en pourcentage pondéral. Quant aux fluides hydrothermaux dans les brèches de cheminée, qui véhiculaient encore du Zr, Hf et F, ils devaient bouillir sous des températures d'environ 210°C, et se composaient d'une saumure eau-KCl-NaCl contenant du FeSO_4 et du KF, avec 40 à 45 % en poids de KCl. Des filons ultramafiques d'affiliation carbonatitique, datés à 76 m.a., permettent de situer la fin de la phase hydrothermale.

Sous une couverture latéritique de 20 à 40 m d'épaisseur et une zone altérée de 15 à 60 m d'épaisseur, les pyrites ont subi une altération secondaire par oxydation jusqu'à des profondeurs de 80 à 140 m. Le front redox est marqué par une couleur de roche passant du jaune-ocre au gris-vert. Au voisinage des fissures aquifères, le front redox atteint de plus grandes profondeurs. La mobilisation minérale dans la zone oxydée et la précipitation juste en dessous du front redox a produit une minéralisation secondaire de pechblende, partiellement en nodules en combinaison avec de la pyrite secondaire. Cette dernière, parfois liée à du Cd, présente un rapport δS de -13 ‰, alors que les pyrites hydrothermales ont un rapport δS de -3.63 à +1.24 ‰. La faible valeur du premier rapport est attribuée à une action bactérienne. Au voisinage immédiat du front redox, la dissolution des feldspaths potassiques devient visible, et la teneur en kaolinite commence à augmenter. Le changement de couleur au front redox est causé par la présence d'oxydes hydreux de fer qui, avec le temps, se transforment d'hydroxydes amorphes de fer en goéthite et hématite. Du côté oxydé du front, on trouve fréquemment de l'alun et de la jarosite. Au front redox, la porosité passe de 5 à 8 % (presque doublée).

On trouve de la gibbsite au contact latérite-roche altérée, lorsque les feldspaths potassiques ont été éliminés. Beaucoup des TRs sont associées à des argiles riches en phosphates, comprenant aussi les minéraux du groupe crandallite. Ces TRs semblent difficilement mobilisables par les fluides d'altération oxydants. On n'a observé qu'une légère décroissance des teneurs en TRs de la roche oxydée à la roche réduite, la décroissance étant toutefois plus marquée pour les Terres Rares légères. Il y a certains indices d'une séparation de Ce et Eu des autres TRs.

Preface

The Poços de Caldas Project was designed to study processes occurring in a natural environment which contains many features of relevance for the safety assessment of radioactive waste disposal. The study area, in the State of Minas Gerais, Brazil, is a region of high natural radioactivity associated with volcanic rocks, geothermal springs and uranium ore deposits. It contains two sites of particular interest on which the project work was focussed: the Osamu Utsumi uranium mine and the Morro do Ferro thorium/rare-earth ore body. The first site is notable in particular for the prominent redox fronts contained in the rock, while Morro do Ferro was already well-known as one of the most naturally radioactive locations on the surface of the Earth, owing to the high thorium ore grade and the shallow, localised nature of the deposit.

The features displayed by these two sites presented the opportunity to study a number of issues of concern in repository performance assessment. The four objectives set after the first-year feasibility study were:

1. Testing of equilibrium thermodynamic codes and their associated databases used to evaluate rock/water interactions and solubility/speciation of elements.
2. Determining interactions of natural groundwater colloids with radionuclides and mineral surfaces, with emphasis on their role in radionuclide transport processes.
3. Producing a model of the evolution and movement of redox fronts, with the additional aim of understanding long-term, large-scale movements of trace elements and rare-earths over the front (including, if possible, natural Pu and Tc).
4. Modelling migration of rare-earths (REE) and U-Th series radionuclides during hydrothermal activity similar to that anticipated in the very near-field of some spent-fuel repositories.

The project ran for three and a half years from June 1986 until December 1989 under the joint sponsorship of SKB (Sweden), NAGRA (Switzerland), the Department of the Environment (UK) and the Department of Energy (USA), with considerable support from a number of organisations in Brazil, notably Nuclebrás (now Urânio do Brasil). The first-year feasibility study was followed by two and a half years of data collection and interpretation, focussed on the four objectives above.

This report is one of a series of 15, summarising the technical aspects of the work and presenting the background data. A complete list of reports is given below. Those in series A present data and interpretations of the sites, while those in series B present the results of modelling the data with performance assessment objectives in mind. The main findings of the project are presented in a separate summary (no. 15).

The work presented in this report is a detailed description of the mineralogy, geochemistry and uranium ore genesis of the Osamu Utsumi mine, which forms the basis for many of the modelling calculations and interpretations, with direct input into all four major objectives.

Poços de Caldas Project Report Series

Series A: Data, Descriptive, Interpretation

Report No.	Topic	Authors (Lead in Capitals)
1.	The regional geology, mineralogy and geochemistry of the Poços de Caldas alkaline caldera complex, Minas Gerais, Brazil.	SCHORSCHER, Shea.
2.	Mineralogy, petrology and geochemistry of the Poços de Caldas analogue study sites, Minas Gerais, Brazil. I: Osamu Utsumi uranium mine.	WABER, Schorscher, Peters.
3.	Mineralogy, petrology and geochemistry of the Poços de Caldas analogue study sites, Minas Gerais, Brazil. II: Morro do Ferro.	WABER.
4.	Isotopic geochemical characterization of selected nepheline syenites and phonolites from the Poços de Caldas alkaline complex, Minas Gerais, Brazil.	SHEA.
5.	Geomorphological and hydrogeological features of the Poços de Caldas caldera and the Osamu Utsumi mine and Morro do Ferro analogue study sites, Brazil.	HOLMES, Pitty, Noy.
6.	Chemical and isotopic composition of groundwaters and their seasonal variability at the Osamu Utsumi and Morro do Ferro analogue study sites, Poços de Caldas, Brazil.	NORDSTROM, Smellie, Wolf.
7.	Natural radionuclide and stable element studies of rock samples from the Osamu Utsumi mine and Morro do Ferro analogue study sites, Poços de Caldas, Brazil.	MacKENZIE, Scott, Linsalata, Miekeley, Osmond, Curtis.
8.	Natural series radionuclide and rare-earth element geochemistry of waters from the Osamu Utsumi mine and Morro do Ferro analogue study sites, Poços de Caldas, Brazil.	MIEKELEY, Coutinho de Jesus, Porto da Silveira, Linsalata, Morse, Osmond.

Report No.	Topic	Authors (Lead in Capitals)
9.	Chemical and physical characterisation of suspended particles and colloids in waters from the Osamu Utsumi mine and Morro do Ferro analogue study sites, Poços de Caldas, Brazil.	MIEKELEY, Coutinho de Jesus, Porto da Silveira, Degueldre.
10.	Microbiological analysis at the Osamu Utsumi mine and Morro do Ferro analogue study sites, Poços de Caldas, Brazil.	WEST, Vialta, McKinley.

Series B: Predictive Modelling and Performance Assessment

11.	Testing of geochemical models in the Poços de Caldas analogue study.	BRUNO, Cross, Eikenberg, McKinley, Read, Sandino, Sellin.
12.	Testing models of redox front migration and geochemistry at the Osamu Utsumi mine and Morro do Ferro analogue study sites, Poços de Caldas, Brazil.	Ed: MCKINLEY, Cross, Haworth, Lichtner, MacKenzie, Moreno, Neretnieks, Nordstrom, Read, Romero, Scott, Sharland, Tweed.
13.	Near-field high-temperature transport: Evidence from the genesis of the Osamu Utsumi uranium mine, Poços de Caldas alkaline complex, Brazil.	CATHLES, Shea.
14.	Geochemical modelling of water-rock interactions at the Osamu Utsumi mine and Morro do Ferro analogue study sites, Poços de Caldas, Brazil.	NORDSTROM, Puigdomènech, McNutt.

Summary Report

15.	The Poços de Caldas Project: Summary and implications for radioactive waste management.	CHAPMAN, McKinley, Shea, Smellie.
-----	---	-----------------------------------

Contents

Abstract	page
Preface	i
	vii
1. Introduction	1
2. Geological setting	1
3. Analytical methods	7
4. Borehole description and sampling	9
5. Host rock mineralogy and geochemistry	10
5.1. Petrography, mineralogy and mineral chemistry	11
5.1.1. Phonolitic rocks	11
5.1.1.1. Modal composition	13
5.1.1.2. Porosity measurements	13
5.1.1.3. Hydrothermal mineral assemblage	17
5.1.1.4. Mineralisation assemblages	20
5.1.1.5. Fluid inclusions	25
5.1.1.6. Clay mineralogy	28
5.1.2. Nepheline syenites	32
5.1.2.1. Modal content	32
5.1.2.2. Hydrothermal assemblage	33
5.1.2.3. Mineralisation assemblage	34
5.1.2.4. Clay mineralogy	34
5.1.3. Breccia bodies	36
5.1.3.1. Nepheline syenite fragments	37
5.1.3.2. Phonolitic fragments	38
5.1.3.3. Breccia matrix	38
5.1.4. Oxidised zone	44
5.1.4.1. Modal content	46
5.1.4.2. Porosity measurements	46
5.1.5. Weathering cover	47
5.1.5.1. Saprolite	48
5.1.5.2. Laterite	49
5.1.5.3. Modal content	50
5.1.5.4. Porosity measurements	50
5.1.5.5. Mineralogy	50
5.2. Geochemistry	59
5.2.1. Phonolites	59
5.2.1.1. Major elements	68
5.2.1.2. Trace elements	69
5.2.1.3. Rare-earth elements (REEs)	76
5.2.2. Nepheline syenites	82
5.2.2.1. Major elements	82
5.2.2.2. Trace elements	87
5.2.2.3. Rare-earth elements	87
5.2.3. Breccia bodies	90
5.2.3.1. Major elements	90
5.2.3.2. Trace elements	95
5.2.3.3. Rare-earth elements	95
5.2.4. Weathering cover	99

	page
6. Fracture mineralogy	108
6.1. Description of selected water-bearing fractures	108
7. Ultramafic lamprophyres	115
7.1. Petrography and mineralogy	116
7.1.1. Phlogopite-bearing ultramafic lamprophyre	116
7.1.2. “Carbonate-apatite” ultramafic lamprophyre	121
7.2. Geochemistry	123
7.2.1. Major elements	123
7.2.2. Trace elements	125
8. Uranium mineralisation	128
8.1. Mineralogy and mineral chemistry	128
8.1.1. Hydrothermal hypogene mineralisation	128
8.1.2. Supergene mineralisation	129
8.2. Geochemistry	131
9. Redox fronts	131
9.1. Mineralogy	134
9.2. Autoradiography	138
9.3. Porosity	138
9.4. Geochemistry	142
10. Discussion	153
10.1. Hypergene alteration	154
10.2. Supergene alteration	157
11. Acknowledgements	158
12. References	159
13. Plates	165
APPENDICES:	
Appendix 1: Mineralogical, geochemical and sulphur isotope studies of selected pyrite samples and pyrite generations from the Osamu Utsumi mine site, Poços de Caldas, Brazil	173
Appendix 2: Selective phase extraction analyses on four rock samples from the Osamu Utsumi mine site, Poços de Caldas, Brazil	225
Appendix 3: Mineral chemistry studies of rocks from the Osamu Utsumi uranium mine, Poços de Caldas, Brazil	249
Appendix 4: Whole-rock geochemical data and geochemical profiles of boreholes F1, F3 and F4	321
Appendix 5: Mineralogy of borehole F4	361
Appendix 6: Mineralogy and geochemistry of redox front I (RFI)	409
Appendix 7: Detailed geological logs of boreholes F1, F3 and F4	485

Abbreviations

LAT	-	laterite
SAP	-	saprolite
LPh	-	leucocratic phonolite
VLP	-	volcanic leucocratic phonolite
CpxPh	-	clinopyroxene-bearing phonolite
PlcPh	-	pseudoleucite-bearing phonolite
PlcCpxPh	-	pseudoleucite-clinopyroxene-bearing phonolite
NeS	-	nepheline syenite xenolith
VBr	-	volcanic breccia
UMD	-	ultramafic dyke (lamprophyre)
PhD	-	phonolite dyke
PL	-	phlogopite-bearing lamprophyre
RF	-	redox front

ox.	-	oxidised
red.	-	reduced

a.	-	argillic
b.	-	brecciated
f.	-	fractured
l.	-	leached
m.	-	mineralised
vm.	-	vein mineralisation

red	-	red
br	-	brown
whi	-	white
yel	-	yellow
gre	-	green

Analysed Sample Series F4-353

Ns	-	nepheline syenite xenolith
VB	-	volcanic breccia
PhD	-	phonolite dyke

1. Introduction

The Osamu Utsumi uranium deposit is located 15 km to the south of the city of Poços de Caldas in the state of Minas Gerais, Brazil (Fig. 1). It is closely related to a circular internal structure positioned within the larger ring structure of the Poços de Caldas Alkaline Complex (Almeida Filho and Paradella, 1977). This ring structure is of Mesozoic age and comprises a suite of alkaline volcanic, subvolcanic and plutonic rocks, generally containing whole-rock concentrations of U, Th and rare-earth elements (REEs) typical for alkaline rocks. Regional postmagmatic (deuteric) hydrothermal alteration of the complex resulted in widespread pervasive argillation and zeolitisation of the rocks. Some mobilisation and concentration of U, Th and REEs probably also occurred at this stage (Schorscher and Shea, this report series; Rep. 1). Subsequently, several different hydrothermal events of local extent, related to the formation of volcanic breccia pipes, led to the formation of a number of radioactive anomalies of economic importance.

In the Osamu Utsumi mine area, extensive prospecting began in 1971 and, six years later, open-pit mining activity commenced; processing of uranium into yellow cake began in 1982. With some short interruptions, the production of uranium continued until 1988 when, for economic reasons, mining activities were finally stopped.

2. Geological setting

The Osamu Utsumi open-pit mine covers an area of about two square kilometres located in the rounded hilly landscape surrounding Poços de Caldas (see Plates 1 and 2). Drainage of the area is controlled by a network of small, shallow valleys which discharge into the main valley heading towards the north-north-west. This valley crosses the northern part of the mine area. The uranium deposit is defined by a primary low-grade disseminated U-Zr (REE-Mo)-mineralisation and a high-grade stockwork vein Zr-REE-U-Th-Mo mineralisation emplaced in various host rocks that have been altered by hydrothermal solutions in a roughly concentric zonal pattern. In the literature these host rocks are described as “potassic rocks” to stress their main geochemical characteristic (Utsumi, 1971; Oliveira, 1974; Gorsky and Gorsky, 1974; Almeida Filho and Paradella, 1977; Ulbrich, 1984). They consist of a suite of hydrothermally and metasomatically altered (femitised) intrusive bodies and flows of volcanic to subvolcanic phonolites, varying in their proportions of mafic minerals, and nepheline syenites. The

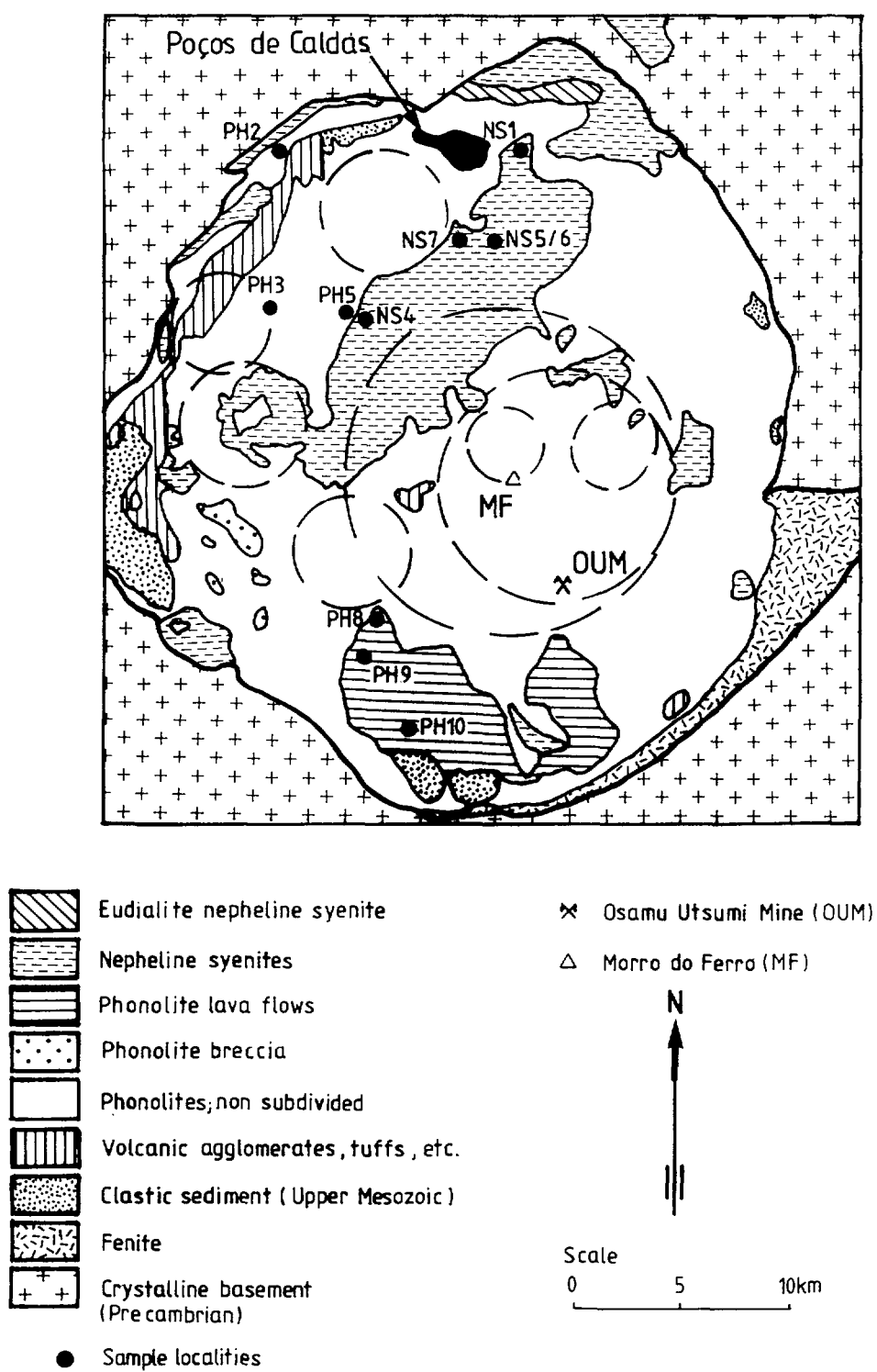


Figure 1. A simplified geological map (after Ellert et al., 1959, and Almeida Filho and Paradella, 1977) of the Poços de Caldas caldera showing the location of all the regional nepheline syenite (NS) and phonolite (PH) samples. Circular features within the caldera are mainly derived from topographic analysis.

hydrothermal alteration and the primary mineralisation are closely related to the intrusion of two major breccia pipes. Late-stage lamprophyric dykes crosscut all rock units, including the breccia pipes, remaining unaffected by these hydrothermal events.

Intense weathering under semi-tropical conditions has resulted in a lateritisation of the uppermost exposed rock, and in a secondary supergene enrichment of uranium along redox fronts, assumed to be the result of downward migrating oxidising groundwaters (Fig. 2). These redox fronts are observed as a marked colour change from reddish-brown to bluish-grey and the transition is sharp, in the order of a few millimetres. The reddish-brown colouration results from the deposition of hydrous ferric oxides. The redox fronts extend to variable depths, following deeply plunging fracture zones and heterogeneities in physical rock properties. The secondary enrichment of uranium on the reduced side of a redox front is very much restricted in its dimensions and occurs adjacent to the front over a distance of a few centimetres to decimetres at the most. The degree of weathering is strongly dependent on the intensity of the hydrothermal alteration and the textural and physical properties of the underlying rock types. A present-day vertical profile within the mine area displays a lateritic cover (including the top soil horizon), followed by a saprolitic horizon, the oxidised hydrothermally altered rock and, finally, the reduced, hydrothermally altered rock (Fig. 3).

For mining activity, the Osamu Utsumi mine has been subdivided into three different areas corresponding to ore bodies A, B and E shown in Figure 4. The ore bodies differ primarily in the type and grade of mineralisation and less in their main geological characteristics (Miranda Filho, 1983; Magno Jr., 1985).

The predominant rock in ore body A is a clinopyroxene-bearing phonolite associated with a leucocratic phonolite and a pseudoleucite-phonolite. A suite of volcanic breccia pipes have intruded these rocks along an old fault system (Miranda Filho, 1983), causing intense fracturing and alteration of the country rocks. The major volcanic breccia pipes have a diameter of about 15 m and intrude the overlying rocks in a near-vertical direction (Fraenkel *et al.*, 1985). Intense brecciation of the country rock induced by these breccia pipes took place over several tens of metres. Late-stage ultramafic lamprophyric dykes not affected by the hydrothermal alteration crosscut the whole lithology. Primary mineralisation mainly occurs within and in the near-vicinity of the volcanic breccia pipes. In contrast, secondary mineralisation along the redox fronts is poorly developed.

Ore body B has a more complex lithology, being composed of nepheline syenites, leucocratic phonolites, clinopyroxene-bearing phonolites and pseudoleucite-phonolites. The intrusion of a major breccia pipe, accompanied by a suite of small-sized breccia pipes, has altered all these rocks to varying degrees of intensity. The major breccia pipe is less

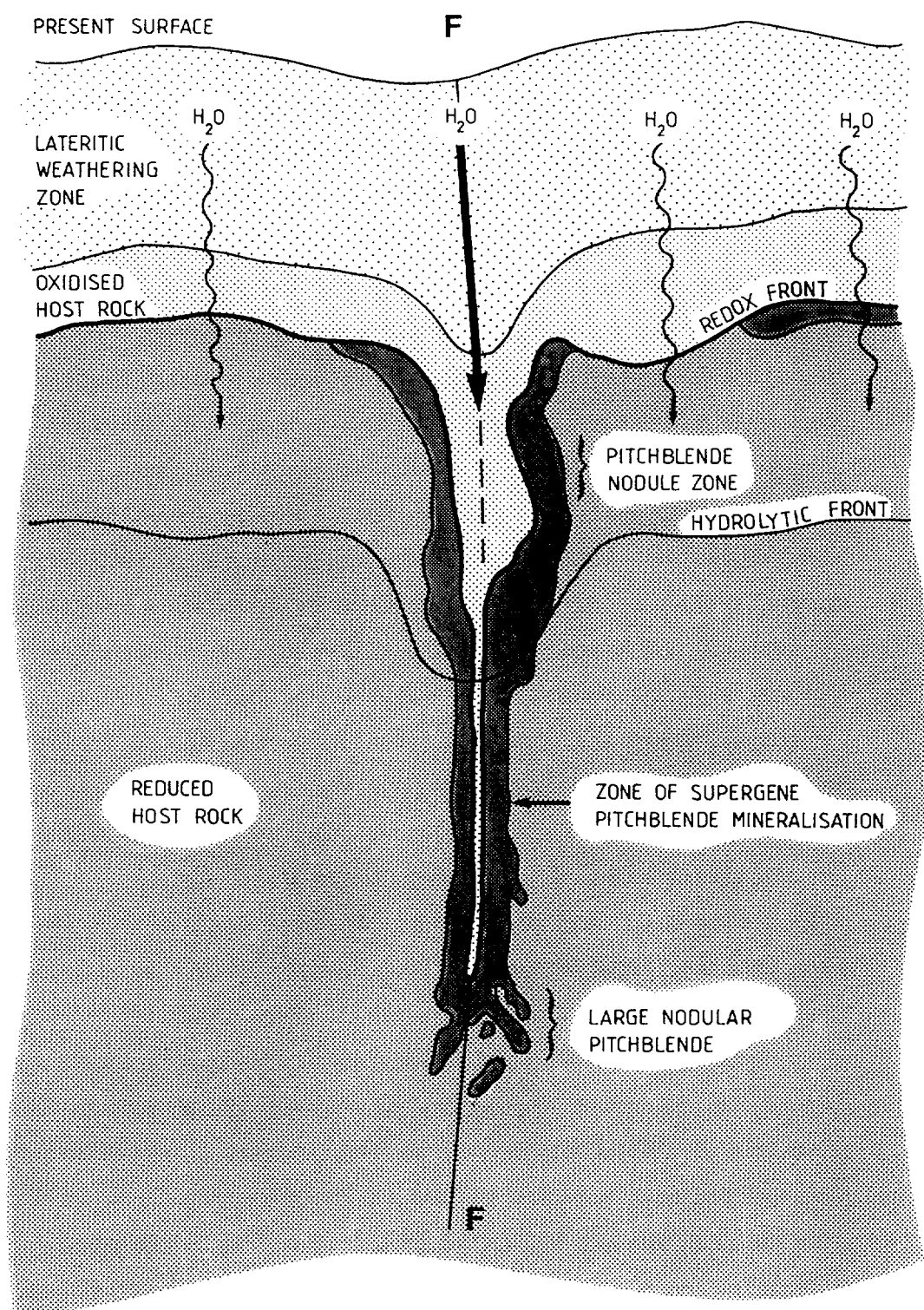


Figure 2. Schematic cross-section from the Osamu Utsumi mine showing the sequence of oxidation with depth, accompanied by supergene uranium mineralisation along the redox front and at greater depths marginal to the conductive fracture zone (F). (After Urânio do Brasil; unpublished report).

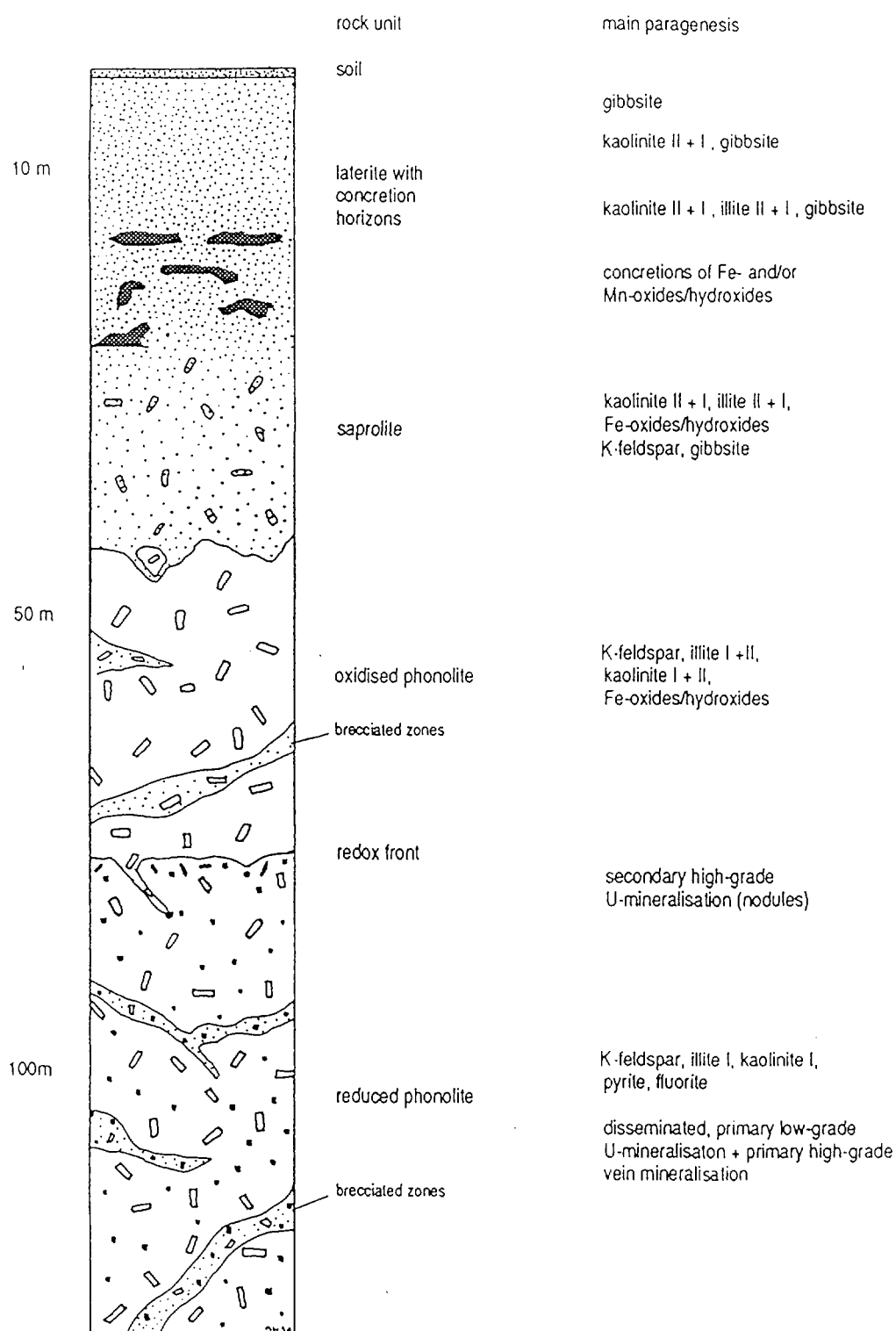
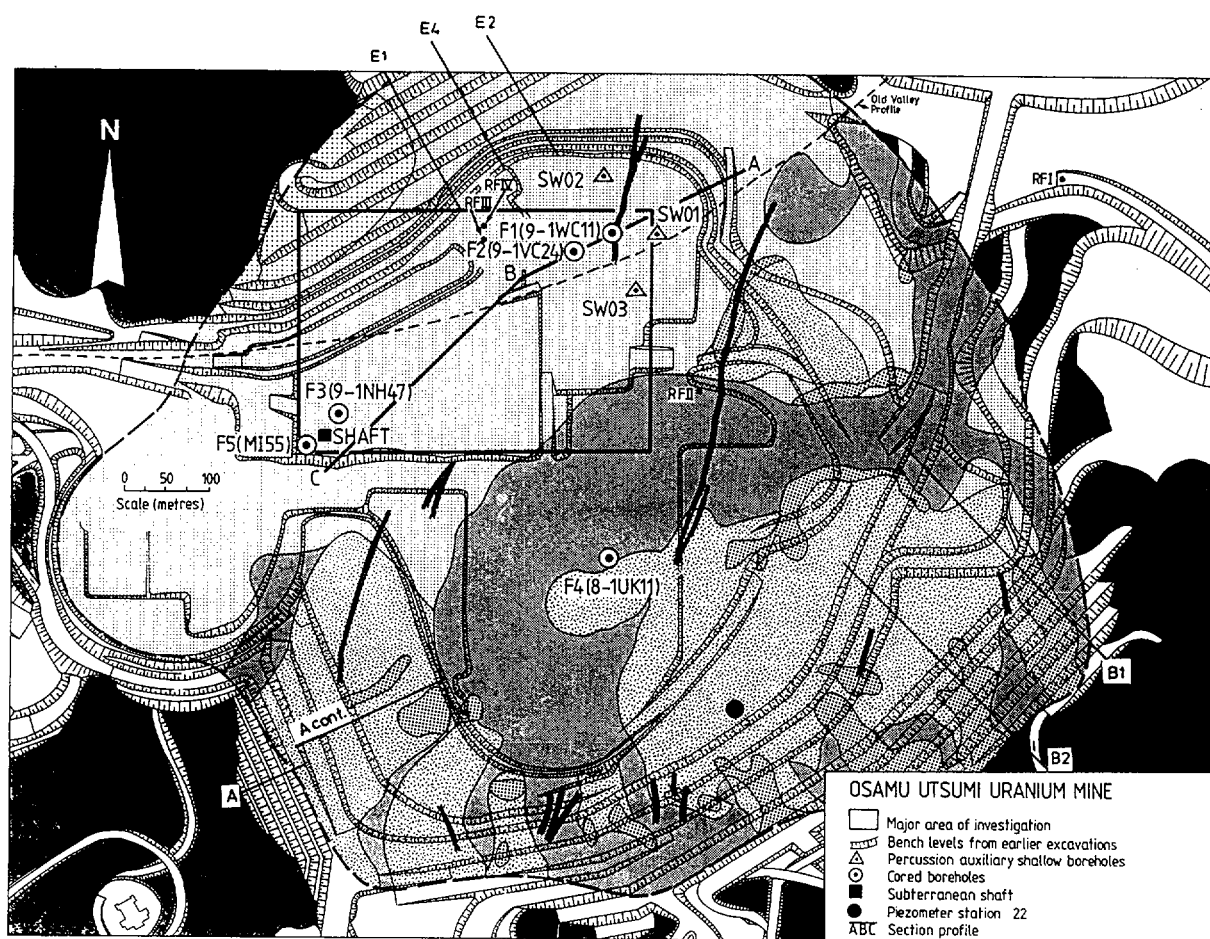


Figure 3. Schematic profile from the original ground surface down to the reduced bedrock in the Osamu Utsumi uranium mine.



- Limit of mapped area**
- (Oldest)
- Subvolcanic phonolite with very weak hydrothermal alteration; no pyrite impregnation.
 - Mainly subvolcanic & minor volcanic phonolites, fractured if near 4.
 - Abyssal & hypabyssal intrusive nepheline syenites (intrusive in 1); fractured if near 4.
 - Subvolcanic pseudoleucite phonolites (intrusive in 1 and 2); fractured if near 4.
 - Subvolcanic conduit breccia, locally grading to extremely xenolithic ultra-fine-grained, flow-textured phonolites.
 - End of major hydrothermal event (formation of "potassic rock" and U-Mo-Zr-REE-pyrite hydrothermal mineralisations).
- (Youngest)
- Biotite-lamprophyre dykes (late-stage intrusive).
- RFI, II, III, IV Location of redox fronts for detailed investigations.
- E1, E2, E4 Vertical profiles in ore body 'E'.
- B1, B2 Vertical profiles in ore body 'B'.
- A Vertical profiles in ore body 'A'.

Figure 4. Osamu Utsumi mine showing the main geological subdivisions, the borehole locations, the groundwater sampling points and the surface exposure rock sampling profiles.

well defined compared to the ones in ore body A and intense brecciation of the country rock occurs to a much larger extent. A well-developed primary vein-type mineralisation dominates, although a similar disseminated mineralisation also occurs to a much more widespread extent than in ore body A. Secondary mineralisation along the redox front is better developed than in ore body A, but is still less intense than in ore body E.

In ore body E, leucocratic phonolites of volcanic and subvolcanic origin and clinopyroxene-bearing phonolites are the predominant rock types. A true volcanic breccia pipe is, however, missing, although the rocks are brecciated to varying degrees. Primary impregnation of the rocks occurred along a complex fracture system and led to a disseminated, medium-grade mineralisation accompanied by a strong vein-type mineralisation. Here, the secondary enrichment along the redox front is best developed, reaching values of up to 2.5 wt.% uranium oxide.

3. Analytical methods

X-ray diffraction (XRD) was used for whole-rock mineral determination and the $<2\mu$ fraction for clay mineral identification. Whole-rock modal content analyses were carried out with a Philips PW1729 diffractometer on a random orientated powder sample using LiF as an internal standard. Using internal calibration curves allowed the quantitative determination of quartz, alkali feldspar, albite, calcite and dolomite with an accuracy of ± 3 wt.%. The internal calibration allows the estimation of the sum of wt.% minerals as compared to 100 wt.%. The difference between the two is then the amount of accessories and sheet silicate minerals. Minerals not detected by this method (amounts of less than about 3 wt.%) were estimated from thin section and verified by pointcounting.

For clay mineralogy investigations, the $<2\mu$ clay fraction was separated through sedimentation of the crushed rock material in an Atterberg cylinder; this procedure was repeated three times. The clay fraction was treated with 2n HCl and saturated with Ca^{2+} . A suspension (clay + solution) was then placed on a glass slide and allowed to evaporate in order to obtain orientated samples. Three preparations were done on each sample (air-dried, glycolated and heated to 550°C) and all were analysed on a Philips APD-system (PW1710) with monochromatic $\text{CuK}\alpha$ -radiation. Clay mineral abundance was estimated using the intensity ratios of the corresponding basal reflections. This method allows only a semi-quantitative determination of the clay mineral content due to variations in crystallinity and mineral chemistry.

Illite-crystallinity was determined to estimate the temperature of formation according to the method of Kübler (1968); a smaller set of samples was corrected according to the methods proposed by Środoń (1980, 1984).

Trace mineral identification was performed using a Guinier camera with FeK α radiation.

Mineral chemical analysis (Appendix 3) was performed on an ARL-SEMQ microprobe equipped with 6 crystal spectrometers and an energy-dispersive system (EDS). Raw data were corrected for beam current drift, dead-time and background (COMIC-ED; Sommerauer, 1981). Final data reduction was performed with a ZAF-correction (EMMA-5/1-86).

Bulk chemical composition (Appendix 4) was determined by automated X-ray fluorescence (XRF) spectrometry on a Philips PW1400 system. Major elements were corrected on-line and trace elements were corrected according to the method of Nisbet *et al.* (1979), modified by Reusser (1986, XRF-System V-86). Glass pellets of fused rock powder mixed with Li₂B₄O₇ in the ratio 5:1 were used to determine major elements, and pressed rock powder pills were used for trace elements. Several samples were analysed for U and Th using a manual XRF-system (Philips PW1410) with internal calibration based on international standards. The advantage of this method compared to the routine analytical XRF-method is the lower detection limit (1 ppm) for U and Th, coupled with better accuracy at low concentrations.

Sulphur and CO₂ were determined by coulometric methods (Coulomat 702).

Atomic absorption was used to determine Cd using a VARIAN SpectrAA300-spectrometer with a graphite tube atomiser (GTA-96).

Scanning electron microscope (SEM) investigations were performed on a CamScan S4 microscope equipped with an energy-dispersive system (Tracor Norton TN 5600). Both secondary and backscatter electron methods were used.

Fluid inclusion analysis was performed on polished sections (100 μ in thickness) using microthermometric methods on a LEITZ microscope equipped with a FLUID INC. adapted USGS gas-flow heating-freezing stage. With this system it is possible to measure temperatures in the range of -180°C to 700°C.

Cathodoluminescence investigations were carried out with a hot cathode instrument with directly heated tungsten filament (Ramseyer *et al.*, 1989). Work conditions were 70 keV and 30 Amps, with exposure times varying from 30 to 240 seconds.

Bulk density (ρ) measurements were also made. The samples were first dried, weighed and coated with molten paraffin wax, followed by immersion in mercury to measure their displaced volume. This method produces errors in the range of 2%. Average grain density

(ρ_g) was determined using He-gas in a Multipycnometer. Total porosity (P) was calculated from grain density and bulk density according to the formula $P = (1 - \rho/\rho_g) \cdot 100$.

REE and selected trace element analyses were performed by Inductively-Coupled Plasma Mass Spectrometry (ICP-MS) at the Scottish Universities Reactor Research Centre (S.U.R.R.C.) at East Kilbride, Scotland (see MacKenzie *et al.*, this report series; Rep. 7).

4. Borehole description and sampling

Five deep boreholes (F1 to F5) were drilled in the Osamu Utsumi mine (Fig. 4). Drillcore logging and sampling of boreholes F1, F3 and F4 was carried out immediately following core extraction at the drill-site (Appendix 7); borehole F5 was percussion-drilled and used only for groundwater sampling.

Borehole F1 (mine coordinates 9-1WC11) was drilled vertically in ore body E from level 9 of the mine (1324 m.a.s.l.) down to a depth of 126 m. The drillcore consisted mainly of oxidised and reduced volcanic and subvolcanic leucocratic phonolites. Redox fronts were encountered at three different depths in the borehole (34 m, 42 m and 67 m), the two deeper fronts being clearly fracture-related. A strong secondary U-mineralisation was present at the 42 m front.

Borehole F2 (mine coordinates 9-1VC24) was located some 30 m away from borehole F1 and reached a depth of 60 m. It was drilled in the same rock suite as F1, although here the phonolites were more intensely brecciated and mineralised. Oxidised bedrock was encountered in the first 21 m of the drillcore and between 36 – 39 m and 43 – 44 m within fracture-related zones.

Borehole F3 (mine coordinates 9-1NH47), located close to ore body A, was drilled to 80 m at an inclination of 55° to the horizontal plane in a south-west direction from level 9 of the mine. The top and bottom of the drillcore consisted of leucocratic pseudoleucite-phonolite with enclosed clinopyroxene-bearing pseudoleucite-phonolite. Generally, the leucocratic phonolite was more strongly affected by brecciation. Mineralisation mainly occurred in breccia veins and along the contact zones of the two rock types. Oxidised bedrock was crossed only in a small zone marginal to a fracture at a depth of 4.5 m.

Borehole F4 (mine coordinates 8-1UK11) was drilled in the brecciated zone of ore body B to study the sequence of hydrothermal alteration and mineralisation around the breccia pipe. The inclined borehole (55°) extends from mine level 8 (1332 m.a.s.l.) and

good core recovery was obtained over the entire length (414.76 m). The core mainly consists of strongly brecciated phonolitic and nepheline-syenitic rocks; unfortunately, unaltered nepheline syenite was not penetrated. Deep-seated U-mineralisations were encountered mainly in two zones at depths of 210 – 250 m and 270 – 275 m respectively within the borehole. The main redox front was crossed at a depth of 42 m and two small, fracture-related oxidised zones occurred at 34 m and 70 m. None of the zones contained secondary U-mineralisation.

To further study the redox front phenomenon, and to understand how weathering processes respond to different parent rocks, additional sampling was done along profiles within the mine area (Fig. 4). In all the ore bodies, weathering processes have been studied in mine exposures representing the lowest mine level up to the original surface. Redox front paragenesis has been studied in four profiles (RFI – RFIV) selected from leucocratic phonolite (RFI and RFIII), clinopyroxene-bearing phonolite (RFII) and phonolitic breccia (RFIV).

From the drillcore samples, one third was kept as reference material, and the remaining two thirds were used for mineralogical, geochemical and isotope analyses. Thin and polished sections were first prepared for microscopic investigations and the remaining core material was then crushed and milled using agate. The rock powder was subsequently split into equal aliquots used for different analytical methods. Special care was taken during the preparation to avoid any contamination of the samples.

5. Host rock mineralogy and geochemistry

The rocks in the Osamu Utsumi mine can be divided into four major units: the phonolitic rocks, the nepheline-syenitic rocks, the breccias and the ultramafic dyke rocks. Phonolitic and nepheline-syenitic rocks suffered intense hydrothermal alteration related to the intrusion of the volcanic breccia pipes. The hydrothermal alteration resulted in very K-feldspar-rich rocks similar to K-feldspar fenites found around the topmost part of certain carbonatite intrusions, for instance at Songwe, Tanzania (Brown, 1964), Kaiserstuhl, Germany (Sutherland, 1967), and Zambia (Bailey, 1966). A subdivision of these host rocks based on inferred primary compositions (e.g. tinguaitite, khibinite, foyaite; see Utsumi, 1971; Magno Jr., 1985) was therefore omitted due to the strong alteration which occurred. Thus a classification of the rocks is impossible in the strict sense of the IUGS Subcommittee on the Systematics of Igneous Rocks (Streckeisen and Le Maître, 1979).

The intrusion of the ultramafic dykes post-dates the hydrothermal alteration of the bulk rocks at the Osamu Utsumi mine. The dykes did not suffer hydrothermal alteration and display only minor deuteritic alteration phenomena.

5.1. Petrography, mineralogy and mineral chemistry

5.1.1. Phonolitic rocks

Hydrothermally altered phonolites represent the major part of the exposed mine area; their occurrence within the mine area and the boreholes is given in Figure 4 and described for the drillcores in Appendix 7. All the phonolites are genetically closely related and represent different phases of emplacement during magmatic activity. Contact phenomena between the single phonolitic stocks and flows are lacking, or only poorly developed, both in the recovered drillcores and mine walls. Well-developed reaction zones only occur around dykes that were intruded during a late stage of the hydrothermal activity.

The phonolitic rocks may be subdivided into the following types according to differences in textural features and modal and chemical composition:

- subvolcanic leucocratic phonolite,
- subvolcanic clinopyroxene-bearing phonolite,
- subvolcanic pseudoleucite phonolite,
- subvolcanic pseudoleucite-clinopyroxene-bearing phonolite,
- volcanic leucocratic phonolite,
- leucocratic phonolitic dykes.

The leucocratic phonolite is the most abundant phonolite within the Osamu Utsumi mine. This light-grey to reddish-grey rock is porphyritic in texture with a fine-grained matrix. Heterogeneously distributed alkali feldspar and pseudomorphically replaced nepheline form the only phenocrysts, varying in size from 1 to 20 mm. The matrix ranges between 40 and 80% of the total rock volume, with an average of about 60%. It is composed of non-orientated small-sized alkali feldspar laths with diameters of 0.2-0.6 mm and clay minerals. Pseudomorphs of primary mafic components and magmatic accessories are rare.

Angular to subrounded xenoliths, either of phonolitic or nepheline-syenitic composition, with diameters ranging from 5 to 30 mm, occur throughout the leucocratic

phonolite. Less frequent are amygdaloidal structures (3 – 20 mm in diameter) with radially arranged intergrowths of alkali feldspar and clay minerals, both pseudomorphic after pseudoleucite.

The clinopyroxene-bearing phonolite (cpx-phonolite) is fine-grained, porphyritic in texture and grey to dark greenish-grey in colour, depending on its alteration state. In the north-western part of the mine this rock is virtually unaffected by the hydrothermal alteration developed in the more central part of the mine. In this state, the cpx-bearing phonolite exhibits preserved clinopyroxene (0.3–3 mm), alkali feldspar (0.5–2 mm) and pseudomorphically replaced nepheline (0.5–2 mm) and minor pseudoleucite as phenocrysts. The fine-grained matrix constitutes up to 75% of the total rock volume and consists of alkali feldspar (0.01–0.1 mm), clinopyroxene (0.05–0.1 mm) and clay minerals, together with minor amounts of giannettite and traces of apatite and sphene.

In the central part of the mine, clinopyroxene and giannettite are completely replaced by cryptocrystalline phases. Here alkali feldspar and clay minerals, together with leucoxene, are the major components of the cpx-phonolite.

Xenoliths of mainly nepheline-syenitic composition and amygdaloidal structures are less frequent than in the leucocratic phonolite.

The pseudoleucite phonolite (plc-phonolite) is mainly exposed in the southern part of the mine (Fig. 4). It is a hololeucocratic porphyritic rock with alkali feldspar and pseudoleucite as the main phenocrysts. The grain-size of the alkali feldspar phenocrysts varies between 0.5 and 5 mm and seldom reaches diameters up to 10 mm. Pseudoleucite, by contrast, has a much larger variation in grain-size (0.5–30 mm); in certain cases it may even reach 6 cm in diameter. Pseudomorphic nepheline is only rarely found as phenocrysts (0.5–3 mm) but is always present in the fine-grained matrix. Alkali feldspar (0.02–0.1 mm) is the main component of the matrix, which makes up about 60–70% of the total rock volume. In addition, clay minerals and very few magmatic accessories occur. In various parts, the matrix alkali feldspar laths display a flow orientation.

Xenoliths of both phonolitic and nepheline-syenitic origin are common. Subordinate amygdaloidal structures with radially arranged infillings of alkali feldspar and clay minerals occur.

The pseudoleucite-clinopyroxene-bearing phonolite (plc-cpx-phonolite) is very similar to its pseudoleucite-free counterpart. It is a leucocratic fine-grained porphyritic rock that has its largest extent in the western part of the mine. This phonolite is characterised by pseudoleucite (0.3–20 mm) as a major phenocryst, besides alkali feldspar (0.3–10 mm), and by the occurrence of pseudomorphically replaced clinopyroxene as a minor component in the matrix. Pseudomorphic nepheline is present

in minor amounts both as phenocrysts (0.2 – 5 mm) and as a matrix component. The fine-grained matrix varies between 55 – 65% of the total rock volume and has an average grain-size of about 0.05 mm. Matrix alkali feldspars are often flow-orientated, especially in marginal parts of the single units where accumulations of xenoliths also occur.

The volcanic leucocratic phonolite has, in contrast to its subvolcanic counterpart, a very fine-grained aphanitic matrix with an average grain-size less than 0.02 mm. Recrystallised vitreous parts may often be observed. The matrix is mainly composed of very fine-grained alkali feldspar and makes up 60 – 70% of the total rock volume. Alkali feldspars in the matrix and as phenocrysts are often flow-orientated. Besides alkali feldspar (0.5 – 10 mm), pseudomorphic nepheline (0.3 – 2 mm) is the only other phenocryst present. Pseudomorphs of mafic components and primary magmatic accessories are very rare.

5.1.1.1. Modal composition

A qualitative compilation of the mineralogical composition derived from microscopic and X-ray diffractometric investigations of the different phonolitic rocks is given in Table I. Components that occur only sporadically in trace or minor amounts, but are important for genetic considerations, are listed in the column labeled “other”. The weight percent modal abundance of alkali feldspar, together with the relative abundance of the clay minerals in the <2 μ fraction (determined by XRD), are listed in Table II.

5.1.1.2. Porosity measurements

Total porosity, density and grain density display a very heterogeneous pattern in the hydrothermally altered rocks of the mine. Strongly leached zones of high porosity randomly alternate with more dense zones of low porosity. There is no doubt that the porosity encountered today in the mine rocks is of hydrothermal and recent weathering origin. Porous zones developed during the hydrothermal alteration act today as conductive zones. During the rainy seasons the high water-flow flushes out the clay minerals, continually increasing the porosity of the zone.

Table III gives a compilation of physical rock properties for the different rock types; it becomes obvious that all the hydrothermally altered phonolites of the mine have elevated porosity when compared to their unaltered counterparts. The increase in

TABLE I

Qualitative mineralogical composition of the different hydrothermally altered rock types from the Osamu Utsumi uranium mine.

Hydrothermally altered rocks	Hydrothermal mineral assemblage												Mineralisation and gangue mineral assemblage			
	Kf	Ne	PsI	Cpx	Ab	Sphe	Ap	Ill	Kao	Chl	Sm	Other	Py	Spha	cryP	U-P
Reduced zone																
nepheline syenite	M	M*	m	m*	0-tr	tr*		M	m	tr	m	tr	m	0-tr	m	0-tr
leucocratic phonolite	M	M*	0-tr	0-tr	0-tr			M	M	tr	tr	tr	m	0-tr	tr-m	0-tr
cpx-bearing phonolite	M	M*	tr	M*	0-tr	tr*	0-tr	M	m	tr	m	tr	tr-m		m	0-tr
pseudoleucite-phonolite	M	m*	M					M	M			tr	m		tr-m	0-tr
plc-cpx-bearing phonolite	M	m*	m	m*		tr*	0-tr	M	M	0-tr	tr	tr	m		m	0-tr
volcanic leucocratic phonolite	M	M*	0-tr	0-tr	0-tr			m	M	0-tr	0-tr	tr	tr-m	0-tr	tr-m	0-tr
Oxidised zone																
nepheline syenite	M	M*	m	m*	0-tr	tr*		M	m	tr	tr	tr			m	
leucocratic phonolite	M	M*	0-tr	0-tr	0-tr			M	M	tr	tr	tr			m	
cpx-bearing phonolite	M	M*	tr	M*	0-tr	tr*		M	m	tr	m	tr			m	
pseudoleucite-phonolite	M	m*	M					M	M			tr			m	
plc-cpx-bearing phonolite	M	m*	m	m*		tr*		M	M	0-tr	tr	tr			m	
volcanic leucocratic phonolite	M	M*	0-tr	0-tr	0-tr			M	M	tr	0-tr	tr			m	
Components: <div style="display: flex; justify-content: space-between;"> <div> <p>Kf – alkali feldspar</p> <p>Ne – nepheline, *replaced</p> <p>M – major, > 10 vol. %</p> <p>m – minor, 1-10 vol. %</p> <p>tr – trace, < 1 vol. %</p> <p>PsI – pseudoleucite</p> <p>Cpx – clinopyroxene, *replaced</p> <p>Ab – albite</p> <p>Sphe – sphene, *replaced</p> <p>Ap – apatite</p> <p>Ill – illite and sericite</p> <p>Kao – kaolinite</p> </div> <div> <p>Chl – chlorite</p> <p>Sm – smectite</p> <p>Py – pyrite</p> <p>Spha – sphalerite</p> <p>cryP – cryptocrystalline phases (mainly Fe-Ti)</p> <p>U-P – cryptocrystalline U-phases</p> <p>Mo-P – cryptocrystalline Mo-phases</p> <p>Zir – zircon, incl. cryptocryst. Zr-REE phases</p> <p>Mon – monazite group minerals</p> </div> <div> <p>Flu – fluorite</p> <p>Carb – carbonate</p> <p>FeOx – hematite, goethite, amorph. Fe-hydroxide</p> <p>Other – pyrophyllite, alunite, jarosite, florencite, goyazite, gorceixite</p> </div> </div>																

TABLE II
Modal and clay mineralogical composition of the different hydrothermally altered rock types from the Osamu Utsumi uranium mine.

Hydrothermally altered rocks	Whole-rock			Clay fraction			
	Kf wt. %	Cpx* vol. %	Other*	Ill %	Kao %	Sm %	Chl %
<u>Reduced zone</u>							
nepheline syenite	76 (60-85)	< 10	5-10	60	18	20	2
leucocratic phonolite	63 (50-75)	< 1	3-10	43	52	2	3
cpx-bearing phonolite	38 (33-45)	15-25	5-10	71	14	14	< 1
pseudoleucite-phonolite	60 (55-80)	< 1	2-5	32	66	< 1	< 1
plc-cpx-bearing phonolite	44 (40-50)	< 10	5-10	58	40	< 1	< 1
volcanic leucocratic phonolite	63 (60-66)	< 1	2-5	11	84	2	3
<u>Oxidised zone</u>							
nepheline syenite	51 (40-65)	< 10	3-7	75	18	6	< 1
leucocratic phonolite	50 (40-60)	< 1	3-10	47	44	2	7
cpx-bearing phonolite	38 (35-45)	15-20	5-10	62	35	2	< 1
pseudoleucite-phonolite	48 (40-57)	< 1	2-5	48	46	5	< 1
plc-cpx-bearing phonolite							
volcanic leucocratic phonolite	55 (50-65)	< 1	2-5	47	47	< 1	5

Abbreviations:

Kf	– alkali feldspar	Ill	– illite
Cpx	– clinopyroxene	Kao	– kaolinite
Other	– pyrite, fluorite, REE-phases, Zr-phases etc.	Sm	– smectite
		Chl	– chlorite

*Contents estimated from thin sections.

TABLE III

Rock physical properties of hydrothermally unaltered regional rocks and altered rocks from the Osamu Utsumi mine.

	Density (g/cc)	Grain density (g/cc)	Porosity (%)
Hydrothermally unaltered regional samples			
phonolites	2.57-2.62	2.63	< 1-2
nepheline syenites	2.49-2.55	2.6	1-3.5
Hydrothermally altered mine samples			
<u>Reduced zone</u>			
leucocratic phonolite	2.33-2.53	2.59-2.62	3.5-12
cpx-bearing phonolite, unaltered	2.61	2.57	< 1
cpx-bearing phonolite, altered	2.37	2.56	7
cpx-bearing phonolite, argillaceous	2.37	2.58	12
pseudoleucite-phonolite	2.21-2.34	2.58-2.63	9-16
<u>Oxidised zone</u>			
nepheline syenite	2.21-2.3	2.56-2.61	12-15
leucocratic phonolite	2.2-2.62	2.62-2.64	1-17
cpx-bearing phonolite	2.28	2.58	12
volcanic leucocratic phonolite	2.11-2.24	2.58-2.84	12-22

porosity ranges from 2% up to 15% for strongly leached samples. Differences in porosity between the single phonolite types can hardly be established. A representative evolution of the porosity during the processes that affected the rocks is displayed by a profile in the cpx-phonolite; the unaltered cpx-phonolite has a porosity of less than 1%. The hydrothermally altered cpx-phonolite with moderate pyrite impregnation has a porosity of about 7%; this is further increased to about 12% in the cpx-phonolite, which displays a strong argillic alteration. The lateral distance between the unaltered sample and the argillic sample is about 30 m. Inbetween these samples occurs a zone with a high pyrite impregnation (<7 vol.%) and a very low porosity of less than 2%.

5.1.1.3. Hydrothermal mineral assemblage

The potassium-rich hydrothermal event resulted in a very similar alteration pattern for all the different phonolites from the Osamu Utsumi mine. In all phonolites, alkali feldspar, illite/sericite and kaolinite are the predominant mineral phases with, depending on the original rock composition, additional pseudomorphically replaced clinopyroxene.

The hydrothermal mineral assemblage, as defined here, comprises all the exchange and replacement products, which includes the accessories of the undisturbed texture of the original igneous rock. Such minerals are mainly alkali feldspar, the replaced nepheline and mafic minerals, and the magmatic accessories.

The clay minerals, which occur as replacement products and precipitates, were formed during the deuteritic and hydrothermal events and are described separately. In the oxidised rock, clay minerals are also formed during weathering.

Minerals formed during different stages of the hydrothermal event, and found as disseminated impregnations in the rocks and/or as vein- and void infillings (e.g. sulphides, fluorite, U-, Th-, REE- and Zr-bearing minerals), are defined here as mineralisation assemblages. K-feldspar precipitated during the hydrothermal event should also be included here; for better comparison, however, it is described together with the bulk of the exchanged alkali feldspar.

A compilation of the chemical analyses for individual minerals is given in Appendix 3.

Alkali feldspar

Alkali feldspar mainly occurs in the phonolites and exhibits four textural variations:

- a) sanidine-shaped euhedral laths and prisms of the matrix,
- b) euhedral laths and tabular phenocrysts,
- c) euhedral tabular alkali feldspar within the amygdaloidal structures, and
- d) xenomorphic to idiomorphic interstitial alkali feldspar that actually belongs to the mineralisation assemblage.

The matrix alkali feldspar and the phenocrysts normally show Karlsbad twinning and exhibit zoning, i.e. a core rich in minute hematite and fluid inclusions grading to a more clear growth rim free of hematite and with few fluid inclusions. The twinning does not continue into this growth rim. A cloudy pigmentation comprising cryptocrystalline material with an easily discernible hematite dissemination is frequently developed along

cleavage planes and microfissures. Additionally, magmatic micropertthitic exsolution structures are commonly observed in the centre of the phenocrysts. A slight argillic alteration is developed in the hematite-dusted cores and along microfissures and grain boundaries.

In the amygdaloidal structures the alkali feldspar occurs as radially arranged euhedral crystals free of hematite inclusions. The slightly argillically altered crystals have a grain-size intermediate between the matrix and the phenocrysts. Clear xenomorphic to idiomorphic alkali feldspar, commonly inclusion-free except for a weak cloudy pigmentation with cryptocrystalline material, is developed in interstices and along fracture planes.

Two different structural states have been distinguished by XRD. The matrix alkali feldspars and the phenocrysts are intermediate microclines varying slightly in the degree of Al-Si ordering. The hydrothermally-formed, clear interstitial alkali feldspars, by contrast, show a readily discernible pattern of a fully ordered, triclinic low microcline.

Under cathodoluminescence, the intermediate microcline phenocrysts show an irregular, patchy red-orange-coloured luminescence in the centre, and a light lilac colouration towards their rims. The same colour zoning occurs in the feldspars of the amygdaloidal structures and the matrix, the latter being mainly lilac-coloured. In contrast, the low microcline which occurs as growth rims and void infillings has a characteristically dull yellow-brown luminescence colouration.

Red luminescence colours in alkali feldspar are due to lattice impurities with Fe^{3+} . Red colours are well-pronounced, for example, in rocks that underwent fenitisation (Marshall, 1988). On the other hand, the dull yellow-brown colour is a characteristic feature of alteration, caused by prolonged electron bombardment of a short-lived luminescence of K-feldspar precipitated from low-temperature solutions (Ramseyer *et al.*, 1989).

Microprobe analyses of all the alkali feldspars yield almost pure orthoclase compositions. Significant chemical variations do not occur between matrix crystals and phenocrysts, between the replaced igneous and the hydrothermally precipitated alkali feldspars, or in the single crystals themselves. Despite the different optical orientation, the albite component of the matrix and phenocryst alkali feldspars have been completely replaced during the hydrothermal events by almost pure, inclusion-free K-feldspar. In a few cases, alkali exchange was not complete so that part of the albite component is still preserved (maximum Ab 9%). Average compositions are:

matrix alkali feldspar	Or _{98.2} Ab _{1.8} An ₀
alkali feldspar phenocrysts	Or _{99.8} Ab _{0.2} An ₀
hydrothermally precipitated low microcline	Or _{98.8} Ab _{1.2} An ₀

In the matrix alkali feldspars and the phenocrysts, iron occurs sporadically as an impurity in measurable contents (0.1 – 0.8 wt.% Fe₂O₃), whereas the hydrothermal low microcline is free of iron impurities. None of the analysed alkali feldspars showed evidence of actinide or lanthanide impurities.

Nepheline

Nepheline is always completely pseudomorphically replaced by illite, kaolinite and, occasionally, subordinate zeolites. Fine-grained illite and kaolinite may be randomly intergrown in such pseudomorphs, but more frequently display a zonal arrangement from a kaolinite-rich central domain to an illite-rich border zone. In the central domain kaolinite is intimately intergrown with similar fine-grained pyrite. In the illite-rich border zone, textural evidence indicates a substitution of kaolinite by somewhat coarser-grained illite/sericite, which also encloses the fine-grained pyrite.

Clinopyroxene

The cryptocrystalline aggregates of iron- and titanium-oxides, together with silicate phases, display an idiomorphic to hypidiomorphic prismatic or acicular habit. By analogy with hydrothermally less altered zones, where relict clinopyroxene (complex zoned aegirine-augite) is still preserved in such aggregates, all these pseudomorphs are considered to be replaced clinopyroxenes. The titanium phases of these aggregates are mainly composed of very fine-grained needle-shaped rutile, but the existence of anatase cannot be excluded. Chemical analyses of the TiO₂-minerals are given in Appendix 3. Iron and niobium are present in minor amounts of up to 4.7 wt.% and 2.8 wt.% respectively; silica, aluminium and yttrium are sporadically present as impurities in trace amounts. The possible presence of REEs was checked by searching for lanthanum, cerium and ytterbium; however, in all the analysed samples these elements were below the level of detection. Uranium and thorium were detected in trace amounts in one sample each, both of which occurred in a massive uranium nodule, and the detected

uranium and thorium concentrations are thought to be contamination from the nodule matrix.

Magmatic accessories

Both magmatic accessory minerals and magmatic mafic minerals occur either in small amounts (<1 and 0–5%, respectively) or are totally absent. Small euhedral zircons (0.05 – 0.6 mm) are sporadically present together with a xenotime-like mineral and apatite. Sphene, otherwise common in the regional rocks, most probably suffered decomposition to Ti-oxides and clay minerals.

Rare metal silicates

A wide variety of these minerals are known from the unaltered regional rocks of the Poços de Caldas complex. They include astrophyllite, aenigmatite, eudialite, lãvenite, catapleite, lamprophyllite and giannettite (Schorscher and Shea, this report series; Rep. 1; Ulbrich, 1984). None of these minerals have been observed in the hydrothermally altered rocks of the mine. Their initial presence, however, is supported by the occurrence of relict giannettite, lamprophyllite and astrophyllite in the unaffected (or only slightly affected) phonolites from the NW delimitation of the open-pit.

5.1.1.4. Mineralisation assemblages

These assemblages include minerals that were formed during the different stages of the hydrothermal event and are found as disseminated impregnations in the rocks and/or as vein and void infillings. They include sulphides, fluorite, U-, Th-, REE-, Ti- and Zr-bearing minerals; K-feldspar and clay minerals, also precipitated during the hydrothermal event, have been described above.

Sulphides other than pyrite (sphalerite, Mo-sulphides, etc), carbonates and Ti-oxides other than the ones replacing mafic minerals sporadically occur in trace amounts in the phonolites, but are more abundant in the breccias (see Section 5.1.3.).

A compilation of the chemical analyses of the individual minerals is given in Appendix 3.

Pyrite

Pyrite is the main ore mineral present in the hydrothermally altered phonolites. Based on textural relationships, pyrite populations of pre-, syn- or post-breccia formation may be discerned. Pre-breccia pyrite, the most important pyrite population in the phonolites, formed during the potassium-rich hydrothermal event, occurs as a finely disseminated mineralisation throughout the phonolites. Syn- and post-breccia pyrites occur in small breccia veins cutting the rocks, in open cavities, and on fracture planes (see below).

The intensity of the pre-breccia pyrite impregnation is strongly dependent on the physical properties of the different phonolite types. The very fine-grained volcanic phonolite is commonly less strongly impregnated than its coarser-grained counterparts. Similarly, zones with strong argillic alteration are devoid of pyrite impregnation. On the other hand, pyrite may easily reach up to six volume-percent in the more porous and leached zones. An average content is difficult to estimate due to irregular distribution, but may lie between 2 and 3 vol.%.

Pre-breccia pyrite exhibits an euhedral cubic shape and ranges in size from very fine-grained to fine-grained (0.005 – 1 mm). Very fine-grained pyrite occurs as a pigmentation throughout the rocks, whereas the somewhat coarser pyrite is more concentrated along grain boundaries and in interstices. There, pyrite often forms clusters of intimately intergrown grains. In the cpx-bearing phonolites, pyrite, together with Ti-oxides and clay minerals, substitutes magmatic aegirine-augite. Frequently, pre-breccia pyrites contain relicts of hematite, indicating earlier hydrothermal (deuteric) processes with lower sulphur activities and/or higher oxygen fugacities.

Chemical compositions of different pyrites are given in Appendix 3. All the analysed grains show an almost pure pyrite composition with an atomic S:Fe ratio of close to 2. Minor detected impurities include Mo (0 – 0.7 wt.%), Pb (0 – 3.7 wt.%) and As (0 – 0.17 wt.%). The impurities of Pb and As are at least partly due to contamination by the sample polishing disk. None of the analysed pyrites indicated detectable amounts of Zn, Co, Ni, Cu, Se, Mn or U.

Pyrites of different textural populations were separated for S-isotope analyses. The sulphur isotope compositions of pre-, syn- and post-breccia pyrites lie within the narrow range of $\delta^{34}\text{S} = +1.24$ to -3.63‰ . Such an isotopic composition is typical for fluids from upper mantle-derived igneous rocks. A detailed description of the S-isotope investigations is given in Appendix 1.

Zircon and Zr-minerals

In the phonolitic rocks zircon and Zr-minerals occur mainly as three morphological types:

- a) fine-grained (<1 mm) idiomorphic to hypidiomorphic zircons randomly distributed as isolated grains in the rock matrix,
- b) idiomorphic to hypidiomorphic zircons of variable grain-size (0.5 – 5 mm) in voids, interstices and along fractures, and
- c) skeletally developed zircons in interstices and along grain boundaries.

Type (a) is subordinate to types (b) and (c). Inhomogeneities in zoning and colour indicate compositional variabilities within single crystals and all are metamict to various degrees. Fine-grained idiomorphic zircon is the least metamict; it is the only zircon that produces a radiation halo in contact with the neighbouring minerals. The other two types of zircon are often merely present as cryptocrystalline mixtures of zircon, baddeleyite and amorphous (hydrous?) Zr-oxide. Single baddeleyite crystals not associated with zircon are present in several phonolite samples.

Microprobe analysis of zircon (Appendix 3) proved to be difficult due to the extent of metamictisation and to an inhomogeneous Zr-standard. Zircon analyses which give a reasonable stoichiometric Zr/Si-ratio normally contain trace amounts of Yb_2O_3 (0 – 0.26 wt.%), Ce_2O_3 (0 – 0.37 wt.%) and Y_2O_3 (0 – 0.68 wt.%); Ce and Y are most probably present as minute monazite and xenotime phases, substituting zircon. HfO_2 is present between 0 – 0.8 wt.% with a $\text{ZrO}_2/\text{HfO}_2$ ratio ranging from 0 – 0.012, values typical for non-metamict zircons from nepheline syenites (Rankama and Sahama, 1950). None of these zircons show measurable contents of U or Th.

Not presented in Appendix 3 is a group of analyses with ZrO_2 -contents which are too high when compared to their SiO_2 -contents, which can be explained by decomposition of zircon to baddeleyite and/or Zr-hydrates during metamictisation. Another group yields similar features, although with additionally high Y_2O_3 -contents (1.2 – 6.3 wt.%), which are most probably due to xenotime substitution. In this group the only detected Th impurities (up to 0.82 wt.%) occur.

Uranium minerals

Cryptocrystalline uranium minerals occur in the phonolites as finely disseminated impregnations. The very fine grain-size of less than 1μ for most of these minerals makes an optical identification very difficult and their localisation is only possible using autoradiography. Higher concentrations of these uranium minerals could be observed in association with aggregates of pyrite and cryptocrystalline semi-opaque phases finely distributed throughout the phonolites and along fractures and in veins. Powder diffraction of uranium mineral concentrates from the pyrite aggregates yielded pure uranium-oxide (pitchblende) ranging between $\text{UO}_{2.25}$ and U_3O_7 . Such uranium-oxides were further observed as inclusions in pyrite. Of the many cryptocrystalline semi-opaque phases, only brannerite (UTiO_6) could be amongst other less well-defined associations of uranium and titanium.

Fluorite

In the phonolitic rocks, fluorite (mostly violet coloured) mainly occurs in interstices and voids and on fracture planes; small amounts of colourless, light yellowish and greenish fluorite can also occur. Grain-size varies from very fine-grained fluorite (<0.2 mm) in interstices to medium-grained, idiomorphic crystals (>10 mm) in open cavities. Interstitial fluorite is always intimately intergrown with pyrite, zircon and low microcline. All the fluorites show abundant fluid inclusions of different generations and inclusions and/or intergrowths of fine-grained carbonate.

Microprobe analyses were performed with F as a fixed element (Appendix 3). All the fluorite investigated was virtually pure; minor impurities found were Ce_2O_3 (0.5 wt.%) in one sample and Y_2O_3 (max. 0.2 wt.%) in seven samples. In all the fluorite samples, K_2O (0.70 – 0.95 wt.%) was detected, and sometimes traces of Na_2O (0 – 0.1 wt.%). At least part of these alkali contents originates from fluid inclusion contamination (see below).

Barite

Barite is a rare mineral in the phonolites. It occurs as well-defined euhedral crystals, mainly in interstices and on fracture planes, where it forms on aggregates of well-preserved K-feldspar, pyrite and clay minerals. Textural evidence indicates that

barite formed during late-stage hydrothermal alteration; in the near-vicinity of the redox fronts, barite is still idiomorphically preserved on corroded K-feldspar.

REE-phases

In the reduced phonolites a broad variety of REE-bearing mineral phases occurs. The list presented below probably does not cover the whole range of REE-phases that occur in the Osamu Utsumi mine. Because of the very fine grain-size and intergrowths of different REE minerals, quantitative chemical analysis was often impossible.

The following REE minerals have been identified by various analytical methods:

monazite (Ce,La,Nd)PO₄

cheralite (Ca,Ce,Th)(P,Si)O₄

bastnaesite (Ce,La)(CO₃)F

crandallite (Ca,REE)Al₃(PO₄)₂(OH)₅ · H₂O

florencite CeAl₃(PO₄)₂(OH)₆

gorceixite (Ba,REE)Al₃(PO₄)₂(OH)₅ · H₂O

goyazite (Sr,REE)Al₃(PO₄)₂(OH)₅ · H₂O

Of the REE-minerals identified, monazite and cheralite are the most abundant. They occur as very fine-grained, idiomorphic crystals disseminated throughout the phonolites, but preferentially cluster around the more porous parts of the rock (Fig. 52). The average grain-size varies between 1–4μ, and, in rare cases, crystals of up to 15μ are observed. Monazite and cheralite occur intimately intergrown with illite, kaolinite, pyrite and K-feldspar and, in several cases, as inclusions in pyrite and fluorite. The textural relationships indicate a purely hydrothermal origin for monazite and cheralite, most probably during an early-stage mineralisation event. The same origin may account for the likewise idiomorphic bastnaesite. Bastnaesite, however, is preferentially found in cavities and interstices and less frequently disseminated throughout the rock matrix.

Less certain is the origin of REE-bearing phases of the crandallite group minerals (crandallite, florencite, gorceixite and goyazite). As discussed below, these minerals are more abundant in the oxidised and lateritic zone. In the reduced zone these minerals occur as small-sized crystals (<3μ) of euhedral shape mainly in open cavities, interstices and on fracture planes. In a few cases crandallite group minerals are found in pyrite as inclusions. Florencite additionally occurs in close association with monazite without

displaying any reaction phenomena. Such textural evidence suggests a hydrothermal origin for the crandallite group minerals. To the authors' knowledge, however, crandallite group minerals have been reported in the literature as being only of supergene origin (e.g. Mariano, 1989, and literature cited therein).

5.1.1.5. Fluid inclusions

Fluid inclusion studies have been performed on three fluorites from the leucocratic phonolite in core samples from borehole F1. The fluorites represent different textural relationships: a xenomorphic, interstitial fluorite (sample WC11-75), a euhedral fluorite from an open cavity (sample WC11-78), and a xenomorphic fluorite mass embedded in clay minerals from a fracture infill (sample WC11-87). All the fluorites are more or less homogeneously violet-coloured.

All inclusions observed in the samples have been investigated for phase transitions in the -80°C to $+500^{\circ}\text{C}$ temperature interval. The following phase transitions were measured (Table IV):

- “first melting” or eutectic temperature (T_{fm}) which indicates the type of dissolved salts,
- liquidus temperature ($T_{\text{m,ice}}$) which indicates the amount of salts present,
- homogenisation temperature (T_{hom}) of the liquid and gas phases which generally gives the minimum temperature at the time the inclusion was trapped in the mineral.

Three different populations of fluid inclusions could be distinguished; all of them are believed to be of secondary origin (J. Mullis, pers. comm., 1990).

Population I

These fluid inclusions have a homogenisation temperature (T_{hom}) of $250^{\circ} - 260^{\circ}\text{C}$ with a liquidus temperature $T_{\text{m,ice}}$ of $-2.9^{\circ} \pm 0.3^{\circ}\text{C}$. The liquid phase belongs to the fluid system $\text{H}_2\text{O-KCl}$ with 7–9 wt.% equivalent KCl. Salt hydrates were observed in all the inclusions. The volume of the gas phase makes up about 15 ± 3 vol.% of the inclusion; no indication of a gas phase other than vapour was detected. This population is found in fluorites occurring interstitially and in fracture infillings (samples WC11-75 and WC11-87), but not in the open cavity fluorites (WC11-78).

TABLE IV
Fluid inclusion data for texturally different fluorites in the leucocratic phonolite from borehole F1.

Sample	Rock	Host mineral	P	N	Type	Gas (vol.%)	S.I.	T _{fm} (°C)	T _{m, ice} (°C)	T _{hom} (°C)	H ₂ O (wt.%)	KCl (wt.%)	CO ₂ (wt.%)
WC11-75	leucocr. phonolite	fluorite, interstitial	I	3	sec.	15	yes	-11	-2.8 ± 0.2	250-260	92-93	7-9	0
			II	4	sec.	10	yes	-10	-2.5 ± 0.3	200-220	92-93	7	0
WC11-78	leucocr. phonolite	fluorite, cavity	II	4	sec.	10	yes	-10	-2.5 ± 0.3	200-220	92-93	7	0
			III	2	sec.	90	yes	-22	-10 ± 1	200-220	55-58	42-45	0
WC11-87	leucocr. phonolite	fluorite, fracture	I	7	sec.	15	yes	-11	-2.9 ± 0.3	250-260	92-93	7-9	0
			II	9	sec.	10	yes	-10	-2.5 ± 0.3	195-220	92-93	7	0
			III	5	sec.	95	yes	-23	-11 ± 1	200-210	55-58	42-45	0

Abbreviations:

Type – sec. = secondary inclusion
P – inclusion population
N – number of measured inclusions
Gas – gas volume in %
S.I. – solid inclusions at room temperature

T_{fm} – first melting temperature in °C
T_{m, ice} – melting temperature of ice in °C
T_{hom} – homogenisation temperature in °C
H₂O – approximate amount of H₂O in weight %
KCl – approximate amount of salt in weight % equivalent KCl

Population II

These have similar characteristics to those of population I, but with a lower homogenisation temperature ($T_{\text{hom}} = 200^{\circ} - 220^{\circ}\text{C}$). The fluid system is again $\text{H}_2\text{O-KCl}$ with an equivalent KCl of 7 ± 1 wt.%. The gas phase makes up about 10 ± 2 vol.%, consisting mainly of vapour. Crystals of salt hydrates are always present. Population II inclusions were observed in all three different fluorites.

Population III

According to textural relationships, these inclusions are the youngest of all observed. They are very rich in gas, which constitutes 90 ± 5 vol.%, indicating fluid boiling. The homogenisation temperature is $T_{\text{hom}} = 210^{\circ} \pm 10^{\circ}\text{C}$ and the melting point for ice is $T_{\text{m, ice}} = 10^{\circ} \pm 1^{\circ}\text{C}$; first melting occurs at -22° to -23°C . The fluid system for the liquid phase is predominantly $\text{KCl-NaCl-H}_2\text{O}$, with about 42–45 equivalent wt.% of KCl, and there are indications of small amounts of FeSO_4 and KF also being present (J. Mullis, pers. comm., 1990). Cubic crystals melting at a temperature of $155^{\circ} \pm 3^{\circ}\text{C}$ are interpreted to be solid KCl (Roedder, 1984). Raman-spectroscopy of the inclusions yielded no evidence of CO_2 , CH_4 , H_2S or N_2 , and the fluid is therefore thought to be of pure saline composition (M. Hügi, pers. comm., 1990).

Inclusions of population III occur in the open cavity and fracture fluorites (WC11-78 and WC11-87), but not in interstitial fluorite (WC11-75).

The following conclusions can be drawn:

The low-salinity inclusions of population I are observed in interstitial fluorite growing into a nepheline pseudomorph, and in the fracture fluorite. Both fluorites are surrounded by completely exchanged K-feldspar of almost pure orthoclase composition. However, the K-feldspars do not display the characteristics for newly precipitated low microcline as observed, for example, in the open cavity of sample WC11-78, or in certain samples of the breccias. Therefore it is assumed that these inclusions represent the fluid composition at an early stage of the hydrothermal alteration and may in fact represent conditions of major potassic enrichment.

Population II inclusions also have low salinity and are present in all the different fluorites. They represent an intermediate stage in the evolution of the fluid, and are considered to be the “starting-point” for boiling as observed for population III.

Open cavity and fracture fluorites with incorporated inclusions of population III are associated with hydrothermally precipitated low microcline, as evidenced by cathodoluminescence and XRD. The highly saline fluid of these inclusions could therefore represent the fluid of formation for low microcline and, taking into account textural relationships, for the major mineralisation as well. Thus, a minimum temperature of formation for the mineralisation would be in the region of 210°C. Unfortunately, all attempts to measure fluid inclusions in the various alkali feldspar types have failed due to the very small size of the inclusions.

5.1.1.6. Clay mineralogy

By far the predominant mineral phases in the $<2\mu$ fraction are illite and kaolinite. Due to their intimate textural relationship, coarser-grained white mica (sericite) is described together with illite. Chlorite and smectite occur as traces in some samples of the cpx-bearing phonolites, although they could not be further identified due to their sparse occurrence in the average phonolite samples. Smectite, which tends to be more abundant in strongly brecciated zones distant from major breccia pipes, was identified as dioctahedral montmorillonite. Chlorite was not found to be more abundant in such zones.

Illite and sericite

The term sericite applies here to a fine-grained (2–60 μ) variety of flaky white mica which is larger than the illite of the clay fraction ($<2\mu$). Illite occurs both as a hydrothermal precipitate and as an alteration product, mainly of nepheline but also of alkali feldspar. The coarser sericite occurs as a hydrothermal phase within the matrix and as a substitute for kaolinite in the nepheline pseudomorphs (population “c”; see below). It normally has a pale green pleochroism indicating a moderate iron content.

The crystallinity index (Kubler, 1968), based on the peak width at half-height of the 001 XRD reflection, lies between 0.13 and 0.18 for the illites of the phonolitic rocks. The illitic material in the $<2\mu$ fraction proved to be almost pure, non-expanding illite in the set of samples studied (Środoń, 1984). Thus, a temperature of formation above about 360°C, or formation at lower temperatures but with a high K^+ -activity, is indicated by

these illites. Unfortunately, no such data are available for illitic material differing in horizontal distance to the breccia pipes, or for illitic material $>2\mu$ in grain-size (sericite).

Microprobe analyses have been performed on four texturally distinct illite/sericite populations:

- a) illites/sericites within the central zone of nepheline pseudomorphs (number of analyses $n=17$),
- b) interstitial illites/sericites in association with pyrite and zircon ($n=12$),
- c) sericites within the border zone of nepheline pseudomorphs ($n=4$), and
- d) illites/sericites that occur as void infillings ($n=5$).

The illites/sericites of populations (a), (c) and (d) are similar in composition and any differences are restricted to the interlayer cation occupation, with an average of 1.79 formula units per 22 O for population (a) and 1.5 formula units for population (c), both with 0.03 Na substituted for K. Furthermore, the Mg/Fe_{tot} ratio decreases from 0.22 for population (a) to 0.18 for population (c) and down to 0.12 for the illites in voids (population (d)). In contrast, the illites of the clay-pyrite-zircon assemblage (b) have the highest Al content in the tetrahedral sheet (average of 1.84 formula units per 22 O), the highest Mg/Fe_{tot} ratio, with an average of 0.3, and no Na substituted for K in the interlayer. The average composition of the illites from nepheline pseudomorphs (i) and from the mineralisation assemblage clay-zircon-pyrite (ii) are



In Figure 5 the analyses are presented in a muscovite-celadonite-pyrophyllite triangle. There is a visible trend from the high interlayer occupation of the earliest illites formed at the centre of nepheline pseudomorphs towards lower interlayer occupation of the late sericite overgrowths on kaolinite and the rims of sericites from population (c). According to Środoń and Eberl (1984), illite normally has an interlayer occupation of around 1.5 formula units per 22 O. On the other hand, Beaufort and Meunier (1983) indicate that hydrothermal illitic material displays a complete range of K-contents, from 1.48 to 2.0 per 22 O, mainly depending on the K^+ -activity of the hydrothermal fluid.

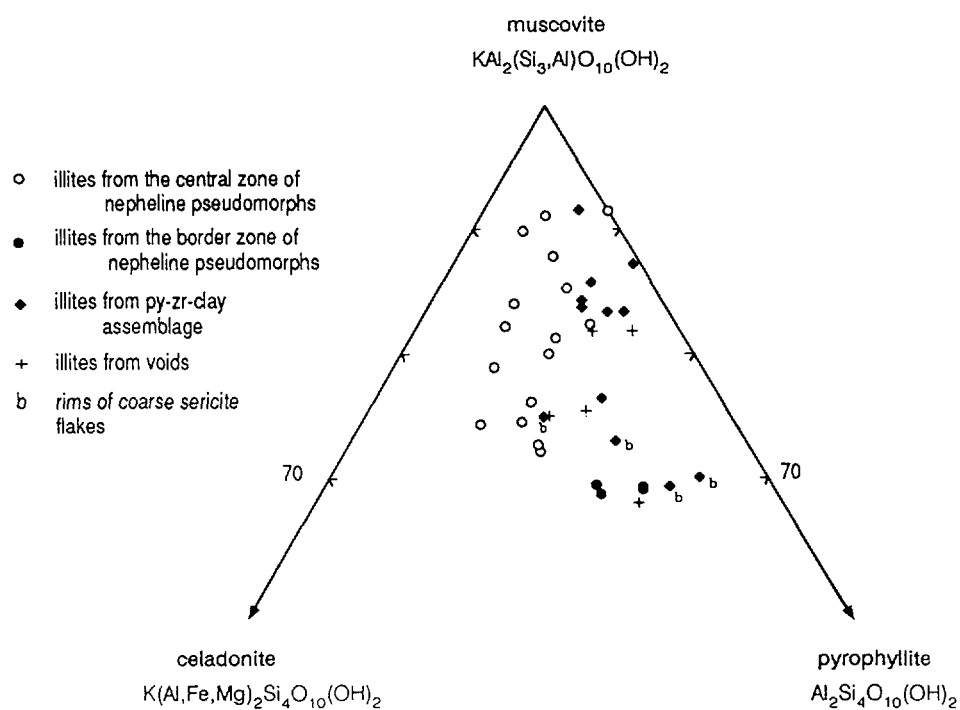


Figure 5. Compositional diagram of illites in different phonolitic rocks from the Osamu Utsumi mine with muscovite, celadonite and pyrophyllite as end members.

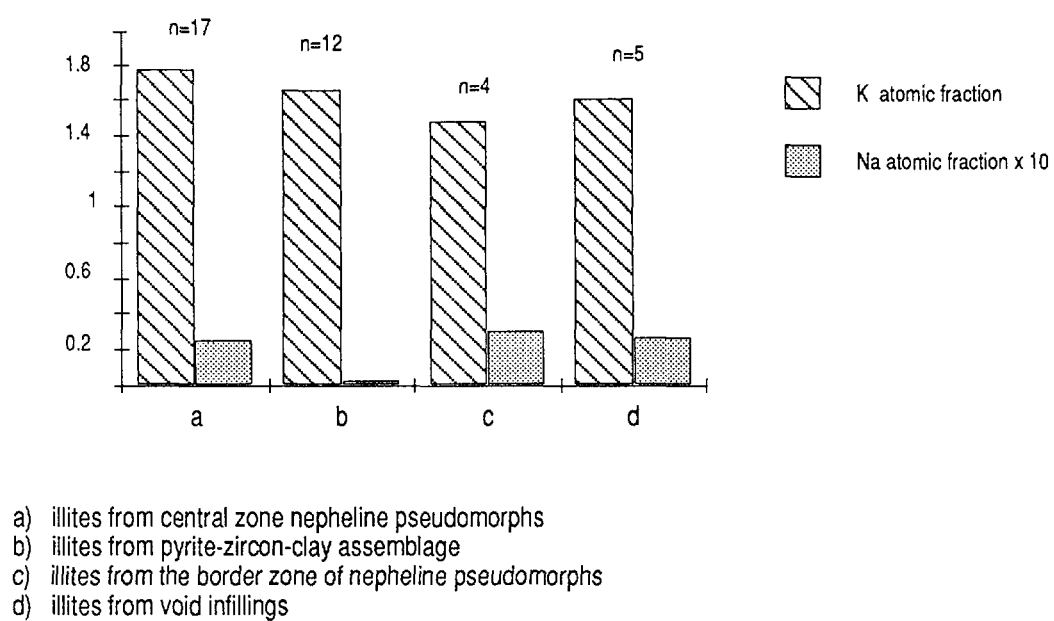


Figure 6. K and Na interlayer occupancy of illites from different parageneses.

Figure 6 shows the interlayer occupation of the different illite populations based on 22 O. Whereas the illites of populations (a), (c) and (d) have nearly the same amount of Na substituted for K, the illites of (b) have a pure K occupation of the interlayer.

Impurities of actinides and lanthanides in the illites are very rare and have no systematic distribution. Only in a few cases were very low concentrations of Y, and in one case of Ce, detected.

Kaolinite

Different populations of kaolinite may be distinguished according to their textural arrangement, grain-size, and by comparison with regional samples. A very fine-grained kaolinite ($<1\mu$), found mainly as an alteration product of alkali feldspar, also occurs in nepheline pseudomorphs and is randomly distributed throughout the matrix. This variety is similar to the small amount of deuteric kaolinite found in regional samples, but is more abundant in the phonolites of the mine. Hence, hydrothermal events must have formed at least part of this kaolinite, although it is no longer discernible from deuteric kaolinite found in the regional rocks.

The predominant kaolinite found in the phonolites from the mine is well-crystallised and forms “booklets” often several tens of microns in thickness. It occurs once again as a hydrothermal alteration product of nepheline and neogenically in rock pores and interstices. It is intimately intergrown with similar fine-grained pyrite of pre-breccia origin, somewhat coarser-grained illite/sericite and, in some cases, zircon. A third major population is kaolinite that occurs as fracture fillings; this is described below in more detail.

The majority of the kaolinite is generally chemically pure; in a few cases impurities of iron (0.32–0.7 wt.%), sodium (0.03–0.11 wt.%) and magnesium (0.05–0.29 wt.%) occur. Both Y and Ce were detected in trace amounts.

Chlorite and smectite

Chlorite and smectite are extremely rare in the hydrothermally altered phonolites. Traces of both were observed in pseudomorphs of clinopyroxene and sphene; smectite additionally occurs on fracture planes.

5.1.2. Nepheline syenites

Nepheline syenites occur in the eastern and southern part of the open-pit, in addition to borehole F4 where they are mainly encountered as fragments and larger bodies (several centimetres to several tens of metres in diameter) incorporated within the brecciated ore body B. In F4, they tend to be more frequent in the lower part, possibly indicating close proximity to the intact massive nepheline syenite country rock.

The major syenite bodies, ranging from several metres to several tens of metres in extent, may in fact represent country nepheline syenite which has intruded older phonolites and subsequently (together with the older phonolites) suffered fracturing, brecciation and injection by younger phonolites, accompanied by highly volatile volcanic phases.

Nepheline syenite samples from the mine walls generally display the same features as the drillcore samples. Unaltered nepheline syenite country rock has not been recovered from the drillcore or the mine walls.

The nepheline syenites are medium- to coarse-grained, equigranular and inequigranular hololeucocratic and leucocratic rocks. Particularly the medium-grained types may be porphyritic. In all the nepheline syenite types studied, there frequently occur pegmatoid veins composed of alkali feldspars (centimetre size), with or without nepheline. Macroscopically, the nepheline syenites have suffered evident hydrothermal alteration, including general pyritisation and argillation, and, less frequently, blue Mo-staining (restricted to distinct zones and individual breccia fragments) and fluorite mineralisation (in voids and fractures). The nepheline syenite fragments in the breccias show evidence of pre-breccia hydrothermal alteration, as do their phonolite equivalents.

5.1.2.1. Modal content

A qualitative compilation of the mineralogy derived from microscopic and XRD investigations is given in Table I. The quantitative alkali feldspar content, together with the relative abundance of clay minerals in the $<2\mu$ fraction determined by XRD, are listed in Table II. A detailed mineralogical account of the F4 drillcore samples (including phonolite fragments) is given in Appendix 5.

5.1.2.2. Hydrothermal assemblage

The hydrothermal mineral assemblage in the nepheline syenite is generally the same as in the phonolitic rocks. The major differences include the much more frequent occurrence of pegmatoid zones consisting of nearly pure K-feldspar (which belongs to the mineralisation assemblage) and the greater abundance of smectites, especially in samples more distant from the breccia pipe.

Alkali feldspar

Two different types of alkali feldspar can be distinguished. The predominant type is a low-temperature alkali feldspar that occurs as a replacement product of its high-temperature magmatic equivalent. It is idiomorphic in shape with grain-sizes varying between 1–10 mm, with an average of about 4 mm; zoning is frequent, from a core rich in inclusions of hematite to a hematite-free growth rim; in both zones abundant tiny fluid inclusions occur. Magmatic microperthitic exsolution structures are common in the centres of these alkali feldspars, but the albite component has been replaced by almost pure K-feldspar during the potassium-rich hydrothermal event. XRD yields a pattern typical for intermediate microcline. All these alkali feldspars show a weak sericitisation and kaolinisation along microfissures and grain boundaries.

The second type belongs to the mineralisation assemblage and occurs mainly along fractures, in open rock pores, interstices and pegmatoid zones; it is normally very closely related to the mineralisation assemblage. These alkali feldspars are hypidiomorphic to idiomorphic in shape and cover a wide range in grain-size (1–30 mm). In contrast to the alkali feldspar of magmatic origin, hydrothermally precipitated K-feldspars are homogeneous, free of hematite inclusions and argillic alteration. Their X-ray pattern is typical of a fully ordered low microcline.

Nepheline

Nepheline is completely replaced by illite and kaolinite, with the idiomorphic pseudomorphs reaching diameters of up to 5 mm. Tectonically undisturbed pseudomorphs, have inclusions of tiny cubic pyrites (10–30 μ), indicating pyrite formation contemporaneous with the alteration of the nephelines. At a later stage the kaolinite is partly substituted by somewhat coarser-grained illite/sericite. In fissured pseudomorphs

coarser-grained pyrite, fluorite, zircon and carbonates of the main mineralisation assemblage can be observed.

Clinopyroxene

Well-defined, acicular structures comprising cryptocrystalline Fe-Ti-oxides, clay minerals, and sometimes pyrite, are interpreted as pseudomorphically replaced clinopyroxenes. Further away from the breccia pipes, relict clinopyroxene could be identified in the core of such pseudomorphs. The replaced clinopyroxene is randomly distributed in the nepheline syenite, displaying a normal magmatic texture; no indications of cumulation textures were observed.

5.1.2.3. Mineralisation assemblage

The mineralisation assemblage of the nepheline syenite fragments and bodies encountered in borehole F4 is generally similar to that observed in the phonolitic rocks. Pyrite and precipitated low microcline are the predominant phases in this assemblage, followed by fluorite, zircon and Zr-minerals, semi-opaque Fe-Ti-Zr-REE aggregates, carbonates, TiO₂-phases, and small amounts of chalcopyrite, sphalerite, galena, Mo-minerals and very fine-grained U-minerals. Because the nepheline syenite bedrock was not encountered, either in borehole F4 or in the mine walls, this assemblage is described in detail in Section 5.1.3. Here it is worth noting that Mn-siderite is the most abundant carbonate that occurs interstitially in the nepheline syenite fragments, and as fracture infillings.

In Appendix 1, a detailed description of the pyrite sulphur isotope composition is given.

5.1.2.4. Clay mineralogy

The clay mineral composition in the nepheline syenite differs somewhat from that of the phonolitic rocks. On average, it is best compared to the clay composition in the cpx-phonolite (Table II).

Illite and kaolinite are the most abundant clay minerals in the near-vicinity of the breccia pipe (the first 120 m in drillcore F4); chlorite and smectite occur in trace amounts.

More distant from the breccia, illite/smectite mixed-layers and smectite increase, with smectite becoming the second most abundant clay mineral. Chlorite does not show such behaviour, occurring with abundances below 5% in all the samples studied.

Illite and sericite

Illite and sericite show similar characteristics in the nepheline syenite as in the phonolitic rocks. However, the bulk of the illite shows a broadening of the X-ray peak pattern with increasing distance from the major breccia pipe (and thus with increasing depth in borehole F4). The bulk illitic material in the nepheline syenite bodies close to the end of drillcore F4 is a mixture of non-expanding pure illite and expanding illite/smectite mixed-layers constituting about 15% of the material (after Šrodoň, 1980, 1984). The illitic material, separated from nepheline pseudomorphs in samples from such depths, gives an X-ray pattern for pure non-expanding illite. Therefore, the nepheline was pseudomorphically replaced under conditions favourable for pure illite, whereas in the rock matrix the bulk illitic material formed under conditions shifting towards the smectite stability field. Such a shift can be produced by two different factors, namely a decrease in K^+ -activity and/or formation of the illite-illite/smectite mixtures at lower temperatures. Compared to other hydrothermal environments, the maximum temperature of formation for such a mixture lies between 200°–240°C (Šrodoň and Eberl, 1984; Innoue and Utada, 1983).

Kaolinite

Kaolinite occurs almost exclusively as a replacement product of nepheline. In the near-vicinity of the breccia pipe, kaolinite additionally occurs as infillings in fractures and open cavities, displaying an X-ray pattern with well-defined peaks. The illite:kaolinite ratio varies between 3:2 and 2:3. Further away from the breccia pipe, the kaolinite peaks become broader, indicating a poorer degree of crystallinity, and the illite:kaolinite ratio changes to 4:1; in some samples it reaches up to 9:1. Halloysite could not be detected.

Smectite

Diocahedral smectite is found in pseudomorphs after the primary mafic components, together with small amounts of chlorite, at greater distances from the breccia pipe. Deeper in borehole F4, smectite becomes increasingly abundant in fractures and cavities, as well as in the matrix, yielding an X-ray pattern similar to montmorillonite. The illite:montmorillonite ratio is about 3:1 on average, reaching 1:1 in several deep-seated samples.

5.1.3. Breccia bodies

The breccia bodies, which have undergone open-pit excavation, are the main host formations of the Zr-U-Th-REE stockwork mineralisation.

The breccias of ore body B, mainly recovered in drillcore F4, have been investigated in detail. Down to a depth of about 320 metres, the core encountered a volcanic breccia with randomly alternating matrix-supported and clast-supported zones. Coherent rock fragments encountered in these breccias vary in thickness from a few millimetres to 1.5 metres at the most. From 320 metres down to the bottom of the hole (414.76 m), the intensity of brecciation decreases and the core consists of larger coherent rock fragments of decimetre to several metres in size. The single fragments are intercepted by small breccia veins of a few centimetres to a maximum of several decimetres in thickness.

The breccias encountered all belong to the group of subvolcanic conduit breccias (Ulbrich, 1984). They cover a broad range of structural and compositional types ranging from relatively poorly fractured (craquelé) nepheline syenites or phonolites, with quantitatively very subordinate fracture fillings, to chaotic breccias with heterogeneous fragments. The latter consist of different types of nepheline syenite and phonolite, as well as breccia fragments, indicating the reworking of earlier, already lithified breccias.

The characteristics of the potassic alteration are essentially the same in fragments of dimensions down to about 5 mm as they are in the coarse and very coarse varieties. Breccia-related hydrothermal processes only played a role in the very fine-grained portions of the matrix. Hence rock and mineral fragments with dimensions less than 2 mm are classified as matrix *sensu strictu* (s.s.). The spaces between the fragments of the breccias are partially or totally filled with matrix (s.s.) cements or mineralisations. Mineralisations associated with, or without, matrix (s.s.) are considered in a broader sense as matrix *sensu lato* (s.l.).

The volumetric content of the matrix (s.s.) covers a broad range varying from clast-supported to matrix-supported breccia types. In addition, breccias with matrix (s.s.) may grade through types with a welded matrix to those with an interstitial, very fine-grained phonolitic (magmatic) matrix and, finally, to xenolithic phonolites. These types were not found to be mineralised.

5.1.3.1. Nepheline syenite fragments

Nepheline syenite fragments occur throughout drillcore F4. In the first 320 metres of the drillcore, nepheline syenite fragments occur subordinate to phonolite fragments, varying in size from millimetres to a few decimetres. Towards the bottom of the core they increase in abundance, as well as in size, reaching diameters in decimetre to the metre range, indicating the proximity of the intrusive nepheline syenite country rock.

In general, the nepheline syenite fragments show very similar mineralogical features to those already described in Section 5.1.2. It is important to note that the degree of pyritisation and impregnation with Mo and fluorite varies between different fragments within the same breccia sample. There is no relationship between this kind of mineralisation and the one observed in the breccia matrix. Hence, the nepheline syenite fragments must have already undergone hydrothermal alteration, including pyritisation, and, in certain cases, Mo- and fluorite-mineralisation, prior to their fragmentation and incorporation into the breccia.

However, the breccia-related hydrothermal alteration affected the fragments marginally, producing, among other changes, an increased argillic alteration of the first few millimetres to centimetres within the fragment rims, and the penetration from the matrix into these rim zones of carbonates (mainly siderite), zircon and, to a minor degree, fluorite. Similarly, a stronger blue Mo-staining can often be observed in the marginal zone compared to the fragment centre. Breccia-related pyrite and low microcline often concentrate around individual fragments; to what degree they also penetrate into the fragments is difficult to determine because of the earlier developed K-feldspathisation and pyritisation in the fragments.

5.1.3.2. Phonolitic fragments

Phonolites are the most abundant fragments in the ore body B breccias, consisting of various structural and textural types described in Section 5.1.1. Additionally, several zones in the breccia body display a matrix with a phonolitic composition consisting of fine- to very fine-grained alkali feldspar that occasionally exhibits flow textures. This type of matrix is of high-temperature origin. Xenoliths contained in this matrix include all the different phonolites and nepheline syenites encountered in the mine area. Further breccia activity at lower temperatures reworked these zones, so that today portions with a matrix of high-temperature phonolite composition mainly occur as detached fragments in the breccia with a low-temperature matrix.

All the phonolite fragments in the breccia show the same evidence of pre-breccia hydrothermal alteration, as do their nepheline syenite equivalents.

5.1.3.3. Breccia matrix

As noted above, the different breccia-related hydrothermal processes acted mainly in the breccia matrix, and resulted in the formation of different mineral assemblages often existing in very close spatial relationship. Texturally, the hydrothermal minerals occur as microcrystalline components of the matrix (s.s.) and as cementing microfragments and infillings between the single fragments of the matrix (s.l.). Six major mineral assemblages could be discerned within the different matrix types, in addition to K-feldspar and clay minerals (Table V). Of these, assemblage 3 (fluorite + pyrite + carbonate \pm clay minerals) is the most abundant, followed by assemblages 2 (clay minerals + pyrite) and 6 (clay minerals + zircon \pm semi-opaque phases \pm fluorite). Assemblages 4 and 5, characterised by their Mo-phase(s) and U-phase(s) respectively, show an accumulation in the central part of the breccia but may also occur in the more marginal parts. The monomineralic pyrite assemblage (1) is subordinate and occurs throughout the breccia body. In spite of the often very close association of the different assemblages it was, however, not possible to relate specific sequences to temperature-time conditions.

TABLE V
 Hydrothermal mineral assemblages deduced from breccias in borehole F4 (compare Appendix 5).

	Assemblage	Short description	Activity
1	Pyrite	Monomineralic, microcrystalline masses to millimetric idiomorphic crystals as infillings of open spaces between breccia fragments.	Background
2	Clay minerals + pyrite	Cryptocrystalline clay masses containing disseminated microcrystalline pyrite; clays are predominantly illite with subordinate kaolinite, montmorillonite and, in certain cases, illite-smectite mixed-layers and chlorite.	Background
3	Fluorite + carbonate + pyrite ± clay minerals	Microcrystalline components of the matrix and coarser masses cementing the breccia fragments; fluorite mainly violet coloured; carbonate as inclusions in fluorite (calcite) and occasionally free (siderite + calcite).	Minor positive anomalies
4	Pyrite + clay minerals + Mo-phases	Microcrystalline pyrite-clay assemblage with bluish, secondary Mo-mineral staining (ilsemannite).	Minor to medium positive anomalies
5	Pyrite + U-oxide phases + unidentified sulphide minerals	Microcrystalline masses filling open spaces between breccia fragments; U-oxides (pitchblende + subordinate uraninite) often as coatings on pyrite and sulphides.	Maximum observed anomalies
6	Clay minerals + zircon + semi-opaque phases ± fluorite	Microcrystalline masses with somewhat coarser zircon and fluorite; semi-opaque phases include metamict, poorly defined Zr-phases (e.g. caldasite), brannerite, as well as undiscernible rare metal oxides (e.g. leucoxene, columbite group?), silicates (e.g. thorite?) and phosphates (e.g. monazite, xenotime).	Minor to medium positive anomalies

Pyrite

Based on textural relationships, populations of pre-, syn- and post-breccia pyrites may be discerned. Pre-breccia pyrites, formed during the potassium-rich hydrothermal event, occur as disseminated mineralisation throughout the non-brecciated phonolites and nepheline syenites and their respective fragments in the breccias. There, associated fragments may show different degrees and textures of pre-breccia pyrite impregnation. The pre-breccia pyrites form the most important pyrite population and are described in the sections above (5.1.1.4. and 5.1.2.3.). Syn- and post breccia pyrites occur in open pores and cavities, and in various mutually intersecting generations of veins and fractures

that cut through the non-brecciated phonolites and nepheline syenites, and their corresponding fragments in the breccias. The total amount of pyrite in the breccias is higher than in the other rocks of the mine and estimates range between 4–7 vol.% of the total breccia.

Syn-breccia pyrites occur in the breccia matrix and commonly constitute a major part of the major mineral content (> 10 vol.%). In certain centimetre-thick zones, syn-breccia pyrite almost forms a monomineralic assemblage of more than 90 vol.%. It is normally of fine grain-size, in the range of 0.5–2 mm, with extremes smaller than 30 μ and larger than 1 cm. They occur as idiomorphic single crystals but more frequently as intergrowth masses. Syn-breccia pyrite is frequently intimately intergrown with sphalerite and with Zr- and U-minerals.

The syn-breccia pyrite displays several stages of formation, indicated by inclusion-rich zones and growth rims free of inclusions. Gangue minerals, especially alkali feldspar (intermediate microcline as well as breccia related low microcline), are the predominant inclusions. In a few cases inclusions of sphalerite and pentlandite are present.

Post-breccia pyrite occurs along fracture planes that cut the breccia bodies and is predominantly fine-grained in the range 0.3–3 mm. Growth textures are of isolated idiomorphic single crystals or intergrown clusters and coatings. The most commonly associated silicate mineral is kaolinite. Post-breccia pyrites commonly exhibit inclusions of pyrrhotite. Certain post-breccia pyrites display a silvery coating that was identified as a Ti-oxide coating (mainly anatase).

S-isotope and chemical analyses of the different pyrite populations are described in Appendices 1 and 3.

Sphalerite

Sphalerite occurs sporadically and normally in trace amounts; it may reach minor contents in certain highly U-mineralised breccia zones. In such zones there is an intimate intergrowth of sphalerite with pyrite, Zr- and U-minerals. Sphalerite has a certain importance as host to a cadmium mineral of which a sulphidic form (greenockite, CdS) occurs associated with the supergene U-mineralisation at the redox front.

Other sulphides

Chalcopyrite (Cu FeS_2) was sporadically observed along fractures in nepheline syenite fragments within the deeper zones of the breccia encountered in borehole F4. Pyrrhotite (FeS) and pentlandite ($(\text{Fe,Ni})\text{S}$) occur in some cases as inclusions in pyrite.

Molybdenum minerals

The main Mo-bearing mineral is the blue-coloured ilsemanite ($\text{Mo}_3\text{O}_8\text{H}_2\text{O}\cdot\text{H}_2\text{SO}_4$) of supergene weathering origin, which occurs finely disseminated in the breccia matrix with a tendency to accumulate along the borders of xenoliths. This mineral is also responsible for the blue staining of the mine walls and the drillcores shortly after their exposure to air. Ilsemanite is a weathering product of sulphidic Mo-minerals such as molybdenite (MoS_2) and/or jordisite (amorphous MoS_2). Only in a few samples was jordisite detected, whereas molybdenite was never observed. Jordisite, as the most probable precursor of ilsemanite, is of very low-temperature hydrothermal origin (Ramdohr, 1975).

Uranium minerals

Cryptocrystalline uranium minerals occur in the higher-grade mineralised zones of the breccia encountered in borehole F4. They occur as dustings in the breccia matrix and as coatings on minerals (pyrite) and fracture planes, and are always in close association with the other minerals of the mineralisation assemblage, particularly with the sulphides. The U-minerals display the same compositional range (by XRD) as observed in the phonolites (Section 5.1.1.4.). Additionally, in some samples of highly mineralised veins, the X-ray pattern signifies a well-formed crystalline uraninite (UO_2). In aggregates of cryptocrystalline semi-opaque phases, brannerite (UTiO_6) could be identified besides other less well-defined associations of uranium and titanium (B. Hofmann, pers. comm., 1990).

Ti-oxides

Besides the Ti-oxides that have resulted from the replacement of the original mafic minerals, there occur microgranular aggregates of needle-shaped Ti-oxides and coatings

of Ti-oxides on sulphides. The titanium phases of such aggregates are mainly in the form of very fine-grained needle-shaped rutile phases, most probably accompanied by minor anatase.

Zircon and Zr-minerals

Zircon forms xenomorphic masses up to 4 mm in size in the breccia matrix, and is commonly concentrated in interstices and along xenolith borders. Zircon in the breccia matrix is strongly metamict, present as cryptocrystalline mixtures of zircon, baddeleyite and amorphous (hydrated?) Zr-oxide. In several breccia samples, well-defined baddeleyite crystals occur as an independent phase besides the cryptocrystalline Zr-aggregates. Radial fibrous aggregates of baddeleyite, known as caldasite from other localities of the Poços de Caldas plateau, were not observed. Non-metamict idiomorphic zircons are rare and occur only as void infillings and on late-stage fractures. Such zircons may reach 5 mm in size and are of a reddish-brown colour that could be due to impurities of Nb and U (Fielding, 1970).

Fluorite

Fluorite is nearly always present in the breccia matrix and may occur as a major component cementing the individual breccia fragments. The grain-size of the fluorites varies between very fine-grained interparticle infillings (<0.2 mm) to hypidiomorphic crystals of about 10 – 25 mm. Fluorite is normally violet-coloured and often displays a certain zoning. Colourless, light yellowish or greenish fluorites also occur, sometimes in close association with violet fluorite. Fluorite often contains abundant carbonate inclusions or is intimately intergrown with carbonates, indicating mutual repeated replacement. Polyphase fluid inclusions are also always present, some of them containing minute solid carbonate inclusions.

Carbonates

Carbonates, although mainly associated with fluorite, are much more abundant in the breccia matrix than in all other rock types, with the exception of the ultramafic dykes (Section 7). Siderite, with varying Fe-Mn ratios, is the most abundant carbonate;

subordinate amounts of relatively pure calcite are found in or around fluorite. A late-stage carbonate generation of post-breccia origin occurs on fractures traversing the breccia. This generation is not associated with fluorite and consists exclusively of Mn-rich siderite.

The carbonates may thus be a product of the hydrothermal assemblage (calcite in association with fluorite), the mineralisation assemblage of the breccia matrix (siderite with varying Fe-Mn ratio), and a late process affecting post-breccia fractures (Mn-siderite).

Alkali feldspar

Alkali feldspar always occurs in varying amounts within the breccia matrix, mainly as a low microcline form. Macroscopically, the low microcline of the breccia is normally blue in colour, which suggests a triclinic potassium feldspar of low-temperature origin (<270°C; Oftedal, 1957). Under cathodoluminescence the low microcline displays a homogeneous dull yellow-brown colour with no indication of zoning. This contrasts with the observed colour zoning of the alkali feldspar formed during the potassic event, which normally shows a preserved red luminescence core.

Clay minerals

The relative abundance of the individual clay minerals in the different breccia types exhibits an extremely large variation. Commonly, illite (including the coarser-grained sericite) and kaolinite are the most abundant; XRD indicates that the illite is a well-crystallised form. The amount of expanding layers does not exceed 10% of the illite.

Kaolinite, by contrast, displays an X-ray pattern with broad peaks, completely different to that found for those kaolinites replacing nepheline in the phonolites and nepheline syenites. This may indicate a low degree of crystallisation or mixed-layers with chlorite and/or smectite. Towards the marginal areas of the breccia, the crystallinity of kaolinite increases again. Textural relationships indicate that illite/sericite substitute for earlier kaolinite in assemblages 1 and 3 in the more central parts of the breccia, with pyrite found as inclusions in the coarser illite/sericite flakes. Smectite and chlorite are normally present in trace amounts within the breccia matrix. In a few special cases smectite reaches major amounts with a montmorillonite composition.

5.1.4. Oxidised zone

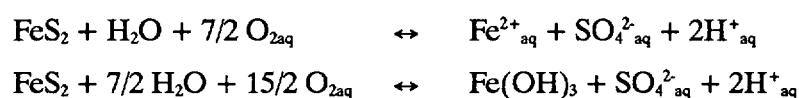
Prior to mining activities, the downward diffusion of oxygen in groundwaters during weathering had produced a distinct redox front, manifested by a clear colour change from greenish-grey to orange-brown. The change is mainly attributed to ferrous-to-ferric oxidation and the formation of clay phases. The absence of pyrite and other sulphides, fluorite, barite and primary U- and Mo-phases is characteristic for the oxidised zone (Table I). In addition, K-feldspar decomposes to illite and kaolinite, a transformation which becomes more and more complete towards the weathering cover.

The minerals formed in the oxidised zone include:

Fe-hydroxides (mainly ferrihydrate and goethite),
kaolinite,
illite,
Mn-hydroxides (mainly pyrolusite and nsutite),
crandallite group minerals (gorceixite, goyazite, florencite),
minerals of the alunite-jarosite family.

Iron-hydroxides

Ferrihydrate (approximately $\text{Fe}_3\text{HO}_8\cdot 4\text{H}_2\text{O}$) and goethite ($\alpha\text{-FeOOH}$) are the most abundant among the newly formed iron phases. Completely amorphous Fe-hydroxide and lepidocrocite ($\gamma\text{-FeOOH}$) occur in subordinate amounts together with hematite. Fe-hydroxides have resulted from the oxidation of pyrite; dissolution occurs according to the equations:



The oxidation of pyrite is already complete some 2–3 cm from the redox front within the oxidised zone. It is within this narrow zone, adjacent to the front, that a few samples of strongly corroded relict pyrite occur in the centre of Fe-hydroxide – clay mineral aggregates. Further away from the front, pyrite is no longer observed.

Ferrihydrate forms spherical aggregates of up to about 70μ in open pore spaces and along fractures. It is commonly intimately associated with completely amorphous Fe-hydroxide, suggesting formation from the latter through aging. Throughout the

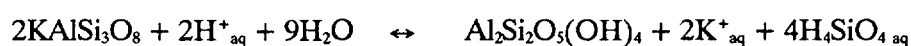
oxidised zone ferrihydrate and amorphous Fe-hydroxide form coatings around the other minerals, making microscopic investigations extremely difficult. Such coatings often display a rhythmic alternation of different crystalline Fe-hydroxide zones. In fractures the single Fe-hydroxide zones are often separated by thin layers of Mn-hydroxides. Such textural evidence suggests Fe-hydroxide formation in several stages.

Goethite, often in close association with ferrihydrate, displays well-defined needle-like crystals normally less than 1 μ in length. These needles are stacked on top of the ferrihydrate concretions, or sometimes even incorporated in them. However, the goethite grain boundaries are always well-defined against the ferrihydrate, indicating coeval formation under equilibrium conditions; there was no evidence that goethite had recrystallised from ferrihydrate.

A qualitative correlation between the crystallinity of the Fe-hydroxides and uranium was observed using the EDS-SEM system. Amorphous Fe-hydroxide and ferrihydrate often have weak to moderate peak intensities for uranium; this contrasts with the goethite needles which normally have no such peak, or only a weak indication. Microprobe analysis of these poorly crystalline Fe-hydroxide phases failed due to instability under the beam. However, specific investigations of the adsorption of uranium on Fe-hydroxides were carried out on four samples using different leaching techniques (Appendix 2). The results obtained support the above observation that the adsorption of uranium is negatively correlated with increasing crystallinity of the Fe-hydroxides.

Illite and kaolinite

Secondary kaolinite and illite are formed in the oxidised zone through decomposition of K-feldspar; the former is more abundant. The transformation of K-feldspar to kaolinite and illite occurs according to the equations:



respectively



Secondary kaolinite and illite display a sparry textural arrangement with a high amount of micropores. In conducting zones such sparry aggregates are often scoured out.

Alunite and jarosite

Both alunite and jarosite are always found in close association with iron-hydroxides. Their occurrence together with such phases in pyrite pseudomorphs suggests formation from pyrite and possibly other sulphides during their oxidation.

5.1.4.1. Modal content

The average modal abundance of K-feldspar is decreased in the range of 5–20 wt.% compared to the reduced zone, depending on the rock type (Table II). By contrast, the average modal abundance of clay minerals is increased. The distribution of clay minerals is similarly heterogeneous, as in the reduced zone, within any given rock type. However, a general trend towards higher kaolinite:illite ratios is observed in the vertical profile towards the weathering cover.

An indirect estimate of the abundance of Fe-hydroxides can be made from the chemical analyses, based on the assumption that the majority of the iron occurs in Fe-hydroxides. This assumption is reasonable because, apart from the Fe-hydroxides, only illite (0.1–0.2 Fe per formula unit) and, rarely, smectite and chlorite, occur as further Fe-bearing phases. The average abundance of total Fe-hydroxides then ranges between 1 and 3 vol.% depending on the rock type, but reaches values up to 8 vol.% for certain samples. At some redox fronts there are greater accumulations of Fe-hydroxides which may account for as much as 17 vol.% of the total rock volume.

Pseudomorphically replaced clinopyroxene ranges between 15–20 vol.% in the cpx-phonolite and is less than 10 vol.% in the oxidised nepheline syenite. In the other phonolites replaced clinopyroxene occurs in trace amounts.

The remaining minerals occurring in the oxidised zone have an average abundance of less than 5–10 vol.%.

5.1.4.2. Porosity measurements

Compared to their counterparts in the reduced zone (Table III), porosity values in the oxidised zone are greater in all the different rock types. This increase is primarily due to the decomposition of K-feldspar, fluorite and pyrite and is, therefore, strongly dependent on the composition of the reduced rock. The scatter of the porosity values is also greater in the oxidised rocks, ranging from about 9% up to about 25%. The best comparison of

porosity for reduced and oxidised rock can be seen in profiles over the redox front where the average porosity increase is between 4–8% (see Table XX and Fig. 57).

5.1.5. Weathering cover

Climatic conditions in the Poços de Caldas plateau have favoured formation of lateritic soils and bauxites during the last 75 Ma, assuming that the magmatic and hydrothermal activity terminated with the intrusion of the ultramafic lamprophyre dykes; one example yielded an Ar-Ar plateau age of 75.7 ± 0.3 Ma. (Shea, this report series; Rep. 4). Factors influencing the mechanisms of formation of the weathered cover include annual mean temperature, the amount and temporal distribution of precipitation, topography, groundwater flow and fluctuation of groundwater level, the dominance of chemical over mechanical erosion, and the vegetation and character of the bedrock (Norton, 1973).

According to the classification of Brazilian climates by Bernardes (in Azevedo, 1975), the climate of the Poços de Caldas plateau may be classified as a “tropical climate of altitude”, characterised by the occurrence of wet and dry seasons. Records over a 30 year period yield average maximum rainfall values of about 3000 mm for the wet season (December – February) and an average minimum rainfall of less than 25 mm during the dry season (May – July); the annual average is about 1700 mm over the same period (INM, 1982). Normal daily temperatures range from 12–24°C, with recorded minimum temperatures around freezing point and maximum temperatures of 35°C. With an annual average of about 17°C, the temperature is lower than for a typical tropical climate (19–20°C; Almeida, 1977).

Within the upper profile of the Osamu Utsumi mine, weathering processes have produced an alteration cover varying in thickness between 40–60 m, reaching extreme values of a minimum of 10 m and a maximum of 100 m, the oxidised bedrock excluded. Deepest weathering is associated with the strongly brecciated and hydrothermally altered zones.

Four profiles were sampled from different bedrock types from the surface down into the mine to obtain information about mineralogical and geochemical changes, in particular the behaviour of U, Th and REEs, produced by the low-temperature weathering cycle (Fig. 4).

The weathered cover in the Osamu Utsumi mine may be divided into an upper laterite horizon and a lower saprolite horizon according to textural characteristics. Laterite and saprolite are separated by a transition zone of about 20–40 cm in thickness. In contrast,

the transition from the saprolite horizon to the underlying oxidised bedrock is normally sharp and displays no marked transition zone. Along fractures, the formation of saprolite may penetrate deep into the oxidised bedrock. Remnants of intact oxidised bedrock (corestones) completely surrounded by saprolitic material are often observed in the saprolite and in some cases in the laterite; the contact is usually sharp with no distinct transition zone. All these observations clearly demonstrate the strong dependence between the formation of the weathering cover and the facility for percolation and precipitation.

An important factor controlling the chemical composition of the weathering cover in the Osamu Utsumi mine area is the mineralogical composition of the underlying parent rocks consisting mostly of hydrothermally altered phonolites and nepheline syenites mainly composed of K-feldspar, illite and kaolinite. Of these major components, kaolinite and, to a lesser degree, illite are fairly resistant to weathering in the Poços de Caldas plateau and therefore occur in large amounts within the weathered cover of the mine. This might also explain the lack of bauxite formation on top of hydrothermally altered (“potassic”) rocks in the plateau; bauxite deposits usually occur in association with all different kinds of phonolitic and nepheline-syenitic rocks unaffected by hydrothermal alteration (Almeida, 1977).

5.1.5.1. Saprolite

The saprolite horizon is defined as a horizon where the original rock texture is still mainly preserved, although its mineralogical composition is transformed to a major degree. The transformation of the original mineralogical composition is combined with an increase in total porosity and a decrease in bulk density from the bedrock to the saprolite horizon.

Saprolite horizons occur in the mine in variable thicknesses. The most massive horizons are observed capping the coarser-grained bedrock types (nepheline syenite about 50 m; plc-phonolite about 25 m) in ore bodies A and B. In contrast, the horizons are less developed when associated with the more fine-grained bedrock varieties (volcanic phonolite about 12 m; cpx-phonolite about 10 m) in ore body E. The saprolite is generally yellowish-white in colour with heterogeneously distributed zones and spots of various colours (yellow, red, brown, violet, black). Yellow and brown colours are mainly due to accumulations of Fe-hydroxides, whereas red, violet and black colours represent accumulated zones of Fe- and Mn-oxides/hydroxides in varying ratios.

Major crystalline components of the saprolite horizon are kaolinite, illite/sericite and iron-hydroxides (mainly ferrihydrate and goethite). K-feldspar may still be present as a major component near the contact to the bedrock, but its modal abundance drastically decreases higher up in the saprolite horizon. Gibbsite, in contrast, is not observed in the lower levels, only occurring higher up, especially within the more porous saprolites capping the nepheline syenite and plc-phonolite. Resistate minerals (Ti-phases, Zr-phases) and concretions of Mn-hydroxides occur in minor and trace amounts. The most important trace and minor components formed under weathering conditions, for example alunite, jarosite, lithiophorite and the crandallite group minerals florencite, goyazite and gorceixite, tend to be heterogeneously distributed within the saprolite horizons.

5.1.5.2. Laterite

The original rock texture is no longer preserved in the laterite horizons. The transition from saprolite to laterite is continuous, although the contact zone is very irregular. The lowest laterite zone is normally composed of consolidated clay material, mainly yellow and white in colour, and is normally quite thin (0.5–1 m) and not always developed. Further up the vertical profile there occurs a zone where Fe- and Mn-hydroxides become more concentrated, forming nodular aggregates (centimetre to decimetre in size) embedded in a fine-grained clay matrix. This zone displays a mottled yellow-red-brown-black colour and varies in thickness between about 2 m and 20 m. Generally, indurated red-brown-coloured layers strongly enriched in nodules occur towards the top of this zone (ferricrete). Such ferricretes, normally in the range of 0.05–0.5 m thick, repeatedly occur, separated by mottled, less rich zones. In its uppermost zone, which ranges in thickness between 0.5–15 m, the laterite consists of unconsolidated fine-grained crystalline and amorphous material. Finely disseminated Fe- and Mn-hydroxides again occur, and are responsible for the fairly homogeneous yellow-brown colour characteristic of these levels.

Kaolinite and gibbsite are the predominant crystalline phases in the laterite, followed by crystalline Fe- and Mn-hydroxides. Illite, another important component, is mainly derived from the parent rock as evidenced by their stable isotope composition (Waber, 1990). Much more abundant than in the saprolite are amorphous Fe- and Al-gel, and heavy minerals more resistant to weathering are mainly found in association with ferricretes or nodules. Newly formed mineral phases such as alunite, jarosite,

lithiophorite and the crandallite group minerals generally show the same heterogeneous distribution as in the saprolite, but are more abundant.

5.1.5.3. Modal content

A compilation of the modal abundance in single samples from the four investigated profiles is given in Table VI. The mineralogical evolution illustrated in the four profiles extending from different bedrock environments to the surface is presented graphically in Figure 7.

5.1.5.4. Porosity measurements

A strong increase in total porosity of 10–15 vol.% occurs at the junction between the oxidised bedrock and the saprolite (Table VII; Fig. 8). This increase is clearly a result of K-feldspar dissolution and its pseudomorphic replacement by sparry clay aggregates. Throughout the saprolite as a whole, total porosity varies between 25–40 vol.%, mainly depending on the original grain-size of the underlying bedrock. A further drastic increase in total porosity of 15–20 vol.% (Table VII; Fig. 8) occurs at the junction between the saprolite and the laterite. In the laterite the porosity (40–60 vol.%) is strongly dependent on the amount of Fe- and Mn-accumulations, resulting in a very heterogeneous distribution. The highest total porosity and the lowest bulk density are recorded for the uppermost laterite zone.

5.1.5.5. Mineralogy

K-feldspar

K-feldspar is no longer stable under the conditions occurring within the weathering zone. In the laterite zone K-feldspar is totally decomposed, and in the saprolite the fine-grained K-feldspar of the rock matrix is completely pseudomorphed by kaolinite and illite, whereas coarser K-feldspar phenocrysts are more frequently preserved, especially in the lower levels. Such K-feldspar displays etch pitting which is crystallographically controlled on the surface, clearly indicating dissolution of the K-feldspar. Textural evidence reveals the decomposition of K-feldspar to mainly

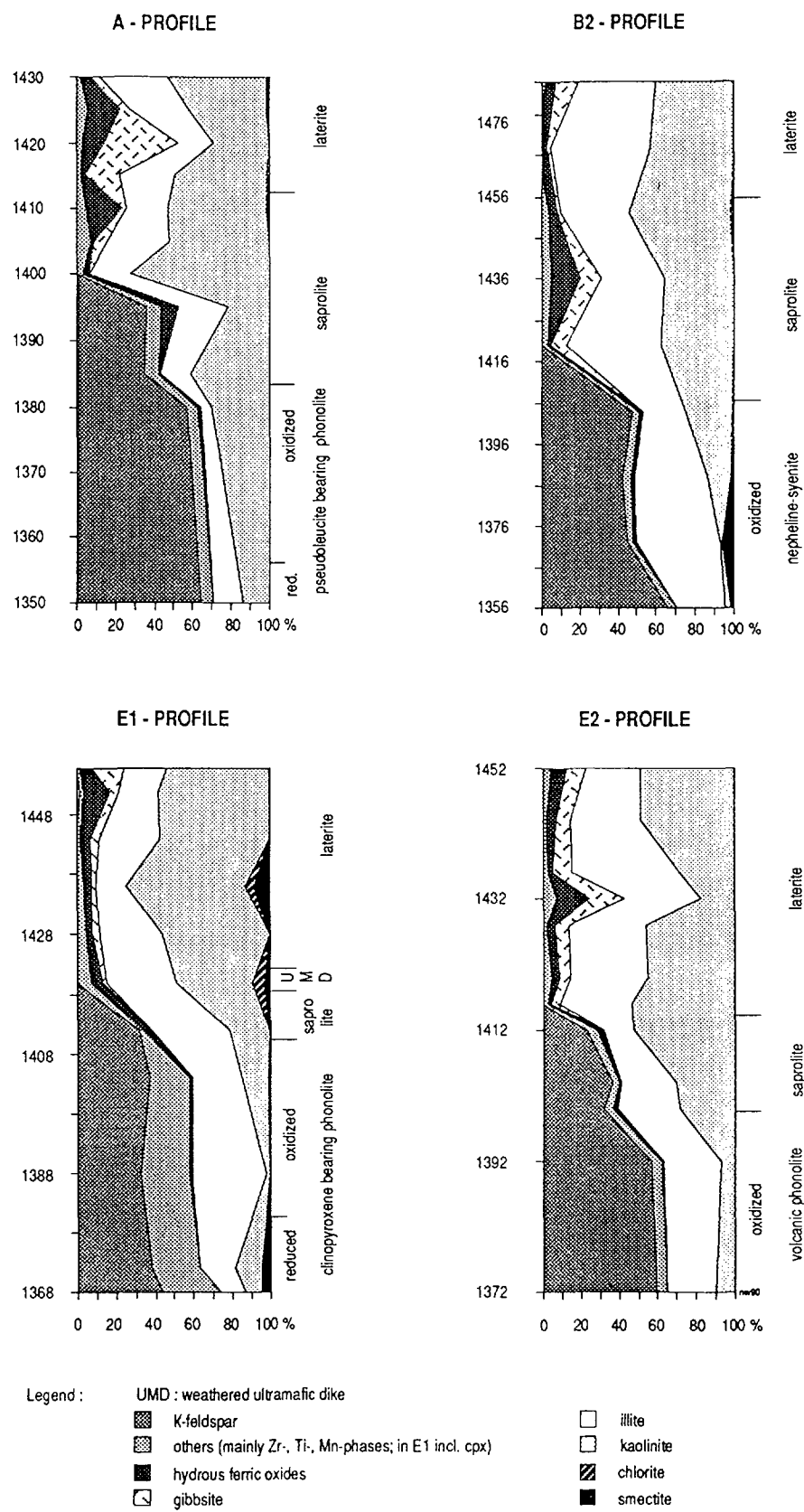


Figure 7. Mineralogical compositions in four weathering profiles from different parent rocks. Profile locations are indicated in Figure 4.

TABLE VI
Mineralogical composition of four profiles from the original ground surface down to the parent rock in ore bodies A, B and E.

Osamu Utsumi mine, ore body A, vertical profile A: Qualitative mineralogical composition																
Sample	Rock type	KF	Gib	HFO	Ill	Kao	Chl	Sm	Alu	Jar	Flor	Gor	Goy	Mn-m	Ti-m	Others
A-60	LAT		m	m	M	M		tr	tr						tr	tr
A-61	LAT		m	M	M	M		tr						m	tr	m
A-62	LAT		M	M	M	M									tr	tr
A-63	LAT		M	m	M	M	tr		m	tr	tr				tr	tr
A-64	SAP		m	M	M	M		m	tr		m	tr		tr	m	m
A-65	SAP		m	m	M	M			tr						tr	tr
A-66	SAP			m	M	M		tr			tr	tr	tr	m		
A-67	SAP	M		m-M	M	M									tr	tr
A-68	SAP	m		m	M	M			m			m		m	tr	tr
A-69	SAP	M		tr-m	M	M	tr-m		m				tr	tr	tr	tr
A-70	PlcPh ox	M		m	M	M	tr	tr	m						tr	tr
A-84-A	PlcPh red	M			M	M	tr	tr							tr	m**
Osamu Utsumi mine, ore body B, vertical profile B2: Qualitative mineralogical composition																
Sample	Rock type	KF	Gib	HFO	Ill	Kao	Chl	Sm	Alu	Jar	Flor	Gor	Goy	Mn-m	Ti-m	Others
B2-41	LAT		M	m	M	M									tr	tr
B2-43	LAT		m	m	M	M									tr	tr
B2-45	SAP		tr	m	M	M	m		tr	tr					tr	m
B2-47	SAP		M	M	M	M			tr					m	tr	tr
B2-49	SAP		m	m	M	M			tr						tr	tr
B2-51	SAP	M		m	M	M	m	m				tr		tr	tr	tr
B2-53	NeS ox	M		m	M	M		m				tr	m		tr	tr
B2-55	NeS ox	M		m	M	m	tr	M			m				tr	tr
B2-57	NeS red	M			M	m		M							tr	m**
Components:																
M	– major, > 10 vol.%	KF	– K-feldspar				Chl	– chlorite		Gor	– gorceixite	Others:				
m	– minor, 1-10 vol.%	Gib	– gibbsite				Sm	– smectite		Goy	– goyazite	mainly Zr-minerals (zircon,				
tr	– trace, < 1 vol.%	HFO	– hydrous ferric oxides				Alu	– alunite		Mn-m	– Mn-hydroxides	baddeleyite), monazite, apatite,				
		Ill	– illite				Jar	– jarosite		Ti-m	– Ti-minerals	reduced rocks: * clinopyroxene				
		Kao	– kaolinite				Flor	– florencite				**pyrite, fluorite				
Rock types:																
LAT	– laterite	NeS	– nepheline syenite						CpxPh	– clinopyroxene-bearing phonolite						
SAP	– saprolite	PlcPh	– pseudoleucite-bearing phonolite						VLP	– volcanic leucocratic phonolite						

TABLE VI (contd.)

Osamu Utsumi mine, ore body E, vertical profile E1: Qualitative mineralogical composition																
Sample	Rock type	KF	Gib	HFO	Ill	Kao	Chl	Sm	Alu	Jar	Flor	Gor	Goy	Mn-m	Ti-m	Others
E1-88	LAT		M	m	M	M								tr	tr	tr
E1-71	LAT		m	M	M	M								tr	tr	tr
E1-91	LAT		m	m	M	M								tr	tr	tr
E1-72	LAT		m	m	M	M	m	m			tr			tr	tr	tr
E1-92C	LAT		m	m	M	M	tr	m					tr	m	tr	tr
E1-73	UMD		tr	m	M	M	m	m			m	m		m	tr	tr
E1-96	SAP	M	tr	m	M	M									tr	tr
E1-74	CpxPh ox	M		m	M	M		m	tr	tr					m	m
E1-75	CpxPh ox	M		m	M	M			tr		tr				m	m
E1-76	CpxPh fresh	M			M	M	tr	M	tr						tr	M*
E1-77	CpxPh red	M			M	M	tr	M							tr	M*
E1-78	CpxPh red	M			M	M	m	M			tr				tr	M*

Osamu Utsumi mine, ore body E, vertical profile E2: Qualitative mineralogical composition																
Sample	Rock type	KF	Gib	HFO	Ill	Kao	Chl	Sm	Alu	Jar	Flor	Gor	Goy	Mn-m	Ti-m	Others
E2-110	LAT		M	m	M	M						tr		m	tr	tr
E2-111	LAT		m	m	M	M									tr	tr
E2-112	LAT		M	m	M	M			tr	tr	tr				tr	tr
E2-113	LAT		M	M	M	M			tr	m				tr	tr	tr
E2-114	LAT		m	m	M	M									tr	tr
E2-115	LAT		m	m	M	M					tr				tr	m
E2-116	LAT		m	m	M	M					tr				tr	tr
E2-118	SAP	M	tr	m	M	M		tr					m		tr	tr
E2-119	SAP	M		tr-m	M	M			tr						tr	tr
E2-120	SAP	M		m	M	M				tr			tr		tr	tr
E2-99	VLPPh ox	M		tr-m	M	M						tr	tr		tr	tr
E2-102	VLPPh red	M			M	M									tr	tr**

Components:																
M	- major, > 10 vol. %	KF	- K-feldspar	Chl	- chlorite	Gor	- gorceixite	Others: mainly Zr-minerals (zircon, baddeleyite), monazite, apatite, reduced rocks: * clinopyroxene **pyrite, fluorite								
m	- minor, 1-10 vol. %	Gib	- gibbsite	Sm	- smectite	Goy	- goyazite									
tr	- trace, < 1 vol. %	HFO	- hydrous ferric oxides	Alu	- alunite	Mn-m	- Mn-hydroxides									
		Ill	- illite	Jar	- jarosite	Ti-m	- Ti-minerals									
		Kao	- kaolinite	Flor	- florencite											
Rock types:																
LAT	- laterite	NeS	- nepheline syenite	CpxPh	- clinopyroxene-bearing phonolite											
SAP	- saprolite	PlcPh	- pseudoleucite-bearing phonolite	VLPPh	- volcanic leucocratic phonolite											

TABLE VII

Porosity in four profiles from the original ground surface down to the parent rock in ore bodies A, B and E.

A-Profile				B2-Profile			
Sample	Rock type	Density	Porosity (%)	Sample	Rock type	Density	Porosity (%)
A-60	LAT	1.42	45.2	B2-41	LAT	1.18	55
A-61	LAT	1.15	49.1	B2-43	LAT	1.15	56.5
A-62	LAT	1.16	57.2	B2-45	SAP	1.16	57
A-63	LAT	1.29	51.9	B2-47	SAP	1.39	50.5
A-64	SAP	1.87	34.6	B2-49	SAP	1.19	55.5
A-65	SAP	1.73	34.5	B2-51	SAP	1.83	30.5
A-66	SAP	1.52	41.3	B2-53	NeS	2.3	12.5
A-67	SAP	1.28	52	B2-55	NeS	2.21	15.5
A-68	SAP	2.18	23.2	B2-57	NeS	2.25	12.5
A-69	SAP	1.59	38.2				
A-70	PlcPh	1.95	25.1				
A-84-A	PlcPh	2.35	8.9				
E1-Profile				E2-Profile			
Sample	Rock type	Density	Porosity (%)	Sample	Rock type	Density	Porosity (%)
E1-88	LAT	1.14	59.3	E2-110	LAT	1.41	46.9
E1-71	LAT	1.31	50.2	E2-111	LAT	1.41	46.5
E1-91	LAT	1.27	51.5	E2-112	LAT	1.36	48.6
E1-72	LAT	1.09	56.9	E2-113	LAT	1.25	55
E1-92C	LAT	1.21	54.9	E2-114	LAT	1.18	51.5
E1-73	UMD	1.3	54.7	E2-115	LAT	1.27	51.8
E1-96	SAP	1.68	35	E2-116	LAT	1.23	53.6
E1-74	CpxPh	2.27	11.8	E2-118	SAP	1.43	45.5
E1-75	CpxPh	2.37	7.8	E2-119	SAP	1.68	35
E1-76	CpxPh	2.61	<1	E2-120	SAP	1.56	41
E1-77	CpxPh	2.41	6.4	E2-99	VLPh	2.3	7.2
E1-78	CpxPh	2.34	7.5	E2-102	VLPh	2.3	7.2

Rock types:

- LAT – laterite
- SAP – saprolite
- UMD – ultramafic dyke
- PlcPh – pseudoleucite-bearing phonolite
- NeS – nepheline syenite
- CpxPh – clinopyroxene-bearing phonolite
- VLPh – volcanic leucocratic phonolite

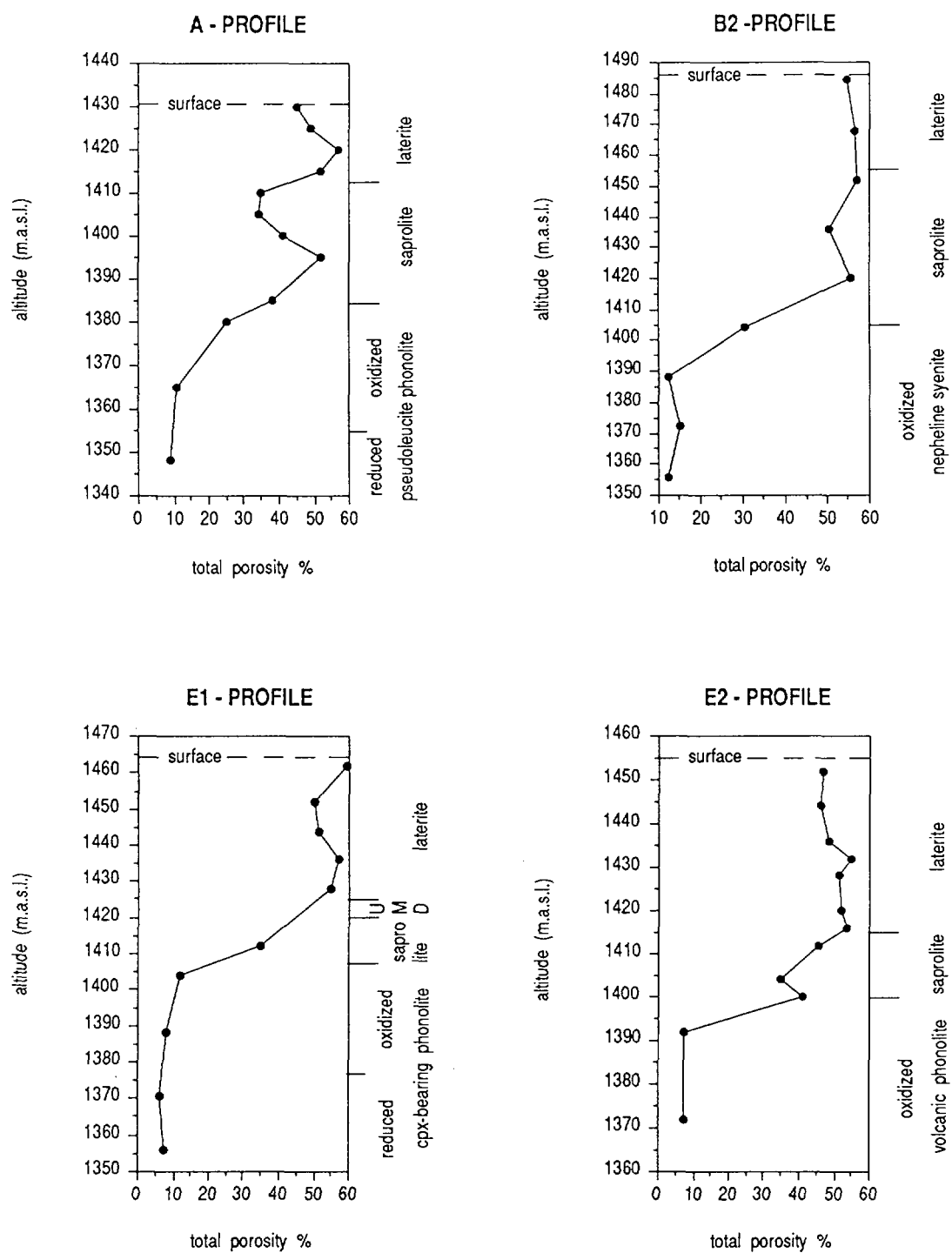
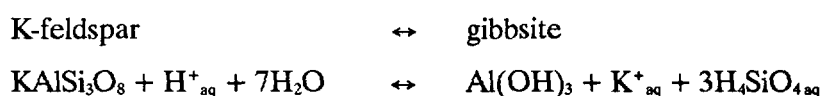
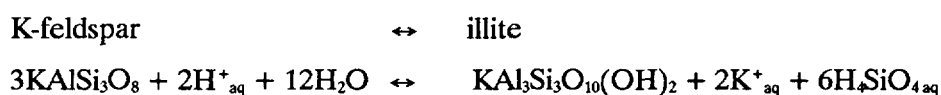
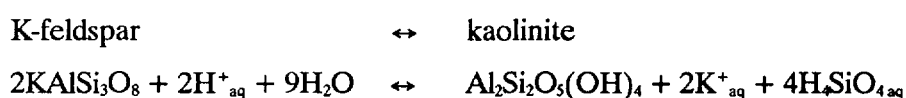


Figure 8. Variation of total porosity in four weathering profiles from different parent rocks. (Profile locations are indicated in Figure 4).

kaolinite and illite and, in certain zones, to gibbsite. This transformation occurs according to the following reactions:



The transformation of K-feldspar to kaolinite is the most abundant decomposition reaction of K-feldspar. This is reflected in the increase of the kaolinite:illite ratio from the lower to the upper levels in the saprolite horizon, always bearing in mind the strongly heterogeneous distribution of these two components in the bedrock.

Kaolinite

Kaolinite is the most abundant silicate mineral phase formed during weathering. However, to quantify the newly formed kaolinite is impossible due the high and heterogeneous abundance of kaolinite in the hydrothermally altered bedrocks. SEM investigations show that kaolinite resulting from secondary weathering tends to form more sparry aggregates comprising less well-defined crystals than in the bedrock. Densely packed kaolinite “booklets”, typical for the hydrothermally altered bedrock, become less frequent towards the higher levels of the saprolite horizon, eventually disappearing in the laterite. The first transformation of kaolinite to halloysite and gibbsite takes place in the upper part of the saprolite; however, transformation of kaolinite to gibbsite in the saprolite is restricted to those horizons covering the nepheline syenite and plc-phonolite, displaying increased total porosity when compared to that above the other bedrock units.

Illite/sericite

In common with kaolinite, difficulties also arise in the case of illite when distinguishing between hydrothermally formed illite/sericite and that formed during weathering. In several saprolite samples a bimodal grain-size distribution is observed. Hydrothermal illite/sericite, mainly occurring along fractures and associated with pseudomorphically replaced nepheline, is present in grain-sizes of about 2μ , with some coarser sericite flakes reaching about 40μ . In contrast, illite/sericite forms larger crystals (about $40\text{--}100\mu$) around corroded K-feldspar and again in fissures. Such sericite flakes partially overgrow fine-grained hydrothermal illite in nepheline pseudomorphs, and is thus thought to be of a weathering origin. Higher up in the laterite profile, illite becomes more and more unstable and breaks down to kaolinite and gibbsite. However, dissolving illite/sericite is found in all four profiles up to the surface. The major part of the partially preserved illite/sericite is of hydrothermal origin, as evidenced by its stable isotope composition. Factors isolating the illite/sericite from complete dissolution include Fe- and Mn-hydroxide coatings and being embedded in a dense framework of kaolinite, both of which protect the illite/sericite from further access to water. The chemical composition of the illite/sericite itself is also an important factor (Waber, 1990). Illite-smectite mixed-layers are only observed in the saprolite horizons overlying the plc-phonolite and nepheline syenite.

Gibbsite

Gibbsite occurs in the saprolite horizon only in the uppermost levels capping the plc-phonolite and nepheline syenite. Here it occurs in grain-sizes of about $2\text{--}20\mu$, mainly infilling pore spaces and fissures. In the laterite, gibbsite becomes more and more abundant towards the surface. Textural relationships indicate the formation of gibbsite mainly from the decomposition of kaolinite according to the following reaction:



In certain zones gibbsite is also formed by the transformation of K-feldspar. Frequently observed is an intimate relationship between gibbsite and amorphous gel material, suggesting gibbsite formation from amorphous Al-gel in the upper zones of the laterite.

Fe-oxides/hydroxides

In contrast to the bedrock oxidised zone, the Fe-hydroxides are no longer dispersed over the whole rock but tend to be more concentrated in specific zones (ferricretes), especially in the laterite. Amorphous to poorly crystalline Fe-hydroxides are the most abundant iron phases in the upper part of the laterite. Within concretions of such phases, goethite and, if further isolated from water, hematite may form through aging. Lower down the profile the abundance of goethite increases compared to the poorly crystalline Fe-hydroxides.

Autoradiography of the laterite and saprolite samples reveals a close relationship between the degree of crystallinity of the iron phases and their capacity for absorbing radionuclides. Thus, around poorly crystalline Fe-hydroxides a more intense α -radiation halo is always developed in contrast to aggregates of goethite and hematite, where such haloes are often lacking. This is further supported by the selective leaching studies performed on samples from the weathering cover (see Appendix 2).

U-, Th- and REE-phases

No secondary uranium phase could be detected in the weathering zone; uranium is mainly absorbed on Fe-hydroxides or partly incorporated in preserved brannerite relicts and in secondary Th- and REE-phases. The latter are fairly abundant in certain zones, the most important among them being florencite, thorogummite, goyazite, gorceixite and crandallite. However, their distribution is very heterogeneous over the entire weathering profile.

Relict minerals

The most important relict minerals unaffected by the weathering solutions are zircon, Zr-minerals, and Ti-oxides (e.g. brannerite, leucoxene). These minerals all become residually enriched towards the surface by the dissolution and removal of the overlying, less resistant minerals. Monazite is also present in such residual mineral assemblages, although it may be of secondary origin.

5.2. Geochemistry

Intense hydrothermal alteration and mineralisation have resulted in the unique chemical composition of the rocks encountered in the Osamu Utsumi mine area, in contrast to analogous rock types generally exposed in the Poços de Caldas alkaline complex (see Ulbrich, 1984; Schorscher and Shea and Shea, this report series; Reps. 1 and 4). As previously stated, the mineralogical investigations revealed three major hydrothermal stages: potassic alteration, disseminated mineralisation (mainly pyritisation) and vein-type mineralisation (mainly Zr-REE-U-Th-Mo). In order to provide a general chemical characterisation of the different rock types, a set of samples were selected which display typical alteration and disseminated mineralisation patterns. Vein-type mineralisation is excluded from these considerations and is discussed in more detail in Section 5.2.3. However, it has to be kept in mind that vein-type mineralisation occurs in all the rocks investigated, although to markedly varying degrees.

Superimposed on the hydrothermal alteration is the oxidation of the rocks due to downward-migrating oxidising groundwaters. These processes which began after hydrothermal activity had ceased, are still taking place at the present time. Oxidation of the rocks occurs at low temperatures and represents the initial stage of meteoric weathering.

5.2.1. Phonolites

The petrography of the phonolite groups, based on relict textural and mineral criteria that survived the magmatic and deuteric stages, shows a marked overlap in chemical composition; within individual groups there is considerable scattering. Comparison of the hydrothermally altered phonolites with those incipiently altered and non-altered phonolites from the mine walls (profile E1, NW-wall, samples E1-77, E1-78 and E1-76, respectively; Table VIII) and the regional phonolites (Table IX) indicates the general trend of the hydrothermalism.

In borehole F1, reduced and oxidised leucocratic phonolites are the predominant rocks, whereas reduced pseudoleucite- and clinopyroxene-bearing phonolites were recovered in borehole F3. Chemical analyses and the elemental variation with depth in these boreholes are given in Appendix 4. Major and trace element distributions for the different phonolitic rocks in the reduced and oxidised states are shown as a Harker diagram in Figure 9. Average compositions are listed in Table VIII.

TABLE VIII

Geochemical average values of the different hydrothermally altered rocks from the Osamu Utsumi mine (data by XRF; breccia data by ICP-EMS).

		Leucocratic phonolite oxidised n=6	Leucocratic phonolite reduced n=21	Volc. leucocrat. phonolite oxidised n=8	Volc. leucocrat. phonolite reduced n=2	Pseudoleucite phonolite reduced n=6	Plc-Cpx phonolite reduced n=9	Cpx-bearing phonolite oxidised n=2	Cpx-bearing phonolite red. "hydroth." n=2	Cpx-bearing phonolite red. "fresh" n=1
SiO ₂	wt. %	55.74	56.89	56.59	56.13	55.50	55.87	56.57	57.14	53.08
TiO ₂		0.53	0.44	0.47	0.53	0.54	0.41	0.47	0.44	0.39
Al ₂ O ₃		23.28	21.80	23.01	21.83	21.70	22.20	22.73	22.22	20.21
Fe _{tot}		3.04	2.53	2.52	2.72	2.75	2.35	1.38	1.37	4.54
MnO		0.00	0.04	0.00	0.00	0.00	0.00	0.02	0.02	0.47
MgO		0.03	0.05	0.03	0.10	0.08	0.15	0.16	0.14	0.26
CaO		0.00	0.19	0.00	0.05	0.02	0.06	0.02	0.66	1.49
Na ₂ O		0.29	0.36	0.33	1.00	0.57	0.99	0.41	0.45	4.85
K ₂ O		12.96	13.72	13.48	13.14	13.06	13.44	12.83	13.14	9.08
P ₂ O ₅		0.07	0.06	0.04	0.11	0.12	0.10	0.08	0.07	0.04
LOI		3.27	3.08	2.58	3.34	3.40	2.64	3.89	2.41	2.54
CO ₂		n.a.	n.a.	n.a.	0.17	0.21	0.24	0.13	0.14	1.58
F	ppm	1218	2085	n.a.	1324	1280	1466	n.a.	n.a.	n.a.
Ba		583	677	823	487	688	913	558	678	453
Rb		315	309	349	273	297	294	263	289	226
Sr		188	198	170	581	335	575	621	868	2163
Pb		30	4	28	40	30	51	b.d.	b.d.	6
Th		46	30	51	43	60	47	28	48	34
U		185	20	54	25	109	46	6	11	12
Nb		225	188	146	268	234	219	187	224	219
La		309	268	326	438	341	403	382	380	278
Ce		673	311	617	384	357	401	318	341	296
Nd		83	61	73	71	72	82	81	79	52
Y		73	54	58	64	97	111	65	82	45
Zr		1360	1009	738	613	2684	1344	678	762	749
V		239	236	167	333	259	218	183	244	74
Cr		7	6	8	b.d.	b.d.	b.d.	b.d.	b.d.	b.d.
Ni		5	b.d.	6	b.d.	4	b.d.	b.d.	b.d.	b.d.
Co		6	5	6	4	11	4	b.d.	b.d.	5
Cu		b.d.	b.d.	b.d.	b.d.	b.d.	b.d.	b.d.	b.d.	b.d.
Zn		24	222	8	104	248	220	62	60	171
Hf		12	10	7	5	20	16	n.a.	n.a.	n.a.
Ga		40	38	36	5	36	n.a.	36	43	36
Sc		3	3	3	6	5	6	4	8	2
S		27	8237	34	8524	12574	5925	766	2149	1601

XRF-data; n.a. = not analysed, b.d. = below detection.

TABLE VIII (contd.)

		Ne-Syenite	Ne-Syenite			Ne-Syenite	Phonol. dyke	Volc. breccia
		oxidised	reduced			F4-353	F4-353	F4-353
		n=4	n=7			reduced	reduced	reduced
		n=4	n=7			n=11	n=1	n=6
SiO ₂	wt. %	56.53	54.65	SiO ₂	wt. %	54.3	53.7	56.73
TiO ₂		0.52	0.68	TiO ₂		1.36	0.66	0.43
Al ₂ O ₃		24.61	19.22	Al ₂ O ₃		19.4	19.6	17.55
Fe _{tot}		1.70	4.34	Fe ₂ O ₃		4.31	5.07	5.34
MnO		0.06	0.61	MnO		0.92	0.73	0.36
MgO		0.16	0.13	MgO		0.2	0.21	0.19
CaO		0.03	0.62	CaO		0.03	0.17	0.03
Na ₂ O		0.01	0.63	Na ₂ O		0.11	0.12	0.33
K ₂ O		13.21	13.30	K ₂ O		13.9	13.7	13.8
P ₂ O ₅		0.08	0.05	P ₂ O ₅		0.04	0.05	0.05
LOI		2.94	2.72	LOI		3.79	4.16	3.75
CO ₂		n.a.	1.08	CO ₂		n.a.	n.a.	n.a.
F	ppm	n.a.	4009	F	ppm	n.a.	n.a.	n.a.
Ba		1217	670	Ba		1406	671	489
Rb		313	383	Rb		305	328	360
Sr		926	215	Sr		286	584	190
Pb		18	11	Pb		n.a.	n.a.	n.a.
Th		54	36	Th		31	27	71
U		14	56	U		24	24	29
Nb		129	377	Nb		293	272	234
La		307	335	La		186	211	248
Ce		299	357	Ce		241	311	327
Nd		90	69	Nd		60	64	80
Y		57	38	Y		n.a.	n.a.	n.a.
Zr		317	1629	Zr		816	1050	8997
V		351	137	V		120	140	57
Cr		5	b.d.	Cr		3	3	2
Ni		7	b.d.	Ni		3	b.d.	4
Co		b.d.	7	Co		1	3	1
Cu		b.d.	b.d.	Cu		5	5	4
Zn		57	306	Zn		167	280	133
Hf		n.a.	18	Hf		15	17	158
Ga		43	n.a.	Ga		n.a.	n.a.	n.a.
Sc		6	4	Sc		1	1	1
S		355	13183	S		n.a.	n.a.	n.a.

XRF-data; n.a. = not analysed, b.d. = below detection.

ICP-MS data; n.a. = not analysed, b.d. = below detection.

TABLE VIII (contd.)

Samples used for average value calculations presented in table.

	Reduced			Oxidised
Leucocratic phonolite	F1-75-1A	F1-101-1A	F1-117-1A	F1-45-1A
	F1-75-1B	F1-104-1A	F1-118-1A	F1-47-1A
	F1-77-1A	F1-106-1A	F1-119-1A	F1-50-1A
	F1-77-1B	F1-107-1A	F1-121-1A	F1-55-1A
	F1-78-1A	F1-112-1AD	F1-126-1A	F1-59-1A
	F1-81-1A	F1-113-1A	F1-126-1AA	F1-63-1A
	F1-95-1A	F1-113-1B	F1-126-1B	
Volcanic leucocratic phonolite	F3-10-1A			F1-1-1B
	E2-102			F1-10-1A
				F1-14-1A
				F1-20-1A
				F1-20-1B
				F1-23-1A
				F1-31-1A
				F1-33-1A
Pseudoleucite-bearing phonolite	F1-91-1A			
	F3-74-1B			
	F3-75-1A			
	F3-79-1A			
	A-84-A			
	A-86-B			
Plc-clinopyroxene-bearing phonolite	F3-20-1B			
	F3-21-1B			
	F3-23-1B-A			
	F3-28-1A			
	F3-36-1A			
	F3-46-1B			
	F3-48-1A			
	F3-64-1A			
	F3-69-1A			
Clinopyroxene-bearing phonolite	E1-77			E1-74
	E1-78			E1-75
Phonolitic dyke	F4-353-PhD			
Nepheline syenite	F4-91-1A			F4-22-1A
	F4-129-1A			B2-53
	F4-413-1AA			B2-55
	F4-413-1AB			B2-57
	F4-413-1AC			
	F4-413-1AD			
	F4-413-1AE			
	F4-353; NS1-1 to 11			
Volcanic breccia	F4-353; NS2-1 to 6			

TABLE IX
 Geochemical average values for hydrothermally unaffected regional samples (XRF-data from Schorscher and Shea, this report series; Rep. 1).

		Reg. subvolc. phonolite n = 2	Reg. volcanic phonolite n = 4	Reg. hypabyss. Ne-Syenite n = 2	Regional Ne-Syenite n = 2
SiO ₂	wt. %	52.87	53.11	52.76	52.44
TiO ₂		0.66	0.56	0.66	0.79
Al ₂ O ₃		19.57	19.64	19.39	19.40
Fe _{tot}		4.14	3.73	4.22	4.00
MnO		0.00	0.00	0.25	0.26
MgO		0.31	0.22	0.31	0.34
CaO		1.85	1.55	1.89	1.67
Na ₂ O		7.55	7.63	7.60	7.03
K ₂ O		8.26	8.26	8.24	7.76
P ₂ O ₅		0.10	0.06	0.09	0.11
LOI		1.44	1.35	1.32	3.29
CO ₂		n.a.	n.a.	n.a.	n.a.
F	ppm	1983	1561	2406	1276
Ba		425	50	316	421
Rb		160	154	160	143
Sr		2327	1421	1973	2423
Pb		5	2	8	12
Th		8	5	11	20
U		b.d.	b.d.	b.d.	b.d.
Nb		212	261	238	275
La		250	279	261	245
Ce		316	379	340	338
Nd		82	100	87	90
Y		36	41	40	48
Zr		880	885	993	1182
V		72	72	73	46
Cr		b.d.	b.d.	b.d.	b.d.
Ni		b.d.	b.d.	b.d.	b.d.
Co		10	19	8	7
Cu		b.d.	b.d.	b.d.	b.d.
Zn		153	165	166	191
Hf		12	10	13	17
Ga		n.a.	n.a.	n.a.	n.a.
Sc		b.d.	b.d.	b.d.	b.d.
S		8153	6229	1027	712

XRF-data; n.a. = not analysed, b.d. = below detection.

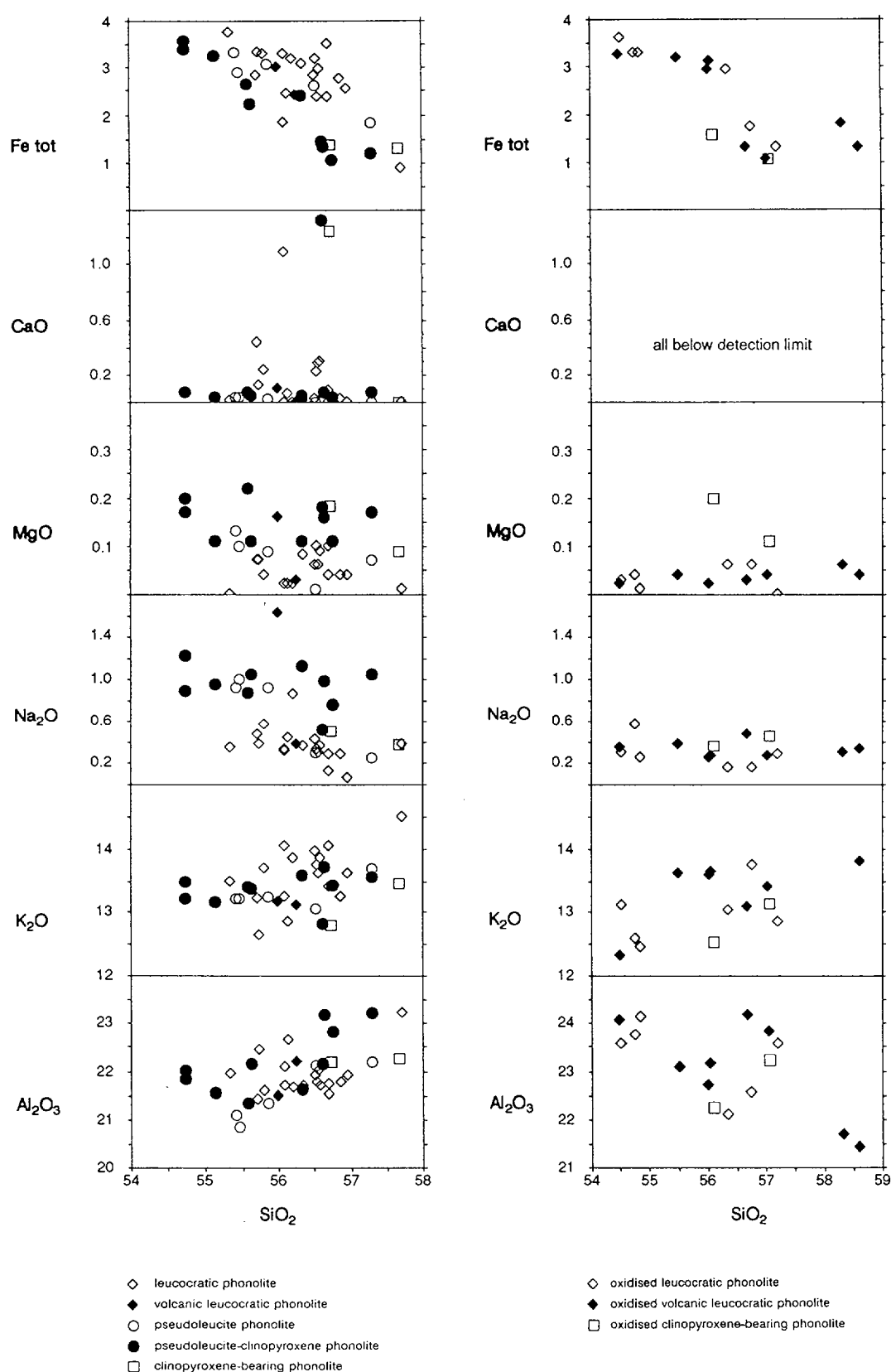


Figure 9. Harker diagrams for selected major and trace elements of hydrothermally altered phonolites from the Osamu Utsumi uranium mine.

(Samples from boreholes F1 and F3; cpx-phonolite from E1-profile: reduced samples E1-77, E1-78, oxidised samples E1-74, E1-75).

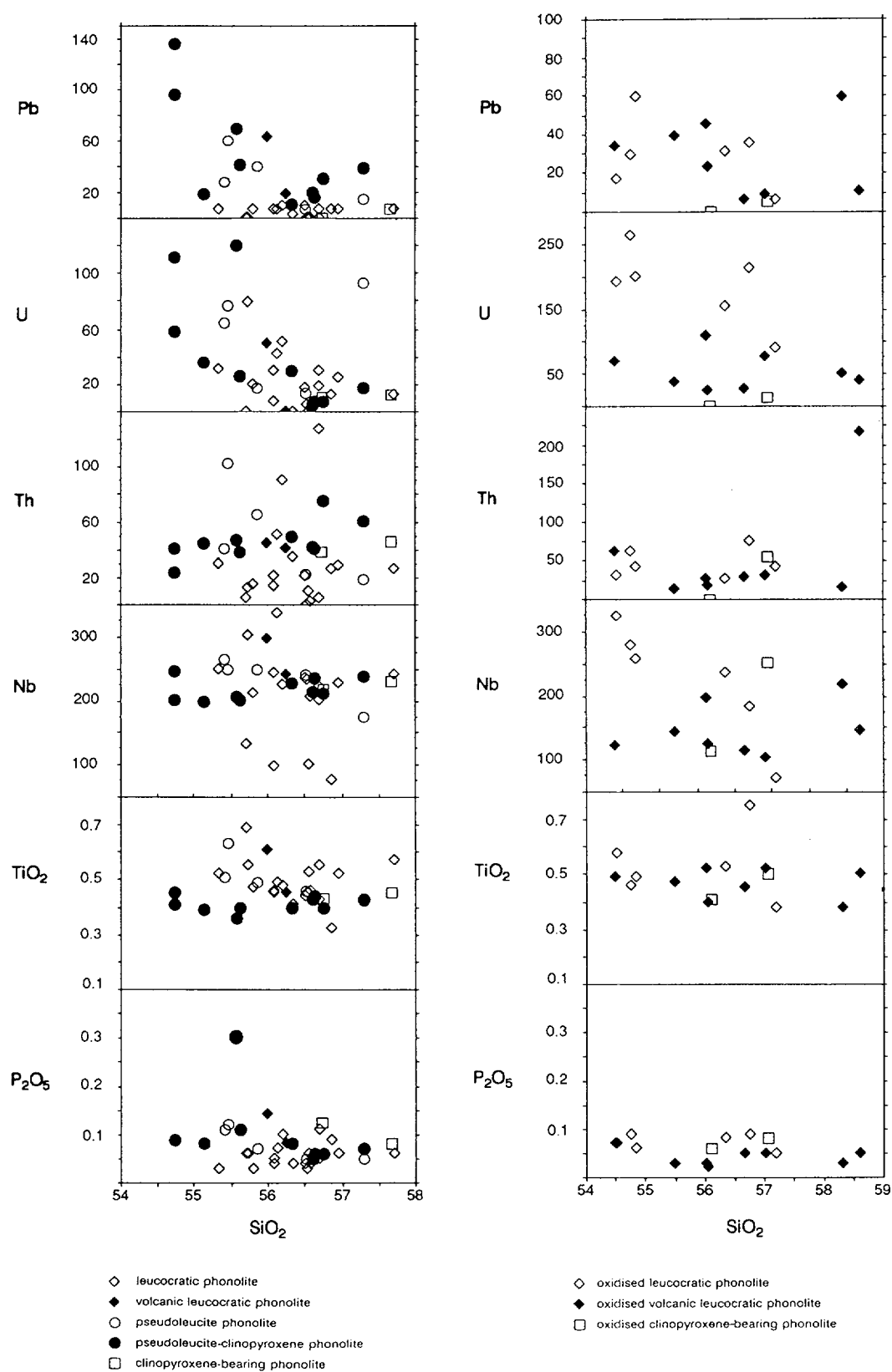


Figure 9 (contd.).

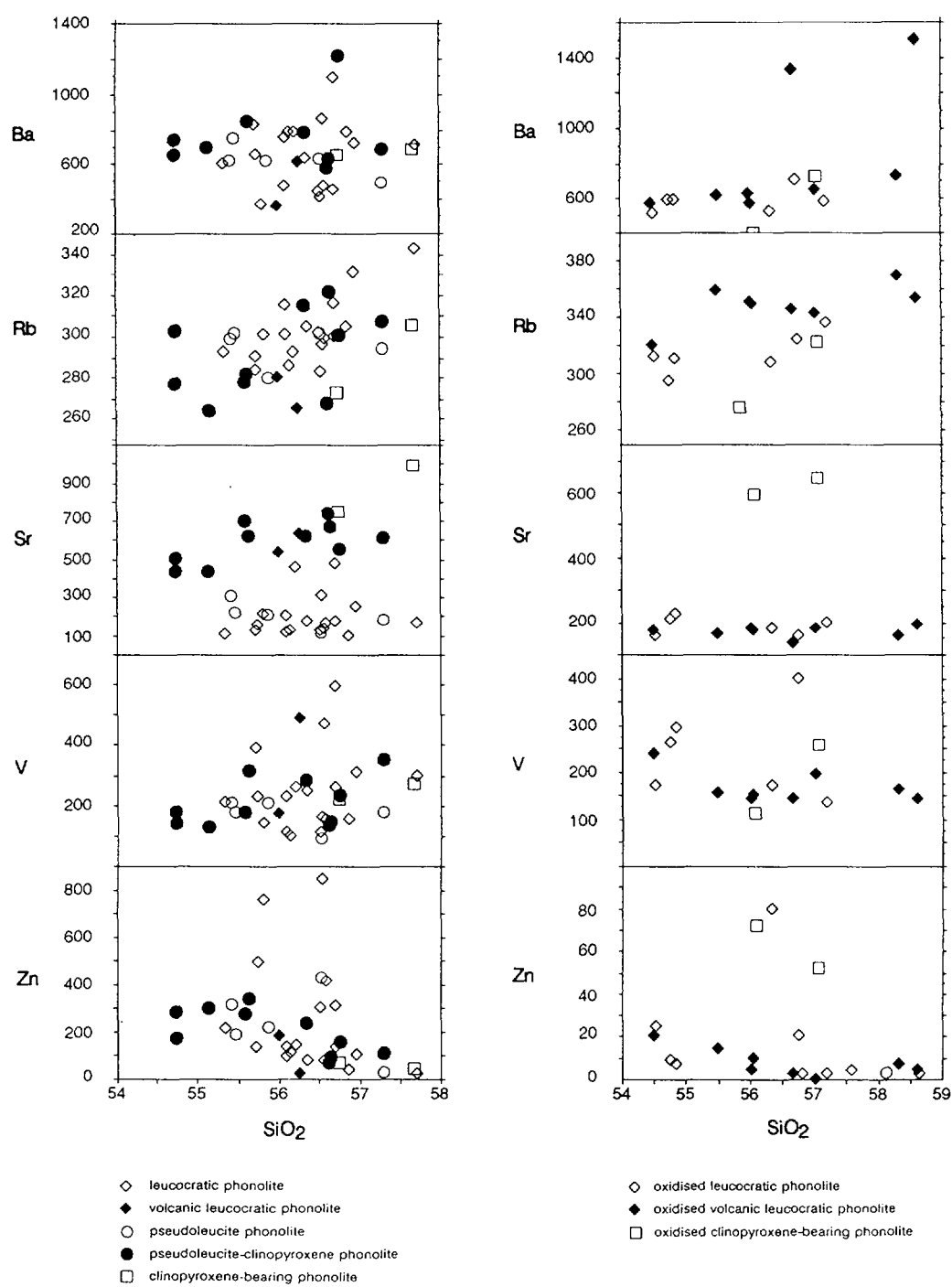


Figure 9 (contd.).

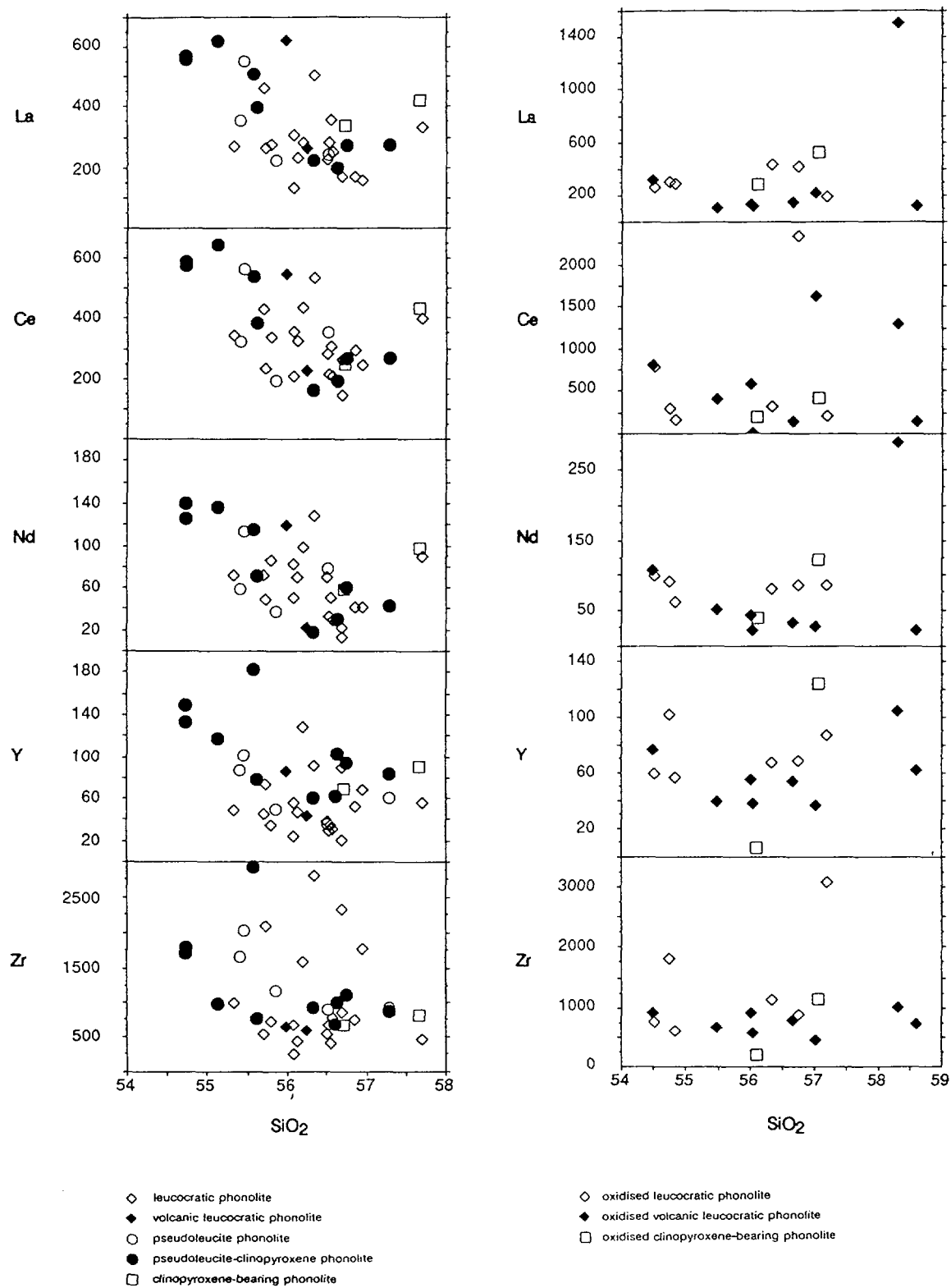


Figure 9 (contd.).

5.2.1.1. Major elements

The reduced phonolitic rocks are all characterised by their strongly elevated potassium contents, a fact that led to the term “potassic rocks” being commonly used in the earlier literature (e.g. Utsumi, 1971; Almeida Filho and Paradella, 1977; Ulbrich, 1984). The potassium contents for the hydrothermally altered phonolites range from 12.5 – 14.5 wt.% K₂O, compared to an average of about 8 wt.% K₂O (Schorscher and Shea and Shea, this report series; Reps. 1 and 4; Ulbrich, 1984) for regional phonolitic rocks not affected by hydrothermal alteration.

In Figure 10 the average compositions of the different hydrothermally altered phonolitic rocks are normalised to the mean value for the regional rocks. SiO₂ and Al₂O₃ are slightly increased, whereas total iron and particularly Na₂O, CaO, MgO and MnO are always strongly to completely depleted in the mine phonolites when compared to the regional phonolites.

Only rare systematic variations in major elements were observed in the phonolite samples when boreholes F1 and F3 are compared with the mine walls. However, the observed mineralogical zoning around the breccia pipes is also reflected in the chemical composition. Thus, a tendency towards a positive SiO₂-Al₂O₃ correlation is developed as a function of decreasing distance from the breccia pipes. Such a trend is represented, for example, by the leucocratic phonolite (Fig. 9). In contrast, the pseudoleucite-clinopyroxene phonolites more distant from the breccia pipes have fairly constant K₂O values over the same range in SiO₂. Al₂O₃ displays an antipathetic pattern with a positive correlation in the pseudoleucite-clinopyroxene phonolite and fairly constant values for the leucocratic phonolite. This is reflected mineralogically in the observed zoning of a central zone rich in K-feldspar when compared to the more argillically altered marginal zones.

The bimodal distribution of Na₂O between the pseudoleucite-clinopyroxene phonolite (average 0.95 wt.%) and the leucocratic phonolite (average 0.37 wt.%) supports the above observations. In the unaltered regional samples sodium mainly occurs in aegirine-augite and, to a lesser extent, in alkali feldspar (Ulbrich, 1983; Ulbrich, 1984). In the potassic rocks clinopyroxene is totally decomposed and the alkali feldspars have suffered an almost complete exchange of the albite component. Yet, this alkali-exchange is less pronounced in the phonolites farther from the breccia pipes, where, in addition, some of the sodium is contained in clay minerals (illite) that occur in the clinopyroxene pseudomorphs.

Both MgO and CaO have very low concentrations in all the phonolitic rocks; MgO is mainly present in clay minerals from the clinopyroxene-bearing types. Hydrothermally induced carbonate is responsible for the elevated CaO-contents found in a few samples.

In the reduced rocks, by far the largest contribution of iron is present as ferrous iron in pyrite. The observed spread in total iron reflects, to a certain degree, the intensity of the hydrothermal pyrite impregnation. In the pseudoleucite-clinopyroxene phonolite, Fe_{ox} is negatively correlated with SiO_2 and Al_2O_3 . This reflects to a certain degree the mineralogical observation that pyrite impregnation decreases with increasing argillic alteration.

5.2.1.2. Trace elements

Trace element compositions of the different phonolite types are very complex (Fig. 9). From the figure it becomes obvious that the multistage hydrothermal overprint did not result in a homogeneous alteration/mineralisation pattern in the different phonolite types. In addition, primary differences in trace element composition are still partly preserved (e.g. Sr). In Figure 11 the average trace element compositions of the hydrothermally altered phonolites are normalised to the mean values for the regional rocks. In common with all the different phonolite types encountered in the Osamu Utsumi mine are the enhanced average contents of Ba, Rb, Pb, U, Th, Y, V, and S, and the strong depletion in Sr and Co compared to the regional samples. F, Zr, Hf and Zn are enriched in some and depleted in other phonolite types of the mine. Of the LREEs, La is commonly slightly enriched, Ce displays similar values, and Nd is depleted compared to the unaltered regional rocks.

Maximum fluorine contents occur in the leucocratic phonolite, the phonolite nearest to the breccia pipe of ore body B, where its concentration is increased by a factor of two compared to all other phonolites. Fluorine is primarily incorporated in fluorite (CaF_2).

Barium is present in similar amounts within all the different phonolites, with the exception of the pseudoleucite-clinopyroxene phonolite where it is slightly enhanced (880 ppm compared to 600–690 ppm). Barite ($BaSO_4$) is the most important Ba-mineral, although in the leucocratic phonolite and the pseudoleucite-phonolite, gorceixite ($BaAl_3(PO_4)_2OH \cdot H_2O$) is also an important Ba-phase. In these rocks Ba is positively correlated with P_2O_5 .

Rubidium displays similar values (289 – 309 ppm) for the hydrothermally altered phonolites. In the weakly hydrothermally altered cpx-phonolite of the NW-wall of the

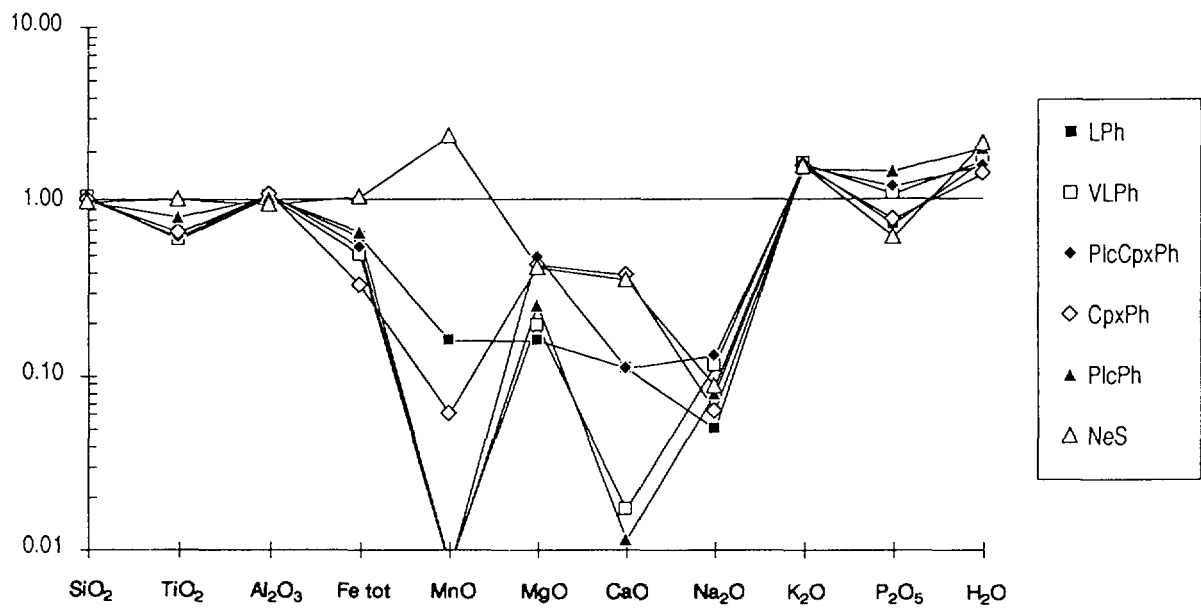


Figure 10. Average major element compositions of hydrothermally altered reduced phonolites and nepheline syenites from the Osamu Utsumi mine normalised to the average composition of unaltered regional rocks.

(LPh: leucocratic phonolite; VLPh: volcanic leucocratic phonolite; PlcCpxPh: pseudoleucite-clinopyroxene bearing phonolite; CpxPh: clinopyroxene-bearing phonolite; PlcPh: pseudoleucite-bearing phonolite; NeS: nepheline syenite).

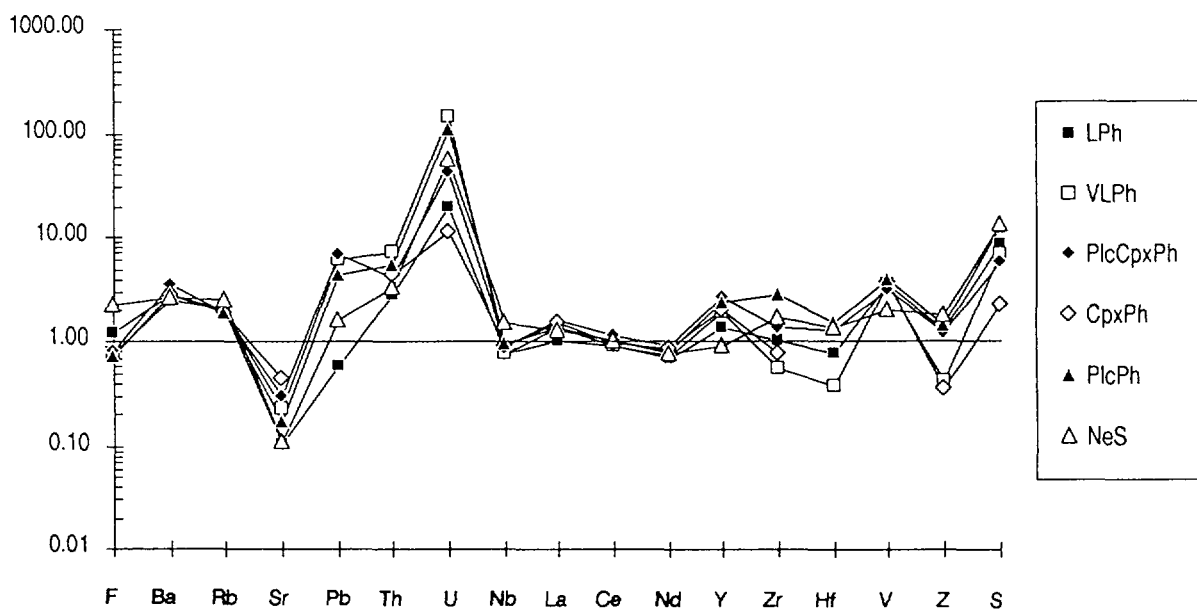


Figure 11. Average trace element compositions of hydrothermally altered reduced phonolites and nepheline syenites from the Osamu Utsumi mine normalised to the average composition of unaltered regional rocks.

(Legend as in Fig. 10).

mine (sample E1-76; Table VIII) rubidium is distinctly lower (226 ppm) but is still higher than in the regional phonolitic rocks (154 – 160 ppm). Rubidium is positively correlated with K_2O and is mainly incorporated into alkali feldspar. The K/Rb-ratio ranges from 399 in the volcanic leucocratic phonolite to 377 in the clinopyroxene-bearing phonolite, compared to K/Rb-ratios of 429 and 445 respectively for the regional subvolcanic and volcanic phonolites. The lowest K/Rb ratio is recorded for the weakly hydrothermally altered cpx-phonolite (sample E1-76) with a value of 334. The Rb/Sr-ratios display a much broader spread, from 1.56 for the leucocratic phonolite to 0.33 for the hydrothermally altered clinopyroxene-bearing phonolite, compared to a Rb/Sr-ratio of 0.10 for the weakly hydrothermally altered cpx-phonolite and of 0.07 and 0.11 for the regional subvolcanic and volcanic phonolites respectively.

Average values for strontium progressively increase from the leucocratic phonolite (198 ppm; n=21) to the pseudoleucite phonolite (335 ppm; n=6), volcanic leucocratic phonolite (436 ppm; n=2), pseudoleucite-clinopyroxene phonolite (591 ppm; n=10) and, finally, clinopyroxene-bearing phonolite (868 ppm; n=2). The cpx-phonolite exposed in the northern mine wall, and only weakly affected by the hydrothermal alteration, has Sr-values of about 2200 ppm. Thus the decreasing Sr-values to a certain degree reflect the proximity of the rock to the breccia pipe. However, one has to bear in mind the primary differences as observed in the unaltered regional samples, where Sr varies between 1421 ppm for the volcanic phonolites and 2327 ppm for the subvolcanic phonolites.

Sr does not show any significant correlation with other elements, except for the pseudoleucite phonolite where it is positively correlated with P_2O_5 due to the occurrence of goyazite ($SrAl_3(PO_4)_2OH \cdot H_2O$). The Ba/Sr-ratio is always considerably larger than unity, with the exception of the clinopyroxene-bearing phonolite (0.78). In contrast, the Ba/Sr-ratio is 0.06 for the regional volcanic phonolites and 0.18 for the regional subvolcanic phonolites.

In the regional rocks unaffected by the hydrothermal alteration, Sr is incorporated predominantly in mafic minerals (in miaskitic rocks) and/or in rare metal silicates (in agpaitic rocks, e.g. lamprophyllite). However, it also occurs as a trace constituent in the alkali feldspars (Ulbrich, M., 1983). In the hydrothermally altered phonolites of the mine, mafic minerals and magmatic rare metal silicates are decomposed and the remaining Sr is thought to occur mainly in fluorite, barite and goyazite (pseudoleucite phonolite).

The behaviour of uranium and thorium is discussed in more detail in Section 8. Both elements are strongly enriched compared to the unaltered regional samples; this is most pronounced in the volcanic leucocratic phonolite and the plc-cpx-phonolite (Fig. 11).

The distribution of U and Th in the bulk of the hydrothermally altered mine rocks, however, is very heterogeneous (compare analyses in Appendix 4).

Niobium is present in similar amounts in all the different phonolites of the mine (averages between 188-234 ppm). Together with titanium it shows a general positive trend, which is best developed in the pseudoleucite-clinopyroxene phonolite. It might therefore be assumed that the bulk of Nb is present in Ti-(Fe-) oxides, as confirmed by mineral chemical analysis. The Nb-values detected for the mine phonolites are similar to the ones found for the regional subvolcanic (212 ppm) and volcanic (261 ppm) phonolites.

Yttrium concentrations are highest in phonolites with pseudoleucite (97 ppm; n=6) and lowest in the leucocratic phonolite (54 ppm; n=21) and the unaltered clinopyroxene-bearing phonolite (sample E1-76, 45 ppm). Particularly in the pseudoleucite-bearing varieties, Y shows a positive correlation with Zr and a less well-defined correlation with P_2O_5 . No similar trend is observed for any of the other elements or REEs. This indicates the close relationship between Zr and Y, which might possibly occur in xenotime solid solutions within zircon (compare Section 5.1.1.4.).

The regional phonolites have slightly lower Y-values (36–41 ppm) than the pseudoleucite-free phonolites of the mine. The pseudoleucite-bearing phonolites display a twofold increase in Y compared to the regional phonolites.

Zirconium varies over a wide range in the different phonolites of the mine, with the highest average value associated with the pseudoleucite phonolite (2684 ppm), and the lowest value with the volcanic leucocratic phonolite (530 ppm). Zircon and subordinate baddeleyite are the most important Zr-bearing mineral phases. Zr occurs in all phonolites positively correlated with Hf; a positive trend of Zr with U is observed in the more distant (>200 m) samples of the breccia pipes, especially in the phonolite types containing clinopyroxene. In the phonolites closer to the breccia pipes, the investigated zircons contain no detectable uranium (Section 5.1.1.4.).

The regional volcanic and subvolcanic phonolites show Zr-values (885 ppm and 880 ppm, resp.) in the range of the peripheral clinopyroxene-bearing phonolite (762 ppm), significantly higher than the volcanic leucocratic phonolite (530 ppm), but lower than the other phonolites (1000 and 2684 ppm).

Vanadium occurs in equal amounts in all of the hydrothermally altered phonolites (averaging 210–259 ppm). The weakly hydrothermally altered cpx-phonolite from the peripheral part of the mine (E1-76) contains similar amounts of V (74 ppm) compared to the regional phonolites (72 ppm), all distinctly lower than the hydrothermally altered phonolites.

Zinc is less abundant in the hydrothermally altered clinopyroxene-bearing phonolite (60 ppm) and the volcanic leucocratic phonolite (70 ppm). In all the other types of phonolite it is present in roughly equal amounts ranging from 205 to 248 ppm. Sphalerite is the only important Zn-phase observed in the mine rocks. Average Zn-values for the regional subvolcanic phonolites are 153 ppm, and for the volcanic phonolites 165 ppm.

Analytical comparison of incompatible elements, normalised to chondritic, and upper mantle norm compositions (Sun, 1980; Thompson, 1982) of the hydrothermally altered phonolites and the regional rocks, enables genetic considerations to be evaluated in terms of hydrothermal alteration and the regional phonolite-nepheline syenite magmatism of the Poços de Caldas complex. Figure 12a shows the very close similarity between the different regional rocks; systematic variations occur only with Ba, Th and Sr between volcanic and subvolcanic rocks. The different hydrothermally altered rock groups of the mine are characterised by the general enrichment of Ba, Rb, Th, K and La, and the strong depletion of Sr (Fig. 12c). Figure 12b compares the mean compositions of unaltered regional volcanic and subvolcanic rocks with the weakly hydrothermally altered cpx-phonolite from the NW-wall of the mine (E1-76) and the mean of incipiently altered samples (E1-77, E1-78). This figure also illustrates the evolutive trend of hydrothermal alteration that has affected the Osamu Utsumi mine site. With increasing hydrothermal influence, one observes a continuous enrichment of the incompatible elements, although the general pattern of the unaltered regional rocks is maintained. Strontium, however, behaves antipathetically and is continuously depleted. This strong relationship in the incompatible element pattern suggests a cogenetic origin for the hydrothermal fluids and for the regional phonolitic-nepheline-syenitic rock suite. However, some characteristic differences between the hydrothermally altered rocks of the mine and the regional rocks have not yet been outlined; these include the overall pyritisation of the mine rocks and their uranium mineralisation.

The oxidised phonolites (Figs. 13 and 14) show, relative to their reduced counterparts, a strong to complete depletion of those elements related with fluorite, carbonate and sulphide dissolution (Ca, Mg, Mn, F, Sr, Zn, S), and an enrichment of elements such as Al, Ba, Pb, U and LREEs, more akin to supergenic enrichment, including secondary mineral formation (e.g. kaolinite, crandallite, gorceixite) and coprecipitation with Fe-hydroxides (e.g. U).

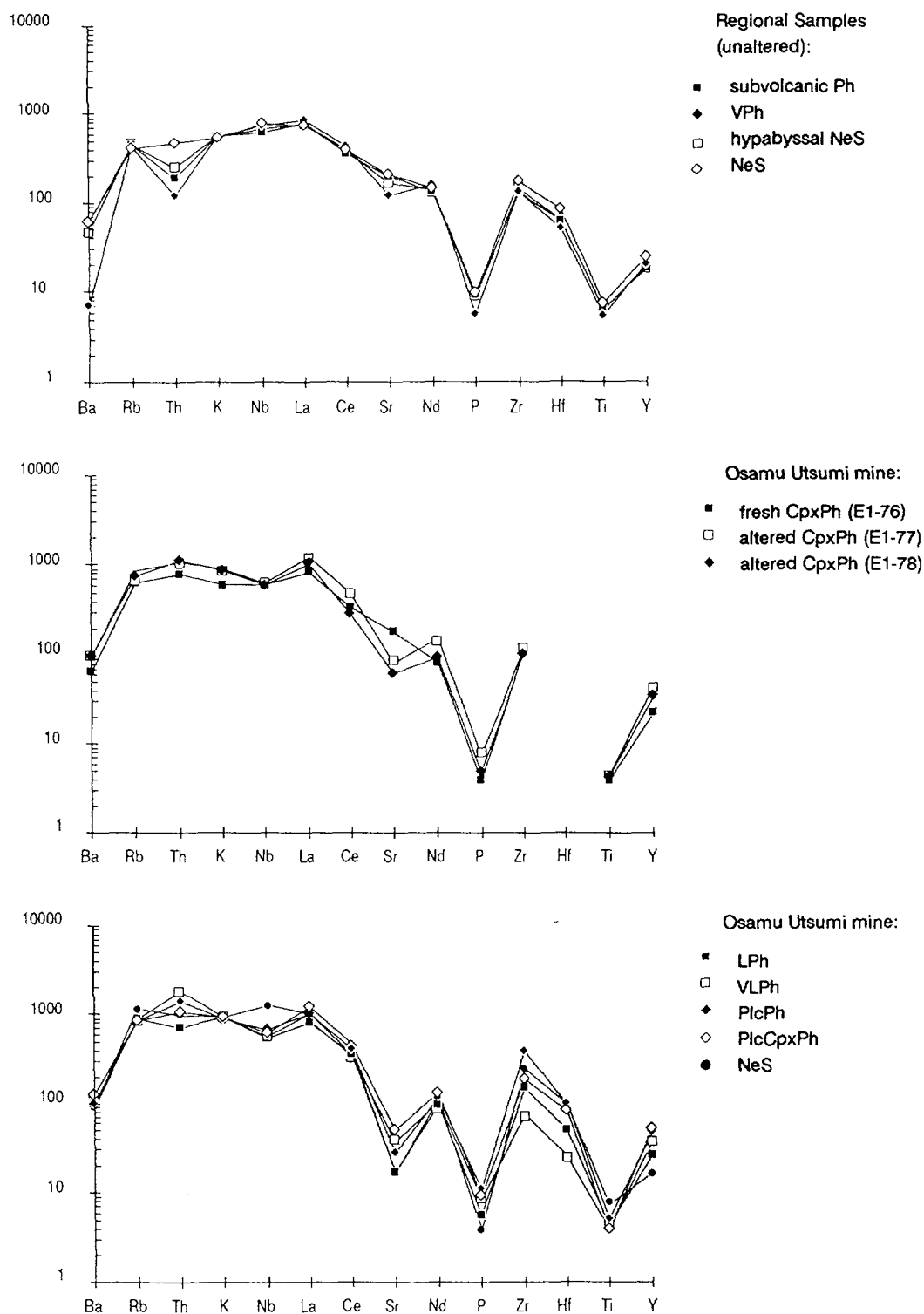


Figure 12. Incompatible elements normalised to chondrite and primitive mantle for:

- unaltered regional rocks,
- unaltered and incipiently altered rocks from the NW-wall of the Osamu Utsumi uranium mine,
- average of hydrothermally altered rocks of the Osamu Utsumi uranium mine.

(Normalisation factors from Thompson, 1982).

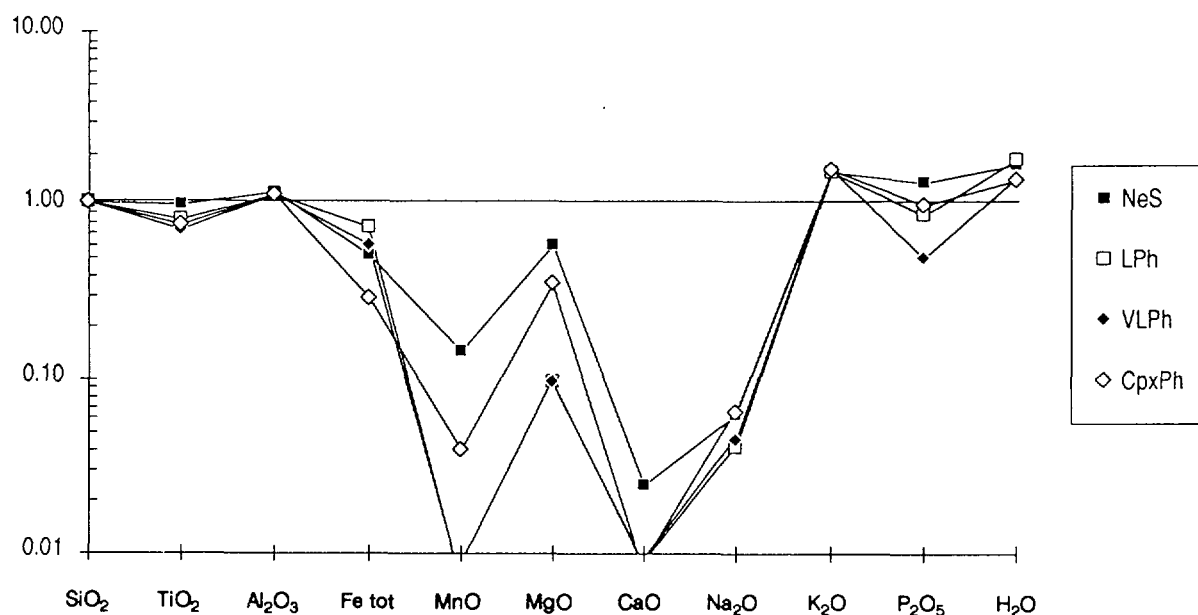


Figure 13. Average major element composition of hydrothermally altered, oxidised phonolites and nepheline syenites from the Osamu Utsumi mine normalised to the average composition of unaltered regional rocks.

(NeS: nepheline syenite; LPh: leucocratic phonolite; VLPh: volcanic leucocratic phonolite; CpxPh: clinopyroxene bearing phonolite).

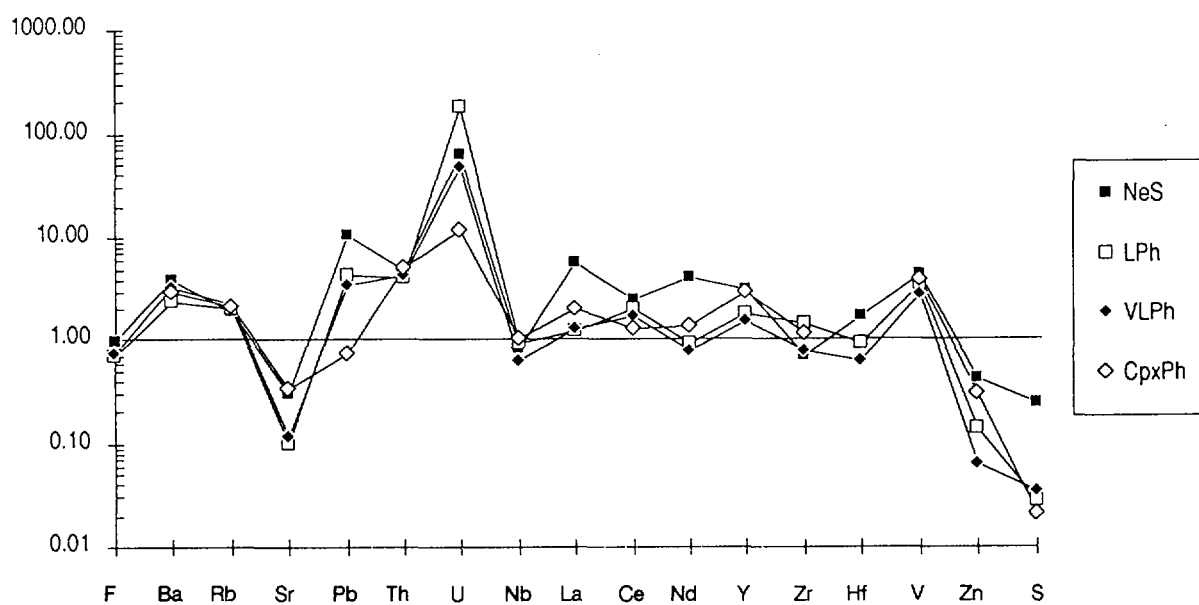


Figure 14. Average trace element composition of hydrothermally altered, oxidised phonolites and nepheline syenites from the Osamu Utsumi mine normalised to the average composition of unaltered regional rocks.

(Legend as in Figure 13).

5.2.1.3. Rare-earth elements (REEs)

The light rare-earth elements (LREEs) show little variation between the different phonolite types (Table VIII, XRF-data). In the mafic-free phonolites, only La shows a slight increase from the leucocratic phonolite to its volcanic counterpart, and to the plc-phonolite. Ce and Nd are similar in composition in all these phonolites. In comparison with the regional phonolitic rocks, the LREEs are slightly increased (Tables VIII-X; Figs. 11 and 16). In all the mine phonolites the inter-element correlation for La, Ce and Nd is fairly good (Fig. 15), and is best pronounced in those phonolites which are richer in primary mafic components, and in those more distant from the breccia pipes. No correlation is observed between the LREEs and Y, suggesting a different mineral phase hosting Y. As described in Section 5.1.1.4., Y is mainly present in zircon, whereas the LREEs occur in monazite, cheralite and the crandallite group minerals.

Analyses of the whole REE-spectra were performed on four leucocratic phonolite samples that are not believed to be influenced by vein-type mineralisation and/or secondary oxidation processes, and thus represent “average samples” (Table X). In Figure 16 the chondrite-normalised REE-patterns for these samples are compared to the hydrothermally unaffected regional phonolites. The steeper decline from La to Sm in the leucocratic phonolites reflects the introduction of LREEs during the hydrothermal phase. This is supported by the increased La/Lu_{cn}-ratio for these phonolites (45.5-82.9) compared to the regional phonolites (28.2 – 33.6). The slight depletion of Eu in the leucocratic phonolite is probably due to the complete exchange of the alkali feldspar to pure orthoclase, and to the removal of plagioclase during the hydrothermal phase.

The heavy rare-earth elements (HREEs) show the same absolute abundance and distribution pattern in both the hydrothermally altered mine phonolites and the unaltered regional samples. Considering the strong preference of clinopyroxene for incorporating HREEs (Henderson, 1984), the regional phonolites would be expected to be richer in HREEs than the leucocratic mine phonolites. However, there are indications that HREEs were introduced during a late stage of the hydrothermal activity (see Section 5.2.3.3.).

A special case is illustrated by the leucocratic phonolite sample WC11-80-1A (Fig. 16). This sample has the same REE-pattern, but with a considerable shift towards lower abundances. This shift can partly be explained by the original spread in REE concentration in the phonolitic rocks of the mine. In addition, the much higher clay content of the total rock volume in the hydrothermal state (45%) compared to the other

TABLE X

Rare-earth element concentrations (ppm) for hydrothermally altered reduced phonolite from the Osamu Utsumi uranium mine, and the hydrothermally unaffected regional samples.

Regional phonolites	La	Ce	Pr	Nd	Sm	Eu	Gd	Tb	Dy	Ho	Er	Tm	Yb	Lu	Eu/Sm
PH-02A	115.09	236.80	22.60	64.45	7.40	2.18	6.66	0.96	4.81	0.93	3.10	0.42	2.95	0.41	0.29
PH-02B	164.72	310.67	29.36	82.80	9.83	2.74	9.49	1.13	6.41	1.41	3.81	0.59	3.31	0.56	0.28
PH-03	92.01	189.93	20.24	64.90	8.64	2.39	6.90	0.94	5.00	0.98	2.76	0.38	2.38	0.34	0.28
PH-05	132.02	323.02	29.79	93.36	12.07	3.18	9.29	1.35	6.70	1.28	3.45	0.49	3.06	0.41	0.26
PH-08	112.29	295.41	25.45	80.11	10.23	2.84	8.12	1.13	6.03	1.13	3.34	0.46	2.79	0.39	0.28
PH-09B	112.14	244.16	26.17	79.75	9.79	2.72	8.14	1.17	6.14	1.19	3.46	0.49	2.89	0.41	0.28
Leucocratic phonolite															
Osamu Utsumi mine															
WC-80-1A	80	127	9.9	25.8	2.67	0.88	2.71	0.32	1.57	0.35	0.98	0.16	1	0.13	0.33
WC-101-1A	195	285	23.1	59.2	5.96	2.11	7.02	1.19	8.33	1.4	3.12	0.39	2.49	0.33	0.35
WC-110-1A	158	313	21	54.4	6.77	2.27	8.54	1.44	9.46	1.67	3.52	0.5	2.74	0.36	0.34
WC-121-1A	208	310	24.2	60.8	5.28	1.77	5.54	0.69	5.23	1.22	3.28	0.41	2.14	0.26	0.34
Normalised to ordinary chondrite															
Regional phonolites	La	Ce	Pr	Nd	Sm	Eu	Gd	Tb	Dy	Ho	Er	Tm	Yb	Lu	La/Lu
PH-02A	386.97	309.83	200.16	112.43	39.69	30.68	26.73	20.86	15.64	13.20	15.41	13.88	13.56	13.22	29.28
PH-02B	553.85	406.48	260.06	144.45	52.74	38.68	38.09	24.64	20.85	20.06	18.93	19.42	16.30	18.07	30.66
PH-03	309.37	248.50	179.28	113.22	46.38	33.68	27.69	20.47	16.25	13.92	13.69	12.40	14.33	10.97	28.21
PH-05	443.91	422.64	263.84	162.88	64.78	44.78	37.30	29.28	21.80	18.23	17.16	16.14	16.07	13.23	33.56
PH-08	377.56	386.51	225.43	139.77	54.89	39.96	32.59	24.47	19.60	16.00	16.58	15.14	11.56	12.70	29.73
PH-09B	377.06	319.46	231.79	139.14	52.51	38.37	32.66	25.40	19.98	16.92	17.21	15.93	14.88	13.45	28.04
Leucocratic phonolite															
Osamu Utsumi mine															
WC-80-1A	269.0	166.2	87.7	45.0	14.3	12.4	10.9	7.0	5.1	5.0	4.9	5.2	4.9	4.2	63.73
WC-101-1A	655.7	372.9	204.6	103.3	32.0	29.7	28.2	25.9	27.1	19.9	15.5	12.7	12.1	10.7	61.20
WC-110-1A	531.3	409.5	186.0	94.9	36.3	32.0	34.3	31.3	30.8	23.7	17.5	16.3	13.3	11.7	45.45
WC-121-1A	699.4	405.6	214.3	106.1	28.3	24.9	22.2	15.0	17.0	17.3	16.3	13.4	10.4	8.4	82.85
Norm. coefficient	0.2974	0.7643	0.1129	0.5732	0.1864	0.07095	0.2491	0.04603	0.3075	0.07039	0.2013	0.03061	0.2059	0.0308	

ICP-EMS-data.

TABLE X (contd.)

F4-413	La	Ce	Pr	Nd	Sm	Eu	Gd	Tb	Dy	Ho	Er	Tm	Yb	Lu	
NeS-xenolith															
413-1A-A	148.40	272.65	24.15	66.31	7.67	2.05	6.15	0.80	4.46	0.89	2.85	0.53	2.76	0.36	
413-1A-B	158.86	629.85	26.90	73.63	9.03	2.21	9.03	0.97	4.78	0.97	3.01	0.44	2.92	0.44	
413-1A-C	150.14	241.61	21.47	59.57	6.74	1.98	6.11	0.72	4.13	0.72	2.34	0.27	2.34	0.27	
413-1A-D	163.00	352.00	19.90	50.90	5.40	1.60	5.40	0.60	3.20	0.50	1.30	0.20	1.25	0.20	
413-1A-E	139.97	236.27	22.45	62.06	7.39	2.11	6.25	0.70	4.05	0.70	2.11	0.35	1.94	0.26	
413-1A-F	195.00	324.00	n.a.	73.10	7.10	2.40	7.40	0.80	n.a.	0.70	n.a.	0.30	1.90	0.30	
413-1A-G	172.00	251.00	n.a.	60.50	6.10	2.10	5.90	0.70	n.a.	0.60	n.a.	0.20	1.30	0.20	
413-1A-H	102.28	180.23	16.03	45.16	6.27	1.87	5.04	0.65	3.17	0.57	1.71	0.33	1.87	0.24	
413-1A-I	156.72	256.29	24.20	67.39	9.37	2.69	8.15	1.13	6.33	1.39	4.42	0.61	4.08	0.69	
413-1A-K	150.83	250.08	23.16	63.71	7.94	2.26	6.52	0.84	3.85	0.67	1.84	0.25	1.59	0.17	
413-1A-L	154.83	258.25	24.29	67.15	8.13	2.14	6.50	0.86	4.02	0.77	2.22	0.26	1.97	0.34	
413-1A-M	188.93	324.71	29.47	83.39	8.86	2.21	7.33	0.85	3.49	0.68	1.87	0.26	1.70	0.17	
413-1A-N	104.20	240.69	20.16	55.85	7.14	1.87	6.07	0.80	2.94	0.54	1.87	0.18	1.52	0.18	
413-1A-O	122.46	225.58	22.12	60.28	7.65	1.97	5.67	0.66	3.45	0.74	1.97	0.33	1.97	0.25	
413-1A-P	21.55	135.51	5.06	16.16	2.61	0.65	2.37	0.24	1.55	0.33	0.98	0.16	0.73	0.16	
Normalised to ordinary chondrite															
F4-413	La	Ce	Pr	Nd	Sm	Eu	Gd	Tb	Dy	Ho	Er	Tm	Yb	Lu	La/Lu
NeS-xenolith															
413-1A-A	499.00	356.73	213.94	115.69	41.12	28.89	24.69	17.43	14.49	12.66	14.17	17.47	13.42	11.58	43.11
413-1A-B	534.15	824.09	238.30	128.46	48.43	31.18	36.24	21.15	15.54	13.83	14.95	14.46	14.18	14.37	37.18
413-1A-C	504.84	316.11	190.21	103.93	36.15	27.86	24.53	15.62	13.44	10.21	11.61	8.81	11.35	8.75	57.69
413-1A-D	548.08	460.55	176.26	88.80	28.97	22.55	21.68	13.03	10.41	7.10	6.46	6.53	6.07	6.49	84.40
413-1A-E	470.64	309.14	198.83	108.27	39.67	29.78	25.09	15.30	13.17	10.00	10.50	11.50	9.41	8.57	54.89
413-1A-F	655.68	423.92	n.a.	127.53	38.09	33.83	29.71	17.38	n.a.	9.94	n.a.	9.80	9.23	9.74	67.32
413-1A-G	578.35	328.41	n.a.	105.55	32.73	29.60	23.69	15.21	n.a.	8.52	n.a.	6.53	6.31	6.49	89.07
413-1A-H	343.92	235.82	141.98	78.79	33.61	26.38	20.25	14.14	10.32	8.09	8.49	10.63	9.09	7.93	43.39
413-1A-I	526.97	335.32	214.33	117.57	50.25	37.89	32.73	24.49	20.59	19.71	21.97	19.83	19.80	22.53	23.39
413-1A-K	507.17	327.20	205.14	111.15	42.61	31.82	26.18	18.16	12.51	9.50	9.14	8.19	7.72	5.43	93.41
413-1A-L	520.60	337.88	215.18	117.15	43.60	30.14	26.10	18.58	13.07	10.94	11.05	8.38	9.56	11.11	46.86
413-1A-M	635.27	424.84	261.05	145.48	47.53	31.21	29.41	18.51	11.36	9.68	9.31	8.35	8.27	5.53	114.85
413-1A-N	350.36	314.91	178.58	97.43	38.29	26.40	24.35	17.44	9.57	7.60	9.31	5.83	7.37	5.79	60.48
413-1A-O	411.75	295.15	195.95	105.17	41.03	27.82	22.78	14.29	11.23	10.52	9.81	10.75	9.59	8.01	51.40
413-1A-P	72.46	177.29	44.83	28.20	14.01	9.20	9.50	5.32	5.04	4.64	4.87	5.33	3.57	5.30	13.67
Norm. coefficient	0.2974	0.7643	0.1129	0.5732	0.1864	0.0710	0.2491	0.0460	0.3075	0.0704	0.2013	0.0306	0.2059	0.0308	
ICP-EMS-data															

TABLE X (contd.)

F4-353 xenolith

Nepheline syenite	La	Ce	Nd	Sm	Eu	Tb	Yb	Lu
Ns 1-11	201	255	64	7.44	3.15	1.00	3.21	0.48
Ns 1-10	195	260	66	7.37	2.98	1.00	3.76	0.57
Ns 1-9	162	208	52	5.76	2.29	0.90	3.80	0.75
Ns 1-8	182	262	65	7.32	2.73	1.00	3.91	0.59
Ns 1-7	226	346	87	10.40	3.94	1.30	4.86	0.75
Ns 1-6	278	409	104	11.80	4.49	1.30	4.43	0.65
Ns 1-5	382	579	147	17.00	5.73	2.00	5.48	0.78
Ns 1-4	275	410	108	12.40	4.44	1.40	4.39	0.64
Ns 1-3	273	408	105	12.10	4.48	1.40	3.98	0.58
Ns 1-2	349	535	140	16.20	6.11	1.90	6.10	0.88
Ns 1-1	265	395	101	11.50	4.23	1.40	4.80	0.70
Phonolitic dyke	211	311	65	8.30	3.17	1.20	6.19	0.99
Volcanic breccia	La	Ce	Nd	Sm	Eu	Tb	Yb	Lu
VB 2-1	233	310	73	8.20	3.05	1.30	4.90	0.73
VB 2-2	218	287	76	7.68	2.93	1.20	4.67	0.70
VB 2-3	253	312	77	8.92	3.69	1.20	3.98	0.58
VB 2-4	255	328	75	9.71	3.79	1.40	10.40	1.81
VB 2-5	254	357	93	11.80	4.84	3.00	30.40	5.47
VB 2-6	277	366	84	12.10	4.97	2.40	26.60	4.55

F4-353 xenolith: REE normalised to ordinary chondrite

Nepheline syenite	La	Ce	Nd	Sm	Eu	Tb	Yb	Lu	La/Lu
Ns 1-11	675.86	333.64	111.65	39.91	44.40	21.72	15.59	15.58	43.37
Ns 1-10	655.68	340.18	115.14	39.54	42.00	21.72	18.26	18.51	35.43
Ns 1-9	544.72	272.14	90.72	30.90	32.28	19.55	18.46	24.35	22.37
Ns 1-8	611.97	342.80	113.40	39.27	38.48	21.72	18.99	19.16	31.95
Ns 1-7	759.92	452.70	151.78	55.79	55.53	28.24	23.60	24.35	31.21
Ns 1-6	934.77	535.13	181.44	63.30	63.28	28.24	21.52	21.10	44.29
Ns 1-5	1284.47	757.56	256.45	91.20	80.76	43.45	26.61	25.32	50.72
Ns 1-4	924.68	536.44	188.42	66.52	62.58	30.41	21.32	20.78	44.50
Ns 1-3	917.96	533.82	183.18	64.91	63.14	30.41	19.33	18.83	48.75
Ns 1-2	1173.50	699.99	244.24	86.91	86.12	41.28	29.63	28.57	41.07
Ns 1-1	891.06	516.81	176.20	61.70	59.62	30.41	23.31	22.73	39.21
Phonolitic dyke	709.48	406.91	113.40	44.53	44.68	26.07	30.06	32.14	22.07
Volcanic breccia	La	Ce	Nd	Sm	Eu	Tb	Yb	Lu	La/Lu
VB 2-1	783.46	405.60	127.36	43.99	42.99	28.24	23.80	23.70	33.06
VB 2-2	733.02	375.51	132.59	41.20	41.30	26.07	22.68	22.73	32.25
VB 2-3	850.71	408.22	134.33	47.85	52.01	26.07	19.33	18.83	45.18
VB 2-4	857.43	429.15	130.84	52.09	53.42	30.41	50.51	58.77	14.59
VB 2-5	854.07	467.09	162.25	63.30	68.22	65.17	147.64	177.60	4.81
VB 2-6	931.41	478.87	146.55	64.91	70.05	52.14	129.19	147.73	6.30
Norm. coefficient	0.2974	0.7643	0.5732	0.1864	0.07095	0.04603	0.2059	0.0308	

ICP-EMS-data.

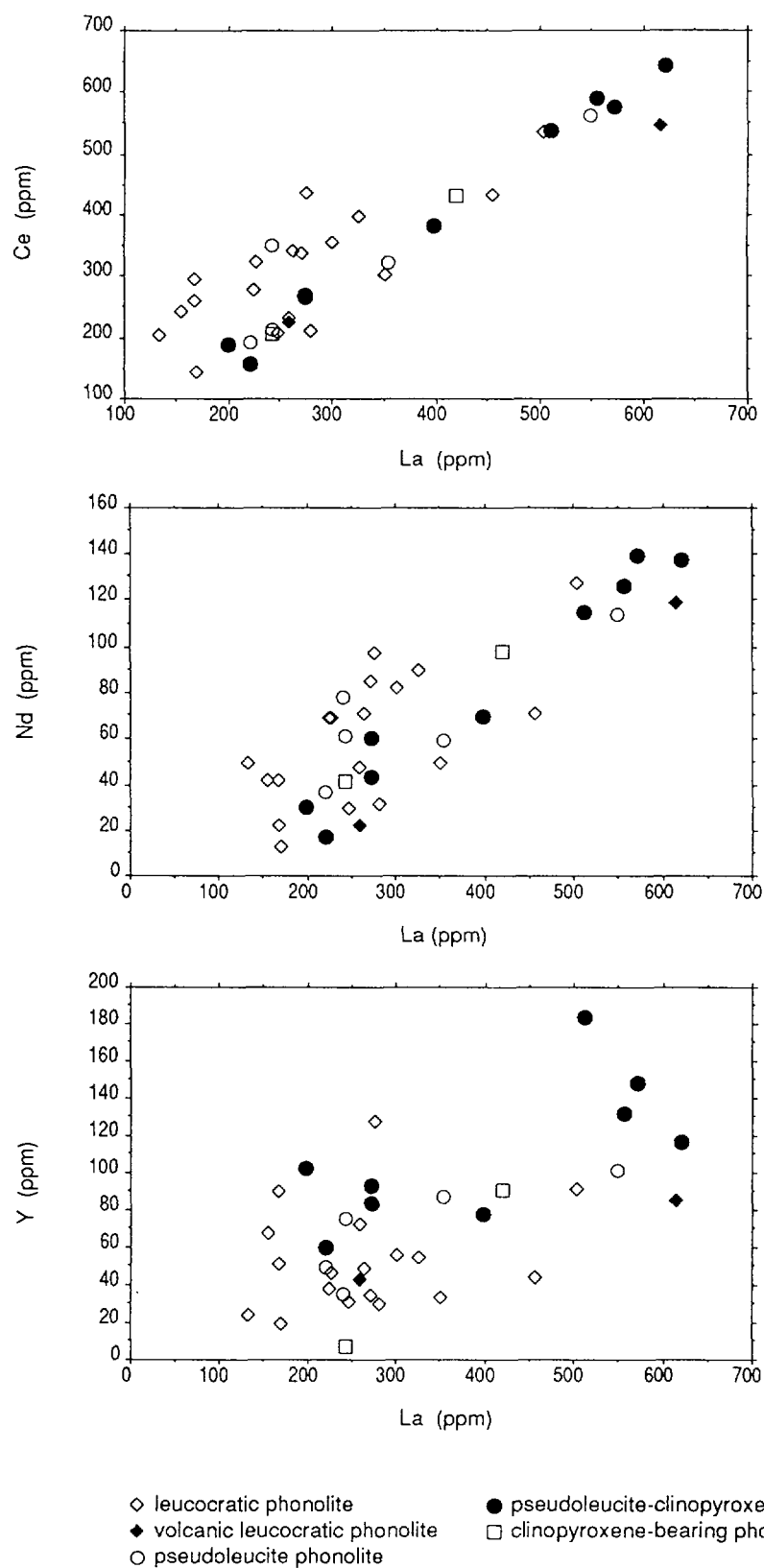


Figure 15. Correlation diagrams for Ce, Nd and Y with La in the hydrothermally altered, reduced phonolites from the Osamu Utsumi mine (data by XRF).

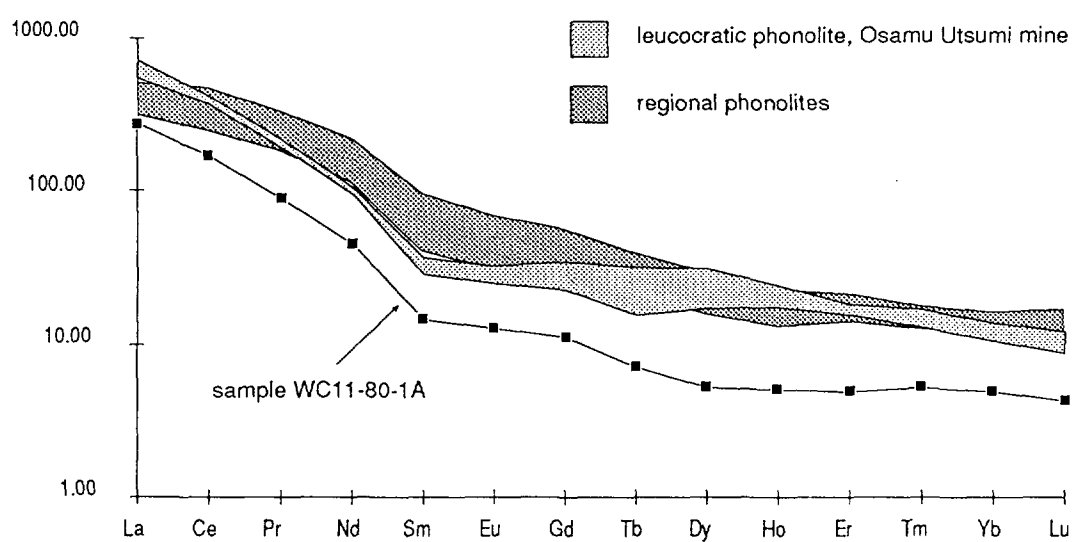


Figure 16. Chondrite normalised REE distribution diagram for hydrothermally altered, reduced phonolites from the Osamu Utsumi mine, compared with unaltered regional rocks (data by ICP-EMS).

hydrothermally altered phonolites (25 – 35%) might have prevented this rock from a more pervasive fluid circulation. This could therefore be an indication that intense argillic alteration had already taken place before the redistribution and minor addition of REEs (mainly LREEs) by the hydrothermal solutions. A leaching effect, either by late-stage hydrothermal solutions or by meteoric weathering processes, can be rejected as an explanation for this phenomenon because of the much more selective behaviour of REEs in such processes.

The distribution of the REEs in reduced and oxidised phonolites is discussed in more detail by MacKenzie *et al.* (this report series; Rep. 7).

5.2.2. Nepheline syenites

As no nepheline syenite stocks were encountered in the boreholes, and only strongly weathered stocks are exposed in the mine, large nepheline syenite breccia components in the F4 core were taken as being representative. As a consequence, there is a continuous transition between nepheline syenite and breccias. The presence or absence of mineralisations was used as a discrimination criterion.

Besides the oxidised samples from 19 m, 22 m, and 39 m, together with oxidised samples from the mine walls (B2 profile: B2-53, B2-55 and B2-57) and reduced bulk samples from 91 m, 107 m, 123 m, 129 m and 265 m in the F4 core, detailed samples were analysed from the 353 m (Ns 1-1 to Ns 1-11) nepheline syenite-phonolite dyke-breccia xenolith, and the 413 m xenolith. The data are presented in Table VIII and Appendix 4 in addition to Figures 17 to 27.

5.2.2.1. Major elements

The major elements of the reduced nepheline syenites are very similar to those of the phonolites. This can be illustrated by comparing Figures 17, 18 and 19 (nepheline syenites) with Figure 10 (phonolites); both are normalised to the mean of the values for the regional samples. In general, there is an enrichment in K₂O and H₂O and a decrease in MgO, CaO and Na₂O, although there is quite a distinction in degree. For the 353 m xenolith samples the changes are remarkable (Fig. 18), whereas in samples from 107 m, for example, the changes are less dramatic (Fig. 17). MnO and P₂O₅ show increases in some samples and decreases in others. The behaviour of MnO seems to be related to

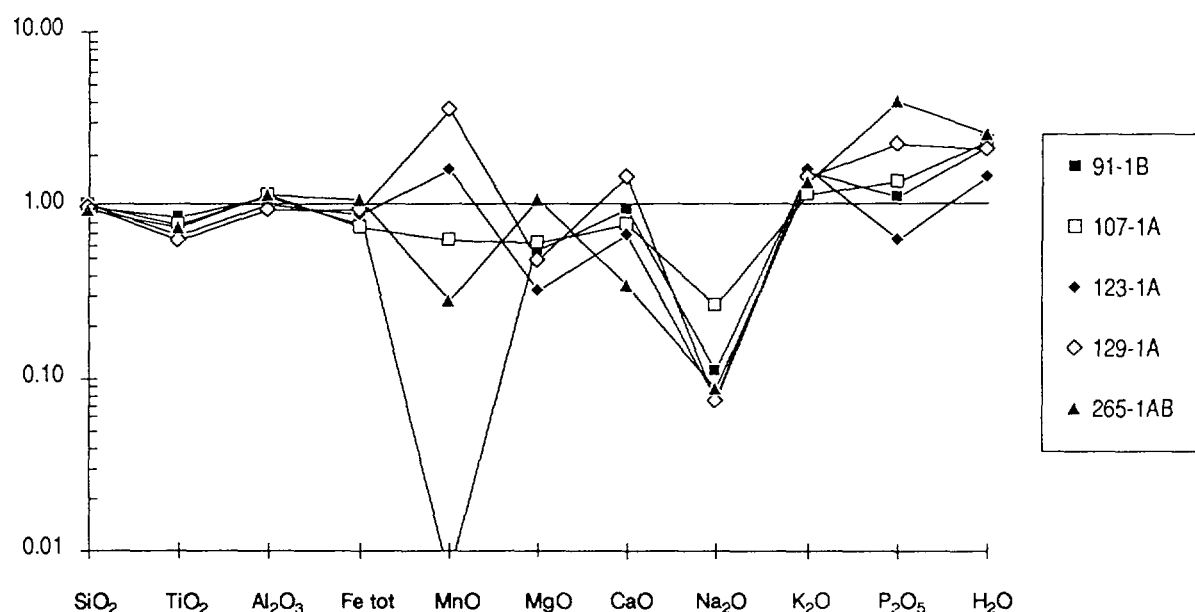


Figure 17. Average major element composition of hydrothermally altered, reduced nepheline syenite xenoliths from borehole F4 normalised to the average composition of the unaltered regional rocks.

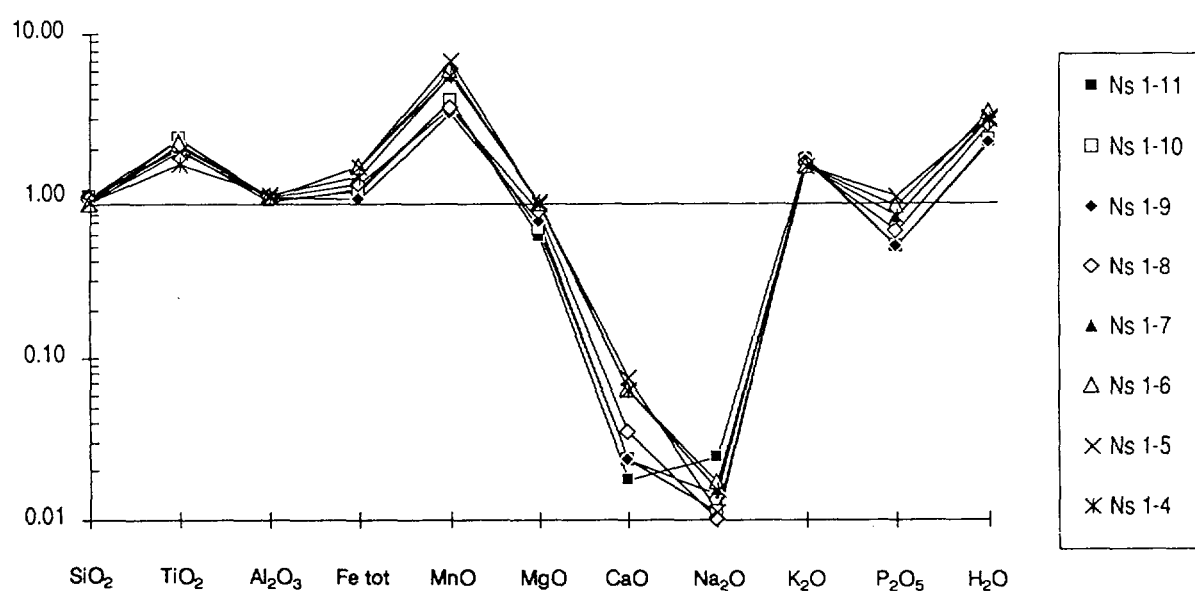


Figure 18. Average major element composition of a hydrothermally altered, reduced nepheline syenite xenolith at 353 m depth from borehole F4, normalised to the average composition of unaltered regional rocks.

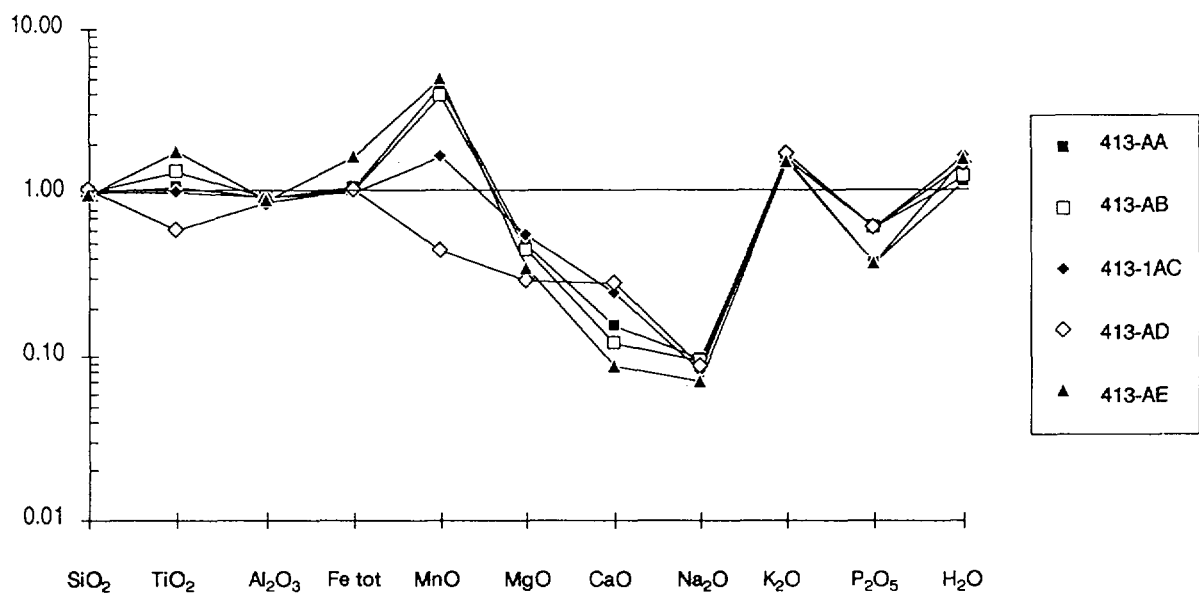


Figure 19. Average major element composition of hydrothermally altered, reduced nepheline syenite xenolith at 413 m depth from borehole F4, normalised to the average composition of unaltered regional rocks.

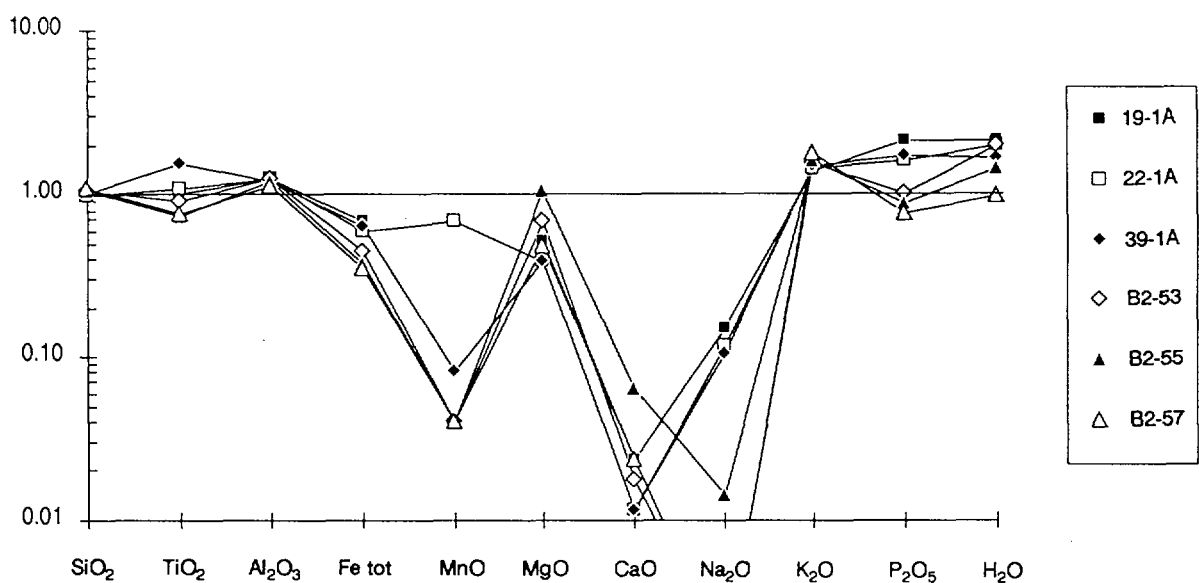


Figure 20. Average major element composition of hydrothermally altered, oxidised nepheline syenite xenoliths from borehole F4 and orebody B, normalised to the average composition of unaltered regional rocks.

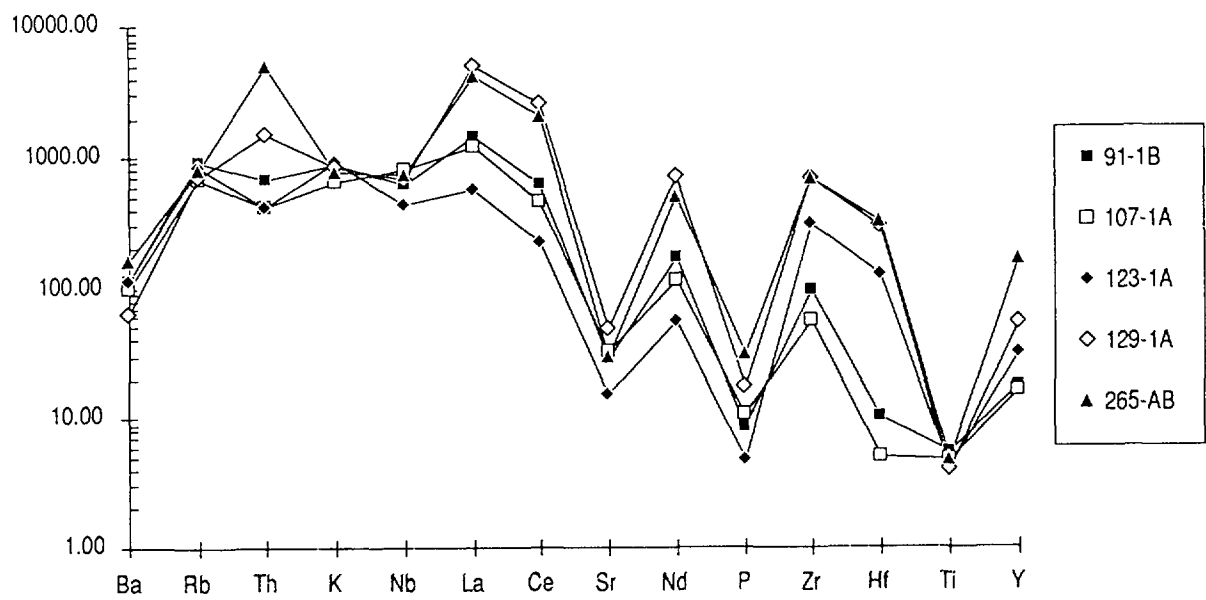


Figure 21. Incompatible elements normalised to chondrite and primitive mantle for hydrothermally altered, reduced nepheline syenite xenoliths from borehole F4, (normalisation factors from Thompson, 1982).

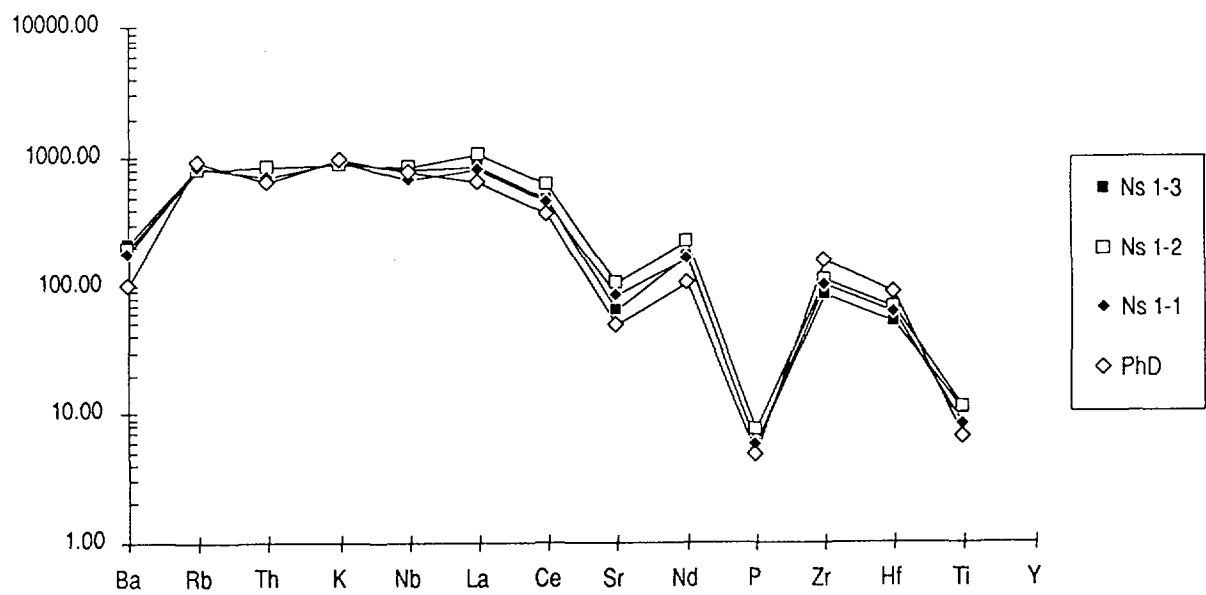


Figure 22. Incompatible elements normalised to chondrite and primitive mantle for hydrothermally altered, reduced nepheline syenite xenolith at 353 m depth from borehole F4 (samples Ns1-1 to 3) and the phonolitic dyke (sample PhD), (normalisation factors from Thompson, 1982).

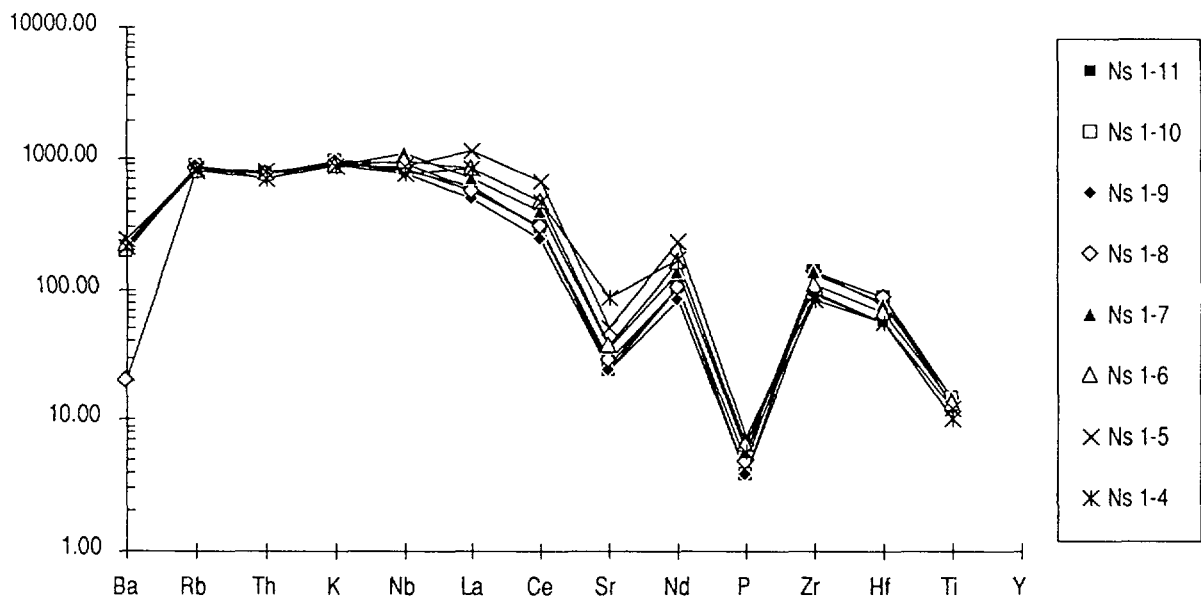


Figure 23. Incompatible elements normalised to chondrite and primitive mantle for hydrothermally altered, reduced nepheline syenite xenolith at 353 m depth from borehole F4; samples Ns 1-4 to 11 (normalisation factors from Thompson, 1982).

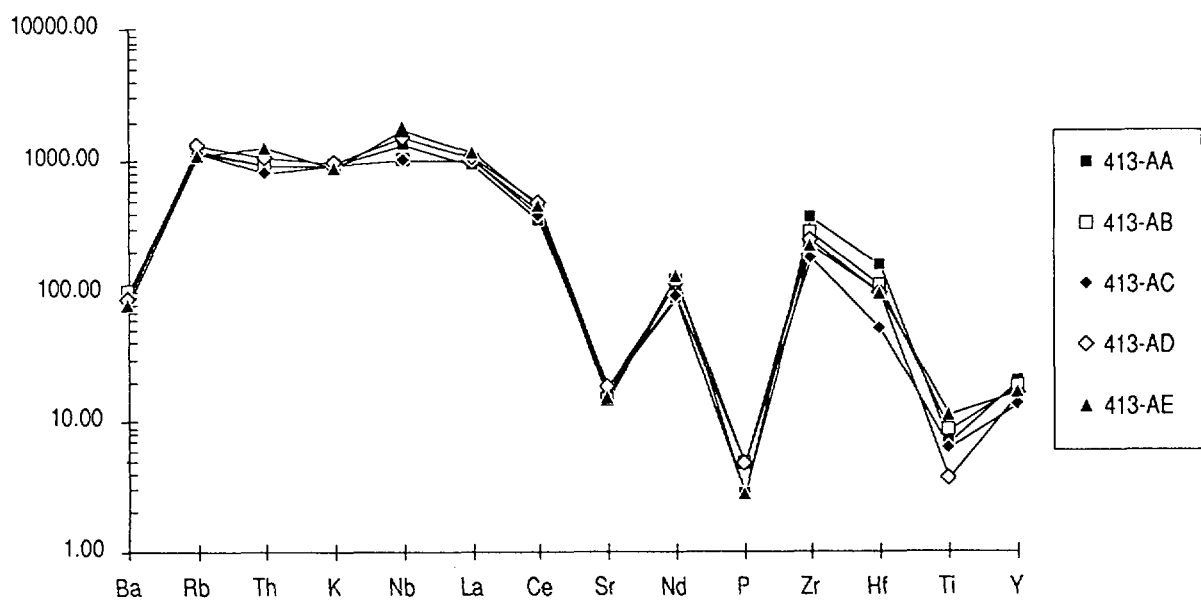


Figure 24. Incompatible elements normalised to chondrite and primitive mantle for hydrothermally altered, reduced nepheline syenite xenolith at 413 m depth from borehole F4, (normalisation factors from Thompson, 1982).

the presence of fissures (Mn-siderite), and for P_2O_5 to the presence of mineralisation (monazite among others). In the oxidised nepheline syenites (Figs. 13 and 20) MnO and FeO contents are depleted in comparison to the reduced rocks.

5.2.2.2. Trace elements

The trace element contents in the nepheline syenites are, like the major elements, very similar to those of the phonolites. The incompatible trace elements normalised to chondrite (Figs. 21-24) show a strong enrichment from Ba to Ce and a somewhat weaker enrichment for the other incompatible elements. Within one xenolith (353 m, Ns 1-6; Figs. 22 and 23; 413 m, Fig. 24) the distribution is very homogeneous, but among different xenoliths (Fig. 21) there is a large spread. In comparison with the non-hydrothermally altered nepheline syenites (Figs. 25 and 26; see also Figs. 10 and 11), the enrichment of U, Th and S is strong and is also significant for F, Ba, Rb, Pb, Zr, Hf and Zn. Only Sr is strongly depleted compared to the non-hydrothermally altered syenites of the Poços de Caldas plateau.

In the oxidised nepheline syenites (Figs. 20 and 27; see also Figs. 13 and 14), as compared to the reduced ones, there is a very strong decrease in sulphur, zinc, uranium and fluorine. The latter explains the high fluorine content in the groundwaters of the mine (Nordstrom *et al.*, this report series; Rep. 6).

5.2.2.3. Rare-earth elements

For the nepheline syenite xenolith sample series from 413 m depth, the whole REE-spectrum has been analysed (Table X; see also Shea, this report series; Rep. 4). The xenolith is fractured and hydrothermally altered but does not display vein-type U-mineralisation ($U > 70$ ppm in all the samples). The chondrite normalised pattern of these samples (Fig. 28) is generally similar to that of the reduced phonolites (Fig. 16). Compared to the regional samples (Schorscher and Shea, this report series; Rep. 1), the xenolith differs in that it exhibits a partial depletion of the intermediate REEs from Pr to Dy. The La/Lu_{cn} ratio for the 15 samples varies between 14 – 115, falling, for 9 samples, within the range of the hydrothermally altered phonolites ($La/Lu_{cn} = 45 - 83$). Three nepheline syenite samples display a higher La/Lu_{cn} ratio (89 – 115); characteristically, all of these samples are cut by a fracture filled with pyrite, zircon and fluorite. Lower La/Lu_{cn}

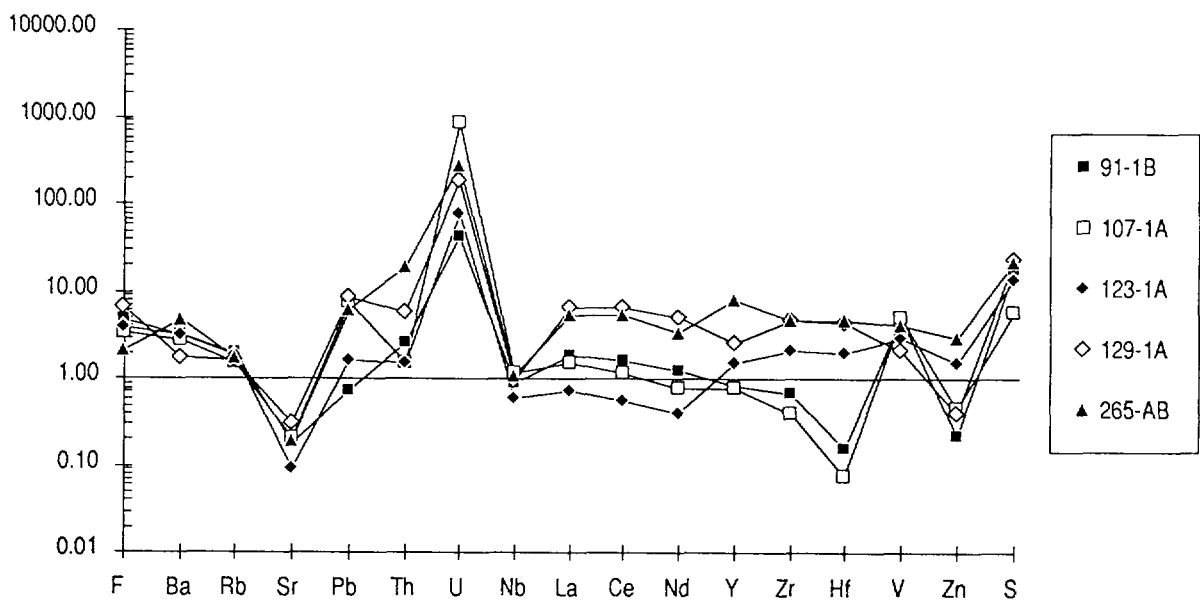


Figure 25. Average trace element compositions of hydrothermally altered, reduced nepheline syenite xenoliths from borehole F4 normalised to the average composition of unaltered regional rocks.

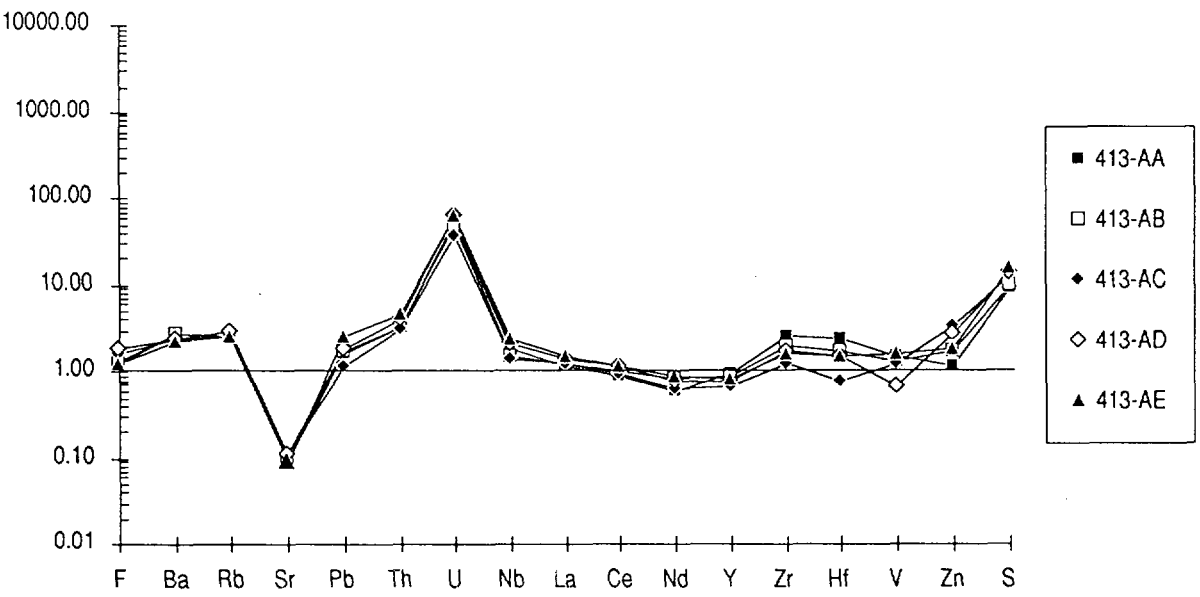


Figure 26. Average trace element compositions of hydrothermally altered, reduced nepheline syenite xenolith at 413 m depth from borehole F4 normalised to the average composition of unaltered regional rocks.

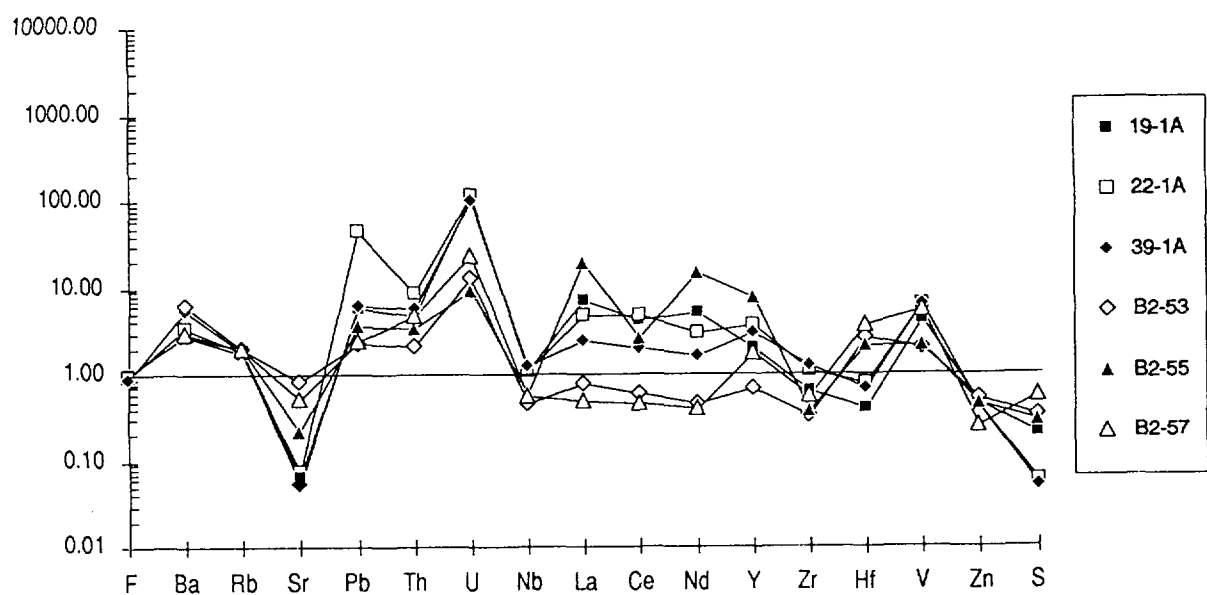
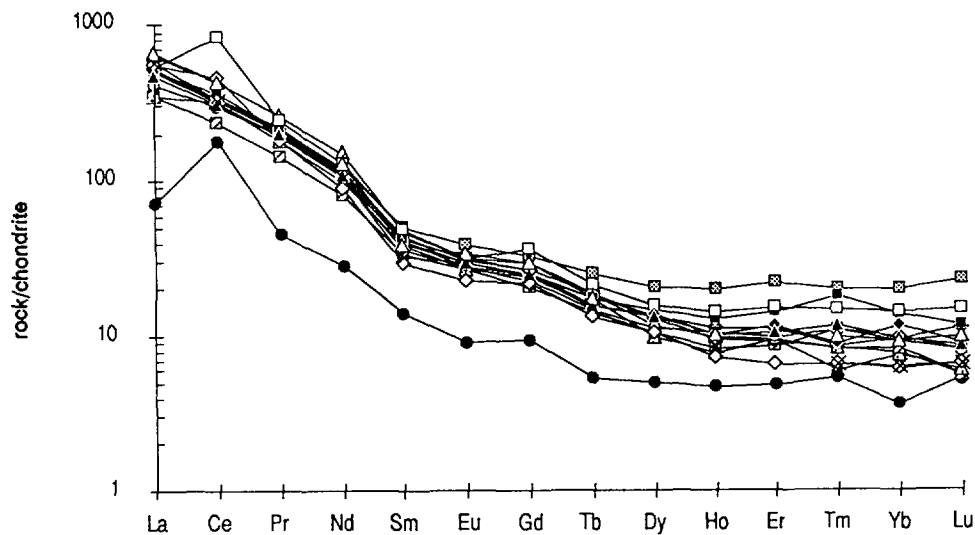


Figure 27. Average trace element compositions of hydrothermally altered, oxidised nepheline syenite xenoliths from borehole F4 and orebody B, normalised to the average composition of unaltered regional rocks.



F4-413 nepheline syenite xenolith: ■ 413-1A-A ▲ 413-1A-E ▣ 413-1A-I △ 413-1A-N
□ 413-1A-B △ 413-1A-F ◆ 413-1A-K × 413-1A-O
◆ 413-1A-C × 413-1A-G ◆ 413-1A-L ● 413-1A-P
◇ 413-1A-D ▣ 413-1A-H ▲ 413-1A-M

Figure 28. Chondrite normalised REE distribution of the reduced nepheline syenite xenolith at 413 m from borehole F4.

ratios (14 – 37), when compared to the phonolites, occur in three samples that either come from the border zone of the xenolith (sample 413-1A-P, $\text{La/Lu}_{\text{cn}} = 14$) or are cut by open fractures. Two of the samples with low La/Lu_{cn} ratios also display a pronounced positive Ce anomaly (samples 413-1A-B and 413-1A-P). The low La/Lu_{cn} ratios, together with the positive Ce anomaly, might indicate preferential LREE leaching under oxidising conditions (weathering), where Ce is retained compared to the other LREEs due to oxidation to less soluble Ce^{4+} .

5.2.3. Breccia bodies

The heterogeneity of the breccias, with their varying ratios of rock fragments and matrix, complicates geochemical characterisation. Added to this, the different degrees of mineralisation makes this task even more difficult. The analyses of the breccias, mainly carried out on samples from drillcore F4, are listed in Table VIII and Appendix 4, and are illustrated in Figures 29 to 40. The nepheline syenite and phonolite fragments of the breccias are geochemically very similar to their non-fractured, hydrothermally altered equivalents from the mine. They represent essentially the pre-breccia stage of the hydrothermal alteration. The syn-breccia hydrothermal stage is represented by the composition of the breccia matrices, whereas the post-breccia stage resulted in hydrothermal mineralisation along minor fracture zones crosscutting the breccias.

One sample at a depth of 353 m from borehole F4 (F4-353 series) represents a profile across a phonolitic dyke (PhD) that separated a nepheline syenite xenolith (samples Ns 1-1 to 11; see section 5.2.2.) from a mineralised, matrix-supported breccia (samples VB 2-1 to 6).

5.2.3.1. Major elements

Compared to the average non-hydrothermally altered phonolites and nepheline syenites from the plateau, MgO , CaO and Na_2O contents are considerably depleted, whereas K_2O and H_2O are enhanced; TiO_2 and Fe_{tot} may show an increase depending on the intensity and type of mineralisation. The behaviour of MnO is highly variable, either slightly enriched or strongly depleted (Figs. 29 – 32). As a whole, the major element composition of the breccias is very similar to that of the hydrothermally altered phonolites and nepheline syenites.

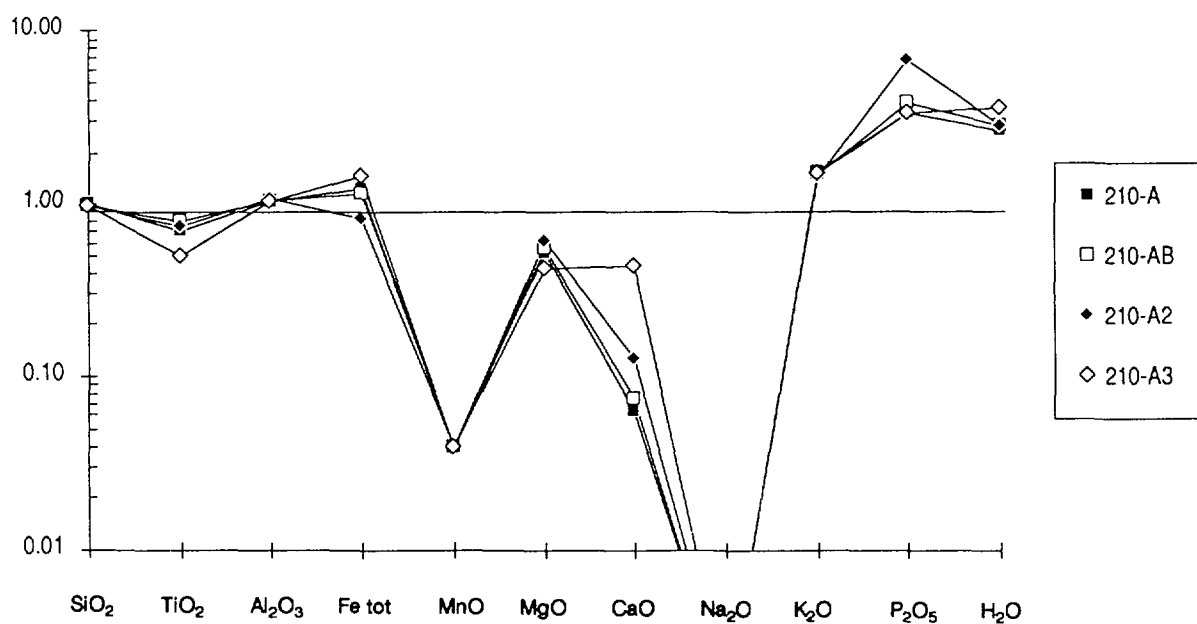


Figure 29. Major element compositions of the highly mineralised breccias at 210 m from borehole F4 normalised to the average composition of unaltered regional samples.

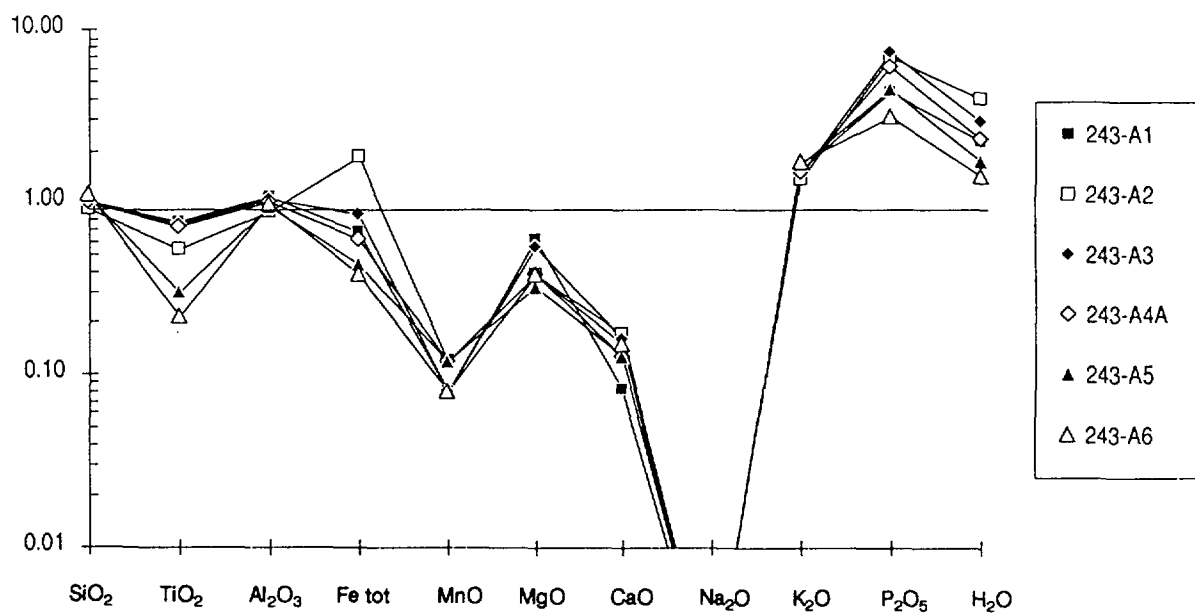


Figure 30. Major element compositions of the highly mineralised breccias at 243 m from borehole F4 normalised to the average composition of unaltered regional samples.

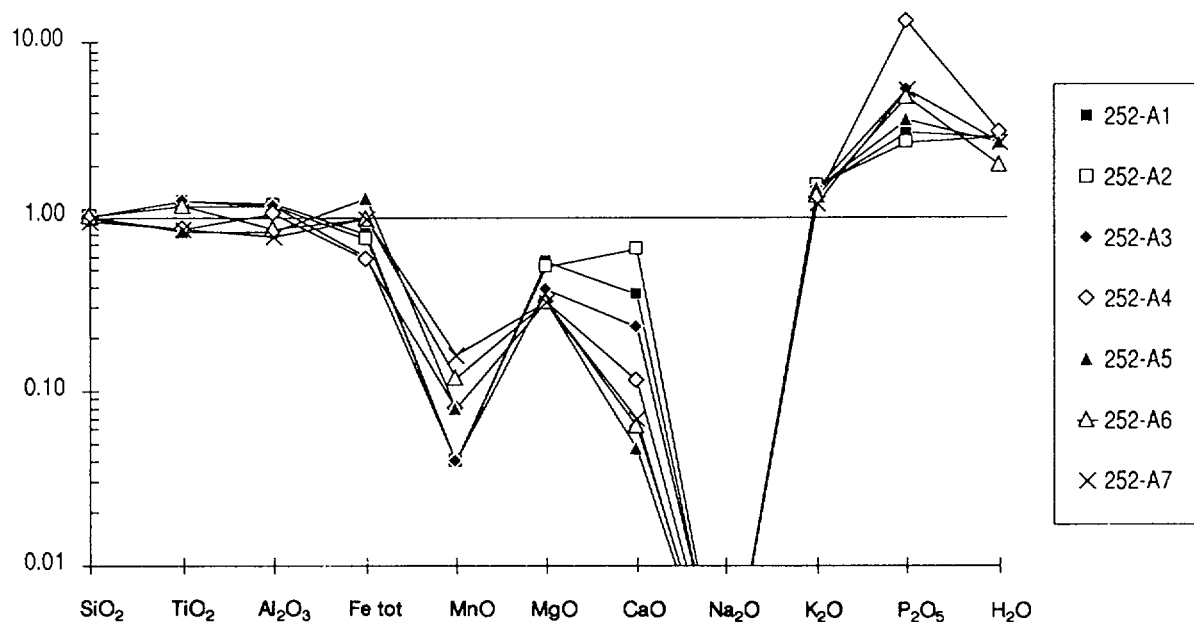


Figure 31. Major element compositions of the highly mineralised breccias at 252 m from borehole F4 normalised to the average composition of unaltered regional samples.

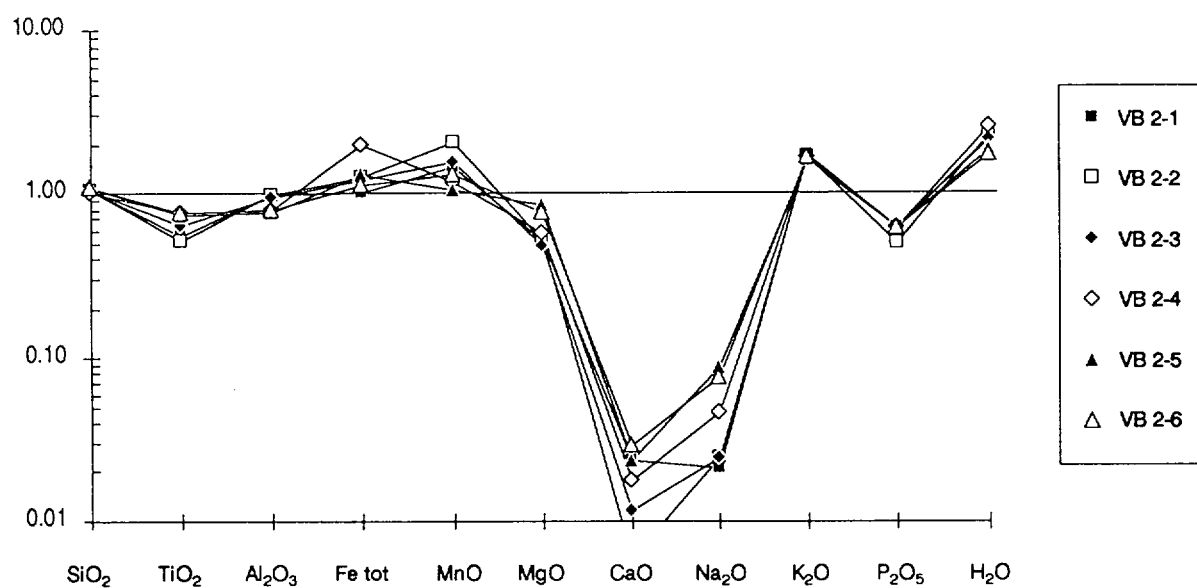


Figure 32. Major element compositions of the mineralised breccias in contact with the nepheline syenite xenolith at 353 m from borehole F4 normalised to the average composition of unaltered regional samples.

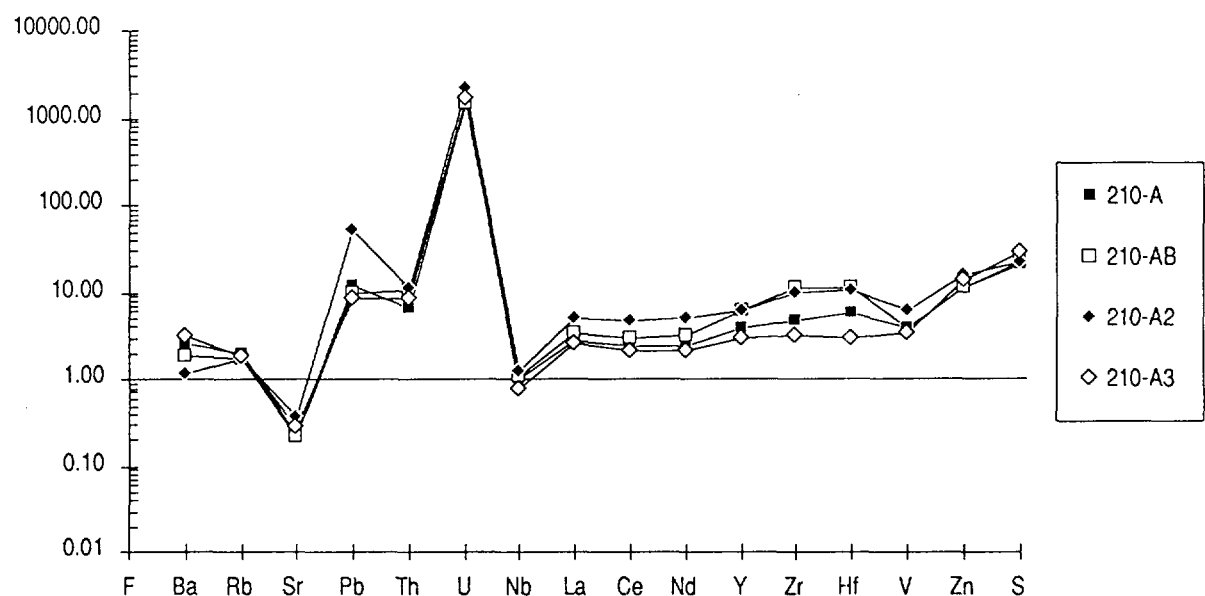


Figure 33. Trace element compositions of the highly mineralised breccias at 210 m from borehole F4 normalised to the average composition of unaltered regional samples.

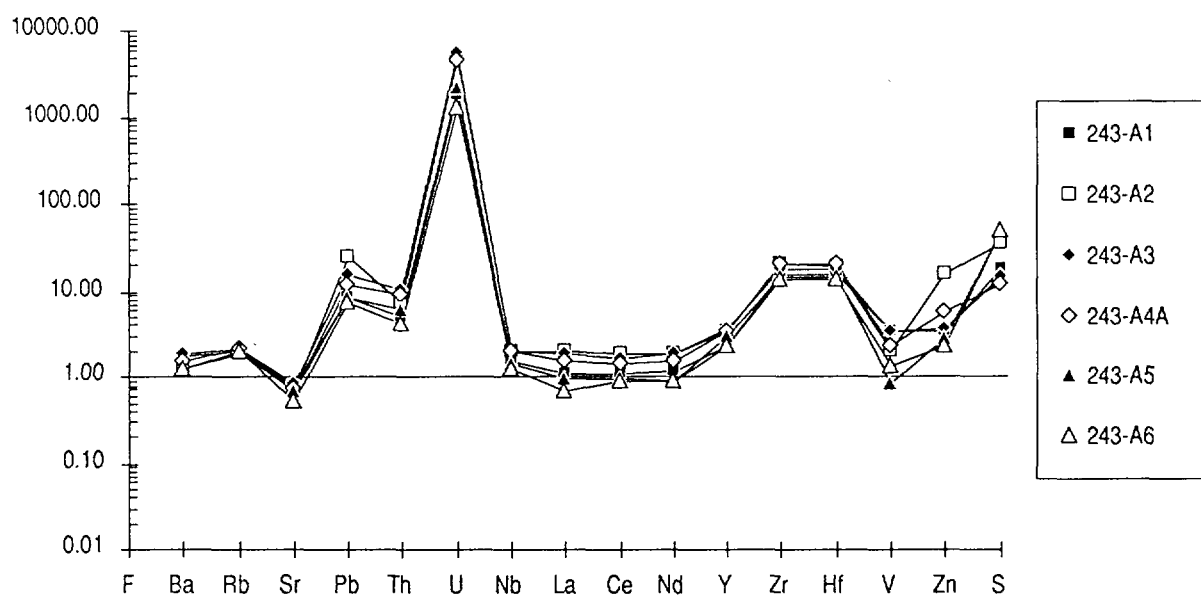


Figure 34. Trace element compositions of the highly mineralised breccias at 243 m from borehole F4 normalised to the average composition of unaltered regional samples.

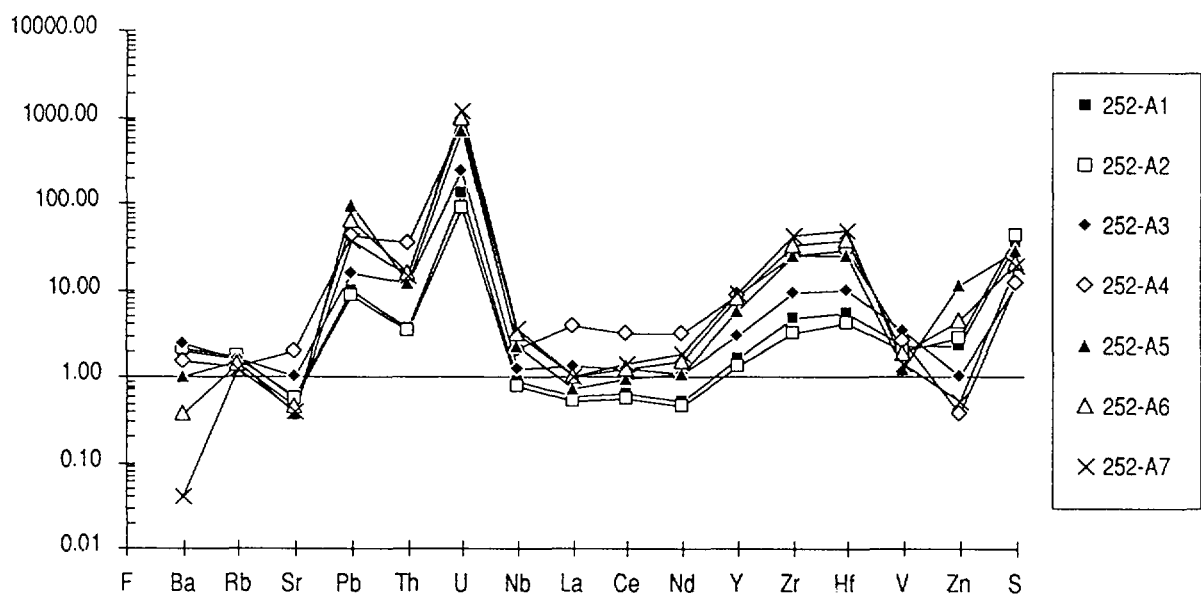


Figure 35. Trace element compositions of the highly mineralised breccias at 252 m from borehole F4 normalised to the average composition of unaltered regional samples.

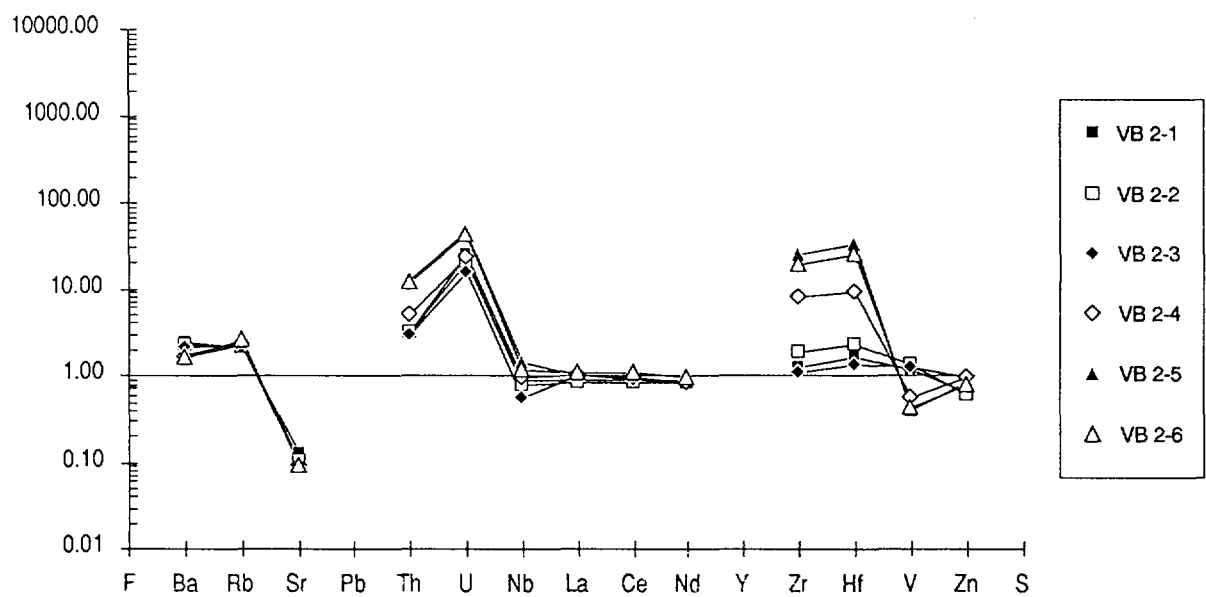


Figure 36. Trace element compositions of the mineralised breccias in contact with the nepheline syenite xenolith at 353 m from borehole F4 normalised to the average composition of unaltered regional samples.

5.2.3.2. Trace elements

Due to the varying degree of mineralisation, the enrichment of certain incompatible elements such as Th, U, Nb, Zr and Hf is extremely high. This results in very high trace element totals (25000 to 65000 ppm) and high ratios shown in the chondrite normalised plots (Figs. 37 – 40). In comparison to the average non-hydrothermally altered regional phonolites and nepheline syenites (Figs. 33-36), the enrichment of Pb, Th, U, Zr, Hf and S is strongly variable and may reach very high values (on average up to 20 ppm, with U up to 1000 ppm). As in all the other rock types, Sr is strongly depleted.

The enrichment of trace elements in the breccias follows a similar pattern to that observed in the hydrothermally altered rocks (compare Figs. 11, 12 and 21-26). This supports the hypothesis that the hydrothermal alteration took place coevally with the volcanic events that resulted in the breccias.

5.2.3.3. Rare-earth elements

In a few breccias, e.g. sample F4-353 from the drillcore F4 profile, the light and heavy REEs were partly determined (Table X; see also Shea, this report series; Rep. 4). The nepheline syenite samples Ns 1-1 to 11 display a similar chondrite normalised pattern (Fig. 41) as observed for the F4-413 nepheline syenite xenolith (compare Fig. 28), only with enhanced total abundances of all REEs. The phonolitic dyke and the breccia matrix samples (VB 2-1 to 6) display a marked enrichment in HREEs, best pronounced in samples VB 2-4 to 6. These three samples have the highest modal abundance of zircon, pyrite and fluorite of this series, and furthermore have the highest values for U and Th, although not of ore grade (<100 ppm). The La/Lu_{cn} ratios for the nepheline syenite samples (Ns 1-1 to 11), ranging from 31 to 51 (with one sample giving a ratio of 22), lie in the same range as in the F4-413 nepheline syenite xenolith and the hydrothermally altered phonolites. In contrast, the La/Lu_{cn} ratio for the breccia samples VB 2-4 to 6 is much lower, with values between 5–15. This might be an indication that the hydrothermal fluid was progressively enriched in HREEs towards its final stage.

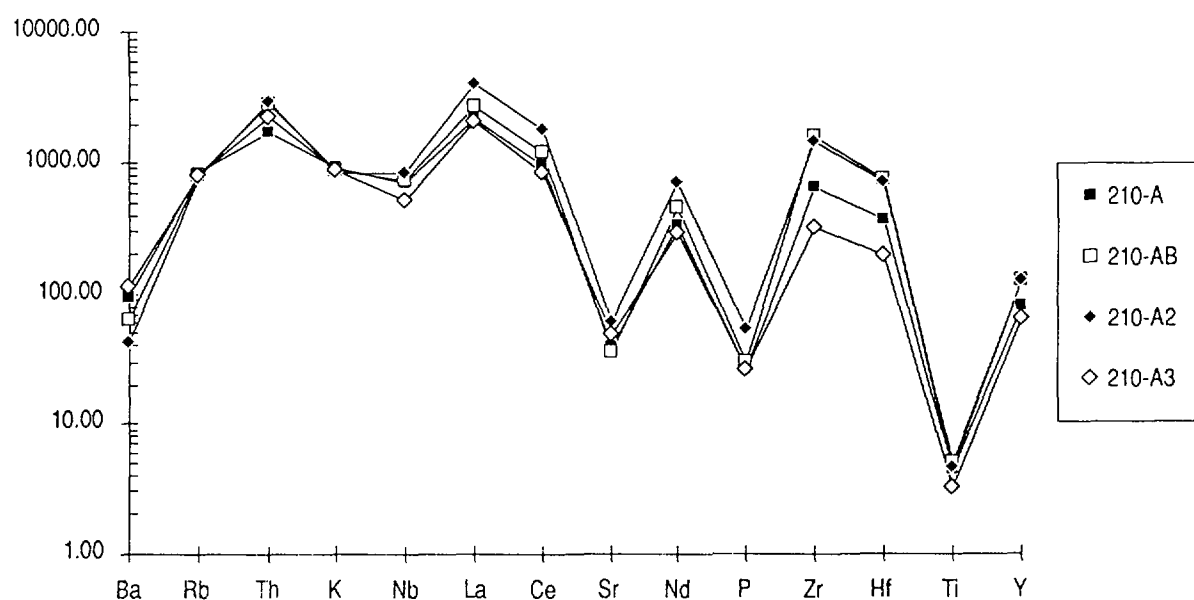


Figure 37. Incompatible elements normalised to chondrite and primitive mantle of the highly mineralised breccias at 210 m from borehole F4 (normalisation factors from Thompson, 1982).

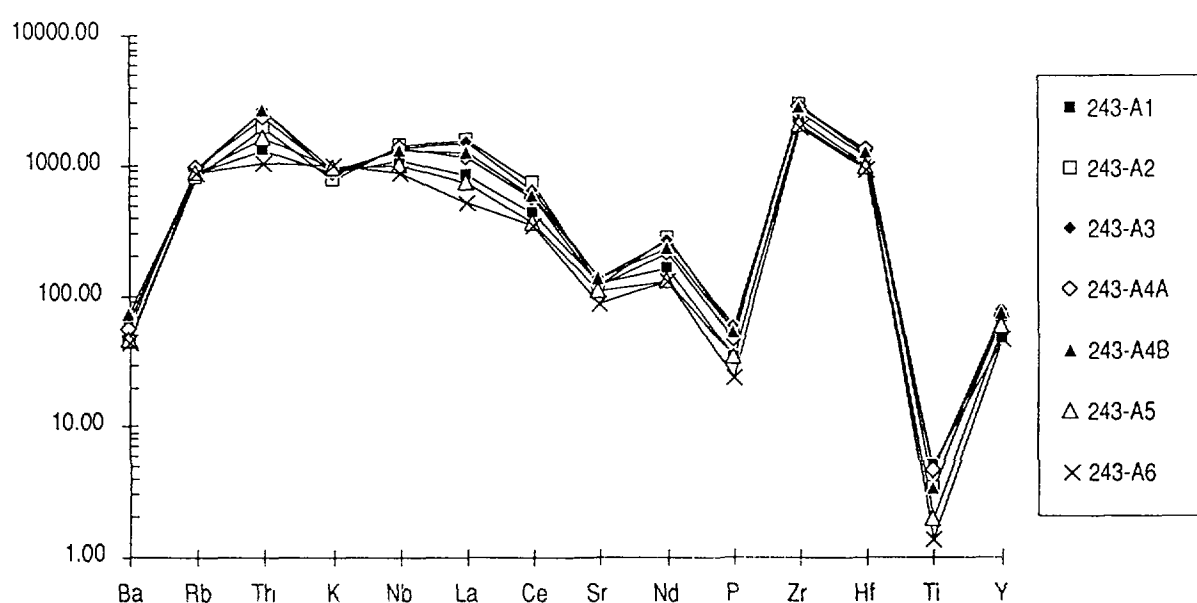


Figure 38. Incompatible elements normalised to chondrite and primitive mantle of the highly mineralised breccias at 243 m from borehole F4 (normalisation factors from Thompson, 1982).

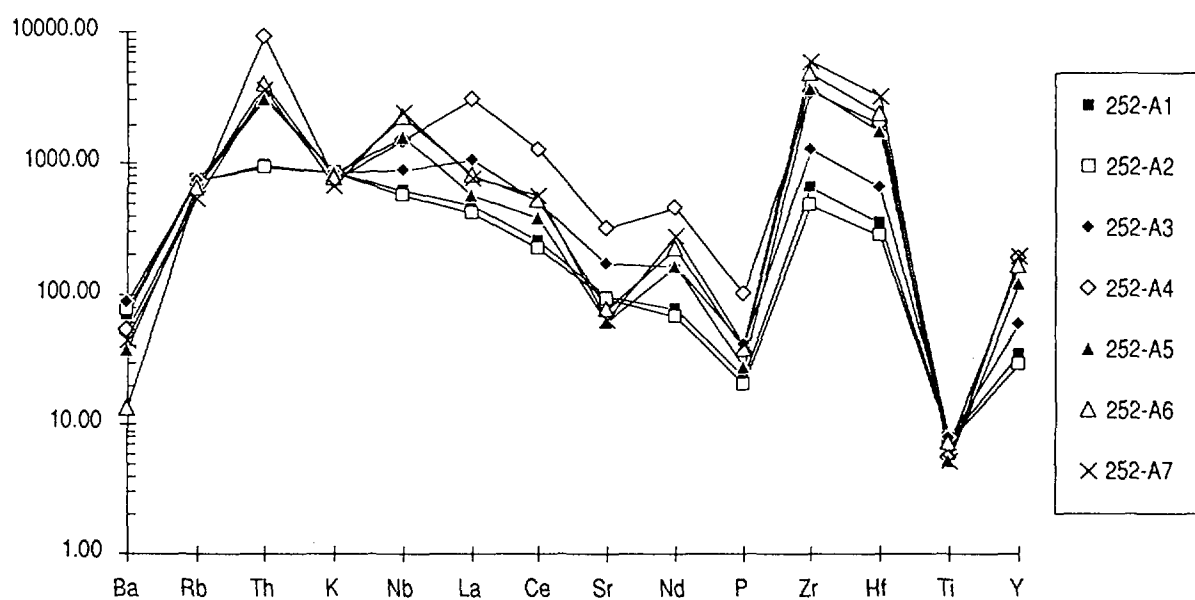


Figure 39. Incompatible elements normalised to chondrite and primitive mantle of the highly mineralised breccias at 252 m from borehole F4 (normalisation factors from Thompson, 1982).

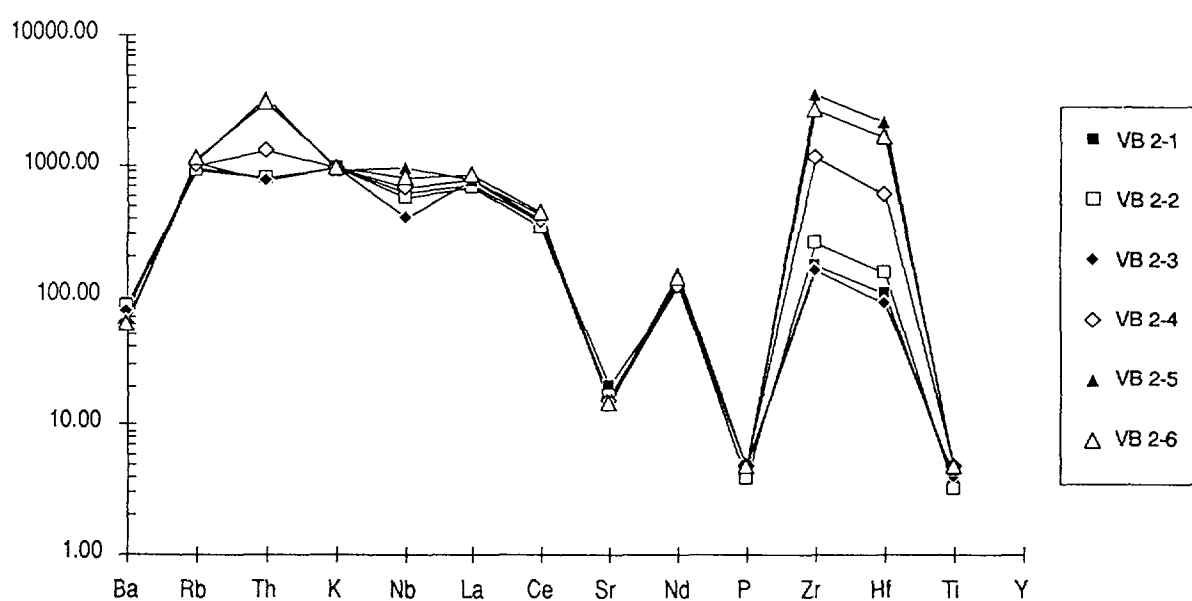


Figure 40. Incompatible elements normalised to chondrite and primitive mantle of the mineralised breccias in contact with the nepheline syenite xenolith at 353 m from borehole F4 (normalisation factors from Thompson, 1982).

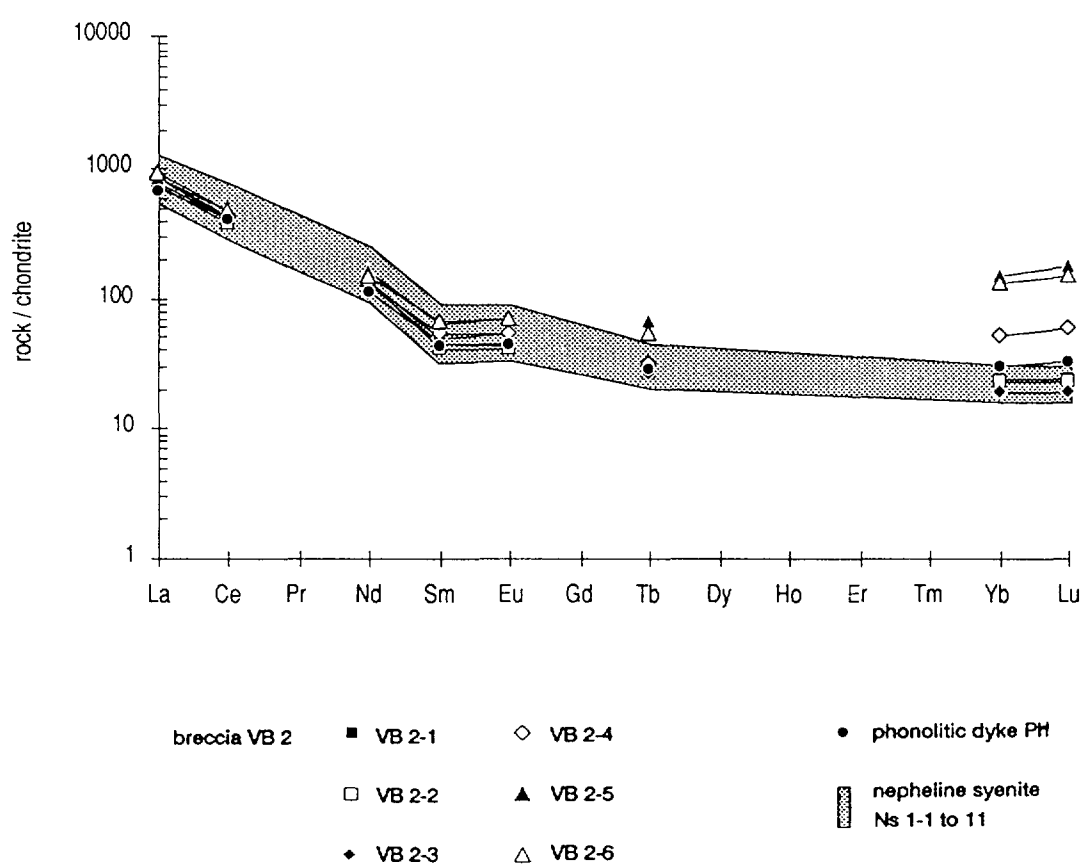


Figure 41. Chondrite-normalised REE distribution in the profile: nepheline syenite (Ns 1-1 to 11) – phonolitic dyke (PhD) – mineralised breccia (VB 2-1 to 6) at 353 m from borehole F4 (Data by ICP-EMS).

A slight positive Eu anomaly is observed in the nepheline syenite samples adjacent to the dyke, in the phonolitic dyke itself, and in the breccia samples (Fig. 41). This anomaly, considering that feldspars invariably show a pronounced positive Eu anomaly, may be related to the formation of hydrothermal low microcline as a result of the potassic alteration. Such low microcline is very abundant in the breccia samples and also occurs in the phonolitic dyke and the nepheline syenite samples adjacent to the dyke.

5.2.4. Weathering cover

With the infiltration of oxidising groundwaters, weathering processes become established, but it is only in higher levels that the geochemical conditions are “stabilised”. Within the first few decimetres above the present redox front, previous redox enrichments (i.e. “fossil” redox fronts) are still being dissolved. In Tables XI – XIV the geochemical data from the four weathering profiles (for location see Fig. 4) are shown and the elemental variation with depth is given in Figures 42 to 45.

The major SiO_2 and K_2O oxides decrease towards the surface, with an accelerated decrease occurring at the foot of the saprolite zone. The behaviour of Al_2O_3 and Fe_{tot} , which increase towards the surface, is totally antipathetic. TiO_2 and P_2O_5 contents generally increase towards the surface; the more erratic TiO_2 distribution reflects primary magmatic enrichments.

In the non-mineralised parent rocks uranium has almost disappeared from the profiles; only in some mineralised Ti- and Zr-rich samples do high U contents occur. These observations support the experience from the U-enrichment plant at the mine that part of the uranium is concentrated in phases resistant to weathering, that prove difficult to dissolve with HCl. This is further sustained by selective leaching experiments of oxidised and laterite samples (Appendix 2). Thorium tends to increase towards the top of the profile, thus confirming its general behaviour of being quite resistant to dissolution during weathering. Rubidium and strontium, in contrast, tend to decrease, as for K_2O and CaO .

La and Ce also show a tendency to decrease, but this general trend is easily offset by the presence of hydrothermally mineralised zones. In most of the profiles Ce increases slightly in the topmost lateritic samples, whereas La remains low. This is related to the less soluble 4+ oxidation state of Ce in the immediate aerated soil horizon (compare also the behaviour of the LREEs in the Morro do Ferro Th-REE deposit; Waber, this report series; Rep. 3).

TABLE XI

Geochemical analyses along profile A (Fig. 4) extending from the surface to the hydrothermally altered parent rock. Ore body A, Osamu Utsumi mine (XRF-data).

Osamu Utsumi mine, ore body A, vertical profile: Major and trace elements

Sample		A-60	A-61	A-62	A-63	A-64	A-65	A-66	A-67	A-68	A-69	A-70	A-84-A
Altitude m.a.s.l.		1430	1425	1420	1415	1410	1405	1400	1395	1390	1385	1380	1350
Rock type		LAT br	LAT br	LAT red	LAT whi	SAP yel	SAP whi	SAP whi	SAP br	SAP whi	SAP whi	PlcPh ox/a.	PlcPh red.
SiO ₂	wt. %	33.83	33.91	32.19	35.94	36.28	40.05	46.25	47.41	42.19	53.99	56.81	57.29
TiO ₂		0.79	0.71	0.87	0.92	2.73	1.13	0.96	0.46	1.58	0.65	0.45	0.42
Al ₂ O ₃		36.14	32.35	36.84	39.23	28.79	37.48	32.45	23.18	32.84	26.62	22.80	22.20
Fe _{tot}		4.49	14.85	10.08	3.09	15.42	2.36	2.64	8.12	2.83	0.97	1.97	1.85
MnO		0.02	0.12	0.03	0.01	0.07	0.01	0.31	0.08	1.82	0.02	0.01	0.00
MgO		0.17	0.10	0.10	0.15	0.20	0.15	0.12	0.14	0.22	0.07	0.05	0.07
CaO		0.00	0.00	0.00	0.00	0.00	0.00	0.00	0.00	0.00	0.00	0.00	0.00
Na ₂ O		0.28	0.24	0.22	0.31	0.25	0.15	0.23	0.27	0.23	0.38	0.38	0.26
K ₂ O		3.33	3.26	4.53	3.96	5.86	4.48	6.61	10.23	9.14	9.81	13.09	13.71
P ₂ O ₅		0.04	0.13	0.19	0.08	0.23	0.09	0.09	0.16	0.33	0.12	0.06	0.05
H ₂ O		19.21	13.05	13.17	14.24	8.42	12.03	8.53	8.82	6.01	5.54	2.98	2.61
CO ₂		0.60	0.23	0.15	0.18	0.17	0.10	0.05	0.13	0.18	0.07	0.00	0.11
Total	wt. %	98.90	98.95	98.37	98.11	98.42	98.03	98.24	99.00	97.37	98.24	98.60	98.57
Ba	ppm	47	65	64	22	341	62	314	674	1870	238	350	603
Rb		132	148	175	135	194	161	179	271	256	297	363	307
Sr		99	58	93	106	184	47	222	91	211	602	247	191
Pb		28	10	33	39	204	7	59	66	174	38	33	b.d.
Th		90	112	106	56	183	45	32	49	142	98	54	25
U		30	82	78	33	62	39	19	32	38	43	35	88
Nb		450	507	487	509	1469	374	295	246	396	345	310	182
La		160	446	662	809	1056	667	1073	974	1674	1213	1318	243
Ce		897	615	950	653	1340	443	882	949	2393	827	677	212
Nd		47	147	193	201	344	200	356	339	554	330	319	61
Y		72	79	116	75	105	88	61	57	119	92	72	75
Zr		1933	1849	2046	1985	3044	1020	711	209	245	1018	874	981
V		182	202	295	173	284	242	81	170	247	116	158	312
Cr		b.d.	17	10	b.d.	20	b.d.	b.d.	12	19	b.d.	b.d.	5
Ni		b.d.	4	8	b.d.	b.d.	b.d.	b.d.	b.d.	b.d.	b.d.	b.d.	b.d.
Co		11	17	12	8	35	9	5	19	9	b.d.	b.d.	b.d.
Cu		b.d.	b.d.	b.d.	b.d.	b.d.	b.d.	b.d.	b.d.	b.d.	b.d.	b.d.	b.d.
Zn		116	124	86	105	142	56	40	117	48	33	40	36
Ga		72	80	86	74	61	60	52	39	59	47	43	43
Sc		b.d.	b.d.	b.d.	b.d.	b.d.	b.d.	b.d.	4	4	4	6	8
S		36	120	628	1948	41	61	29	b.d.	488	718	708	11773

XRF-data; n.a. = not analysed, b.d. = below detection.

TABLE XII
Geochemical analyses along profile B2 (Fig. 4) extending from the surface to the hydrothermally altered parent rock. Ore body B, Osamu Utsumi mine (XRF-data).
 Osamu Utsumi mine, ore body B, vertical profile B2: Major and trace elements

Sample		B2-41	B2-43	B2-45	B2-47	B2-49	B2-51	B2-53	B2-55	B2-57
Altitude m.a.s.l.		1484	1468	1452	1436	1420	1404	1388	1372	1356
Rock type		LAT whi-br	LAT red-whi	SAP whi	SAP yel-whi	SAP gre	SAP gre	NeS ox/a.	NeS ox.	NeS ox.
SiO ₂	wt. %	41.22	33.23	43.4	35.25	41.91	54.43	56.18	57.56	58.99
TiO ₂		0.71	1.18	0.71	1.34	0.86	0.46	0.6	0.47	0.49
Al ₂ O ₃		33.94	44.91	36.97	33.5	38.67	26.71	24.57	23.93	22.54
Fe _{tot}		4.45	4.8	3.44	12.53	1.92	1.85	1.82	1.51	1.42
MnO		0.01	0.01	0.01	1.29	0.03	0.16	0.01	0.01	0.01
MgO		0.22	0.25	0.26	0.22	0.19	0.11	0.21	0.33	0.15
CaO		0.03	0.01	0.01	0.01	0.02	0.01	0.03	0.11	0.04
Na ₂ O		0.01	0.01	0.01	0.01	0.01	0.01	0.01	0.1	0.01
K ₂ O		4.14	5.31	4.79	4.9	5.87	12.43	12.62	13.17	14.58
P ₂ O ₅		0.18	0.13	0.05	0.16	0.23	0.11	0.08	0.07	0.06
H ₂ O		15.43	10.65	10.45	10.9	10.7	3.57	3.54	2.51	1.71
CO ₂		n.a.	n.a.	n.a.	n.a.	n.a.	n.a.	n.a.	n.a.	n.a.
Total	wt. %	100.34	100.49	100.1	100.11	100.41	99.85	99.67	99.77	100
Ba	ppm	b.d.	b.d.	b.d.	989	51	1373	1542	684	736
Rb		183	174	140	187	220	308	315	299	316
Sr		383	194	496	274	550	195	1569	416	1014
Pb		31	9	17	46	3	22	16	25	17
Th		74	64	122	48	61	86	24	36	51
U		85	82	228	20	19	4	13	9	24
Nb		429	373	337	302	227	146	109	140	131
La		164	53	259	322	413	593	201	4922	127
Ce		655	106	354	398	460	531	208	865	157
Nd		37	28	107	103	187	194	42	1312	35
Y		69	97	180	37	120	72	27	315	71
Zr		1884	2682	6514	754	463	106	307	371	537
V		236	145	476	245	385	567	130	137	357
Cr		11	6	8	19	5	8	b.d.	21	5
Ni		6	10	19	b.d.	11	8	4	32	8
Co		9	b.d.	14	21	b.d.	b.d.	b.d.	6	b.d.
Cu		b.d.	b.d.	b.d.	b.d.	b.d.	b.d.	b.d.	b.d.	b.d.
Zn		64	70	49	173	52	40	88	75	43
Hf		81	70	76	48	57	51	33	27	46
Ga		42	52	120	13	11	1	7	9	11
S		157	352	531	409	193	204	318	276	542

XRF-data; n.a. = not analysed, b.d. = below detection.

TABLE XIII

Geochemical analyses along profile E1 extending from the surface to the hydrothermally altered parent rock. Ore body E, Osamu Utsumi mine (XRF-data).

Osamu Utsumi mine, ore body E, vertical profile E1: Major and trace elements

Sample		E1-88	E1-71	E1-91	E1-72	E1-92C	E1-73	E1-96	E1-74	E1-75	E1-76	E1-77	E1-78
Altitude m.a.s.l.		1456	1452	1444	1436	1428	1420	1412	1404	1388	1372 w	1372 e	1368
Rock type		LAT yel-br	LAT red-br	LAT yel-whi	LAT yel-whi	LAT red-whi	UMD red-br	SAP yel-whi	CpxPh ox.	CpxPh ox/a.	CpxPh "fresh"	CpxPh red.	CpxPh red.
SiO ₂	wt. %	34.90	33.68	40.95	39.89	40.24	34.79	48.93	57.06	56.07	53.08	57.67	56.60
TiO ₂		0.79	0.79	0.80	0.59	0.77	0.62	0.48	0.50	0.43	0.39	0.45	0.43
Al ₂ O ₃		38.04	33.52	36.09	37.09	34.80	30.37	28.69	23.24	22.21	20.21	22.28	22.15
Fe _{tot}		5.81	12.72	4.55	4.17	3.28	6.05	4.16	1.18	1.57	4.54	1.30	1.44
MnO		0.13	0.18	0.12	0.14	2.08	7.20	0.00	0.01	0.03	0.47	0.01	0.02
MgO		0.03	0.12	0.00	0.06	0.09	0.10	0.00	0.11	0.20	0.26	0.09	0.18
CaO		0.01	0.00	0.02	0.00	0.00	0.00	0.00	0.00	0.04	1.49	0.00	1.32
Na ₂ O		0.19	0.19	0.12	0.20	0.18	0.15	0.34	0.46	0.36	4.85	0.38	0.52
K ₂ O		4.40	3.08	3.55	1.77	4.26	3.50	8.75	13.15	12.51	9.08	13.45	12.83
P ₂ O ₅		0.12	0.14	0.18	0.15	0.19	0.07	0.07	0.08	0.07	0.04	0.08	0.05
H ₂ O		13.95	13.32	12.06	13.79	11.60	11.93	6.83	2.48	5.30	2.54	2.09	2.73
CO ₂		n.a.	1.21	n.a.	0.55	n.a.	0.27	n.a.	0.05	0.20	1.58	0.15	0.12
Total	wt. %	98.37	98.95	98.44	98.4	97.49	95.05	98.25	98.32	98.99	98.53	97.95	98.39
F	ppm	518	n.a.	300	n.a.	691	n.a.	894	n.a.	n.a.	n.a.	n.a.	n.a.
Ba		113	90	135	117	491	8916	363	724	391	452	688	668
Rb		143	125	91	60	116	98	196	323	203	226	306	272
Sr		308	305	455	398	477	143	661	649	593	2163	991	745
Pb		36	78	13	113	b.d.	235	b.d.	5	b.d.	b.d.	7	b.d.
Th		75	158	154	161	64	67	36	56	b.d.	34	46	49
U		b.d.	42	b.d.	9	b.d.	b.d.	b.d.	12	b.d.	12	12	10
Nb		423	462	478	324	388	354	253	251	123	219	230	218
La		221	472	537	567	436	539	437	522	242	278	421	338
Ce		802	861	513	994	554	2622	310	429	207	296	432	250
Nd		35	67	134	42	95	160	92	121	41	52	98	60
Y		83	124	150	118	99	99	73	123	7	45	91	72
Zr		1882	2195	1937	798	1172	1769	762	1133	222	749	815	708
V		356	419	691	315	634	311	405	259	107	74	272	215
Cr		7	8	b.d.	b.d.	55	19	b.d.	b.d.	b.d.	b.d.	b.d.	b.d.
Ni		b.d.	7	b.d.	5	b.d.	b.d.	b.d.	b.d.	b.d.	b.d.	b.d.	b.d.
Co		4	17	b.d.	10	b.d.	45	6	b.d.	b.d.	5	b.d.	b.d.
Cu		b.d.	b.d.	b.d.	b.d.	b.d.	b.d.	b.d.	b.d.	b.d.	b.d.	b.d.	b.d.
Zn		149	180	102	87	160	247	113	52	72	171	47	72
Hf		22	n.a.	24	n.a.	17	n.a.	7	n.a.	n.a.	n.a.	n.a.	n.a.
Ga		n.a.	94	n.a.	84	n.a.	66	n.a.	46	26	36	45	40
Sc		3	4	4	b.d.	3	5	4	8	b.d.	2	8	7
S		b.d.	53	82	367	620	258	b.d.	b.d.	1532	1601	2044	2253

XRF-data; n.a. = not analysed, b.d. = below detection.

TABLE XIV													
Geochemical analyses along profile E2 (Fig. 4) extending from the surface to the hydrothermally altered parent rock. Ore body E, Osamu Utsumi mine (XRF-data).													
Osamu Utsumi mine, ore body E, vertical profile E2: Major and trace elements													
Sample		E2-110	E2-111	E2-112	E2-113	E2-114	E2-115	E2-116	E2-118	E2-119	E2-120	E2-99	E2-102
Altitude m.a.s.l.		1452	1444	1436	1432	1428	1420	1416	1412	1404	1400	1392	1372
Rock type		LAT whi-br	LAT yel	LAT whi	LAT yel-br	LAT red-br	LAT red-yel	LAT whi	SAP yel-whi	SAP whi	SAP whi	VLPh ox.	VLPh red.
SiO ₂	wt. %	30.94	36.62	39.00	25.35	34.69	38.65	43.79	48.03	54.61	52.90	55.84	56.25
TiO ₂		0.76	0.71	0.81	0.69	0.75	0.70	0.64	0.64	0.53	0.51	0.48	0.45
Al ₂ O ₃		37.26	38.39	38.84	36.30	39.26	36.88	36.42	29.21	26.90	27.06	24.11	22.18
Fe _{tot}		7.05	4.73	2.10	15.21	4.46	3.86	1.84	3.48	0.94	2.20	1.31	2.41
MnO		1.38	0.03	0.00	0.82	0.03	0.12	0.01	0.03	0.05	0.00	0.00	0.00
MgO		0.07	0.06	0.11	0.07	0.01	0.04	0.03	0.08	0.09	0.06	0.03	0.03
CaO		0.00	0.01	0.00	0.00	0.00	0.00	0.00	0.02	0.00	0.00	0.01	0.00
Na ₂ O		0.13	0.15	0.10	0.04	0.05	0.12	0.09	0.23	0.13	0.34	0.26	0.38
K ₂ O		3.28	3.38	5.11	4.39	3.47	3.21	4.80	7.60	10.70	9.74	12.79	13.12
P ₂ O ₅		0.07	0.10	0.09	0.14	0.14	0.07	0.12	0.27	0.12	0.08	0.06	0.08
H ₂ O		16.60	14.08	12.41	15.47	15.76	13.18	10.71	7.96	5.01	5.86	2.91	3.21
CO ₂		n.a.	n.a.	n.a.	n.a.	n.a.	n.a.	n.a.	n.a.	n.a.	n.a.	n.a.	n.a.
Total	wt. %	97.54	98.26	98.57	98.48	98.62	96.83	98.45	97.55	99.08	98.75	97.80	98.11
F	ppm	24	113	659	62	240	366	369	688	1134	1079	1220	1152
Ba		455	88	113	402	135	143	231	458	548	385	655	616
Rb		107	99	152	140	99	81	116	169	233	219	277	265
Sr		138	123	51	138	190	100	230	1157	477	851	688	630
Pb		57	b.d.	b.d.	39	b.d.	b.d.	b.d.	4	22	b.d.	b.d.	18
Th		89	43	43	75	78	31	52	66	57	39	28	41
U		b.d.	b.d.	b.d.	3	b.d.	b.d.	b.d.	4	b.d.	b.d.	b.d.	b.d.
Nb		394	345	407	264	429	369	350	323	258	278	200	240
La		88	315	350	199	548	558	489	795	626	857	319	259
Ce		890	306	465	169	638	605	369	522	329	300	311	222
Nd		13	60	84	37	158	153	101	180	125	196	54	22
Y		66	69	79	68	134	77	92	191	176	134	91	42
Zr		1497	1371	1345	1153	1571	2800	1036	1768	1297	1119	971	582
V		316	276	340	382	443	150	748	550	453	299	390	490
Cr		b.d.	b.d.	b.d.	6	b.d.	b.d.	b.d.	7	b.d.	b.d.	b.d.	b.d.
Ni		b.d.	b.d.	b.d.	b.d.	b.d.	b.d.	b.d.	b.d.	b.d.	b.d.	b.d.	b.d.
Co		b.d.	b.d.	b.d.	5	b.d.	b.d.	b.d.	b.d.	b.d.	b.d.	4	3
Cu		b.d.	b.d.	b.d.	b.d.	b.d.	b.d.	b.d.	b.d.	b.d.	b.d.	b.d.	b.d.
Zn		90	70	73	167	82	84	60	78	38	103	39	22
Hf		22	17	18	17	21	38	12	28	18	16	9	4
Sc		b.d.	b.d.	b.d.	b.d.	4	b.d.	2	6	6	5	8	6
S		b.d.	597	1136	1613	653	532	426	473	797	764	b.d.	8549

XRF-data; n.a. = not analysed, b.d. = below detection.

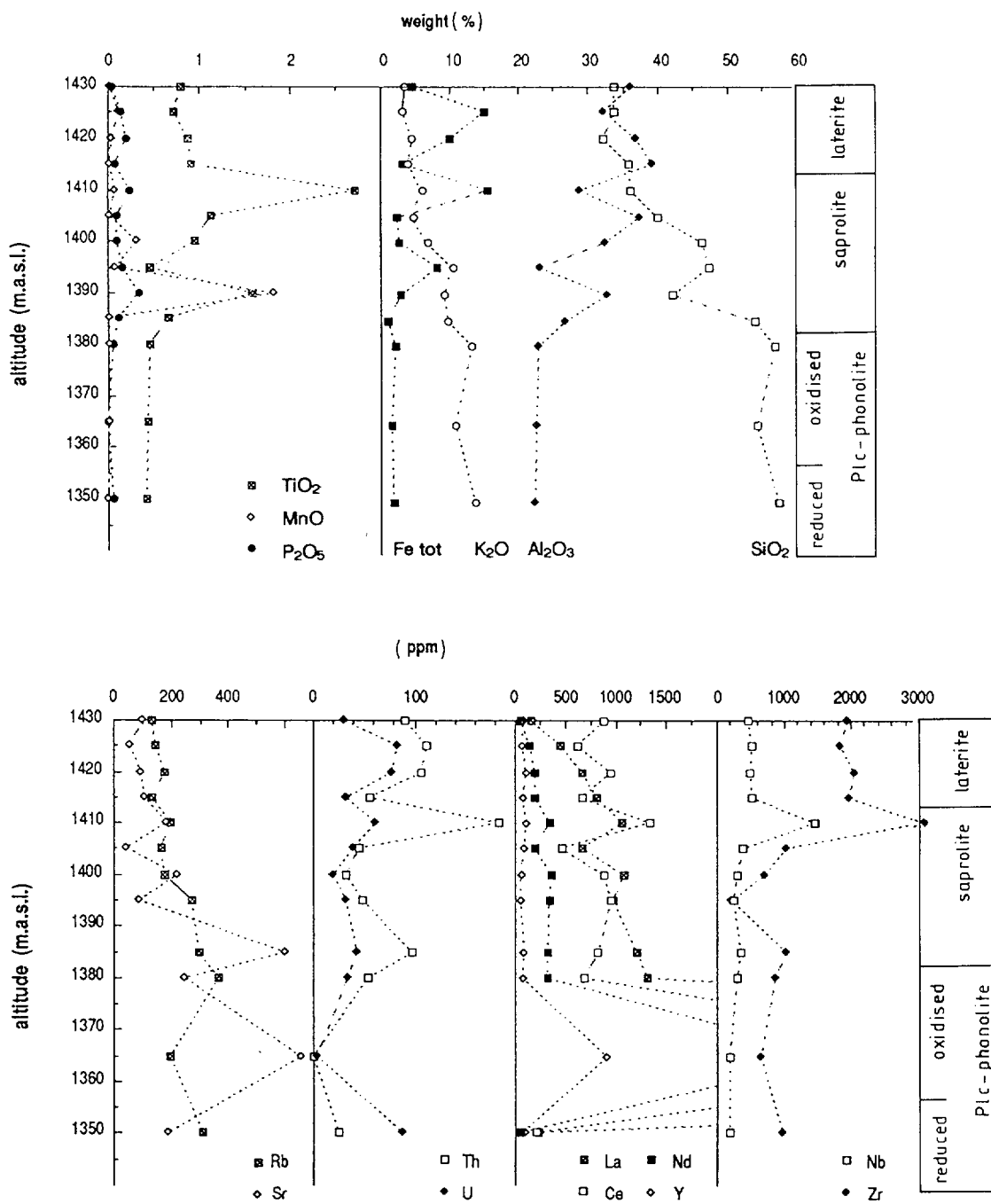


Figure 42. Geochemical variation of selected major and trace elements with depth from the surface to the hydrothermally altered parent rock. Ore body A, profile A, Osamu Utsumi uranium mine (see Fig. 4 for location).

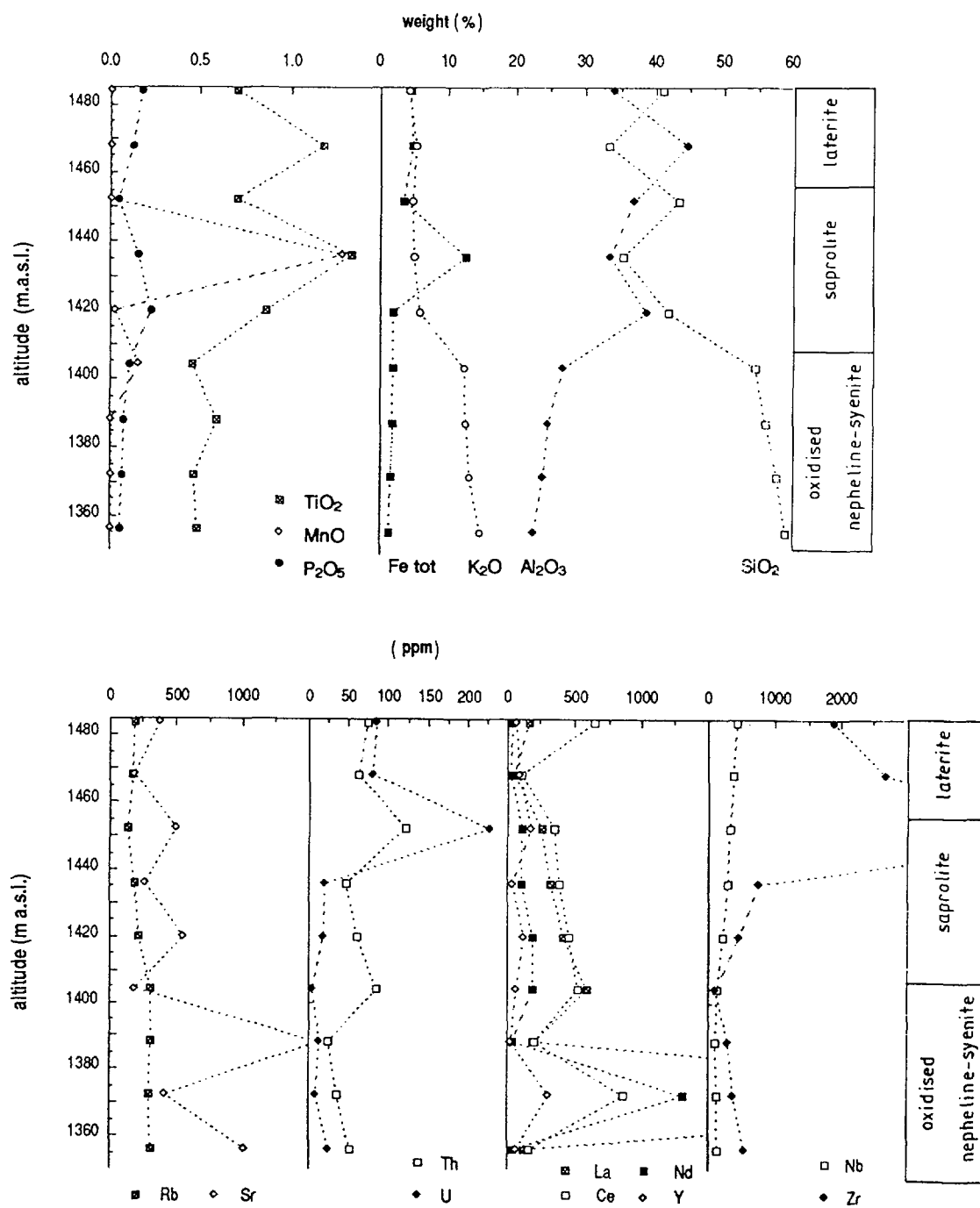


Figure 43. Geochemical variation of selected major and trace elements with depth from the surface to the hydrothermally altered parent rock. Ore body B, profile B2, Osamu Utsumi uranium mine (see Fig. 4 for location).

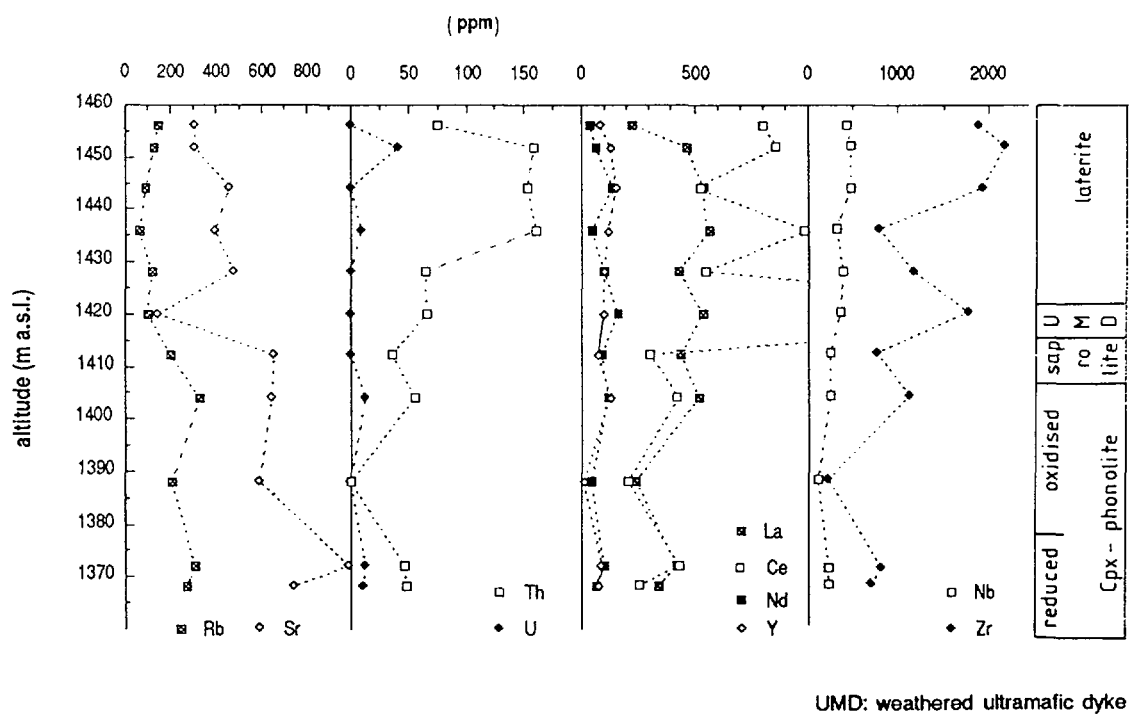
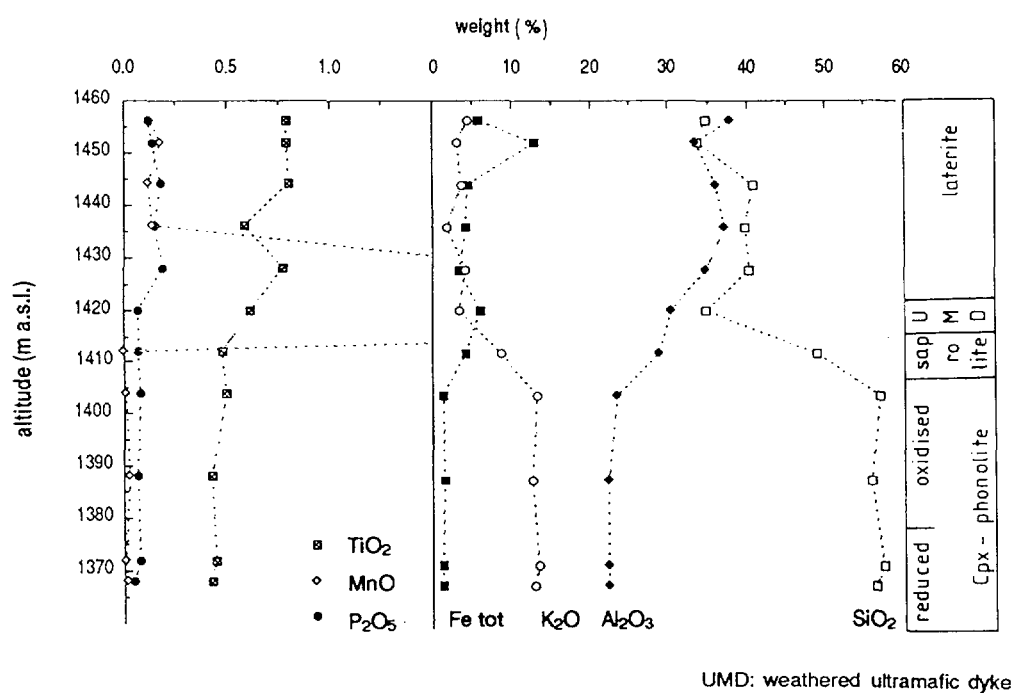


Figure 44. Geochemical variation of selected major and trace elements with depth from the surface to the hydrothermally altered parent rock. Ore body E, profile E1, Osamu Utsumi uranium mine (see Fig. 4 for location).

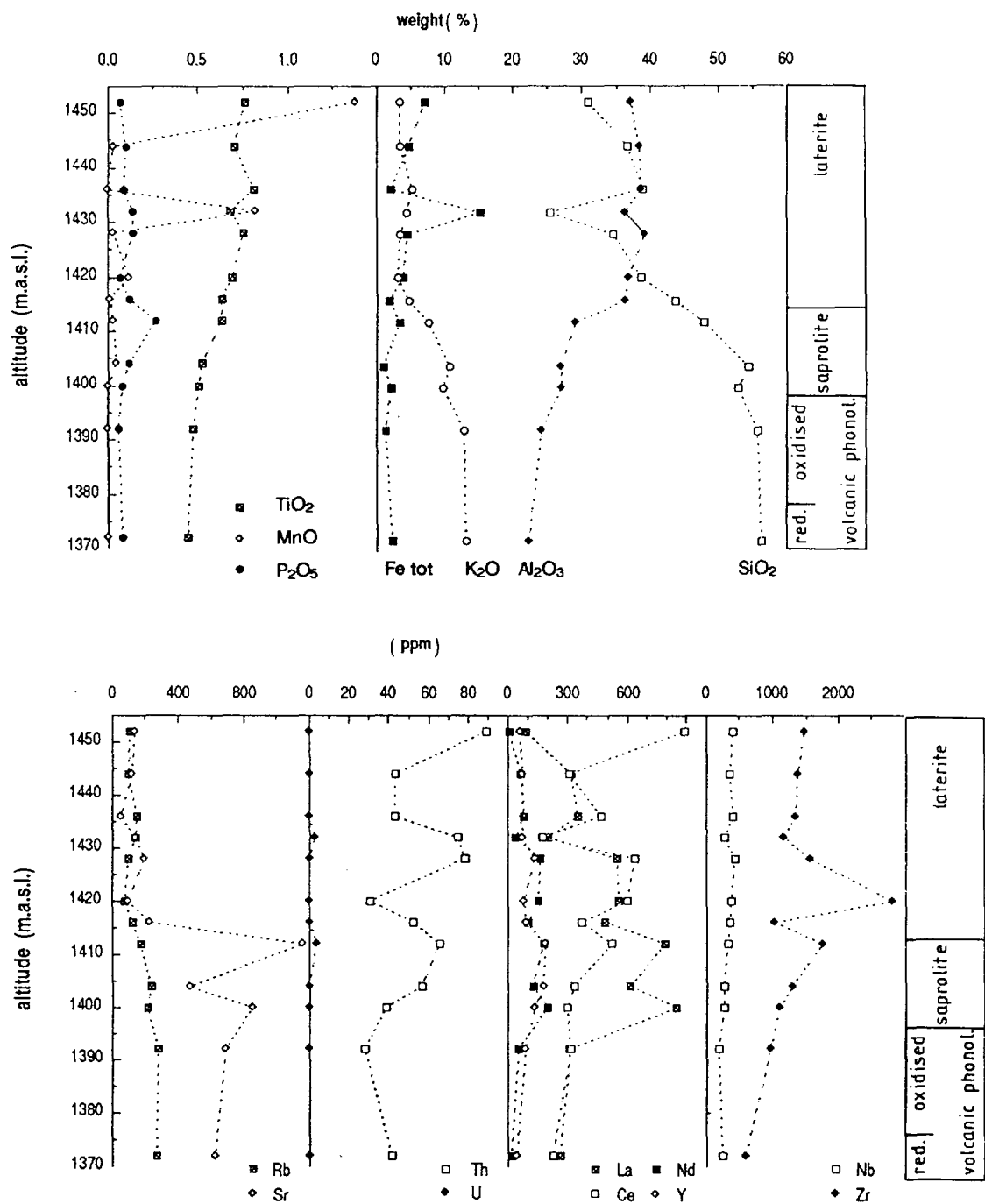


Figure 45. Geochemical variation of selected major and trace elements with depth from the surface to the hydrothermally altered parent rock. Ore body E, profile E2, Osamu Utsumi uranium mine (see Fig. 4 for location).

6. Fracture mineralogy

A compilation of the fracture minerals present in drillcore F1 is given in Table XV. The list contains only those minerals that could be positively identified by microscopy and standard XRD techniques. There are two main fracture inclinations in drillcore F1: 40 – 50° and 70 – 80° to the horizontal plane. Additionally, there are a great number of fractures and fissures that were produced through local brecciation and have no distinct orientation. There is no obvious correlation between fracture fillings and the orientation of the two main fracture sets.

Kaolinite, illite, K-feldspar, pyrite and iron hydroxides are by far the most abundant fracture minerals. Kaolinite and illite are present in nearly all investigated samples, whereas K-feldspar could be identified only in the first 100 m of the core. The first pyrite was found at 60 m, and then continued to be observed down to the bottom of the hole at 126 m. Iron hydroxides could be found in small amounts down to 118 m, whilst zircon and barite are restricted as fracture minerals to a zone between 85 and 100 m. At the maximum depth of the hole, pitchblende could be detected on two fracture planes (123 m and 126 m) as circular concretions together with pyrite.

The fracture and vein mineral infillings of drillcore F4 are listed in the petrographic descriptions of the investigated F4-samples given in Appendix 5.

6.1. Description of selected water-bearing fractures

Five water-bearing fractures, representing the packed-off sections sampled for the hydrochemical programme, were selected from drillcores F1, F2 and F3 to study radionuclide isotope behaviour. There was thus the possibility that these fractures may be in isotopic equilibrium with the groundwaters sampled. A profile from the hydrothermally altered host rock through the leached zone to the fracture infilling surfaces was sampled in three of these fracture samples; the location of the sampling points is shown in Figures 46 to 48. In four of these fracture samples a profile consisting of three samples has been selected, comprising the fracture fillings, the adjacent first centimetre of rock, and one sample about 10 cm away from the fracture. Two samples consist of the fracture fillings only (drillcore F3). Table XVI summarises the mineralogy of these samples.

TABLE XV
Qualitative mineralogical composition of fracture filling phases in phonolites from borehole F1.

Sample	ill	kao	sme	chl	ML	hal	pyp	kf	flu	zir	bar	py	HFO	rut	pit
F1-11-1A	XXX	XX				X		XX					X		
F1-28-1A	XXX	X											X		
F1-35-1B	X	XXX													
F1-45-1A	X	XXX				X		XX					X		
F1-47-1B	XX	XX	X	X		X	X	XX					X		
F1-50-1A		XXX						XX					X		
F1-57-1A	X	X						XXX							
F1-58-1A	X	XXX				X		XX	XX				X		
F1-60-1B-2	X	XXX				X		XX					X		
F1-69-1B	X	X						XXX				XXX		X	
F1-78-1A	X	XXX						XXX							
F1-79-1A	X	XXX						XXX				XX			
F1-85-1C-1		XX			XXX			X		XXX		XX			
F1-85-1C-2		XX			XXX					XXX			X		
F1-90-1A		XXX	X					XXX				X		XX	
F1-94-1A										X	XXX				
F1-100-1A	X	X						XX		XX		XX			
F1-1A-2	X	X								XX		XX			
F1-100-1A-3										XX				XX	
F1-104-1A	X	XXX		X								XXX			
F1-109-1A	X	X										XXX			
F1-118-1A-1	X	XXX	X										X		
F1-118-1A-2		XXX		X	X										
F1-119-1B		XXX			X										
F1-123-1B-1	X	XXX													
F1-123-1B-3	X	X										XXX			XX
F1-126-1B-1	X	X										XXX			XX
F1-126-1B-2	XX	XX	X	X											

Abbreviations:

ill – illite
kao – kaolinite
sme – smectite
chl – chlorite
ML – ill/sme mixed-layers
hal – halloysite
pyp – pyrophyllite
kf – K-feldspar

flu – fluorite
zir – zircon
bar – barite
py – pyrite
HFO – hydrous ferric oxides
rut – rutile
pit – pitchblende

TABLE XVI
Qualitative mineralogical composition of conductive fractures in boreholes F1, F2 and F3.

Sample	Sample description	kf	py	flu	zir	ill	kao	ill/sme	others
F1-114-1A-A	Porous, porphyritic leucocratic phonolite	XXX	X	X	X	XX	XX		
F1-114-1A-B	Porous, porphyritic leucocratic phonolite	XXX	XX	XXX	X	XX	XX		
F1-114-1A-C	Fracture filling, external part	XXX	XX	XXX	XXX	X	X		
F1-114-1A-D	Fracture filling, internal part	X	XX	X	X	XXX	XXX		pitchblende
F2-60-1A-A	Porous leucocratic phonolite	XXX	X	X	X	X	XX		
F2-60-1A-B	Porous leucocratic phonolite, leached	XXX	X	XX	X	XX	XX		alum minerals
F2-60-1A-C	Fracture filling	XXX	XXX	XX		XX	XX		alum minerals, pitchblende
F3-54-1A-A	Cpx-phonolite	XXX	XXX	X		XX	XX		
F3-54-1A-B	Cpx-phonolite, leached	XX	XX	XX	X	XX	XX		
F3-54-1A-C	Fracture filling	XX	XXX	XX		XX	XX		alunite, plumbogummite
F3-74-1A-K	Fracture filling, in porous cpx-phonolite	XXX	XXX	X		X	X		
F3-67-1A-K	Fracture filling, in dense cpx-phonolite	XXX	XX	X		XXX	XXX		barite, lepidolite

Mineral occurrence:

XXX – dominant
XX – major
X – minor

Abbreviations:

kf	–	K-feldspar	ill	–	illite
py	–	pyrite	kao	–	kaolinite
flu	–	fluorite	ill/sme	–	mixed layer
zir	–	zircon			

Fracture sample F1-114-1A (113.03 – 113.33 m)

Sample F1-114-1A (Fig. 46) represents a reddish-grey-coloured phonolite with an extensive micro- and macroporosity. In the macropores, which often reach a diameter of 1–2 cm, idiomorphous pyrite, fluorite, K-feldspar and zircon can be observed. Clay minerals are present in different quantities. The pyrite crystals are often covered with a thin black film, in contrast to the pyrite embedded in the rock matrix.

The fracture transects the drillcore with an inclination of about 70° to the horizontal plane. It has open connections with several of the described macropores. The fracture filling material shows zoning on both sides of the fracture from the open centre towards the rock. The internal part is up to 2 mm thick and is dominated by clay minerals and pyrite. Here, pyrite is covered with a thin film of poorly crystalline pitchblende. A few small crystals of fluorite also occur. In niches of this zone, needle-like white crystals occur, partly covered with a colloidal black film. The tiny crystals look very similar to the ones found in sample F2-60-1A, which could be identified as minerals of the alum family (see below).

The external part of the fracture is dominated by the hydrothermal mineral association K-feldspar, zircon, pyrite and fluorite. Here pyrite has a clean surface when covered with the internal filling material. Clay minerals only occur in small amounts (less than 5%).

Two zones have been carefully separated from one other to be analysed for the uranium decay series (subsamples C and D). Subsample B is taken adjacent to the fracture and shows slightly higher contents of pyrite, fluorite and zircon than subsample A, which was taken 10 cm from the fracture. The latter is also more strongly coloured.

Fracture sample F2-60-1A (59.07 – 59.29 m)

Sample F2-60-1A (Fig. 47) is a strongly fractured and porous phonolite heavily impregnated with pyrite and containing several water-bearing fractures; various thin fractures also occur and are completely filled with clay minerals and pyrite. The normally grey phonolite exhibits striking alteration features, showing a change in colour to bluish-grey and yellowish-green-grey around the open fractures. In these alteration zones powdery secondary U-minerals and tiny white and bluish needles can be observed. These needles were identified as members of the alum family (kaolinite $\text{KAl}(\text{SO}_4)_2 \cdot 11\text{H}_2\text{O}$, pickeringite $\text{MgAl}_2(\text{SO}_4)_4 \cdot 22\text{H}_2\text{O}$, bilinite $\text{Fe}_3(\text{SO}_4)_4 \cdot 22\text{H}_2\text{O}$ and tschermigite $\text{NH}_4\text{Al}(\text{SO}_4)_4 \cdot 22\text{H}_2\text{O}$).

Fracture F1 - 114-1A (113.03 - 113.33m)

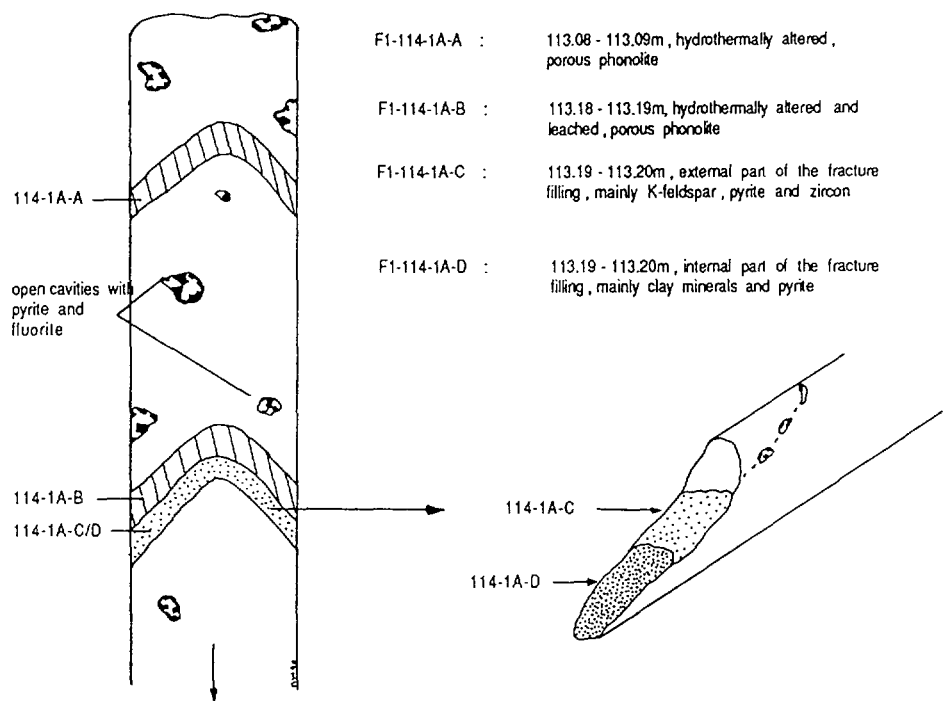


Figure 46. Conductive fracture in drillcore F1 at a depth of 113 m; sample location is indicated by the hatched areas.

Fracture F2 - 60-1A (59.07 - 59.25m)

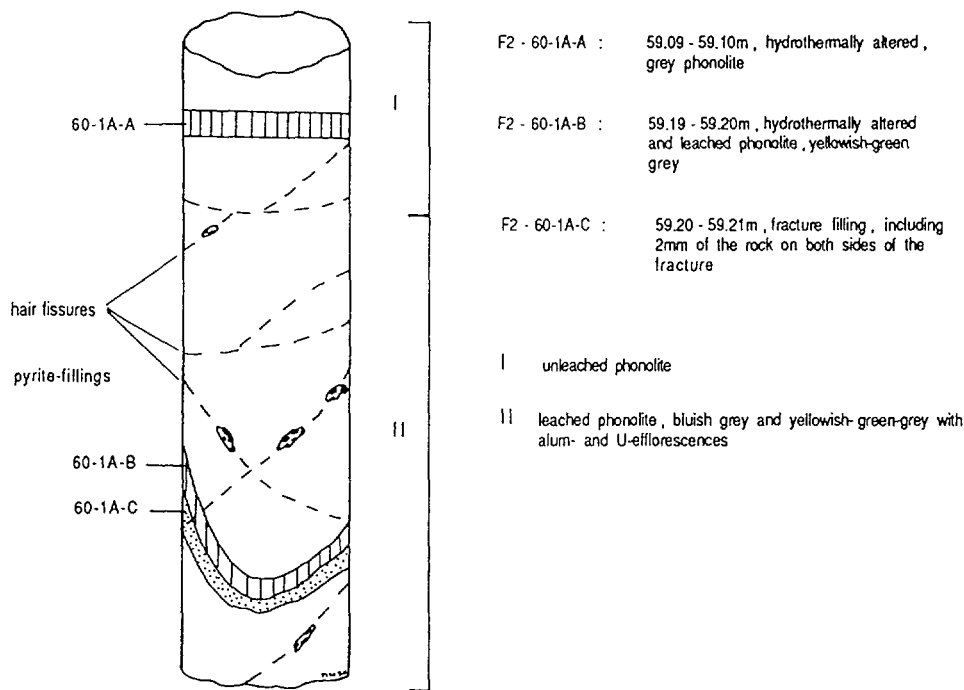


Figure 47. Conductive fracture in drillcore F2 at a depth of 59 m; sample location is indicated by the hatched areas.

The filling material of the separated fracture (subsample C) consists mainly of K-feldspar and pyrite with subordinate fluorite. In addition to illite and kaolinite, the above mentioned alum minerals occur. Pyrite displays two different features mainly depending on the grain-size of the crystals. Small pyrites (<0.5 mm) are coated with a black film and usually form concretions in niches with small amounts of an intergranular black spherical material that was identified as pitchblende. Larger pyrite crystals exhibit clean, yellow surfaces. The same features can be observed in the macropores.

Subsample B again comes from the first few cm adjacent to the fracture. The mineralogical composition is similar to the fracture filling material except that the pyrite content is significantly lower. Subsample A was taken 10 cm away from the fracture where the phonolite is grey in colour and there is no evidence of secondary U-phases.

Fracture sample F3-54-1A (53.20 – 53.40 m)

This fracture, with an inclination of about 40° to the horizontal plane (Fig. 48), cuts a porphyritic, dense pseudoleucite-clinopyroxene phonolite. Within the same core sample there are two more open fractures and several hair-fissures, all filled with clay minerals. The alteration zones around the water-bearing fractures are rather small (0.5–1 cm), brighter in colour and have a slightly lower K-feldspar content than the “fresh” host pseudoleucite-clinopyroxene phonolite.

The fracture filling (subsample C) consists mainly of pyrite, K-feldspar and clay minerals, together with a small amount of fluorite. The pyrite occurs in small crystals which are partly coated with a black film, whereas larger crystals exhibit a clean yellow surface; no pitchblende could be detected. Illite and kaolinite are the dominant components of the clay fraction, followed by alunite, $(\text{KAl}_3(\text{SO}_4)_2(\text{OH})_6)$ and plumbogummite, $\text{PbAl}_3(\text{PO}_4)_2(\text{OH})_5$.

In common with the above samples, subsample B contains the alteration zone around the fracture and subsample A was selected some 10 cm away from the fracture.

Fracture sample F3-67-1A-K (66.77 – 66.87 m)

Only the infill material has been separated from this fracture sample, which has an inclination of 40° to the horizontal plane and is located at a depth of 66.82 m. It cuts a porphyritic, porous phonolite containing K-feldspar up to 0.5 cm and pseudoleucites up to 2 cm. The fracture is 5 mm wide and about 80% of the infilling phases comprise clay

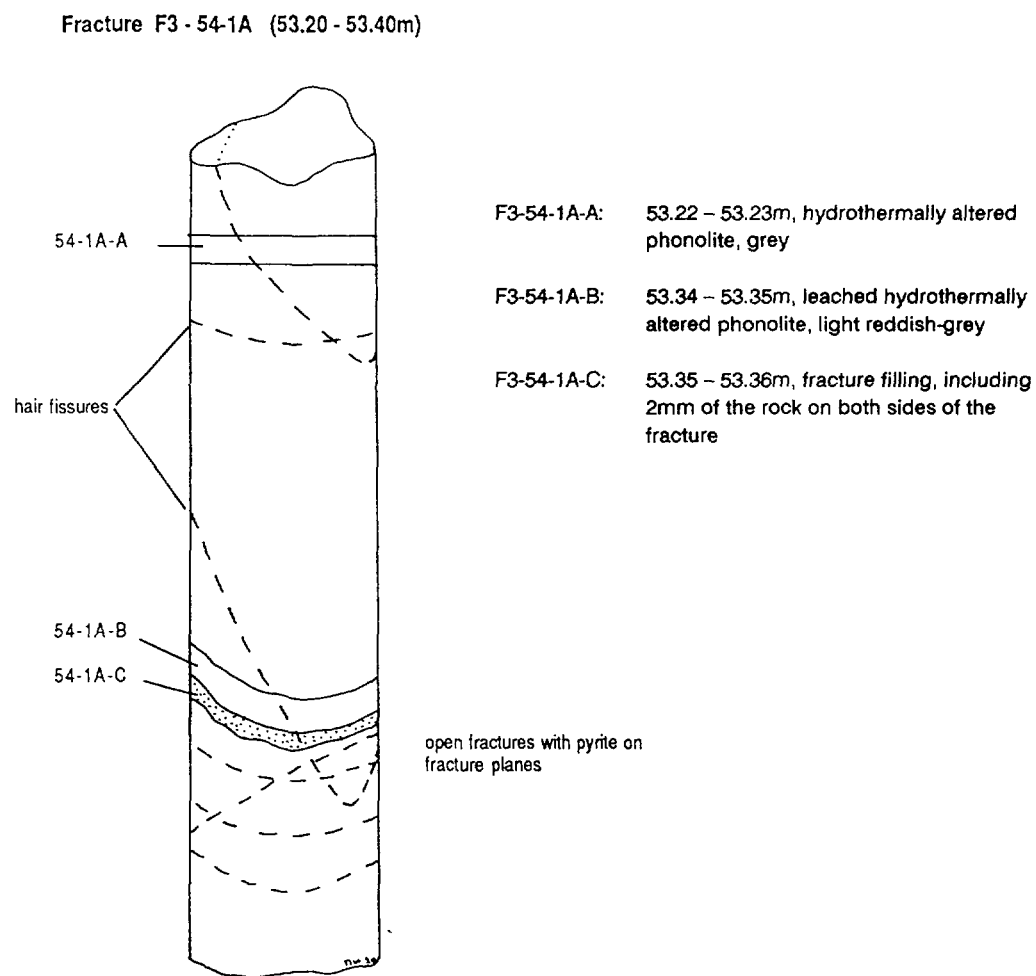


Figure 48. Conductive fracture in drillcore F3 at a depth of 53 m; sample location is indicated by the hatched areas.

minerals, pyrite, K-feldspar and barite, with subordinate fluorite. The clayey material consists of illite, kaolinite and lepidolite. Pyrite is coated with a black film when the crystals are small (<0.05 mm) and is fresh in the larger grain-sizes. The alteration zone around the fracture is 2–5 mm thick and is bright reddish-grey in colour.

Fracture sample F3-74-1A-K (73.26 – 73.52 m)

This fracture, inclined at 70° to the horizontal plane, is located at a depth of 73.28 m in a dense, fine-grained phonolite containing a few pseudomorphically replaced nepheline crystals. The porosity is significantly lower than in sample F3-67-1A and no leaching features can be observed around the fracture. The fracture filling is rudimentary and consists mainly of pyrite, K-feldspar and subordinate fluorite, illite and kaolinite. Again, the small pyrite crystals are coated with a black film and the larger crystals seem to be fresh.

7. Ultramafic lamprophyres

Ultramafic dykes are exposed at several places in the Osamu Utsumi open-pit mine (Fig. 4); in borehole F4 they were intersected at nine different depths (see drillcore log, Appendix 7). The dykes are all ultrapotassic in view of their high K₂O content compared to other ultramafic rocks (see below) and transect all lithological components present in the mine area, including the breccia bodies. All the observed dykes have similar orientations and nowhere are they found crosscutting each other. They did not undergo hydrothermal alteration, although they underwent a specific deuteric alteration indicated by partial carbonatisation, zeolitisation and argillation. Low-temperature meteoric weathering is strongly pronounced in the higher mine levels where the dykes are completely decomposed to clay minerals (mainly smectite, vermiculite and illite), including secondary Sr- and REE-phases such as goyazite and florencite. Weathering affected the ultramafic dykes down to considerable depths as indicated by marginally increased argillation and the formation of iron-oxyhydroxides at a depth of 330 m in borehole F4.

The mineralogical and chemical compositions of the dyke rocks fall into the ultramafic lamprophyre category of Rock (1987). They can be further subdivided into the ouachitite and alnöite families, otherwise only found in association with alkaline rock-carbonatite complexes (Wimmenauer, 1973; Rock, 1977, 1987; Streckeisen and Le Maître, 1979 and Bergman, 1987). All the dykes consist of a very fine-grained groundmass with vitreous parts (although mainly recrystallised) and different fine- to medium-grained phenocrysts and/or xenocrysts, including a large variety of xenoliths ranging from cognate inclusions to country rock xenoliths. Ocellar and amygdaloidal structures are present in the groundmass and in cognate xenoliths.

Compositional differences have resulted in a subdivision into two suites of ultramafic dykes: the first suite is characterised by elevated abundances of phlogopite, olivine and clinopyroxene, referred to as a “phlogopite-bearing” ultramafic lamprophyre; the second group is characterised by increased abundances of carbonates, apatites, opaque phases and cognate xenoliths, referred to as a “carbonate-apatite” ultramafic lamprophyre. The prefixes “phlogopite-bearing” and “carbonate-apatite” are not internationally recognised classifications (Streckeisen and Le Maître, 1979; Rock, 1987). They are used in this work to provisionally facilitate the distinction between the two dyke suites exposed in the Osamu Utsumi mine until more mineral compositional and isotopic data are available to allow a more precise classification. Compiled mineralogical compositions and a semiquantitative modal composition derived from microscopy investigations of the two suites are listed in Table XVII.

7.1. Petrography and mineralogy

7.1.1. Phlogopite-bearing ultramafic lamprophyre

Groundmass

This melanocratic rock has a very fine-grained, partly vitreous groundmass with embedded phenocrysts/xenocrysts of phlogopite, clinopyroxene and olivine, and various xenoliths of cognate and country rock origin. The main components of the groundmass include vitreous parts, clinopyroxene and phlogopite, with the latter two normally displaying flow orientation.

Vitreous parts occur interstitially between the groundmass components. They are preserved as relicts and are mainly recrystallised to carbonate, zeolites, cryptocrystalline

TABLE XVII
Mineralogical composition of the ultramafic lamprophyres exposed at the Osamu Utsumi uranium mine.

			Phlogopite-bearing ultramafic lamprophyre	Carbonate-apatite ultramafic lamprophyre
			n=36 (vol.%)	n=6 (vol.%)
Phenocrysts	phlogopite/biotite	mag.phen. or xen.	5 – 10	3 – 7
	clinopyroxene	mag. phen. or xen.	5 – 10	1 – 3
	olivine	mag. phen. or xen.	1 – 3	1 – 2
	apatite		<1	2 – 5
	leucite			<1
Total phenocrysts			15 – 25	8 – 18
Groundmass	isotropic gm	mag. glass, devitrified	20 – 25	15 – 25
	phlogopite/biotite	mag. gm min.	20 – 25	10 – 15
	clinopyroxene	mag. gm min.	22 – 26	2 – 5
	opaque ore min.	mag. gm min.	2 – 3	4 – 7
	leucite	mag. gm min.	1 – 4	1 – 2
	apatite	mag. gm min.	<1	3 – 5
	carbonate	mag. gm min.	<1	40 – 45
	rutile	mag. gm min.	<1	<1
	Cr-spinel	mag. gm min.	tr	tr
	amphibole	mag. gm min.	tr	<1
	zeolites	second. replac. min.	n.q.	n.q.
	clay minerals	second. replac. min.	n.q.	n.q.
	serpentine	second. replac. min.	n.q.	n.q.
	talc	second. replac. min.	n.q.	n.q.
	carbonate	second. replac. min.	n.q.	n.q.
	Ti-oxides	second. replac. min.	n.q.	n.q.
	Fe-oxides	second. replac. min.	n.q.	n.q.
Total groundmass			70 – 80	50 – 60
Xenoliths	cognate	biotite-pyroxenite, pyroxenite, olivine-nodules, biotites, carbonatite (?)	5 – 10	40 – 50
	country rock	hydrotherm. altered nepheline syenite	<1	<1

mag. phen. or xen. – magmatic phenocryst and/or xenocryst
mag. gm min. – magmatic groundmass mineral
second. replac. min. – secondary replacement mineral
n.q. – not quantified

clay minerals, and opaque phases. Small drop-like inclusions of preserved glassy material occur in apatite.

Clinopyroxene forms hypidiomorphic to idiomorphic prisms and needles (0.01 – 0.03 x 0.06 – 0.15 mm) which are colourless to light yellowish-green, weakly pleochroitic, and optically identified as diopsidic clinopyroxenes. Larger crystals in the groundmass display compositional zoning in their central parts and often have a green-coloured growth rim of a more hedenbergitic composition. The clinopyroxenes are often surrounded by a thin biotite rim and display alteration to carbonate, chlorite, smectite and Fe-Ti-oxyhydrates, especially adjacent to small fractures.

Phlogopite is of idiomorphic to hypidiomorphic, tabular to platy shape, with a grain-size of 0.05 – 0.4 mm. The majority of the phlogopite shows typical central zoning with a bright yellowish-brown to bright red-brown pleochroism. Chemically the phlogopites are Ti-rich, with the Ti-content decreasing towards the rims (Waber, 1990). Tiny inclusions of primary opaque phases and carbonate are present. The groundmass phlogopites are well-preserved, except in the near-vicinity of fractures where they are decomposed to chlorite, smectites, vermiculite and Fe-Ti-oxyhydroxides.

Minor components of the groundmass include replaced leucite, carbonate and opaque phases together with the secondary carbonate, zeolites, serpentine and clay minerals. Tiny idiomorphic inclusions of carbonate in phlogopite, clinopyroxene and apatite are thought to be of magmatic origin. The same accounts for coarser-grained carbonates present in drop-shaped aggregates. However, the bulk carbonate is very fine-grained to cryptocrystalline and of secondary origin, representing a recrystallisation product of the very carbonate-rich glass in the groundmass. Apatite, rutile, chromian spinel, amphibole and talc occur as traces, together with secondary cryptocrystalline Ti- and Fe-oxyhydrates and unidentified phases of primary and secondary origin.

Phenocrysts and xenocrysts

Phlogopite, olivine and clinopyroxene are the coarse components of the “phlogopite-bearing” ultramafic lamprophyre. Phlogopite plates vary in grain-size between 1 and 3 mm; in several cases they form booklets with dimensions up to 20-40 mm. Well-preserved phlogopites of this type have been used for radiometric dating (Shea, this report series; Rep. 4). They often show a more complex and inhomogeneous zoning pattern than in the groundmass, usually with an intensely reddish-brown coloured core surrounded by a broad, weakly coloured zone and rimmed by a small, red-brown zone similar to that

observed in the groundmass phlogopite. Clinopyroxene, chromian spinel, opaque phases (magnetite, ilmenite) and idiomorphic carbonate occur as magmatic inclusions. Marginal chloritisation is more strongly developed compared to the groundmass phlogopite and much more pronounced in the near-vicinity of fractures. Chemically the phlogopites are low in Al but high in Ti. The composition of core and rim is of a phlogopite-annite solid solution without any significant amount of siderophyllite and annite (Waber, 1990), and comparable with phlogopites from lamproites and kimberlites (Boettcher and O'Neil, 1980; Bachinski and Simpson, 1984).

Olivine occurs as single crystals between 1–10 mm in diameter, and in pure olivine aggregates up to 30 mm. It is xenomorphic to idiomorphic in shape and always partly to totally replaced by serpentine and skeletal iron-oxides with subordinated talc and carbonate. A thin reaction rim (<0.2 mm) is normally developed around the olivine, consisting mainly of phlogopite, opaque phases and cryptocrystalline silicate phases. Phlogopite, chromian spinel and, in a few cases, apatite, occur as magmatic inclusions.

Hypidiomorphic clinopyroxene varies in grain-size between 1–2 mm and displays three different types according to their optical behaviour. There is a colourless, non-pleochroitic diopsidic type, a greenish pleochroitic hedenbergitic type and a slightly brownish type with brownish-violet pleochroism and anomalous interference colours otherwise typical for Ti-augite. It occurs as single crystals and is often rimmed by the two other clinopyroxenes; all the clinopyroxenes exhibit zoning. In the pyroxene quadrilateral the pyroxenes plot close to the diopside-hedenbergite line, with the greenish-coloured cores being richest in the hedenbergite component (30-40%). The colourless clinopyroxenes are of a more diopsidic composition with a hedenbergite component of 10-20%. Brownish-coloured clinopyroxenes plot outside the quadrilateral, being too rich in Ca and indicating the presence of pyroxenoid (wollastonite) exsolution (Waber, 1990). Such clinopyroxene compositions are typical for mantle-derived ultramafic lamprophyres and lamproites (Bergman, 1987; Rock, 1987). Marginal decomposition to phlogopite and, in certain cases, to chlorite is more pronounced than in the groundmass. Apatite, phlogopite and opaque phases occur as magmatic inclusions.

Cognate xenoliths

Cognate xenoliths, comprising a wide compositional range of mafic and ultramafic rocks, are by far the most common inclusions in the “phlogopite-bearing” ultramafic

lamprophyre. Most of the mafic inclusions are mineralogically quite similar to the surrounding rock, primarily representing different structural and textural varieties. They are generally more coarse-grained than the groundmass variety and show internally developed flow orientation. Ocellar and amygdaloidal structures filled with carbonate and/or devitrified glass, zeolites, clay minerals and opaque phases are often present in these inclusions. Major mafic minerals of the different inclusions are homogeneous phlogopite, clinopyroxene, opaque ore minerals and olivine. In addition, a type enriched in apatite, carbonate and opaque ore minerals occurs, similar to the “carbonate-apatite” ultramafic lamprophyre described below. In a few cases, not further identified, corroded amphibole is present. The ultramafic inclusions consist of phlogopitic biotite-pyroxenites, pyroxenites, olivine-pyroxenites, phlogopitites and polycrystalline olivine aggregates with inclusions of chromian spinel.

Country rock xenoliths

Country rock xenoliths are much less frequent than the cognate ones, but they are of special interest due to their potential for explaining:

- a) the relative time relationships between the different hydrothermal events and
- b) the intrusion of the ultramafic dykes and the related U-mineralisation of the nepheline syenites and phonolites.

All the country rock xenoliths consist of hololeucocratic fine- to medium-grained, subvolcanic to hypabyssal phonolites and nepheline syenites. They range from a few millimetres to centimetres in size and are rounded to subrounded in shape. A thin reaction rim (<0.2 mm) consisting of clinopyroxene, biotite, opaque ore minerals and clays is usually present. The mineralogical composition of the xenoliths is identical to that described for the phonolites and nepheline syenites presented above. It includes advanced argillic alteration with pseudomorphically replaced nepheline, exchanged alkali feldspar, and pseudomorphosed aegirine-augite, which underwent partial biotitisation due to reaction with the enclosing lamprophyre. The xenoliths display an impregnation with pyrite and bear interstitial zircon mineralisation. All these features are unique for the country rock xenoliths and lead to the conclusion that they underwent hydrothermal alteration and mineralisation prior to the intrusion of the ultramafic dykes.

7.1.2. “Carbonate-apatite” ultramafic lamprophyre

The melanocratic “carbonate-apatite” ultramafic lamprophyres are characterised by their high content of cognate xenoliths (about 40–50 vol.%), carbonate, apatite and opaque phases. All the observed textural features indicate an explosive emplacement for these dykes.

Ocellar and amygdaloidal structures are often observed in the groundmass as well as in cognate xenoliths filled with coarse euhedral carbonate. Only in a few cases is the infilling polymineralic, consisting of carbonates, zeolites, clay minerals and opaque phases.

Groundmass

The very fine-grained, partly vitreous groundmass displays a weak flow orientation, especially around xenoliths. Major components are carbonate, recrystallised vitreous parts, phlogopite, opaque phases and apatite (Table XVII).

Carbonate forms fine-grained euhedral crystals in the groundmass in addition to cryptocrystalline aggregates, and its optical character points to an Fe-rich (sideritic) composition. Minute euhedral carbonate occurs as inclusions in phlogopite, clinopyroxene, apatite and opaque phases. Vitreous parts of the groundmass are recrystallised and of similar occurrence to the “phlogopite-bearing” ultramafic lamprophyre.

Phlogopite forms idiomorphic to hypidiomorphic tabular to platy crystals with a grain-size of 0.05–0.2 mm. In addition, biotite occurs with a green-brown pleochroism of common biotite composition.

Opaque phases occur as very fine-grained cubes (0.01–0.1 mm) disseminated throughout the groundmass, although they tend to be somewhat concentrated around xenoliths. Opaque phases are always present in replaced mafic minerals.

Apatite is developed as euhedral needles (0.05–0.5 mm), often intimately intergrown with carbonate and displaying a spinifex-like texture. Apatites in the groundmass are free of inclusions except for tiny carbonate and preserved glass grains.

Minor and trace components of the groundmass include clinopyroxenes (diopsidic-hedenbergitic pyroxene), pseudomorphically replaced leucite, Ti-phases (rutile and cryptocrystalline aggregates) and amphibole, together with secondary zeolites, clay minerals, serpentine, talc and carbonate. Amphibole displays strongly

corroded crystals 0.03–0.5 mm in size, and mainly decomposes to biotite, chlorite and carbonate. Optical identification of the amphibole yields a barkevikitic composition.

Phenocrysts and xenocrysts

Phlogopite, apatite and subordinate clinopyroxene and olivine are the coarse components of the “carbonate-apatite” ultramafic lamprophyre. Phlogopite forms hypidiomorphic plates of 1–3 mm in size, rarely reaching 5 mm in diameter, usually with a small rim of green-brown pleochroitic biotite. Inclusions of euhedral apatite and carbonate are common, the latter clearly discernible from carbonate penetrating into the phlogopite along the 001-planes. In several phlogopites, tiny, almost isotropic inclusions with a yellowish red-dark brown pleochroism are present. These may either correspond to perovskite or belong to the pyrochlore group. In some zones of the rock a weak chloritisation of the phlogopite is developed.

Apatite occurs as euhedral needles of considerable length (up to 3 mm), and inclusions of tiny euhedral carbonate crystals are frequently observed. In some apatites there occur inclusions of biotite, opaque and semi-opaque phases (perovskite?, pyrochlore?) which could not be further identified microscopically.

Clinopyroxene and olivine present the same features as described for the “phlogopite-bearing” ultramafic lamprophyre .

Cognate xenoliths

The same cognate xenoliths as observed in the “phlogopite-bearing” ultramafic lamprophyre occur in the “carbonate-apatite” ultramafic lamprophyre. However, in the latter the xenoliths have a much more developed reaction rim up to 1 mm. The rims consist mainly of carbonate, opaque phases, biotite and zeolites. Additionally, ocelli filled with coarse carbonate are much more abundant than in the “phlogopite-bearing” ultramafic lamprophyre. The only distinct xenolith type observed consists of coarse carbonate with apatite arranged in a spinifex-like texture. Xenoliths of this type do not display a reaction rim with the matrix.

Country rock xenoliths

Country rock xenoliths are subordinate when compared to the cognate xenoliths. They are hydrothermally altered with a mineralised nepheline syenite and phonolite composition. As with the “phlogopite-bearing” ultramafic lamprophyre, the country rock xenoliths underwent hydrothermal alteration and mineralisation prior to their incorporation into the “carbonate-apatite” ultramafic lamprophyre.

7.2. Geochemistry

The ultramafic dykes encountered in the Osamu Utsumi mine have a unique chemical composition. Chemically, they are distinct from any other mineralogically similar rock of the lamprophyric, lamproitic and kimberlitic suites (Wimmenauer, 1973; Rock, 1977, 1987; Bergman, 1987; Foley *et al.*, 1987). However, it has to be borne in mind that mineralogical investigations indicate a slight postmagmatic alteration for these dyke rocks, although this is distinctly different to the hydrothermal alteration observed in the mine host rocks (Section 5). In addition, the dykes have incorporated small amounts of mineralised host rock xenoliths. These two observations may explain at least part of the aberrant chemical composition when compared to other lamprophyric rocks suites.

7.2.1. Major elements

Both mineralogically distinct ultramafic lamprophyre suites are characterised by their very low SiO₂ values and high K₂O values (Table XVIII). Total iron, and particularly MnO, are relatively high whereas the other major elements occur in amounts comparable to worldwide average values for lamprophyres, lamproites and kimberlites (Bergman, 1987). The Mg-number ranges between 86–90 for the “phlogopite-bearing” ultramafic lamprophyre and 39–63 for the “carbonate-apatite” ultramafic lamprophyre, with the fresh sample having a value of 63. Rock (1987) subdivides the lamprophyric suite into four branches: calc-alkaline, alkaline and ultramafic lamprophyres and the lamproites. According to this classification the major element composition of the Osamu Utsumi mine dykes, with the exception of MnO, agrees best with the ultramafic lamprophyres.

K₂O is greater than 3 wt.% in all dyke samples analysed, except for the two slightly altered “carbonate-apatite” ultramafic lamprophyre samples (K₂O = 2.50 and 2.58 wt.%). The K₂O/Na₂O ratio (wt.%) varies between 7–12 for the “phlogopite-bearing”

TABLE XVIII

Geochemical composition of the ultramafic lamprophyres from the Osamu Utsumi uranium mine.

		PL-3	PL-7	PL-8	PL-9	F4-331-AA	F4-331-AB	F4-331-AC
SiO ₂	wt. %	37.90	36.80	37.35	37.57	34.05	30.00	25.41
TiO ₂		2.25	2.18	2.23	2.22	1.86	1.83	1.83
Al ₂ O ₃		10.91	10.58	10.48	10.96	11.80	10.12	9.50
Fe _{tot}		16.22	17.67	16.79	17.09	19.81	22.52	25.88
MnO		1.89	2.40	2.13	2.21	4.72	6.51	8.41
MgO		9.73	8.73	9.40	8.87	4.47	4.19	3.09
CaO		8.17	7.12	8.46	7.57	7.48	6.89	4.99
Na ₂ O		0.32	0.51	0.31	0.53	0.01	0.01	0.01
K ₂ O		3.89	3.64	3.30	3.81	3.06	2.50	2.58
P ₂ O ₅		1.01	0.88	0.96	0.85	1.25	1.23	1.23
LOI		7.74	9.10	8.35	8.58	11.54	13.97	17.01
CO ₂		n.a.	n.a.	n.a.	n.a.	n.a.	n.a.	n.a.
Total	wt. %	100.03	99.61	99.76	100.26	100.05	99.77	99.94
Ba	ppm	2671	2750	2952	2864	1597	1749	1837
Rb		2366	2496	1868	2910	100	85	84
Sr		1238	1184	1323	1289	606	597	531
Pb		18	20	16	24	16	11	24
Th		21	22	29	26	34	35	32
U		b.d.	b.d.	b.d.	b.d.	5	b.d.	6
Nb		117	123	119	135	293	293	297
La		237	284	228	304	198	241	275
Ce		326	384	296	417	341	403	453
Nd		147	163	130	172	175	185	224
Y		42	45	48	52	46	43	48
Zr		384	297	336	303	831	719	740
V		266	261	266	269	223	241	256
Cr		793	786	820	784	232	227	249
Ni		399	431	401	419	58	55	60
Co		59	58	58	56	52	51	58
Cu		26	23	22	25	b.d.	b.d.	b.d.
Zn		1408	1688	1738	1512	339	379	521
Ga		19	21	19	22	23	17	21
Hf		9	8	9	9	12	10	13
S		1999	1381	1188	1493	1410	1287	1559

n.a. = not analysed

b.d. = below detection limit

Samples PL-3, PL-7, PL-8, PL-9 (ore body E): "phlogopite-bearing" ultramafic lamprophyres

Samples F4-331-AA to AC: "carbonate-apatite" ultramafic lamprophyres

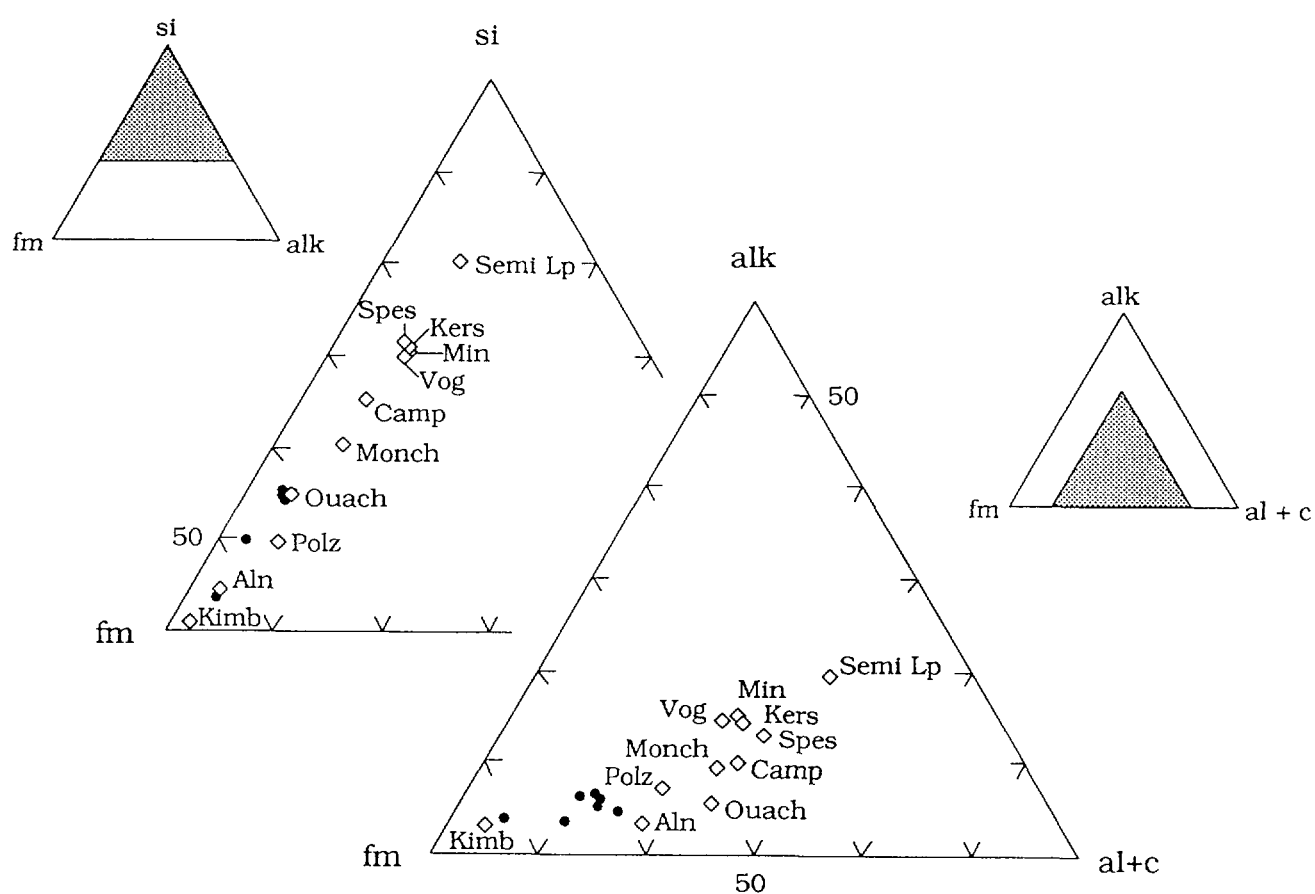
ultramafic lamprophyre and as high as 250–306 for the “carbonate-apatite” ultramafic lamprophyre, with the fresh sample corresponding to 306. Such extremely high K_2O/Na_2O ratios have not been observed either in worldwide lamprophyres or in lamproites or kimberlites (Bergman, 1987; Rock, 1987; Dawson, 1987). According to Foley *et al.* (1987), both the “phlogopite-bearing” ultramafic lamprophyre and the “carbonate-apatite” ultramafic lamprophyre should be called ultrapotassic.

In Figure 49 the Niggli-values for the dykes are illustrated as triangular plots with axes fm-si-alk and fm-alk-(al+c). Compared to the average values given by Wimmenauer (1973), the dykes of the Osamu Utsumi mine plot in the fm-si-alk diagram around the ouachitite average value, with the two “carbonate-apatite” ultramafic lamprophyre samples most affected by hydrothermal alteration shifting towards the averages for polzenites and alnöites. In the fm-alk-(al+c) diagram the dyke analyses all plot towards higher fm-values compared to ouachitites and alnöites. The “carbonate-apatite” ultramafic lamprophyre sample most affected by hydrothermal alteration plots very close to average kimberlite values.

7.2.2. Trace elements

Figure 50 shows a spidergram of the incompatible elements normalised to chondritic abundances, except for K, Rb and P which are normalised to primitive terrestrial mantle values (Thompson *et al.*, 1983). The general pattern of the dykes differs markedly from that of the regional rock and of the hydrothermally altered rocks, indicating a contrasting genetic evolution. The most striking differences between the two dyke groups are the enormous enrichment of Rb and the greater amounts of Ba, K, Sr and Ti present in the “phlogopite-bearing” ultramafic lamprophyre compared to the “carbonate-apatite” ultramafic lamprophyre. In contrast, the “carbonate-apatite” ultramafic lamprophyre is richer in Th, Nb, P, Zr and Hf. In comparison with worldwide potassic to ultrapotassic rocks, the pattern displayed by the “phlogopite-bearing” ultramafic lamprophyre shows the best agreement with ultrapotassic lavas from the western branch of the East African Rift (Davies and Lloyd, 1988), although with a much greater abundance for all the incompatible elements. The “carbonate-apatite” ultramafic lamprophyre displays a pattern very similar to group II kimberlites (Smith *et al.*, 1985).

The K/Rb ratio is high in the “carbonate-apatite” ultramafic lamprophyre but unusually low in the “phlogopite-bearing” variety. Similarly, the K/Ba and Ca/Sr ratios are higher in the “carbonate-apatite” ultramafic lamprophyre, whereas the Ti/Nb and



Legend: • ultrapotassic, ultramafic dykes from the Osamu Utsumi mine

◇ average compositions of worldwide lamprophyric rocks including kimberlites after Wimmenauer (1973):

Spes	- Spessartite	Camp	- Camptonite
Kers	- Kersantite	Monch	- Monchiquite
Min	- Minette	Ouach	- Ouachitite
Vog	- Vogesite	Polz	- Polzenite
semi lp	- semi-lamprophyre	Aln	- Alnöite
		Kimb	- Kimberlite

Figure 49. Chemical compositions of the ultramafic dykes from the Osamu Utsumi mine compared with world-wide lamprophyric rocks presented in si-fm-alk and alk-fm-al+c (Niggli) diagrams.

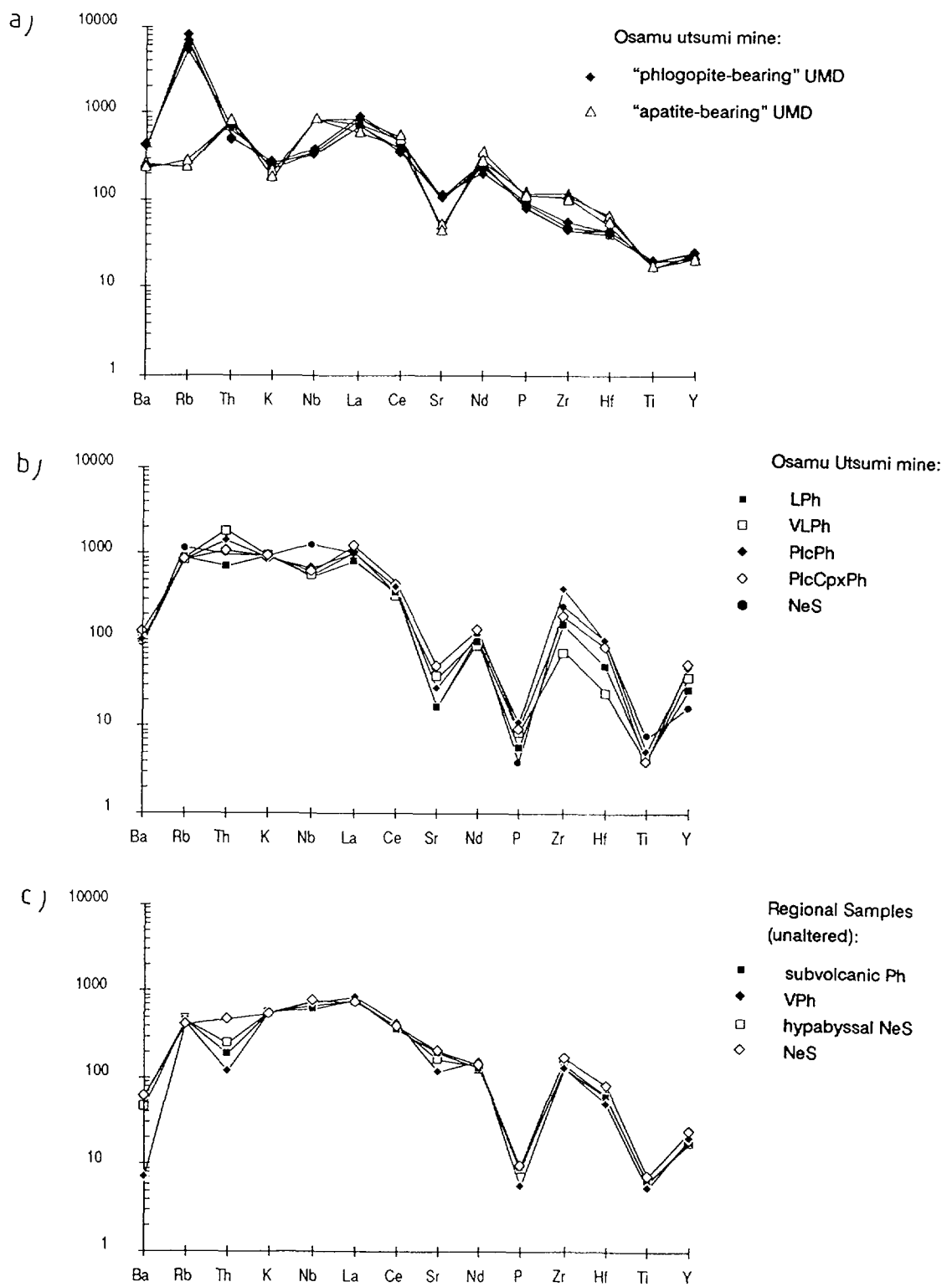


Figure 50. Incompatible elements normalised to chondrite and primitive mantle for:
 a) lamprophyric dykes from the Osamu Utsumi mine,
 b) average of hydrothermally altered rocks from the Osamu Utsumi uranium mine,
 c) unaltered regional rocks.
 (Normalisation factors from Thompson, 1983).

Rb/Sr ratios are considerably lower than in the “phlogopite-bearing” ultramafic lamprophyre. Zr/Nb is similar in both types. With respect to the compatible elements, it is interesting to note that the “phlogopite-bearing” type shows more kimberlite affinity than the “carbonate-apatite” variety, and has considerably greater contents of Ni, Cr, Cu and Zn. Ni and the LREEs occur in similar amounts in both types.

8. Uranium mineralisation

The presence of the uranium mineralisation played a key factor in the choice of the Osamu Utsumi mine for an analogue study. An understanding of the mineralogy, geochemistry and genesis of the mineralisation is an obvious prerequisite for this work. In the preceding chapters it could be shown that uranium enrichment initially took place during a strong hydrothermal event, and later during supergene weathering.

8.1. Mineralogy and mineral chemistry

8.1.1. Hydrothermal hypogene mineralisation

Two types of hydrothermal U-enrichments can be observed:

- a) a disseminated enrichment, and
- b) an enrichment contained in the matrix of the breccias and within veins.

In the disseminated enrichment, uranium shows a similar radiographic distribution pattern (see Chapter 9, “Redox fronts”) to the finely dispersed pyrites (grain-size range 50 – 100 micron). In the pyrite aggregates the uranium content is also elevated. Within the disseminated enrichment, small veinlets filled with pyrite and clay minerals frequently occur; autoradiography shows that this pyrite is also U-bearing. Some of the small inclusions in pyrite that can be observed under reflected light indicate high U-contents with the microprobe, although their size (< 1 micron) prevented quantitative analysis. Under the scanning microscope (Fig. 51; SEM 2816/8) these inclusions proved to be pure uranium oxides, and XRD studies yielded a compositional range from $\text{UO}_{2.25}$ to U_3O_7 . In general, the reflections of the pitchblendes with compositions near $\text{UO}_{2.25}$ have somewhat sharper lines, indicating higher crystallinity. In the course of the same investigation small grains of monazite/cheralite were observed growing on the pyrites

(Fig. 52; SEM 2814/4). This provides a strong indication as to which phases the REEs are concentrated in following the hydrothermal processes, and subsequent to their release from the primary magmatic mafic minerals.

In the breccia matrix and vein-type enrichments uranium is partly intergrown with pyrite, but is also present in other phases. During the initial phases of this study it was thought that most of the hydrothermal uranium was present in zirconium minerals. Microprobe investigations, however, did not confirm this assumption, because uranium concentrations were too low, always below the detection limit of 200 to 300 ppm. On the other hand, uranium was found to be associated with brannerite (UTiO_6) and other TiO_2 -bearing phases, of which anatase is the most common. The silvery, high-reflectance pyrites, that can sometimes be mistaken for galena, are characterised by high contents of TiO_2 (mainly anatase) inclusions.

The abundances of the different hydrothermal minerals in the breccia matrices and veins vary considerably and can be compared to those in the fissures described in Chapter 6 (see Appendix 5). By analogy with these, it can be assumed that the mineralisation took place in several phases, some characterised by a preponderance of certain phases (Zr-minerals, etc.), or a certain type of phase (violet fluorite \rightarrow colourless fluorite \rightarrow green fluorite). At certain stages appreciable amounts of pitchblende must have been precipitated, yielding U-contents in the order of 5000 ppm (see Appendix 4).

8.1.2. Supergene mineralisation

The pitchblende nodules that occur in the Osamu Utsumi mine are the most spectacular products of the supergene mineralisation (Plate 4). In the homogeneous, porous phonolite (E-body; Fig. 4), they are developed along the whole redox front, in contrast to the breccia bodies (B-body; Fig. 4) where large nodules (>5 cm in diameter) are found mainly along the deeply penetrating tips of the oxidation fronts associated with SW-trending conducting faults (Fig. 2). Mineralogically, the uranium is mostly present as botryoidal aggregates of pitchblende, illustrated by very broad lines on X-ray films. These pitchblendes are generally less well crystallised than those formed during the hydrothermal event. In the nodules, pitchblende is finely intergrown with illite, K-feldspar, pyrite and others. For this reason, microprobe analyses of pitchblende (Appendix 3) always contain traces of SiO_2 , K_2O and Al_2O_3 . Scanning electron microscope investigations (Fig. 53; SEM 2815/10) show the initial growth of the botryoidal pitchblende in pores between the clay aggregates. In detail (Fig. 54,

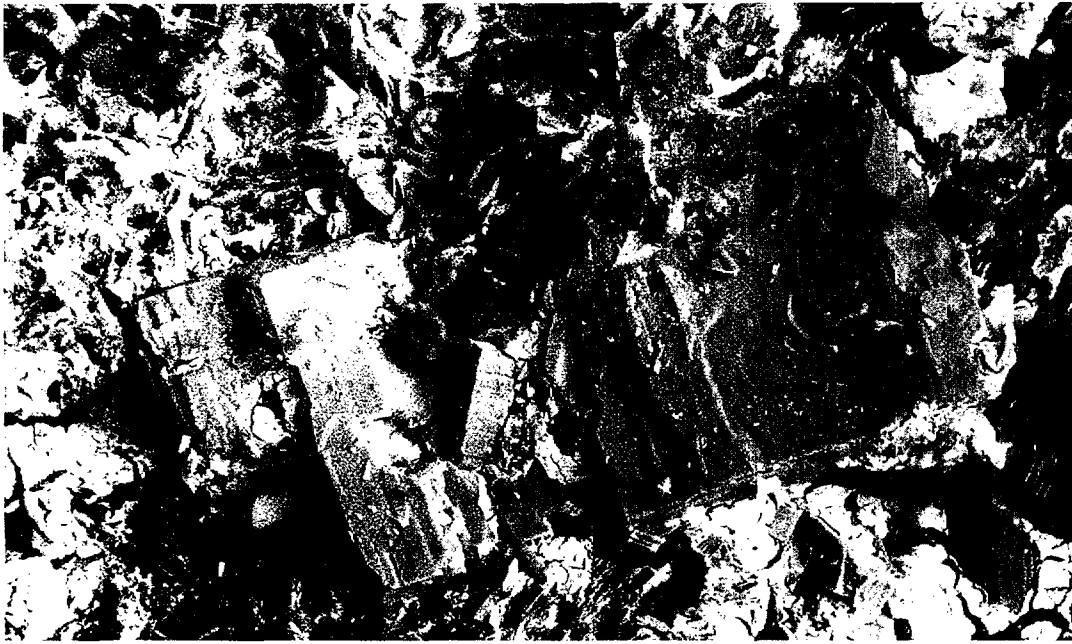


Figure 51. Back-scattered scanning electron micrograph of pyrite with pitchblende inclusions (SEM 2816/8); on the left side pitchblende is visible as bright inclusions. (Reduced leucocratic phonolite at 114 m from borehole F1).



Figure 52. Scanning electron micrograph (SEM 2814/4) of idiomorphic monazites on pyrite. (Reduced leucocratic phonolite at 111 m from borehole F1).

SEM 2816/4), cauliflower textures and zoning, indicative of successive growth stages, can be observed.

As discussed by Schorscher and Fallick (Appendix 1), two generations of pyrites can also be recognised. Pyrites with values for $\delta^{34}\text{S}$ around 0 are attributed to the hydrothermal event, whereas very low $\delta^{34}\text{S}$ values (-12 to -14‰) are attributed to supergene weathering combined with bacterial activity.

8.2. Geochemistry

In the preceding chapters, the geochemistry of the phonolites, nepheline syenites and breccias showed that, during hydrothermal alteration, a general uranium enrichment in the affected rocks took place, accompanied by enrichment in potassium, sulphur and, mainly in the breccias, zirconium and hafnium (Figs. 33 to 36). During supergene enrichment all the elements apart from sulphur were relatively immobile and mainly only the uranium was mobilised.

9. Redox fronts

The redox fronts exposed at the Osamu Utsumi mine have, from the beginning, been a source of interest. The fronts exhibit a very irregular surface (Fig. 55) due to variations in the rock physical properties and to downward extensions around water-conducting fractures. As most of these fractures are oblique, borehole F1 intersected such fingers of oxidised rock at 33.40 m and between 42.0 and 66.2 m. It is of importance to note that at 42.0 m the reduced rock is above and the oxidised rock below. This is essential for the interpretation of the geochemical and decay series results (see MacKenzie *et al.*, this report series; Rep. 6). Normally with oxidised rock overlying reduced rock, advective transport with downward-percolating groundwaters can be assumed. In the case of the reverse situation, however, only a diffusion mechanism could have taken place.

The three redox fronts (Plates 3-5) in drillcore F1 occur in subvolcanic phonolites. The front at 33.40 m intersects the core at a small angle; within the first 3 cm on the oxidised side some patches of reduced rock are left. In the oxidised part the “inverse” front at 42.0 m shows (on a millimetre scale) a type of oscillatory zoning of iron hydroxides. It also contains a 5 mm thick white zone (consisting of 80% kaolinite) separating the front from the reduced rock. Two to three centimetres into the reduced

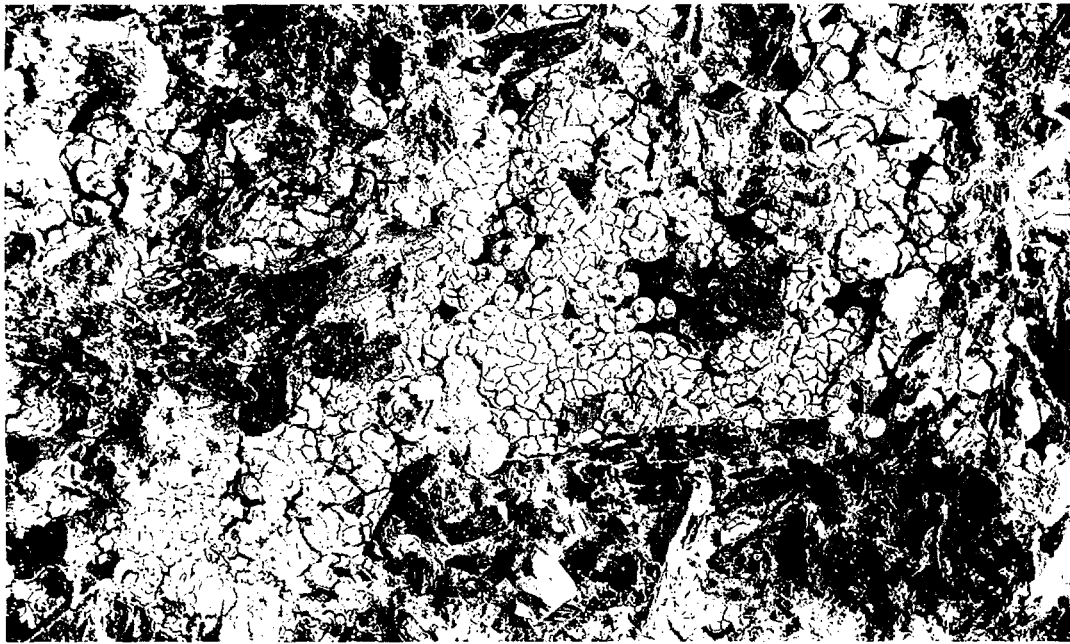


Figure 53. Back-scattered scanning electron micrograph (SEM 2815/10) of botroidal supergene pitchblende along a fissure in leucocratic phonolite (RFIII redox front).

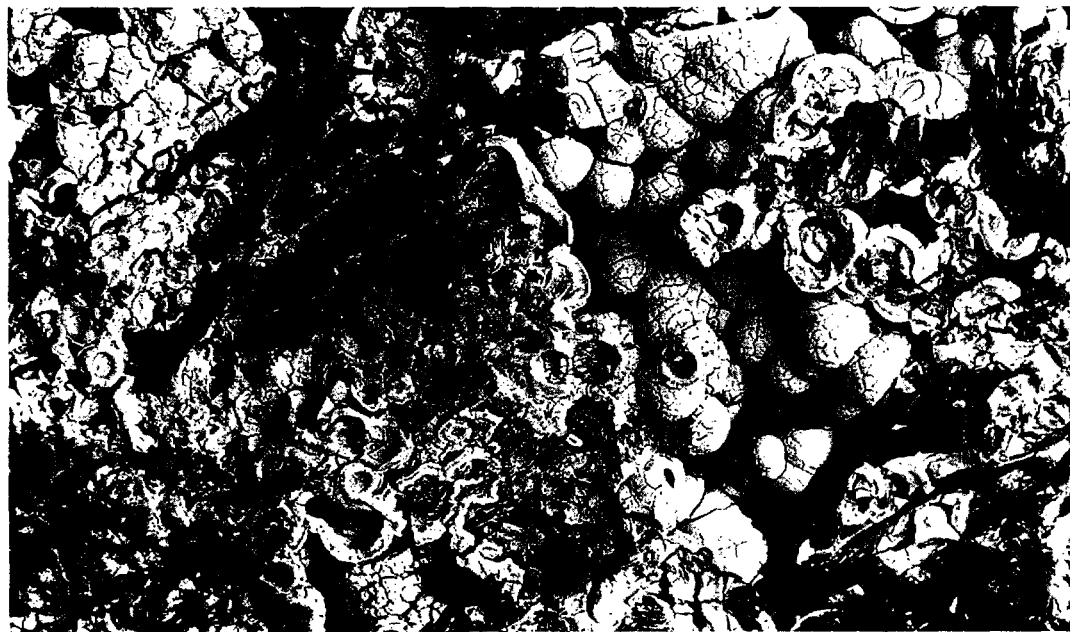


Figure 54. Back-scattered scanning electron micrograph (SEM 2816/4) of botroidal supergene pitchblende along a fissure in leucocratic phonolite (RFIII redox front; detail of Fig. 53).

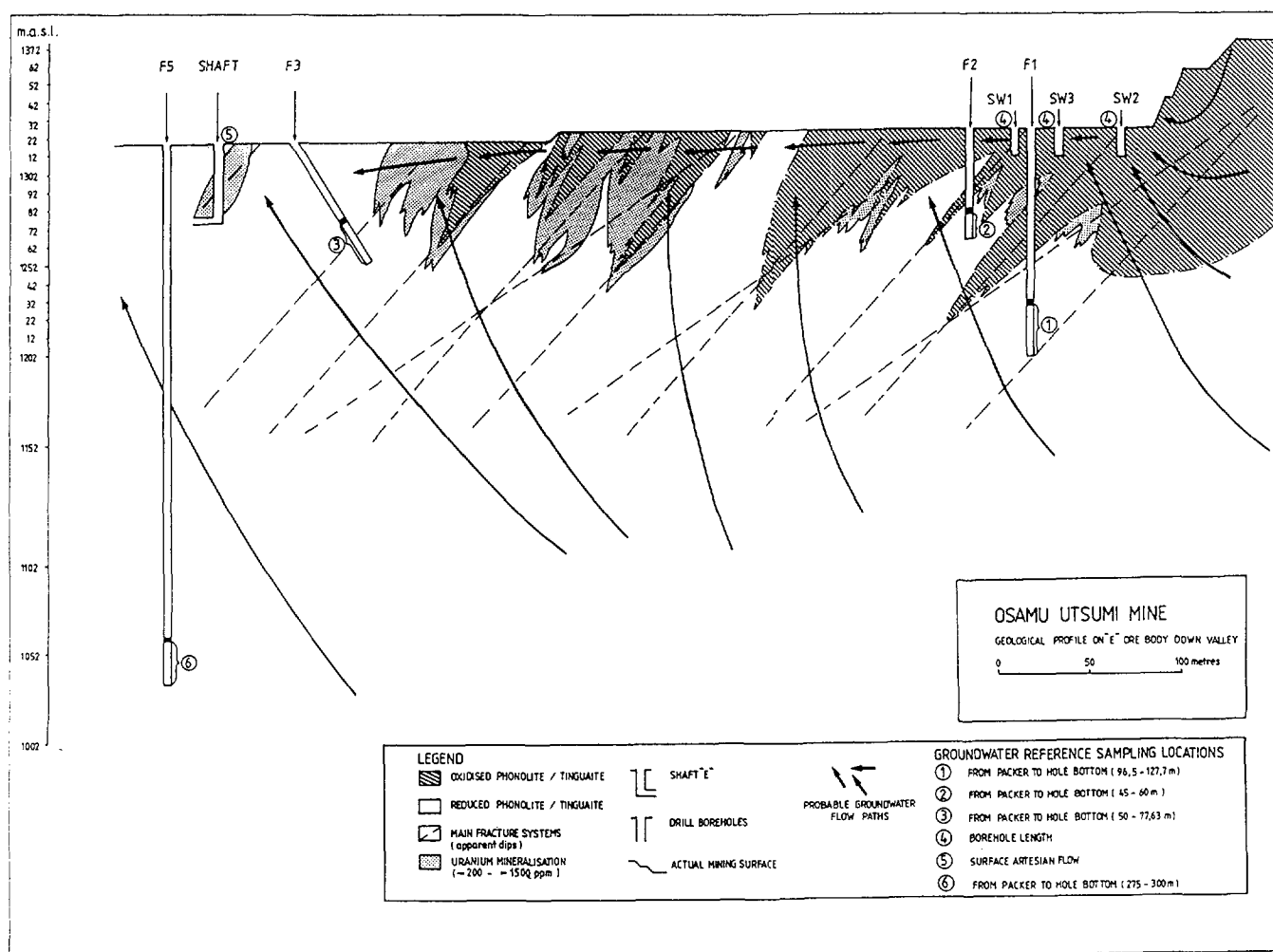


Figure 55. Cross-section along profile A-C of Figure 4 showing the relationships of the boreholes and groundwater sampling locations to the geology, geochemistry and hydrogeology of the site.

part a nodular pitchblende mineralisation occurs. The 66.20 m redox front has an irregular surface but a very sharp transition from oxidised to reduced rock occurs, transecting single mineral grains.

The RFI front (Plate 6) occurs in a dense mineralised phonolite. On the oxidised side it displays oscillatory zoning of iron hydroxides with white spots (1–2 cm) representing former pitchblende nodules. Pitchblende nodules occur either a few centimetres from the front or up to 10 cm within the reduced phonolite. The nodules are concentrated in transecting faults, which determines their often irregular shape.

The RFII front (Plate 7) occurs in a volcanic breccia body and transects the breccia components and matrix. Zoning of iron hydroxides is only observed in the oxidised part of the matrix.

The RFIII front (Plate 8) is situated in a dense phonolite associated with a fracture mineralisation. Iron hydroxides are concentrated as a band within the first few centimetres of the oxidised zone.

The RFIV front (Plate 9) occurs in a porous, slightly mineralised phonolite. It is characterised by a homogeneous dark-brown 20 cm wide zone rich in iron and manganese oxides.

Redox fronts RFI to IV were sampled on a decimetre scale, whereas the fronts from drillcore F1 were sampled with centimetre spacings, as illustrated in MacKenzie *et al.* (op. cit.; Figs. 7 and 58).

9.1. Mineralogy

Basically, the mineralogy at the redox fronts is identical to the mineralogies of the hydrothermally altered (“reduced”) and the oxidised phonolites, nepheline syenites and breccias described in the preceding chapters. Some specific mineralogical features can, however, be observed at the redox fronts:

- Primary pyrite disappears at the front within a fraction of a millimetre. Some dissolving pyrites occur as mantle relicts persisting up to a maximum of 3 cm in the oxidised rock.
- Fluorite disappears on the oxidised side within the first few millimetres.
- Sphalerite and other sulphides occur only on the reduced side.
- Carbonates abruptly disappear on the oxidised side.

- K-feldspar already starts to diminish 1/2 to 3 cm into the reduced zone (Table XIX). Using XRD this decrease is difficult to detect, but under the SEM etching phenomena (Fig. 56 SEM; 2815/7) can be observed on the surface of the K-feldspar.
- Secondary pitchblende nodules may be formed 1 to 3 cm into the reduced zone. The location of their occurrence is directly related to the commencement of K-feldspar dissolution.
- Secondary pyrite is formed at roughly the same locations as the pitchblende nodules.
- Macroscopically, iron hydroxides and hydrous ferric oxides delineate the oxidised part of the redox front. In the RFIV front in particular, the aging sequence can be observed: amorphous hydrous ferric oxides → poorly crystalline hydrous ferric oxides → goethite → hematite.
- The amount of illite slowly begins to decrease in the oxidised zone.
- There is a general slight decrease of kaolinite when compared to illite in the oxidised zone adjacent to the front. In some cases, however, kaolinite is concentrated at the front, where it can constitute up to 80% of the minerals.
- Crandallite group minerals can be observed as the main REE-bearers in the oxidised part.
- Jarosite and alunite type minerals are formed in the vicinity of the front.
- Sporadically, CdS (greenockite) is formed in the pitchblende nodules (see Appendix 6).

It is important to note that the macroscopically visible front, determined by the iron hydroxides, does not exactly coincide with other mineral fronts. This can be explained by the results of the geochemical modelling (P.C. Lichtner in McKinley (Ed.), this report series; Rep. 12).

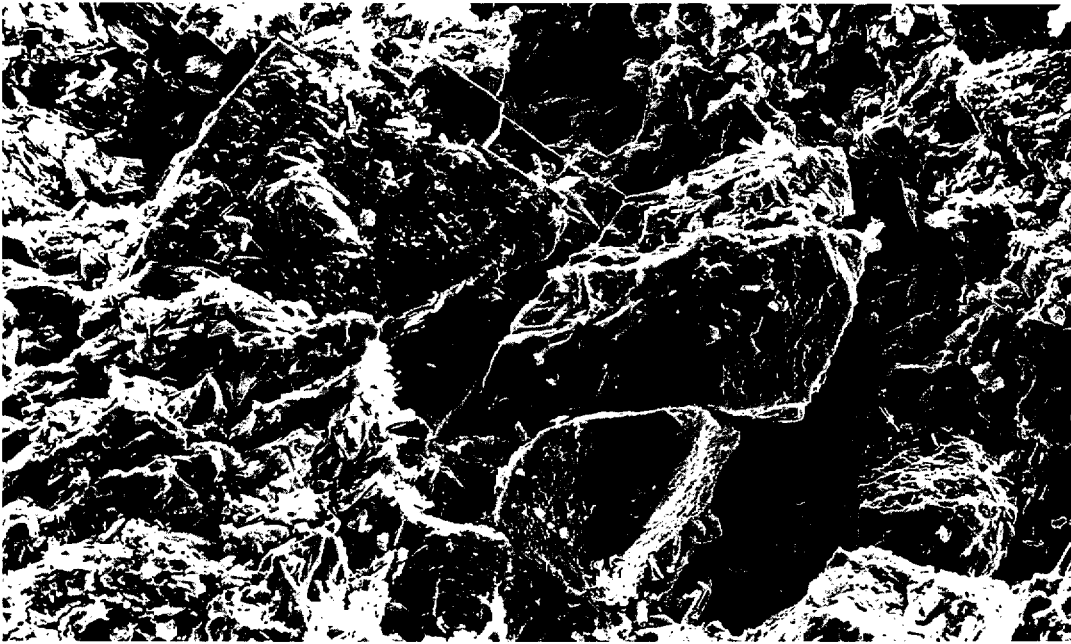


Figure 56. Scanning electron micrograph of K-feldspar showing etch phenomena. (Leucocratic phonolite, 2 mm on the reduced side of the redox front RFIII; SEM 2815/7).

TABLE XIX
Distribution of the modal abundance of K-feldspar across the redox fronts RFI, RFIII and RFIV determined by X-ray diffractometry (XRD).

Redox front RFI				Redox front RFIII			
	Rock type	Distance from the front (cm)	Alkali feldspar content (wt.%)		Rock type	Distance from the front (cm)	Alkali feldspar content (wt.%)
RFI-1A	ox. LPh	-20	52	RFIII-A	ox. LPh	-50	40
RFI-1B	ox. LPh	-10	48	RFIII-B	ox. LPh	-25	35
RFI-1C	ox. LPh	-5	46	RFIII-C ox.	ox. LPh	-5	52
RFI-3	red. LPh	5	52	RFIII-C red.	red. LPh	5	44
RFI-4B	red. LPh	20	52	RFIII-D	red. LPh	25	39
RFI-5A	red. LPh	75	54	RFIII-E	red. LPh	50	48
RFI-6B	red. LPh	195	56	RFIII-F	red. LPh	100	57
				RFIII-G	red. LPh	150	48

Redox front RFIV			
	Rock type	Distance from the front (cm)	Alkali feldspar content (wt.%)
RFIV-A	ox. CpxPh	-200	61
RFIV-B	ox. CpxPh	-150	66
RFIV-C	ox. CpxPh	-100	74
RFIV-D	ox. CpxPh	-50	64
RFIV-E	ox. CpxPh	-20	68
RFIV-F ox.	ox. CpxPh	-5	70
RFIV-F red.	red. CpxPh	5	77
RFIV-G	red. CpxPh	20	78
RFIV-H	red. CpxPh	50	80
RFIV-I	red. CpxPh	100	79
RFIV-K	red. CpxPh	150	71
RFIV-L	red. CpxPh	200	70

9.2. Autoradiography

For some of the fronts α -track autoradiography was carried out to illustrate the distribution of uranium and thorium.

- RFII: In the reduced part, the strongest uranium accumulations are found around breccia components and fissures transecting these components; in the matrix the mineralisation is dispersed. In the oxidised part, the uranium enrichment around the breccia components is diminished compared to the reduced side. Secondary enrichments tend to occur in association with clay and iron hydroxide aggregates, and in pores. At the front itself, there is only an enrichment in the porous nepheline syenite components, whereas the dense clay matrix is not enriched.
- RFIII: In the reduced part, the nodular secondary enrichment is concentrated in open pores and fissures overprinting the finely dispersed distribution of the hydrothermal enrichment. Moreover, enrichments can be observed at the intersections of cracks with xenoliths. On the oxidised side, a finely dispersed secondary accumulation of α -emitters occurs as impregnations associated with hydrous ferric oxides.
- RFIV: On the reduced side, uranium is concentrated in pores and along grain boundaries. In the oxidised part, which is adjacent to the front and strongly impregnated with hydrous ferric oxides, enrichments occur only in the rare pore spaces coated with hydrous ferric oxides (Fig. 57).

9.3. Porosity

The porosities of samples across the four redox fronts RFI to IV were determined on the basis of rock and grain densities and are presented in Table XX and Figure 58.

The oxidised parts have a much higher porosity than the reduced parts; only in front RFIV is the difference less pronounced as the porosity of the reduced rock was already initially high. The porosities vary around 18% in the oxidised samples and around 10% in the reduced varieties. This large difference implies an important dissolution and loss of bulk material at the site of the redox fronts. A more evident increase in porosity is also predicted from the redox front modelling carried out by P.C. Lichtner in McKinley (Ed.) (this report series; Rep. 12).

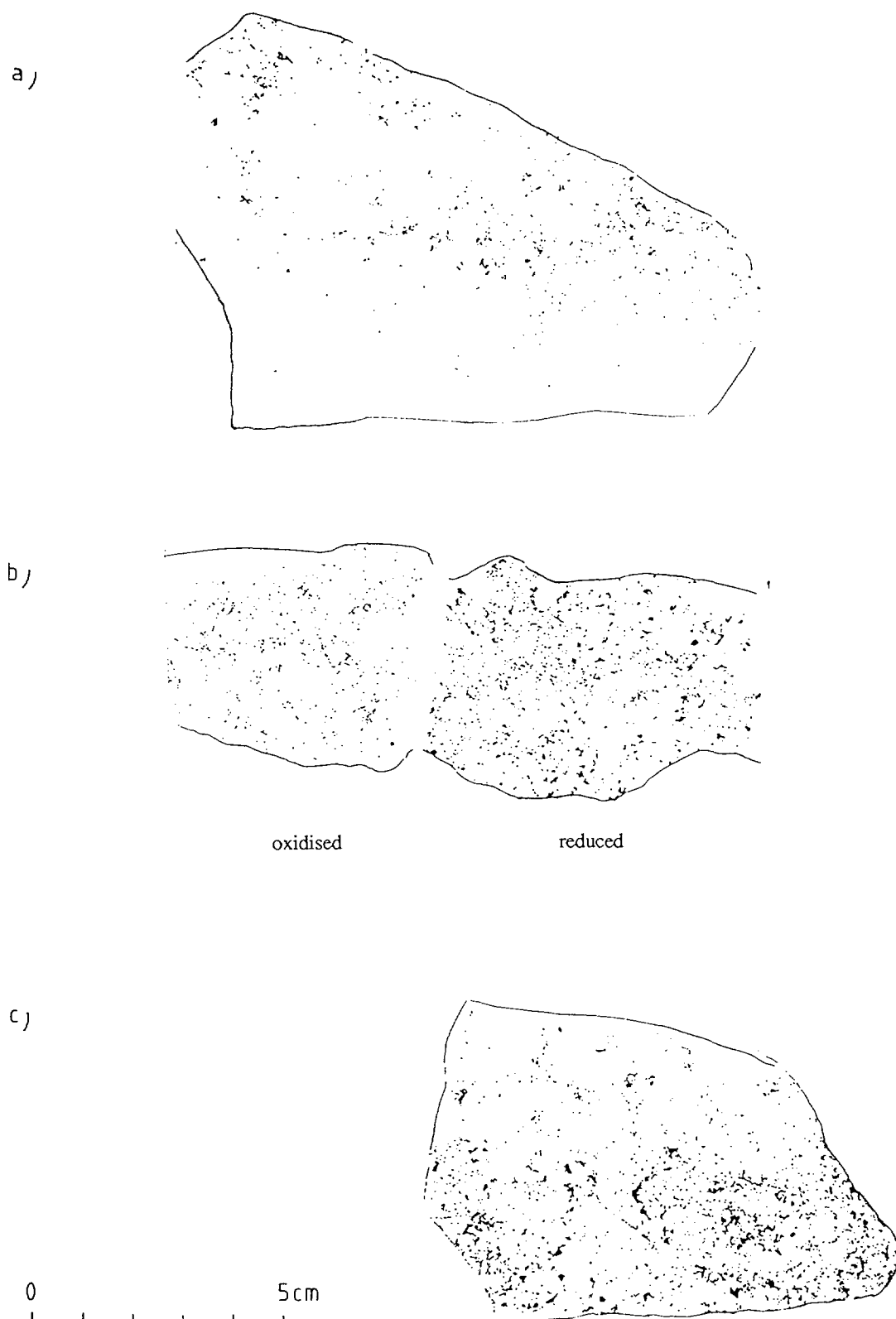


Figure 57. Autoradiographs from redox front RFIV.

a) Oxidised part 20 cm from the front.

b) Across the front, where the sample is broken apart.

c) Reduced sample, 20 cm from the front.

(Exposure time 8 weeks).

TABLE XX
Rock physical properties across redox fronts RFI to RFIV.

Redox front RFI					Redox front RFII				
	Rock type	Distance from the front (cm)	Bulk density (g/cc)	Total porosity (%)		Rock type	Distance from the front (cm)	Bulk density (g/cc)	Total porosity (%)
RFI-1A	ox. LPh	-20	2.17	17.1	RFII-A	ox. VBr	-200	2.29	12.8
RFI-1B	ox. LPh	-10	2.2	15.9	RFII-B	ox. VBr	-150	2.19	17.1
RFI-1C	ox. LPh	-5	2.18	17.8	RFII-C	ox. VBr	-100	2.2	16.3
RFI-3	red. LPh	5	2.17	17.8	RFII-D	ox. VBr	-50	2.23	15.4
RFI-4B	red. LPh	20	2.2	15.5	RFII-E	ox. VBr	-20	2.13	18.9
RFI-5A	red. LPh	75	2.35	9.4	RFII-F ox.	ox. VBr	-5	2.34	11.2
RFI-6B	red. LPh	195	2.33	10.6	RFII-F red.	red. VBr	5	2.17	18
					RFII-G	red. VBr	20	2.25	15
					RFII-H	red. VBr	50	2.32	12.3
					RFII-I	red. VBr	100	2.29	13.3
					RFII-K	red. VBr	150	2.36	10.4
					RFII-L	red. VBr	200	2.35	10.4
Redox front RFIII					Redox front RFIV				
	Rock type	Distance from the front (cm)	Bulk density (g/cc)	Total porosity (%)		Rock type	Distance from the front (cm)	Bulk density (g/cc)	Total porosity (%)
RFIII-A	ox. LPh	-50	2.38	13.2	RFIV-A	ox. CpxPh	-200	2.08	20.5
RFIII-B	ox. LPh	-25	2.23	13.3	RFIV-B	ox. CpxPh	-150	2.06	22.5
RFIII-C ox.	ox. LPh	-5	2.31	10.5	RFIV-C	ox. CpxPh	-100	2.08	19
RFIII-C red.	red. LPh	5	2.38	8.2	RFIV-D	ox. CpxPh	-50	2.14	17.4
RFIII-D	red. LPh	25	2.34	9.4	RFIV-E	ox. CpxPh	-20	2.11	18.7
RFIII-E	red. LPh	50	2.41	7.7	RFIV-F ox.	ox. CpxPh	-5	2.65	3.6
RFIII-F	red. LPh	100	2.42	6.8	RFIV-F red.	red. CpxPh	5	2.18	16.4
RFIII-G	red. LPh	150	2.39	7.7	RFIV-G	red. CpxPh	20	2.22	14.2
					RFIV-H	red. CpxPh	50	2.16	16.6
					RFIV-I	red. CpxPh	100	2.19	15.1
					RFIV-K	red. CpxPh	150	2.24	13.7
					RFIV-L	red. CpxPh	200	2.22	14.1

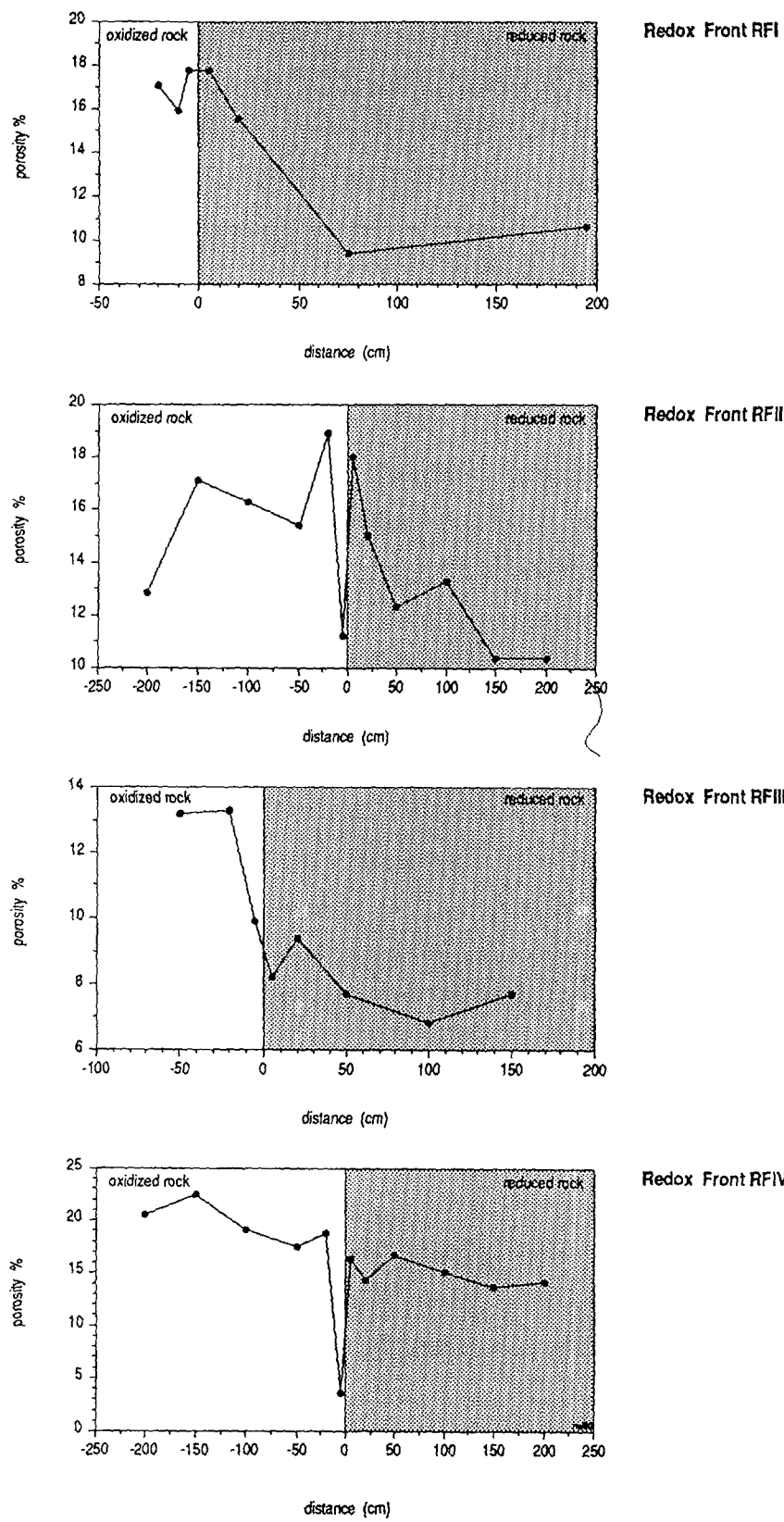


Figure 58. Variation of total porosity across the redox fronts. RFI from a mineralised dense phonolite; RFII from a breccia; RFIII from a dense leucocratic phonolite; RFIV from a porous cpx-bearing phonolite.

9.4. Geochemistry

Considerable analytical effort has been invested in the study of the redox fronts. Part of the analyses of drillcore F1 are presented in Appendix 4 and a detailed discussion of REEs and selected trace elements is given in the contribution by MacKenzie *et al.* (this report series; Rep. 6). The analyses of the four redox fronts RFI to IV are listed in Tables XXI – XXIV and are partly shown in Figures 59 – 62. The mineralogy and geochemistry of redox front RFI is detailed in Appendix 6.

The inhomogeneous distribution of the primary rock-forming minerals and their alteration products, together with the irregular hypogene and patch-like supergene mineralisations, complicate interpretation of the geochemical data. Comparison of oxidised and reduced rocks in Section 5.2. showed that the elements S, Zn, Fe, Ti, Mg and Ca are depleted, and Th, Pb, Ba and, in certain cases, also U are enriched in the oxidised bulk rocks. In the vicinity of the redox fronts, the relationships are less clear-cut and variable among the different fronts that have been studied.

Among the major elements, Fe_{tot} tends to be enriched in the immediate vicinity of the redox contact, as in the case of RFI, RFIII and RFIV; in RFIV, Fe-enrichment is accompanied by Mn. In RFs II, III and IV there is also a significant enrichment of P_2O_5 at the front, but it can also occur on the oxidised as well as the reduced side.

Uranium is normally enriched in the first 20 cm on the reduced side of the front, reflected by the occurrence and distribution of pitchblende (Fig. 53). The exceptional behaviour of U in RFII can be explained by the primary hydrothermal distribution in the breccia. Thorium is enriched in F1 on the reduced side of the fronts at 33.40 m, 42.0 m and 66.20 m, and also in the mineralised parts of RFI (compare Appendix 6). In the other fronts there is hardly any enrichment and, if there is, it can also occur on the oxidised side (Fig. 60).

Lead tends to be enriched on the reduced side if the mineralisation is strong; if not, some enrichment can also occur on the oxidised side (Fig. 61).

Molybdenum, which results in a bluish-green staining (ilsemanite) when mineralised rocks in the mine are exposed to the air, is depleted by a factor of two on the oxidised side of the front in RFI (Fig. 62). This behaviour contrasts with the results from drillcore F1 where the oxidised rocks and fronts are enriched in comparison to the reduced phonolites.

Cadmium data are only available for the RFI front where the oxidised rocks contain 3 to 4 ppm Cd and the reduced rocks 2 ppm Cd (Fig. 63). Only in the pitchblende nodule is an extremely high enrichment of 20 ppm Cd found.

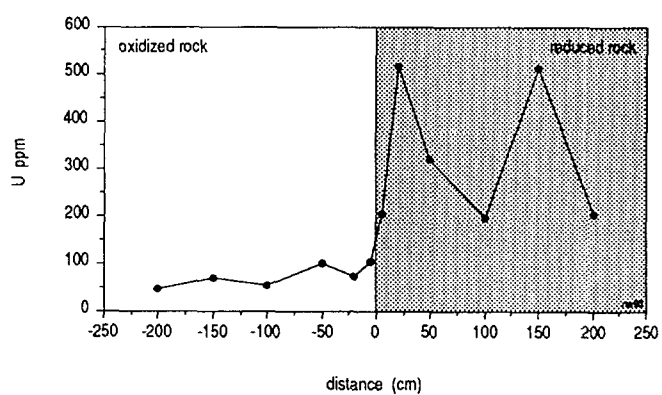
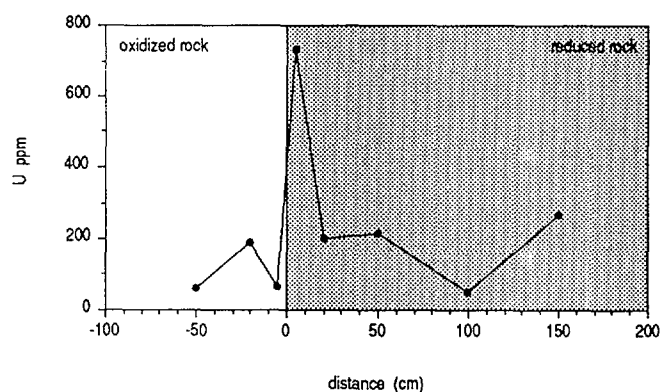
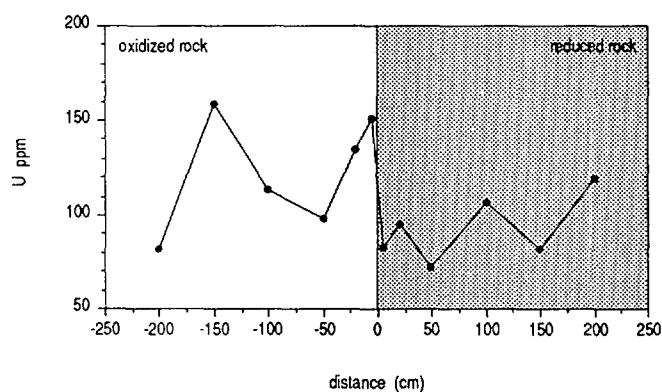
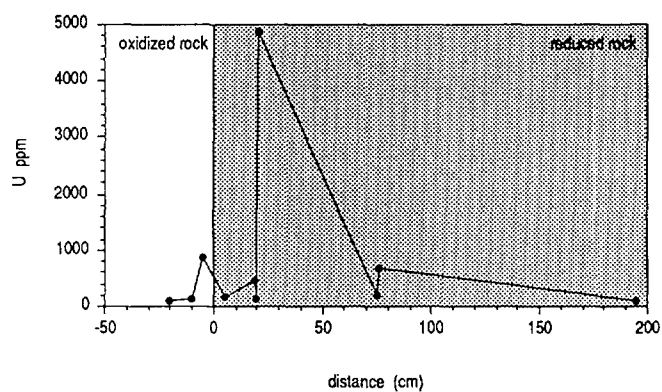


Figure 59. Distribution of uranium across the redox fronts (data by XRF). RFI in a mineralised dense phonolite; RFII in a breccia; RFIII in a dense leucocratic phonolite; RFIV in a porous cpx-bearing phonolite.

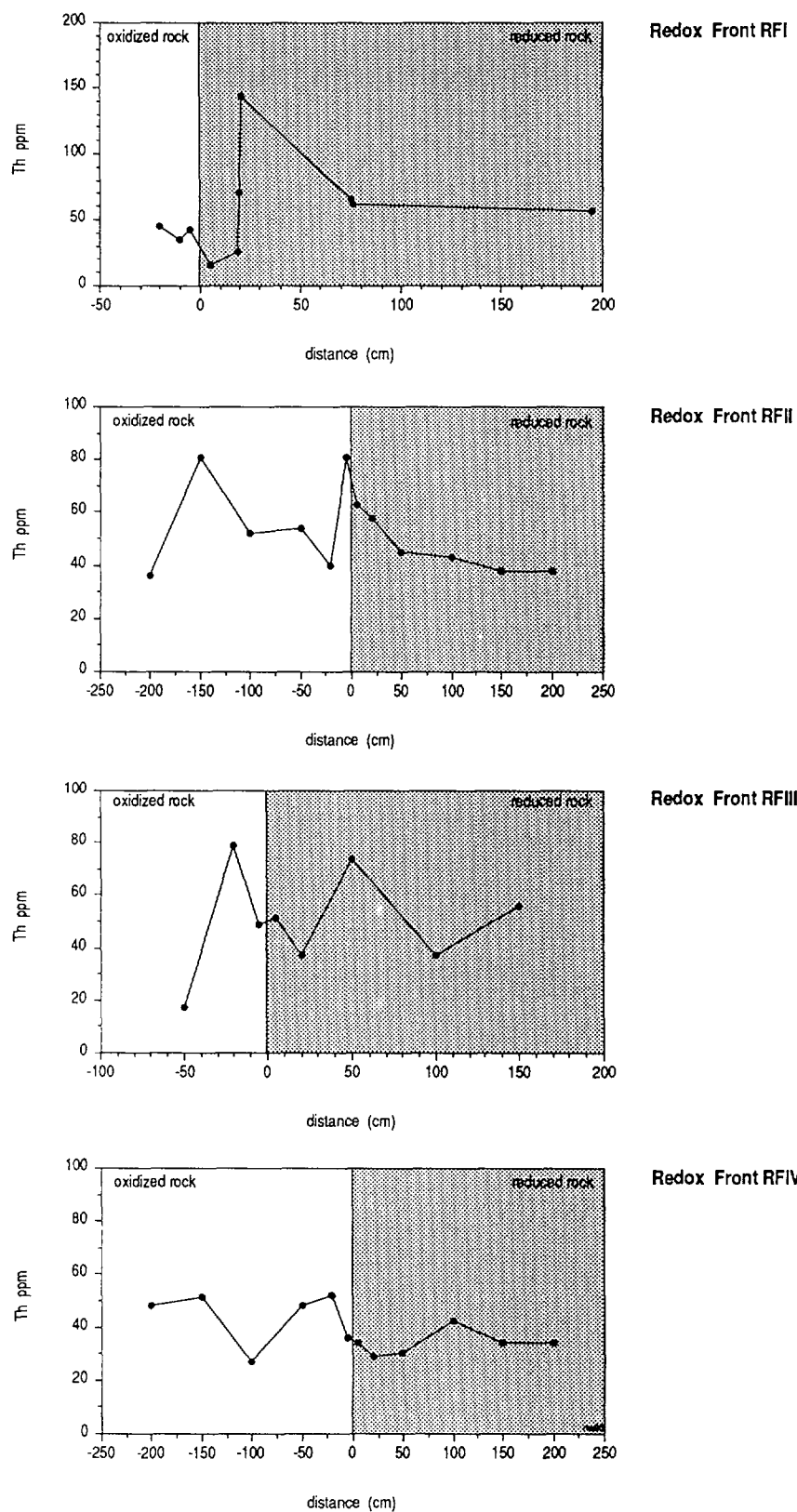


Figure 60. Distribution of thorium across the redox fronts (data by XRF). RFI in a mineralised dense phonolite; RFII in a breccia; RFIII in a dense leucocratic phonolite; RFIV in a porous cpx-bearing phonolite.

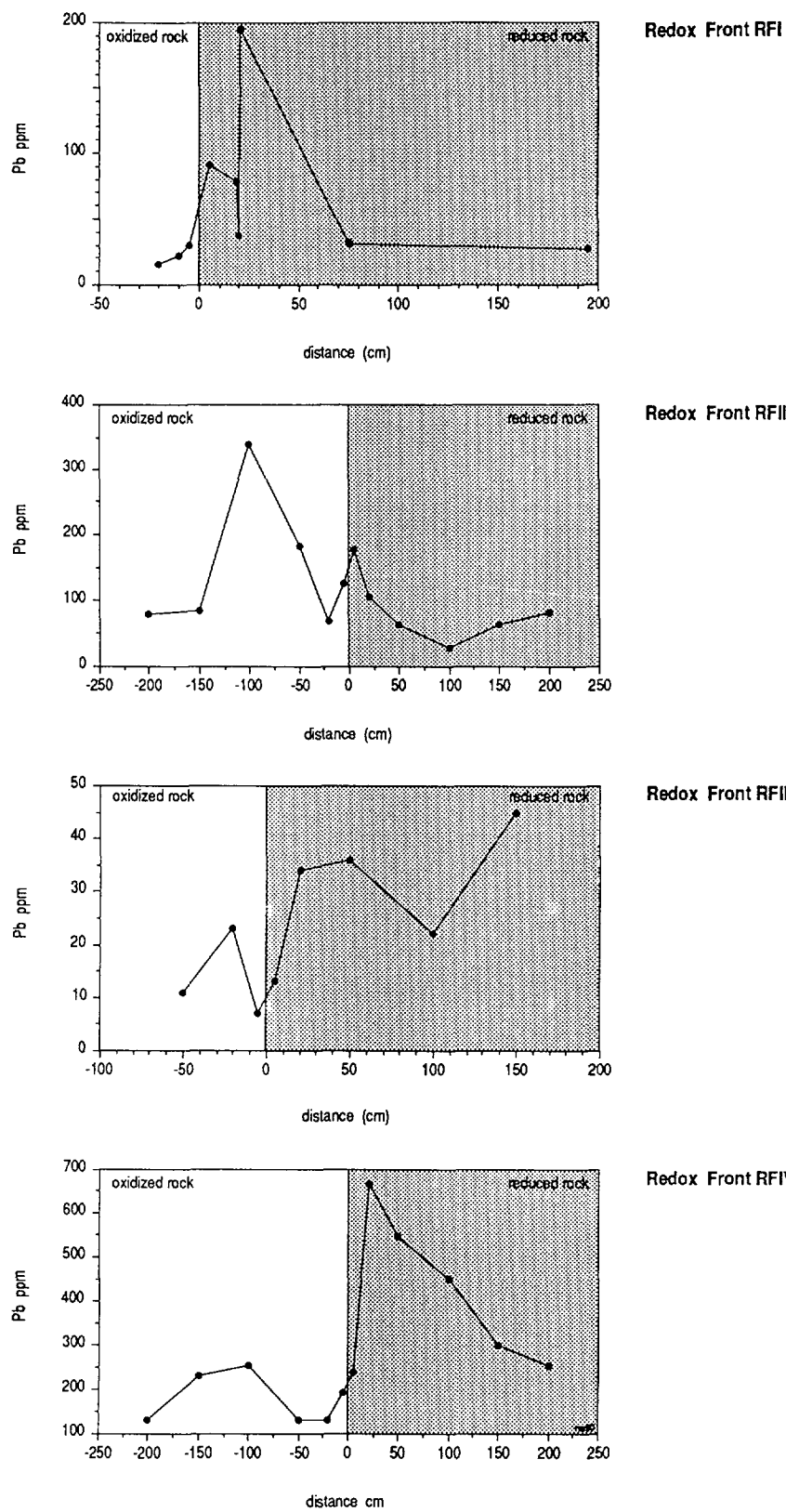


Figure 61. Distribution of Pb across the redox fronts (data by XRF). RFI in a mineralised dense phonolite; RFII in a breccia; RFIII in a dense leucocratic phonolite; RFIV in a porous cpx-bearing phonolite.

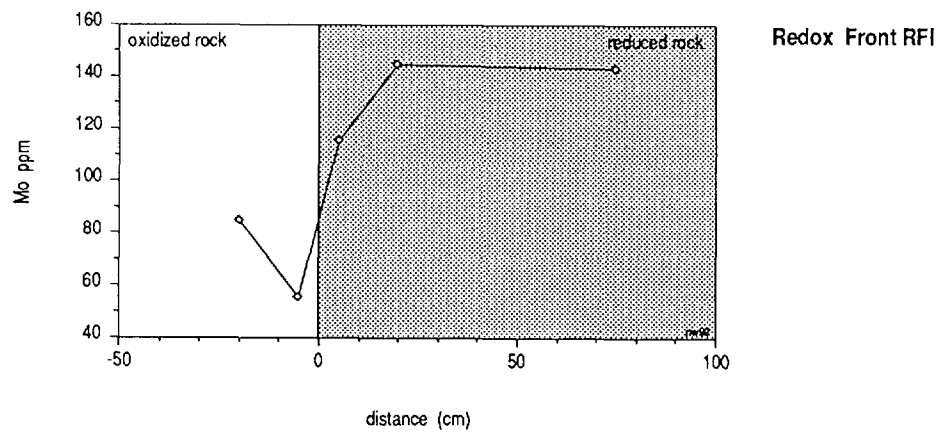


Figure 62. Distribution of Mo across redox front RFI; dense leucocratic phonolite.

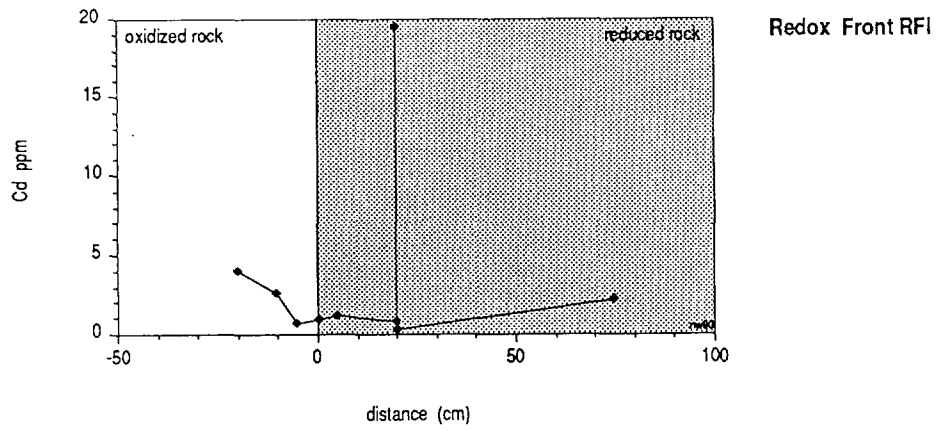


Figure 63. Distribution of Cd across redox front RFI; dense leucocratic phonolite.

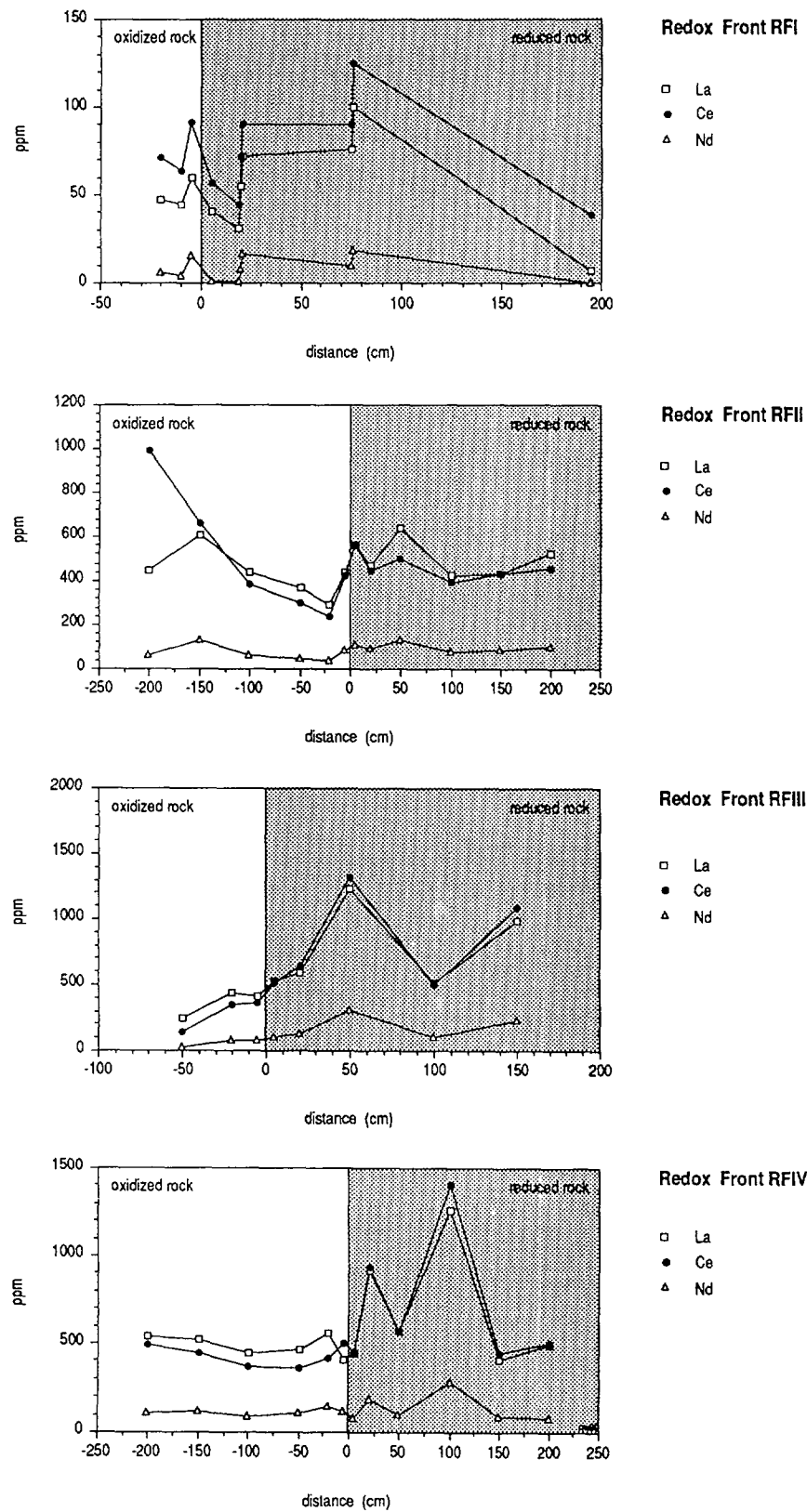


Figure 64. Distribution of LREEs across the redox fronts (data by XRF). RFI in a mineralised dense phonolite; RFII in a breccia; RFIII in a dense leucocratic phonolite; RFIV in a porous cpx-bearing phonolite.

TABLE XXI

Geochemical composition across redox front RFI (data by XRF; Mo and Cd by AAS).

Redox front RFI (leucocratic phonolite), ore body B

Sample		RFI-1A	RFI-1B	RFI-1C	RFI-3	RFI-4A-1	RFI-4A-2	RFI-4B	RFI-5A	RFI-5B	RFI-6B
Distance to front (cm)		-20	-10	-5	5	20	20	20	75	75	195
Rock type		LPh ox.	LPh ox.	LPh ox.	LPh red.	LPh red.	LPh red.	LPh red.	LPh red.	LPh red.	LPh red.
SiO ₂	wt. %	59.90	59.42	58.45	60.06	60.90	60.83	60.00	60.42	59.31	58.45
TiO ₂		0.46	0.53	0.46	0.49	0.45	0.41	0.43	0.41	0.42	0.57
Al ₂ O ₃		22.41	22.05	22.07	22.11	20.93	20.04	21.42	20.48	21.05	23.39
Fe ₂ O ₃		1.37	2.06	2.52	0.97	1.00	0.93	0.90	1.35	1.74	1.24
FeO		0.00	0.00	0.00	0.00	0.00	0.00	0.00	0.00	0.00	0.00
MnO		0.01	0.01	0.01	0.01	0.01	0.01	0.01	0.01	0.01	0.01
MgO		0.14	0.10	0.10	0.10	0.10	0.10	0.10	0.10	0.10	0.10
CaO		0.03	0.01	0.01	0.01	0.01	0.01	0.01	0.01	0.01	0.01
Na ₂ O		0.01	0.01	0.01	0.01	0.01	0.01	0.01	0.01	0.01	0.01
K ₂ O		14.23	14.18	14.04	14.36	14.48	14.51	14.06	14.11	13.87	13.26
P ₂ O ₅		0.10	0.09	0.09	0.09	0.08	0.14	0.09	0.14	0.13	0.07
LOI		2.29	2.35	2.80	2.32	2.35	2.82	2.65	3.35	3.68	3.50
CO ₂		n.a.	n.a.	n.a.	n.a.	n.a.	n.a.	n.a.	n.a.	n.a.	n.a.
Total	wt. %	100.95	100.81	100.56	100.53	100.32	99.81	99.68	100.39	100.33	100.61
Ba		327	285	235	225	198	483	114	292	293	523
Rb		284	283	287	282	273	253	320	258	254	273
Sr		554	436	448	454	445	869	488	834	743	345
Pb		16	22	30	91	78	37	195	32	31	27
Th		45	34	42	15	26	71	144	65	62	57
U		106	130	861	175	448	121	4876	204	660	84
Nb		262	299	266	290	282	251	361	270	241	295
La		47	44	60	40	31	55	72	76	100	7
Ce		71	63	91	57	44	72	90	90	125	38
Nd		b.d.	b.d.	15	b.d.	b.d.	b.d.	16	b.d.	18	b.d.
Y		40	37	34	56	55	132	59	159	105	89
Zr		82	97	86	99	114	459	153	678	326	545
V		357	342	307	293	170	91	175	115	197	322
Cr		5	8	8	b.d.	b.d.	b.d.	b.d.	5	5	10
Ni		6	6	9	6	6	17	9	20	17	16
Co		b.d.	b.d.	3	b.d.	b.d.	5	b.d.	6	12	3
Cu		b.d.	b.d.	b.d.	b.d.	b.d.	b.d.	b.d.	b.d.	b.d.	b.d.
Zn		46	56	93	139	177	353	158	354	392	38
Ga		57	55	54	50	32	17	34	23	33	59
Hf		b.d.	b.d.	3	b.d.	b.d.	11	4	15	7	15
S		1039	1534	27354	4536	9196	12956	10359	13162	15532	58618

XRF-data; n.a. = not analysed, b.d. = below detection.

TABLE XXI (contd).

Redox front RFI: Cd- and Mo-analyses

	Rock type	Distance	Cd	Mo
RFI-1A	ox. LPh	-20	4.00	85
RFI-1B	ox. LPh	-10	2.60	–
RFI-2B	ox. LPh	-10	0.66	55
RFI-2C	ox. LPh	-5	0.84	–
RFI-3B	red. LPh	5	1.10	115
RFI-4B	red. LPh	20	0.79	145
RFI-4B-1	red. LPh	20	19.50	–
RFI-4B-2	red. LPh	20	0.30	–
RFI-5B	red. LPh	75	2.20	143

Analyses by AAS.

TABLE XXII
Geochemical composition across redox front RFII (data by XRF).

Redox front RFII (volcanic breccia), ore body B

Sample		RFII-A	RFII-B	RFII-C	RFII-D	RFII-E	RFII-Fox	RFII-Fred	FII-G	RFII-H	RFII-I	RFII-K	RFII-L
Distance to front (cm)		-200	-150	-100	-50	-20	-5	5	20	50	100	150	200
Rock type		VBr	VBr	VBr	VBr	VBr	VBr	VBr	VBr	VBr	VBr	VBr	VBr
		ox.	ox.	ox.	ox.	ox.	ox.	red.	red.	red.	red.	red.	red.
SiO ₂	wt. %	54.17	53.71	54.91	54.55	52.97	54.35	54.94	55.35	55.31	56.23	55.36	56.15
TiO ₂		0.35	0.45	0.40	0.47	0.40	0.38	0.45	0.43	0.47	0.41	0.44	0.37
Al ₂ O ₃		24.13	23.49	22.56	24.24	24.88	22.73	23.39	22.82	22.09	22.43	22.30	21.40
Fe _{tot}		3.06	3.78	4.09	2.88	3.71	4.09	2.87	3.16	3.69	2.97	3.56	3.58
MnO		0.04	0.00	0.00	0.00	0.00	0.00	0.00	0.00	0.00	0.00	0.00	0.00
MgO		0.14	0.14	0.17	0.17	0.20	0.19	0.14	0.14	0.12	0.14	0.15	0.18
CaO		0.00	0.00	0.00	0.00	0.00	0.03	0.00	0.00	0.00	0.00	0.00	0.02
Na ₂ O		0.22	0.29	0.24	0.27	0.31	0.33	0.30	0.30	0.39	0.45	0.44	0.62
K ₂ O		13.03	12.81	13.07	13.15	12.66	13.05	13.20	13.40	13.43	13.52	13.33	13.49
P ₂ O ₅		0.16	0.23	0.16	0.18	0.13	0.17	0.18	0.14	0.12	0.13	0.13	0.16
H ₂ O		3.10	3.09	2.85	2.88	3.38	3.12	3.89	3.57	3.89	3.39	3.94	3.85
CO ₂		n.a.	n.a.	n.a.	n.a.	n.a.	n.a.	n.a.	n.a.	n.a.	n.a.	n.a.	n.a.
Total	wt. %	98.40	97.99	98.45	98.79	98.64	98.44	99.36	99.31	99.51	99.67	99.65	99.82
F	ppm	1843	1896	1713	1598	1752	1738	1676	1678	1579	1764	1704	1799
Ba		662	710	511	619	563	634	744	816	644	632	572	534
Rb		316	291	327	326	327	299	304	292	292	292	285	286
Sr		598	981	598	703	435	552	659	590	529	578	669	912
Pb		79	84	339	182	68	125	177	106	63	28	65	83
Th		36	81	52	54	40	81	63	58	45	43	38	38
U		82	159	113	98	135	151	83	95	72	107	82	119
Nb		188	234	215	229	251	223	212	244	211	190	211	188
La		450	609	435	366	293	435	565	469	640	421	431	526
Ce		992	658	382	301	239	426	562	446	501	392	427	457
Nd		59	128	65	50	42	88	111	89	128	75	88	102
Y		75	180	88	57	87	145	119	139	83	89	82	84
Zr		1031	2051	1267	751	1815	1615	1410	1812	1151	1121	1400	1585
V		183	270	205	192	195	171	247	236	215	229	213	166
Cr		b.d.	b.d.	b.d.	b.d.	b.d.	b.d.	b.d.	b.d.	b.d.	b.d.	b.d.	b.d.
Ni		b.d.	b.d.	b.d.	b.d.	b.d.	b.d.	b.d.	b.d.	b.d.	b.d.	b.d.	b.d.
Co		b.d.	b.d.	b.d.	b.d.	b.d.	b.d.	b.d.	b.d.	b.d.	b.d.	b.d.	b.d.
Cu		b.d.	b.d.	b.d.	b.d.	b.d.	b.d.	b.d.	b.d.	b.d.	b.d.	b.d.	b.d.
Zn		47	36	29	19	27	23	15	10	10	16	28	22
Hf		13	31	15	8	24	19	19	25	14	14	17	22
Sc		4	5	4	4	4	5	4	5	4	4	4	4
S		5829	6836	4959	4392	5818	51685	15301	16783	17362	14754	16511	18612

XRF-data; n.a. = not analysed, b.d. = below detection.

TABLE XXIII
Geochemical composition across redox front RFIII (data by XRF).

Redox front RFIII (leucocratic phonolite), ore body E									
Sample		RFIII-A	RFIII-B	RFIII-C ox.	RFIII-C red.	RFIII-D	RFIII-E	RFIII-F	RFIII-G
Distance to front (cm)		-50	-25	-5	5	25	50	100	150
Rock type		LPh ox.	LPh ox.	LPh ox.	LPh red.	LPh red.	LPh red.	LPh red.	LPh red.
SiO ₂	wt. %	57.11	57.55	57.35	57.46	57.14	56.53	57.34	57.55
TiO ₂		0.44	0.47	0.46	0.48	0.42	0.41	0.46	0.46
Al ₂ O ₃		23.81	22.23	23.82	23.53	23.34	21.89	22.35	23.44
Fe _{tot}		1.31	2.73	1.56	1.48	1.49	2.70	2.22	1.22
MnO		0.00	0.00	0.00	0.00	0.00	0.00	0.00	0.00
MgO		0.12	0.05	0.06	0.08	0.07	0.11	0.12	0.12
CaO		0.03	0.00	0.01	0.01	0.00	0.02	0.01	0.02
Na ₂ O		0.70	0.51	0.80	0.69	0.54	0.48	0.27	0.36
K ₂ O		12.72	13.01	12.56	12.87	13.30	13.52	13.86	13.56
P ₂ O ₅		0.08	0.18	0.08	0.10	0.09	0.16	0.08	0.08
LOI		3.55	2.95	3.04	2.81	2.72	3.20	2.84	2.57
CO ₂		0.00	0.00	0.00	0.00	0.00	0.00	0.00	0.00
Total	wt. %	99.87	99.68	99.74	99.51	99.11	99.02	99.55	99.38
F	ppm	1416	1599	1748	1615	1587	1905	1758	1936
Ba		715	1011	704	642	628	649	690	677
Rb		232	247	238	250	252	260	254	268
Sr		847	1087	925	1046	773	723	352	661
Pb		11	23	7	13	34	36	22	45
Th		17	79	49	51	37	74	37	56
U		62	190	68	732	199	217	52	266
Nb		235	308	234	263	225	210	243	249
La		239	430	405	525	592	1225	515	988
Ce		145	351	365	513	642	1326	505	1085
Nd		24	74	82	105	134	303	108	231
Y		68	154	75	74	85	197	103	108
Zr		876	1283	813	1030	1003	2537	1080	825
V		542	480	584	512	370	297	445	415
Cr		b.d.	b.d.	b.d.	b.d.	b.d.	b.d.	b.d.	b.d.
Ni		b.d.	b.d.	b.d.	b.d.	b.d.	b.d.	b.d.	b.d.
Co		b.d.	b.d.	b.d.	b.d.	b.d.	b.d.	b.d.	b.d.
Cu		b.d.	b.d.	b.d.	b.d.	b.d.	b.d.	b.d.	b.d.
Zn		34	65	41	125	250	270	249	161
Hf		9	15	9	14	13	36	12	11
Sc		6	11	5	6	6	10	7	7
S		1195	1111	1291	5246	5047	15432	14955	3354

XRF-data; n.a. = not analysed, b.d. = below detection.

TABLE XXIV
Geochemical composition across the redox front RFIV (data by XRF).

Redox front RFIV (cpx-bearing phonolite), ore body E

Sample		RFIV-A	RFIV-B	RFIV-C	RFIV-D	RFIV-E	RFIV-F ox.	RFIV-F red.	RFIV-G	RFIV-H	RFIV-I	RFIV-K	RFIV-L
Distance to front (cm)		-200	-150	-100	-50	-20	-5	5	20	50	100	150	200
Rock type		CpxPh ox.	CpxPh ox.	CpxPh ox.	CpxPh ox.	CpxPh ox.	CpxPh ox.	CpxPh ox.	CpxPh red.	CpxPh red.	CpxPh red.	CpxPh red.	CpxPh red.
SiO ₂	wt. %	56.29	57.56	58.39	57.32	57.31	46.30	56.92	55.18	57.14	57.27	57.09	57.49
TiO ₂		0.21	0.12	0.11	0.17	0.25	0.31	0.38	0.50	0.51	0.18	0.59	0.22
Al ₂ O ₃		21.57	22.32	21.36	22.17	21.16	17.83	21.37	21.81	21.74	2.68	21.68	21.05
Fe _{tot}		3.17	0.91	0.81	1.29	2.04	16.63	1.45	1.54	2.12	1.74	1.80	1.96
MnO		0.04	0.00	0.00	0.00	0.00	0.12	0.00	0.00	0.00	0.00	0.00	0.00
MgO		0.01	0.00	0.00	0.00	0.00	0.00	0.00	0.00	0.00	0.00	0.00	0.00
CaO		0.00	0.04	0.00	0.03	0.01	0.01	0.00	0.05	0.04	0.03	0.02	0.01
Na ₂ O		0.23	0.15	0.15	0.14	0.16	0.16	0.14	0.15	0.18	0.17	0.18	0.17
K ₂ O		13.91	13.93	14.93	13.49	14.12	11.17	14.45	13.66	13.91	14.31	14.39	14.33
P ₂ O ₅		0.14	0.17	0.12	0.16	0.15	0.38	0.14	0.41	0.23	0.24	0.14	0.16
H ₂ O		2.22	2.18	1.37	2.54	1.94	4.38	2.16	2.90	2.89	2.53	2.20	2.55
CO ₂		n.a.	n.a.	n.a.	n.a.	n.a.	n.a.	n.a.	n.a.	n.a.	n.a.	n.a.	n.a.
Total	wt. %	97.79	97.38	97.24	97.31	97.14	97.29	97.01	96.2	98.76	98.15	98.09	97.94
F	ppm	1515	1256	1216	1248	1372	1035	1255	2203	1584	2178	1276	1409
Ba		473	472	394	473	467	566	441	736	598	575	410	473
Rb		292	293	317	291	297	237	311	284	295	303	318	308
Sr		312	501	325	419	377	321	341	1095	653	626	269	345
Pb		130	230	253	132	131	191	240	664	546	449	300	255
Th		48	51	27	48	52	36	34	29	30	42	34	34
U		46	69	55	99	74	104	203	517	319	197	512	204
Nb		514	364	382	289	327	321	411	784	582	590	572	357
La		543	521	442	464	562	405	446	916	566	1263	404	494
Ce		491	438	361	359	413	498	450	928	566	1407	447	502
Nd		110	115	82	102	144	117	80	187	100	276	91	81
Y		107	121	92	162	143	101	100	180	127	137	140	96
Zr		1621	1969	1344	2267	1722	1053	1383	1027	1876	1273	1872	980
V		171	200	215	231	217	282	375	316	320	308	340	332
Cr		b.d.	b.d.	b.d.	b.d.	b.d.	15	b.d.	b.d.	b.d.	b.d.	b.d.	b.d.
Ni		b.d.	b.d.	b.d.	b.d.	b.d.	b.d.	b.d.	b.d.	b.d.	b.d.	b.d.	b.d.
Co		9	5	b.d.	4	5	21	3	4	4	3	5	4
Cu		b.d.	b.d.	b.d.	b.d.	b.d.	b.d.	b.d.	b.d.	b.d.	b.d.	b.d.	b.d.
Zn		58	20	16	23	34	419	10	113	157	188	108	38
Hf		15	20	11	21	16	7	11	11	18	12	17	6
Sc		5	6	5	6	6	3	5	6	6	6	6	5
S		b.d.	190	b.d.	112	709	6520	9293	25045	14239	15811	11327	14987

XRF-data; n.a. = not analysed, b.d. = below detection.

Barium is enriched on the reduced side of the front in RFII and RFIV, whereas in RFIII it is enriched on the oxidised side.

Across redox fronts RFI to RFIV, the LREEs are generally slightly enriched in the reduced rock, displaying an oscillating distribution pattern, although the (primary) hydrothermal distribution displays a large scatter (Fig. 64). MacKenzie *et al.* (this report series; Rep. 7) observed a depletion of REEs in the oxidised rock of drillcore F1, where the degree of depletion decreased along the series. This observation was confirmed by additional data for F1; in the reversed redox front at 42.0 m the normal predominance of LREEs over HREEs for the rocks of the Poços plateau is inverted. The La/Lu_{cn} ratios on the reduced side change from 30 – 50 to 10 – 15 further into the reduced rock. Most other fluctuations of REE abundances in drillcore F1, and along the profiles across the redox front, are thought to be related to primary enrichments of REE-bearing minerals. The preferential loss or gain as in the case of Ce in section 42.0 – 66.2 m of drillcore F1 (Fig. 60 in MacKenzie *et al.*, op. cit.) might therefore be related to the formation of secondary minerals such as florencite, which can enter the Ce lattice. No mineral containing tetravalent Ce could be detected, which contrasts with reports from the Morro do Ferro Th-REE deposit (see Waber, this report series; Rep. 3).

The geochemistry around the redox fronts can only be explained if the fronts are regarded as geologically short-lived transitional phenomena. Under certain conditions, elements released during decomposition of the mineral phases are incorporated in other mineral lattices and strongly immobilised; for example Al or Si in kaolinite. Others are sorbed on incomplete phases and are released during aging, for example uranium associated with amorphous hydrous ferric oxides. Most of these observations indicate that the redox fronts retard the mobility of many of the elements either by sorption or by incorporation into new recrystallised mineral phases.

10. Discussion

The Poços de Caldas Alkaline Complex comprises a suite of alkaline volcanic and plutonic rocks (mainly phonolites and nepheline syenites) with normal background amounts of U, Th and REEs. Magmatic evolution included deuteric processes, indicating a volatile-rich parent magma. Pneumatolytic and auto-hydrothermal processes initially resulted in partial alkali exchange in alkali feldspar, rare metal silicate and fluorite formation to hematite pigmentation, and incipient kaolinisation and zeolitisation. Geochemically, the resulting rocks are enriched in potassium when compared to global

nepheline syenites and phonolites. Mobilisation and concentration of U, Th and REEs could not be detected at this stage (Shorscher and Shea, this report series; Rep. 1). Subsequent intense hydrothermal alteration and mineralisation, partly associated with contemporaneous formation of magmatic breccias, occurred locally, as exemplified in the Osamu Utsumi uranium mine.

Comparing the results reported by Schorscher and Shea (op. cit.) with those from the Osamu Utsumi mine, it becomes evident that the rocks in the mine were affected by an additional subvolcanic event. This event resulted in pervasive hydrothermal alteration of the mine rocks and the formation of several breccia pipes. Evidence from xenoliths contained in these breccias indicates that the brecciation took place after the sequence of volcanic and subvolcanic phonolites (with intrusions of nepheline syenites) had been emplaced and deuterically altered, similarly to the bulk of the rocks in the plateau. The clay mineral parageneses (kaolinite) of these rocks show that they were substantially cooled down.

Investigations at the mine were expected to give a clearer picture of the hydrothermal processes that resulted in the primary uranium and REE mineralisation, and to provide some insight into the mobility of uranium and REEs under hydrothermal conditions. Furthermore, after magmato-hydrothermal activity ceased, downward-migrating oxidising groundwaters produced a thick lateritic weathering cover and well-defined redox fronts, leading to the redistribution of the hydrothermal mineralisation which provided the opportunity to study the behaviour of U and REEs under low-temperature conditions.

10.1. Hypergene alteration

The hydrothermal alteration at the Osamu Utsumi uranium mine can be divided into two successive major processes. First, a potassium-rich hydrothermal event led to a pervasive potassium metasomatism with associated disseminated pyrite and minor low-grade uranium-, fluorite- and REE-mineralisation and argillic alteration of the country rocks. The major characteristics of this event are the almost complete alkali-exchange and structural reorganisation of the magmatic alkali feldspar, leaving an intermediate microcline of almost pure orthoclase composition behind, and the complete decomposition of magmatic mafic minerals and their replacement by clay minerals and Fe-Ti-oxides. The strong hematite pigmentation observed in these microcline phases suggests a comparably high oxygen fugacity at the very beginning of

this event. Hematite pigmentation is also observed in the unaltered regional country rocks where it is assigned to the oxidising deuteric alteration (Schorscher and Shea, op. cit.). Thus, the stronger hematite pigmentation in the hydrothermally altered host rocks might be explained by a local increase in heat flow due to the upward-migrating hydrothermal fluids.

The initial hydrothermal fluid was reducing, with increasing sulphur activity during its evolution leading to the widespread precipitation of pyrite. The sulphur isotope signatures of the disseminated pyrite clearly indicate a magmatic origin for the fluid. Well-crystallised illite in the centre of the pseudomorphically replaced nepheline occurs in the hydrothermally altered rocks as well as in the virtually unaffected country rocks represented by the mine walls. These country rocks, in contrast, suffered only a weak alkali-exchange in the feldspar. The formation of such illite thus occurred under a moderate K^+ -activity and indicates a temperature estimate of around 350°C.

Further on in the hydrothermal evolution of the mine, the K^+ -activity increased. At this juncture, the main alkali-exchange in the feldspars and overall argillic alteration took place, together with the pervasive disseminated pyrite mineralisation with subordinate fluorite, pitchblende and most probably monazite. The oldest generation of fluid inclusions in fluorite indicate a KCl-H₂O-type fluid with 7 wt.% of KCl and a homogenisation temperature of about 260°C for this period. The same temperature is recorded for the bulk of clay minerals (illite) based on their stable isotope composition (Waber, 1990). The $\delta^{18}O$ - and δD -signatures of the clay minerals further indicate a mixing of the magmatic-derived fluid ($\delta^{34}S$ pyrite) with meteoric water. This mixing might be responsible for the lower temperatures found in the subsequent generation of fluid inclusions in the fluorites (200–220°C). This marked the final stage of the potassium-rich hydrothermal event, which resulted in the host rock chemistry observed today (“potassic” rocks).

Subsequent hydrothermal activity occurred associated with the phreatomagmatic eruption of phonolitic magma and resulted in the formation of several small breccia pipes. Altered and pyrite-impregnated phonolite and nepheline syenite xenoliths clearly reveal that these breccias were formed after the pervasive potassic alteration.

The occurrence of magmatic flow textures in the phonolitic matrices of the breccia pipes suggest a high temperature (approx. 500–600°C) during the initial stages of the mineralising hydrothermal event. Boiling of the fluid is evidenced by fluid inclusions from breccia veins, which indicate a fluid composition approximating to a KCl-NaCl-brine with 44 equivalent wt.% KCl and traces of FeSO₄ and KF. This brine is exclusively localised

in the breccias and mineralised veins and has mobilised appreciable amounts of U, Th, Zr, Hf, Y, and occasionally REEs, and resulted in the precipitation of low microcline.

The hydrothermal alteration caused by the breccias is much more restricted in extent and is mainly associated with the breccia matrix and veins. The main breccia pipes display a diameter of several decimetres, whereas the potassic alteration affected an area of at least 2 km². Major mineral assemblages of such veins are pyrite-fluorite-carbonate, pyrite- pitchblende, pyrite-Mo minerals, zircon-fluorite-monazite-brannerite and low microcline, all of them associated with clay minerals. The feeding of the system with magmatic-derived fluid ceased after the main formation of pyrite and the influence of meteoric water increased.

In comparison with the unaltered regional rocks, the hydrothermally altered phonolites and nepheline syenites are enriched in K, Rb, S, U, Th, Pb and Ba, and the matrices of the breccias and the breccia-related vein mineralisation are intensively enriched in U, Th, Pb, Zr, Hf, F, Y, S and REEs and enriched in K, Rb, and Ba. The agreement in the chondrite normalised patterns of the incompatible elements between the hydrothermally altered rocks of the mine and the non-hydrothermally altered rocks of the Poços de Caldas plateau indicates that two sources for the elemental content in the hydrothermal fluids have to be taken into account: a) uptake through leaching of phonolites and nepheline syenites in deeper parts of the plateau, and b) a late-stage differentiate from the same magma source that produced the huge volume of regional alkaline rocks comprising the Poços de Caldas plateau. This second source is strongly favoured by the fact that the chondrite normalised patterns of incompatible elements from the highly mineralised breccias resemble the pattern of “late-stage” ultramafic lamprophyric dykes. The only exceptions are the increased Zr and Hf contents of the breccias. Furthermore, the breccia pipes display an explosive formation which certainly involved a rapid rise from their source up through the overburden. Therefore, the possibility of strong, long-term leaching processes occurring in the lower levels is less credible.

The intrusion of ultramafic lamprophyre dykes post-dates the hydrothermal alteration in the Osamu Utsumi mine and the radiometric Ar-Ar age of 76 Ma for phlogopites from one of these dykes (Shea, this report series; Rep. 4) indicates the onset of meteoric weathering in the area. The primitive composition of the dykes is indicative of a mantle origin. Both dyke suites display, in certain aspects, lamproite to kimberlite affinities, properties that can only be confirmed or rejected by detailed isotopic investigations. The two suites are very dissimilar in some respects and similar in others. Thus, the “phlogopite-bearing” ultramafic lamprophyres show more affinity to primitive silicate

rocks, whereas the “carbonate-apatite” ultramafic lamprophyres display a greater affinity to carbonatites, both having incorporated the same xenoliths (of primitive mantle compositions) during their generation. Taken together with the fact that they only occur within a few metres in the same tectonic environment, this strongly suggests a similar source. As discussed by Waber (this report series; Rep. 3), the occurrence of a carbonatitic melt can no longer be excluded when discussing the genesis of the Poços de Caldas alkaline complex.

10.2. Supergene alteration

The Osamu Utsumi mine has also provided the opportunity to study the supergene processes under which uranium was mobilised and redeposited at the redox fronts, as well as the formation of the lateritic weathering cover. Although today’s groundwater movement in the mine is largely upwards, this is mostly a consequence of mining excavation since the early seventies; on a geological timescale, the weathering front has moved downwards at a rate comparable to erosion (0.02 – 0.1 mm/a). Only the uppermost 20 to 40 m of the weathering zone consists of lateritic soil, followed by 15 to 50 m of saprolite and, finally, an oxidised zone of 20 to 60 m.

The thickness of the different weathering zones is strongly dependent on the texture, permeability, porosity and intensity of argillic alteration of the underlying parent rock. In these zones there is a considerable amount of hydrothermal clay minerals inherited from the parent rocks, as evidenced by the stable isotope signatures of the clays. These clays are less sensitive to Eh-pH-related dissolution than the predominant leucocratic minerals (mainly feldspars) and mafic minerals (mainly clinopyroxenes) comprising the unaltered rocks of the plateau. In addition, these clays are coated with minerals formed during weathering which effectively shield them from further contact with water. The evolution of a true laterite profile, as observed for unaltered rocks of the Poços de Caldas plateau, is thus retarded here and the formation of bauxite inhibited. Therefore, the lateritic cover produced on top of the Osamu Utsumi mine parent rock must be classified as mineralogically immature.

Within the oxidised zone, the uranium concentration only reaches 20 ppm U in the uppermost 10 to 40 m, which is half the concentration of the hydrothermally affected reduced phonolites. The bottom 10 to 20 m of the oxidised zone is enriched to a mean content of 55 ppm U. This implies that the partial remobilisation of the uranium that was precipitated on the reduced side of the redox front is much slower than at the front

itself, where pitchblende nodules do not survive the passing of the redox front. This retardation is caused by the incorporation of uranium in minerals such as brannerite, and/or by adsorption of uranium on amorphous and poorly crystalline phases, mainly iron-oxyhydroxides. Dehydration of such phases during dry seasons and rehydration during wet seasons have led to an alternating release and readsorption of uranium within the weathering column. The fact that uranium does not strongly correlate with iron and titanium (the major residual uranium-bearing phases are Ti-oxides) in the weathering zone shows that uranium is also adsorbed onto other amorphous and poorly crystalline phases (e.g. Al-gel and amorphous gibbsite) and clay mineral surfaces.

The dissolution of the pitchblende nodules on the oxidised side and their precipitation on the reduced side are a function of Eh-charge related to pyrite oxidation. The accompanying Eh-charge relates the pyrite transformation to the silicate transformations such as potash feldspar dissolution and the formation of kaolinite. The presence of relatively small amounts of pyrite (2-3%) strongly influences the mobility of uranium and other elements during supergene weathering. It exerts an influence not only on Eh-sensitive reactions, but also on those that are pH-dependent.

It is not only redox-sensitive elements that are remobilised and concentrated around these downward- migrating front systems. Work reported by MacKenzie *et al.* (this report series; Rep. 7) shows enhancement of a whole series of trace elements in and around the fronts, these having been effectively scavenged and concentrated from the parent rock during front migration.

11. Acknowledgements

This study would not have been possible without the field support from, and helpful discussions with the Osamu Utsumi mine geologists Luiz Barroso Magno Jr., Helio Antonio Scalvi and Marcus. For one of the authors (N.W.), the hospitality of many Brazilian friends is greatly appreciated, especially Ruy Frayha for providing logistic support throughout the project and making working in Poços de Caldas a pleasure.

Considerable thanks are due to Dagmar Riesen for careful geochemical sample preparation, Heidi Haas for porosity measurements and Jürg Megert for preparing excellent thin and polished sections at the University of Bern. Karl Ramseyer and Alfred Zweili (University of Bern) are acknowledged for support in the cathodoluminescence and SEM analytical work. Further thanks go to Johnny M. Bucher and Ivan Mercolli (University of Bern) for support in the microprobe analytical work and geochemical data

handling, to Michael Hügi (University of Bern) and Joseph Mullis (University of Basel) for help with the fluid inclusion studies, and Beda Hofmann (Natural History Museum, Bern) for discussions on ore petrography.

The authors are grateful to Peter Lichtner (University of Bern), Kirk Nordstrom (USGS), Mike Shea (University of Chicago), Gus MacKenzie and Roger Scott (SURRC, East Kilbride) for close collaboration and stimulating discussions, and to Horst-Peter and Mabel Ulbrich (University of São Paulo) for helpful advice and support.

Considerable thanks are due to Lina Bobade for typing the various versions of the manuscript and to the Poços de Caldas Technical Committee, particularly John Smellie, for reviewing and improving the manuscript.

12. References

- Almeida, E.B. de, 1977. Geology of the bauxite deposits of the Poços de Caldas District, State of Minas Gerais, Brazil. *PhD-Thesis*, Stanford University, CA, USA.
- Almeida Filho, R. and Paradella, W.R., 1977. Estudo do maciço alcalino de Poços de Caldas através de imagens Landsat com ênfase em mineralizações radioativas. São José dos Campos, *INPE* (11/2 – TPT/065).
- Azevedo, A. de, 1975. Geografia do Brasil. *Cia Editoria Nacional*, São Paulo, 325 pp.
- Bachinski, S.W. and Simpson, E.L., 1984. Ti-phlogopites of the Shaw's Cove minette: a comparison with micas of the other lamprophyres, potassic rocks, kimberlites, and mantle xenoliths. *Am. Min.*, 69, 41-56.
- Bailey, D.K., 1966. Carbonatite volcanoes and shallow intrusions in Zambia. In: O.F. Tuttle and J. Gittins (Editors), *Carbonatites*. Wiley, New York, 127-154.
- Beaufort, D. and Meunier, A., 1983. A petrographic study of phyllic alteration superimposed on potassic alteration: the Sibert porphyry deposit (Rhône, France). *Econ. Geol.* 78, 1514-1527.
- Bergman, S.C., 1987. Lamproites and other potassium-rich igneous rocks: a review of their occurrence, mineralogy and geochemistry. In: J.G. Fitton and B.G.J. Upton (Editors), *Alkaline Igneous Rocks*, *Geol. Soc. Spec. Publ.*, 30, 103-190.
- Boettcher, A.L. and O'Neil, J.R., 1980. Stable isotope, chemical, and petrographic studies of high-pressure amphiboles and micas: evidence for metasomatism in the mantle source regions of alkali basalts and kimberlites. *Am. J. Sci.*, 280-A; 594-621.

- Brown, P.E., 1964. The Songwe scarp carbonatite and associated feldspathization in the Mbeya Range, Tanganyika. *Q.J. Geol. Soc.*, 120, 223-240.
- Davies, G.R. and Lloyd, F.E., 1988. Pb-Sr-Nd isotope and trace element data bearing on the origin of the potassic subcontinental lithosphere beneath south west Uganda. In: Proc. 4th Int. Kimberlite Conf., Perth, Western Australia, *Blackwell Scientific Publ.*, Oxford.
- Dawson, J.B., 1987. The kimberlite clan: relationship with olivine and leucite lamproites, and interferences for upper-mantle metasomatism. In: J.G. Fitton and B.G.J. Upton (Editors), *Alkaline Igneous Rocks, Geol. Soc. Spec. Publ.*, 30, 95-103.
- Ellert, R., Björnberg, A.J.S., Coutinho, J.M.V., 1959. Mapa geológico do Maciço Alcalino de Poços de Caldas, Brasil. In: Ellert, R., 1959. Contribuição à geologia do Maciço Alcalino de Poços de Caldas. *Bol. Fac. Fil., Ciênc. Letras*, Univ. São Paulo (Geologia 18), 237, 5-63.
- Fielding, P.E., 1970. The distribution of uranium, rare earths, and color centers in a crystal of natural zircon. *Am. Min.*, 55, 428-440.
- Foley, S.F., Venturelli, G., Green, D.H. and Toscani, L., 1987. The ultrapotassic rocks: Characteristics, classification, and constraints for petrogenetic models. *Earth Sci. Rev.*, 24, 81-134.
- Fraenkel, M.O., Santos, R.C. de, Loureiro, F.E.d.V.L. and Muniz, W.d.S., 1985. Jazida de urânio no planalto de Poços de Caldas, Minas Gerais. In: C. Schobbenhaus and C.E.S. Coelho (Editors), *Principais depósitos minerais do Brasil*, Vol. 1, *MME, DNPM and CVRD*, Brasília, 89-103.
- Gorsky, V.A. and Gorsky, E., 1974. Contribuição à mineralogia e petrografia do planalto de Poços de Caldas. *Com. Energia Nucl. Bull.*, Rio de Janeiro, 13, 93 pp.
- Henderson, P. (ed.), 1984. *Rare Earth Element Geochemistry*. Elsevier, Amsterdam, 510 pp.
- INM, 1982. Instituto Nacional de Meteorologia (INM). 5 Distrito Meteorologia, Brasil. (Written Comm. Eduardo Penna Franca, Fed. Univ. Rio de Janeiro, 1988).
- Inoue, A. and Utada, M., 1983. Further investigations of a conversion series of dioctahedral mica/smectites in the Shinzan hydrothermal alteration area, northeast Japan. *Clays and Clay Miner.*, 31, 401-412.
- Kübler, B., 1968. Evaluation quantitative du métamorphisme par la cristallinité de l'illite. *Bull. Centre Rech.*, Pau-SNPA, 2, 385-397.

- Magno Jr., L.B., 1985. The alkaline district of Poços de Caldas. *Nuclebrás – CIPC Intern. Publ.*, Poços de Caldas, Brasil, pp. 16.
- Magno Jr., L.B., 1985. The Osamu Utsumi Mine – Geological Presentation. *Nuclebrás – CIPC Intern. Publ.*, Poços de Caldas, Brasil, pp. 15.
- Mariano, A.N., 1989. Economic Geology of Rare Earth Minerals. In: Lipin, B.R. and McKay, G.A. (Editors), *Geochemistry and Mineralogy of Rare Earth Elements, Mineral. Soc. Am., Reviews in Mineralogy*, 21, 309-348.
- Marshall, D.J., 1988. Cathodoluminescence of Geological Materials. *Unwin Hyman Ltd*, London.
- Miranda Filho, M.C., 1983. Síntese do modelo geológico-estrutural da Mina de Caldas, Parte 1. *Nuclebrás – CIPC Intern. Publ.*, Poços de Caldas, Brasil, pp. 45.
- Nisbet, E.G., Dietrich, V.J., and Eisenwein, A., 1979. Routine trace element determination in silicate minerals and rocks by X-ray fluorescence. *Fortschr. Miner.* 57/2, 264-279.
- Norton, S.A., 1973. Laterite and bauxite formation. *Econ. Geol.*, 68, 353-361.
- Oftedal, I., 1957. Heating experiments on amazonite. *Mineral. Mag.*, 31, 417-419.
- Oliveira, A.G., 1974. Mineralização de urânio e molibdênio no planalto de Poços de Caldas-MG. In: Congresso Brasileiro de Geologia, 28, Porto Alegre, *Anais*, 1, 207-221.
- Ramdohr, P., 1975. Die Erzminerale und ihre Verwachsungen, 4th ed., *Akademie-Verlag*, Berlin, 1277 pp.
- Ramseyer, K., Fischer, J., Matter, A., Eberhardt, P. and Geiss, J., 1989. A cathodoluminescence microscope for low intensity luminescence. *Res. Meth. Pap.*, 619-622.
- Rankama, K. and Sahama, Th.G., 1950. Geochemistry. In: W.A. Deer, R.A. Howie and J. Zussman, *Rock Forming Minerals*, Vol. 1, 1962, *Longmans*, London.
- Reusser, E., 1986. Das XRF-System Version 86: Softwarepaket mit unpubl. Manual, ETH-Zürich.
- Rock, N.M.S., 1977. The nature and origin of lamprophyres: Some definitions, distinctions and derivations. *Earth Sci. Rev.*, 13, 123-169.
- Rock, N.M.S., 1987. The nature and origin of lamprophyres: an overview. In: J.G. Fitton and B.G.J. Upton (Editors), *Alkaline Igneous Rocks, Geol. Soc. Spec. Publ.*, 30, 191-226.
- Roedder, E., 1984. Fluid Inclusions. *Min. Soc. Am., Reviews in Mineralogy*, Vol. 12.

- Smith, C.B., Gurney, J.J. and Skinner, I.N.W., 1985. Geochemical character of S.African Kimberlites. A new approach based on isotopic constraints. *Trans. Geol. Soc., S. Africa*, 88, 267-280.
- Sommerauer, J., 1981. COMIC-ED Manual, Version 2.EXT, Institut für Kristallographie und Petrographie, *ETHZ-Zürich*, Switzerland.
- Środoń, J., 1980. Precise identification of illite/smectite interstratifications by X-ray powder diffraction. *Clays and Clay Miner.*, 28, 401-411.
- Środoń, J., 1984. X-ray powder diffraction identification of illitic material. *Clays and Clay Miner.*, 32, 337-349.
- Środoń, J. and Eberl, D.D., 1984. Illite. In: S.W. Bailey (Editor), *Micas. Min. Soc. Am., Reviews in Mineralogy*, Vol. 13.
- Streckeisen, A. and Le Maître, R.W., 1979. A chemical approximation to the modal QAPF classification of the igneous rocks. *N. Jb. Miner. Abh.*, 136/2, 169-206.
- Sun, S.S., 1980. Lead isotopic study of young volcanic rocks from mid-ocean ridges, ocean islands and island arcs. *Phil. Trans. R. Soc., London*, A297, 409-445.
- Sutherland, D.S., 1967. A note on the occurrence of potassium-rich trachytes in the Kaiserstuhl carbonatite complex, West Germany. *Min. Mag.*, 36, 334-341.
- Thompson, R.N., 1982. Magmatism of the British tertiary volcanic province. *Scott. J. Geol.*, 18, 49-107.
- Thompson, R.N., Morrison, M.A., Dickin, A.P. and Hendry, G.L., 1983. Continental flood basalts.... arachnids rule OK?. In: C.J. Hawkesworth and M.J. Norry (Editors), *Continental basalts and mantle xenoliths. Nantwich, Shiva*, 158-185.
- Ulbrich, H.H.G.J., 1984. A petrografia, e estrutura e o quimismo de nefelina sienitos do Maciço Alcalino de Poços de Caldas, MG-SP. *Tese de Livre Docência* apresentada ao Instituto de Geociências da Universidade de São Paulo, 2 Vol.
- Ulbrich, H.H.G.J. and Gomes, C.B., 1981. Alkaline rocks from continental Brazil. *Earth Sci. Rev.*, 17:135-154.
- Ulbrich, M.N.C., 1983. Aspectos mineralógicos et petrólogicos de nephelina sienitos de Poços de Caldas, MG-SP. *Tese de Doutorado* apresentada ao Instituto de Geociências da Universidade de São Paulo, pp. 369.
- Utsumi, O., 1971. Mineralização urano-molibdenífera no planalto de Poços de Caldas. In: Congresso Brasileiro de Geologia, 25, São Paulo, *Res. Comun.*, 40-41.

- Waber, N., 1990. Hydrothermal and supergene evolution of the Osamu Utsumi uranium deposit and the Morro do Ferro thorium – rare earth deposit, inas Gerais, Brazil, 179 pp. *PhD-Thesis*, Universität Bern.
- Wimmenauer, W., 1973. Lamprophyre, Semilamprophyre und anchibasaltische Ganggesteine. *Fortschr. Miner.*, 51, 3-67.

13. Plates 1 – 9



PLATE 1. Panoramic view of the Osamu Utsumi mine looking S.E. (observed from top left-hand corner of Fig. 4).

NOTE: Colour variations clearly show oxidised (yellow-brown) and reduced (grey-blue) rock exposures.



PLATE 2. Panoramic view of the Osamu Utsumi mine looking S.S.W. (observed from top left-hand corner of Fig. 4).



PLATE 3. Redox front at 33.5 m; drillcore F1.



PLATE 4. Redox front at 42.0 m; drillcore F1. Nodular pitchblende on reduced side of front (black circle), kaolinite-rich layer (white layer) separating reduced (grey) and oxidised (brown) rock.

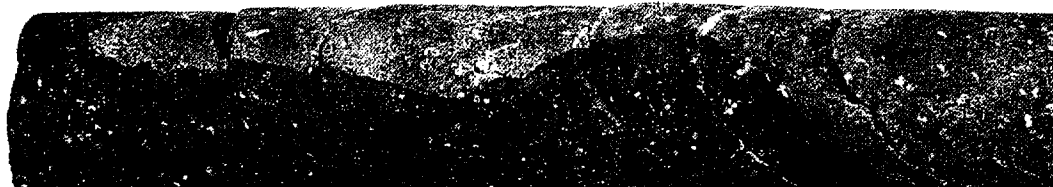


PLATE 5. Redox front at 66.1 m; drillcore F1.

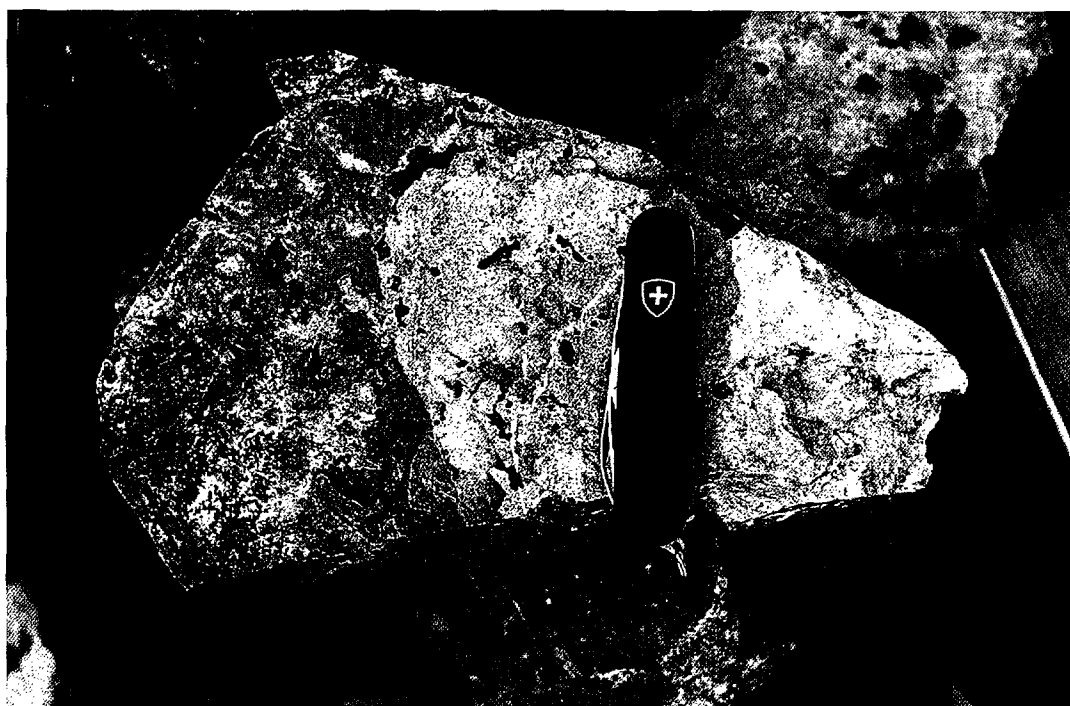
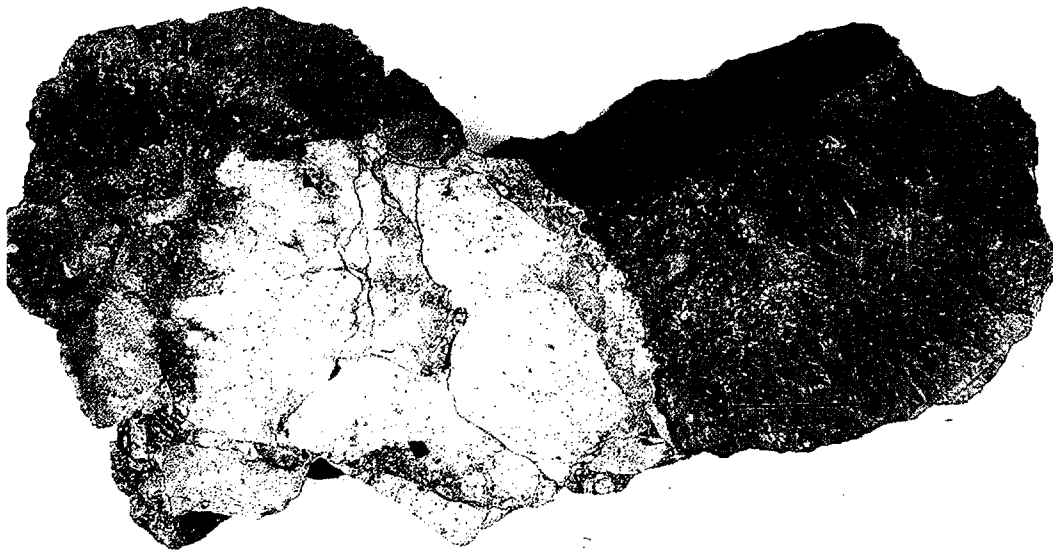


PLATE 6. Redox front RFI; mine exposure. Highly mineralised with black pitchblende nodules on reduced side of front; circular white areas in the oxidised rock (yellow-brown) represent relicts of dissolved pitchblende nodules.

OSAMU UTSUMI MINE



RF II - F

PLATE 7. Redox front RFII; mine exposure. Non-mineralised front in volcanic breccia (scale in cm).

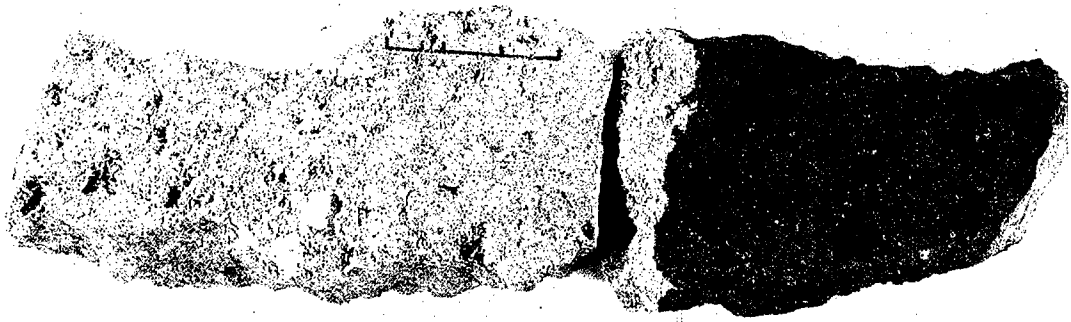
OSAMU UTSUMI MINE



RF III - F

PLATE 8. Redox front RFIII; mine exposure. Mineralised front in dense leucocratic phonolite; small black nodules are located along fissures on the reduced side of the front (scale in cm).

OSAMU UTSUMI MINE



RF IV - F

PLATE 9. Redox front RFIV; mine exposure. Secondary non-mineralised redox front in a porous cpx-phonolite rich in primary uranium. Note the extreme enrichment of Fe-hydroxides at the front (scale in cm).

Appendix 1

**Mineralogical, geochemical and sulphur isotope studies
of selected pyrite samples and pyrite generations from
the Osamu Utsumi mine site, Poços de Caldas, Brazil.**

Contents

	page
1. Introduction	177
2. Sampling and mineral separation	177
3. Results	182
3.1. Mineralogy of the samples, geochemical considerations and classification of the pyrite generations	182
3.2. Sulphur isotopes	196
4. Conclusions and summary	203
APPENDIX:	
Appendix 1:1: PLATES 1:1-1 – 1:1-18	205

Appendix 1

Mineralogical, geochemical and sulphur isotope studies of selected pyrite samples and pyrite generations from the Osamu Utsumi mine site, Poços de Caldas, Brazil.

H.D. SCHORSCHER¹, M.M.G MONTEIRO¹ and A.E. FALLICK²

¹Universidade de São Paulo, Instituto de Geociências – DMP. C.P. 20 899, 014 98 São Paulo (Brazil).

²Scottish Universities Research and Reactor Centre (SURRC), East Kilbride, Glasgow G75 0QU (United Kingdom).

1. Introduction

Pyrite is the major ore mineral of the host “potassic rock” at the Osamu Utsumi mine which shows reducing hydrothermal alteration; this contrasts with the oxidising, hematite-bearing regional hydrothermal alteration. Petrographic studies at the Osamu Utsumi uranium mine revealed the occurrence of texturally distinct types of pyrites that occur in specific lithological and structural environments.

Based on these preliminary studies, subsequent investigations have included the detailed mineralogical, ore petrographic and textural study of pyrite generations in the potassic rocks and uranium ores of the Osamu Utsumi mine. Mineral separations, S-isotope studies, and some complementary bulk geochemical routine X-ray fluorescence (XRF) and microprobe analyses have also been carried out. Mineralogical studies, textural classification and the main mineral separations were made at São Paulo; S-isotope studies were carried out at SURRC and complementary XRF analysis and 2 pyrite separates by N. Waber, University of Bern. Microprobe analysis of the pyrites were made by the first author during two research visits at the University of Bern.

2. Sampling and mineral separation

Drillcore samples from F1 and F4 and hand specimens from surface exposures in the open pit, together with massive U-nodules from the Urânio do Brasil collections, were included in the investigation (Table 1-I).

TABLE 1-I
Samples for sulphur isotope studies.

Current no.	Sample, location	Description	Radioactivity, cps	PLATES, see Appendix 1:1
1	F1(9-1WC11), 69.43 – 69.63	Reduced medium- to coarse-grained hypabyssal phonolite (with minor nepheline syenite pegmatoids) from a conductive zone. The rock is very porous to microcavernous and strongly pyritised and argillised (kaolinite and illite). Pyrites of max. grain-size ~0.5 mm occur throughout the rock and in the pores.	bg – 15	1:1-1
2	F1(9-1WC11), 113.65 – 113.79	Reduced porphyritic phonolite of low microporosity, unfractured, finely pyritised (mean grain-sizes of pyrite ~0.25 mm) disseminated throughout the rock and in the pores.	bg – 5	1:1-2
3	F1(9-1WC11), 125.30 – 125.41 (126-1A)	Reduced subvolcanic medium- to coarse-grained phonolite (with minor nepheline syenite pegmatoids), of low microporosity and very subordinate fracturing. Pyrites are finely disseminated (mean grain-size ~0.25 mm) throughout the rock and in the pores. The pyrite separate was prepared by N. Waber and identified as “matrix pyrite”.	bg – 5	1:1-3
4	F4(8-1UK11), 242.57 – 242.95 (243-1A)	Pyrites (with minor sulphide minerals, silicates and possibly U oxide impurities) of deep-seated truly hydrothermal (i.e. high temperature) high grade U – Zr mineralisations; with +0.01 (± 0.27) $\delta^{34}\text{S}^{\circ}_{\text{‰}}$ CDT perfectly within the range of the other Osamu Utsumi mine hydrothermal pyrites.	40-100-180	1:1-4
5	F4(8-1UK11), 276.15	Open fracture crosscutting reduced breccia. The fracture surfaces are argillised (kaolinite) and pyritised with medium-grained pyrite crystals (mean grain-size: 1 – 2 mm).	bg – 10	1:1-5
6	F4(8-1UK11), 382.49 – 382.63 (383-1A)	Reduced breccia cut by younger pyritised fractures (with clear uncoated and dark coated pyrites). Pyrites have mean grain-sizes ~1.5 mm.	bg – 10	1:1-6

TABLE 1-I (contd.)

Current no.	Sample, location	Description	Radioactivity, cps	PLATES, see Appendix 1:1
7	F4(8-1UK11), 385.40 – 385.64 (386-1A)	Reduced breccia cut by younger pyritised fractures (with clear uncoated and dark coated pyrites). Pyrites have mean grain-sizes ~ 1.8 mm.	bg – 10	1:1-7
8	F4(81UK11), 394.42 – 394.60 (394-1A?)	Reduced nepheline syenite xenolith cut by younger pyritised fractures (with clear uncoated and dark coated pyrites). Pyrites have mean grain-sizes of ~ 1-2 mm.	bg – 10	1:1-8
9	F4(8-1UK11), 396.57 – 396.83	Massive, reduced, medium- to coarse-grained transitional phonolite/nepheline syenite rock, weakly microporous and unfractured, argillised and with finely disseminated pyritisation (max. dimensions of pyrite < 0.3 mm).	bg – 5	1:1-9
10	F4(8-1UK11) 407.57 – 407.67	Reduced, medium- to coarse-grained, strongly porous to microcavernous hypabyssal phonolite with strong pyritisation mainly of the rock pores with pyrites of mean grain-size ~ 1 mm.	bg – 5	1:1-10
11	F4(8-1UK11) 414.10 – 414.24	Reduced breccia (clast matrix-supported type) with strongly pyritised breccia matrix (mean dimensions of pyrites ~ 0.2 mm).	bg – 10	1:1-11
12	U – 4, (near 9-1 RH)	Cavernous (extremely porous) reduced phonolite of argillic decomposition, variable light-grey to almost black colour, strongly pyritised with very fine- to very coarse-grained pyrites (grain-sizes vary from < 0.1 to > 15.0 mm) and local Mo-mineralisation.	10 – 20	–

TABLE 1-I (contd.)

Current no.	Sample, location	Description	Radioactivity, cps	PLATES, see Appendix 1:1
13	U – 7 (near 8-1 KK)	Redox front with strong U-mineralisation in fine-grained phonolite; locally advanced argillic decomposition. Pyritisation occurs as fine disseminations in the reduced phonolite and associated with the redox front-related pitchblende mineralisation.	40 – 50	1:1-12 and 1:1-13
14	OUM – 102	Sample collected and pyrite separated by N. Waber; identified as “matrix pyrite”.	n.i.	–
15	S/N – 24	Massive pitchblende nodule (from the Urânio do Brasil collection) containing various, texturally different pyrite generations.	> 1.500	1:1-14
16	KU – 3	Massive pitchblende nodule (from the Urânio do Brasil collection) with two texturally different pyrite generations.	470	–
17	KU – 6	Massive pitchblende nodule (from the Urânio do Brasil collection) with secondary pyrite in the pitchblende zone.	1.220	–
18	VII	Massive pitchblende nodule (from the Urânio do Brasil collection) with various texturally different pyrite generations.	> 1.500	1:1-15 1:1-16
19	04/02 (near 8-2 AH)	“Laboratory grown” sulphates formed on a specimen of fine-grained reducing phonolite that hosts pitchblende nodules (mineralised redox front). Sulphates were morphologically similar to those from sample M-1. All the recovered material was sent for S-isotope analysis and yielded practically identical results to M-1 ($\delta^{34}\text{S} = +0.53 (\pm 0.28) \text{‰ CDT}$). For interpretation see M-1.	220 – 270	1:1-17

TABLE 1-I (contd.)

Current no.	Sample, location	Description	Radioactivity, cps	PLATES, see Appendix 1:1
20	M-1 (near 9-1 RH)	Bluish coloured sulphate crystals as flakes and needles (of recent origin) formed since collection (i.e. while stored in our specimen deposit) on a sample of fine-grained, non-U-mineralised, but strongly pyritised phonolite. The sulphates were identified using a combined XRD and Energy Dispersion System (EDS) microanalysis on mixtures of kaolinite – $KAl(SO_4)_2 \cdot 11H_2O(?)$ and halotrichite – $Fe^{2+}Al_2(SO_4)_4 \cdot 22H_2O$. The S-isotopes indicate that the “laboratory” process was by reaction only via atmospheric reaction; in spite of chemical reactions and reprecipitation there occurred no noticeable isotopic fractionation. $\delta^{34}S$ remained at $+ 0.52 (\pm 0.17) \text{ ‰ CDT}$, i.e. within the original values for the hydrothermal pyrites.	bg – 10	1:1-18
21	U-1A (near 9-1 RH)	Botryoidal yellowish sulphates collected in the Osamu Utsumi open pit, having formed on fracture planes within the reducing, fine-grained, strongly pyritised and weakly U-mineralised phonolite. Combined EDS and XRD identified halotrichite and minor kaolinite. S-isotopic values of the sulphates are $\delta^{34}S = -2.6 (\pm 0.7) \text{ ‰ CDT}$, i.e. within the range of the hydrothermal pyrites. The co-existing pyrites yielded $\delta^{34}S$ of -0.49 to $-2.40 (\pm 0.2) \text{ ‰ CDT}$ for various grain-size fractions (sample nos.: U-4A, B, D under current no. 12 in the report). This indicates that the collected mine sulphates are also products of atmospheric reactions without any fractionation and formed after the development of the open pit.	bg – 5	–

n.i. = not informed
cps = counts per second
CDT = Cañon Diablo Troilite (International standard).

All the samples selected for pyrite separation and S-isotope analysis were carefully studied macroscopically and microscopically (thin sections; polished sections; polished thin sections), and in some cases with X-ray diffraction (XRD), bulk geochemical routine X-ray fluorescence (XRF), and microprobe techniques.

Microscopic studies revealed that several samples contained more than one pyrite generation with distinct textural associations and different grain-sizes.

Pyrite separation involved repeated crushing, sieving and heavy liquid separation (Bromoform, Merck – for mineral separation, $d = 2.870 - 2.890 \text{ g/cm}^3$) in order to obtain pyrite preconcentrates of the original size fractions. Each preconcentrate was further purified by preliminary hand-picking, regrinding, sieving, additional heavy liquid separation, washing and final hand-picking of all, or the major, concentrated pyrite sieve fractions. In the case of some samples, only a low total pyrite recovery was obtained in the course of preconcentration (particularly of the very fine pyrites), necessitating the use of less pure concentrates for the isotope analysis. However, silicate mineral impurities (Table 1-II) had no evident influence on the S-isotope analyses (Table 1-III).

For most of the samples processed, more than one pyrite concentrate/size fraction was obtained and analysed isotopically. In addition to the pyrites, recent sulphate occurrences (three samples) were included in the S-isotope studies. These sulphates form abundantly as individual crystals (of needle and flaky shape) or botryoidal masses covering fracture planes and external surfaces.

3. Results

3.1. Mineralogy of the samples, geochemical considerations and classification of the pyrite generations

Samples 1 – 3 (Table 1-I). These comprise phonolite core specimens from borehole F1. The bulk rock mineralogy of the three rocks is quite similar and consists of varying proportions of K-rich alkali feldspars, sericite/illite and kaolinite (>10 vol.%); pyrite is the only significant minor constituent (1-10 vol.%), while zircon, unidentified clay minerals (probably smectites) and Ti-oxide minerals (Nb-bearing) are the common trace constituents (<1 vol.%). Fluorite and carbonates occur as trace constituents in samples (2) and (3), but are absent in sample (1) (Table 1-I) and generally in the conductive zone at 69-70 m depth. However, major differences characterise the rock textures and quantitative proportions of their major minerals. Sample (1) is extremely porous to

TABLE 1-II
Pyrite mineral separates.

Current no.	Sample location	Pyrite separates			Observations
		No.	size (#)	weight (g)	
1	F1 69.43 – 69.63	1.1	80–115	0.05	Pure concentrate of fresh pyrite.
		1.2	80–115	1.35	Concentrate of fresh pyrite with minor silicate impurities.
		1.3	115–170	1.10	Pure concentrate of fresh pyrite.
2	F1 113.65–113.79	2.1	80–115	0.01	Pure concentrate of fresh pyrite.
		2.2	115–170	0.02	Pure concentrate of fresh pyrite.
3	F1(WC126-1A) 125.30 – 125.41	3.1	n.i.	n.i.	Concentrate of “matrix pyrite” prepared by N. Waber from a deep-seated hydrothermal phonolite.
4	F4 242.57 – 242.95	4.1	– 80	0.50	Impure concentrate of fresh pyrite with impurities of silicates and pitchblende from a deep-seated hydrothermal U-mineralisation.
5	F4 276.15	5.1	– 80	0.50	Pure concentrate of fresh pyrite.
6	F4 382.49 – 382.63 (383-1A)	6.1	– 16	0.50	Pure concentrate of fresh, uncoated pyrite.
		6.2	– 16	0.50	Mixed concentrate of coated < uncoated pyrite.
7	F4 385.40 – 385.64 (386-1A)	7.1	– 16	0.50	Pure concentrate of fresh, uncoated pyrite.
		7.2	– 16	0.50	Mixed concentrate of coated < uncoated pyrite.
8	F4 394.42 – 394.60 (394-1A?)	8.1	– 16	0.50	Pure concentrate of fresh, uncoated pyrite.
		8.2	– 16	0.50	Mixed concentrate of coated < uncoated pyrite.

TABLE 1-II (contd.).

Current no.	Sample location	Pyrite separates			Observations
		No.	size (#)	weight (g)	
9	F4 396.57 – 396.83	9.1	80–115	0.04	Pure concentrate of fresh pyrite.
		9.2	80–115	0.33	Concentrate of fresh pyrite with minor silicate impurities.
		9.3	115–170	0.01	Pure concentrate of fresh pyrite.
		9.4	115–170	0.52	Concentrate of fresh pyrite with minor silicate impurities.
10	F4 407.57 – 407.67	10.1	80–115	0.14	Pure concentrate of fresh pyrite.
		10.2	80–115	6.71	Concentrate of fresh pyrite with minor silicate impurities.
11	F4 414.10–414.24	11.1	60– 80	0.10	Pure concentrate of fresh pyrite.
		11.2	60– 80	2.0	Concentrate of fresh pyrite with minor silicate impurities.
		11.3	80–115	0.05	Pure concentrate of fresh pyrite.
		11.4	80–115	2.20	Concentrate of fresh pyrite with minor silicate impurities.
		11.5	115–170	0.05	Pure concentrate of fresh pyrite.
		11.6	115–170	2.30	Concentrate of fresh pyrite with minor silicate impurities.
12	U-4(A)	12.1	≤ 0.5 mm	0.5	Pure concentrate of fine-grained fresh pyrite associated with Mo-mineralisation.
	U-4(B)	12.2	1–3 mm	1.0	Pure concentrate of medium-grained fresh pyrite.
	U-4(D)	12.3	≥ 8 mm	2.0	Pure concentrate of very coarse-grained fresh pyrite.
13	U-7(E)	13.1	115–170	0.1	Concentrate of very fine-grained fresh pyrite from the rock matrix of a redox front sample.
	U-7(G)	13.2	115–170	0.1	Concentrate of very fine-grained fresh pyrite from the rock matrix of a redox front sample.
14	OUM-102	14.1	n.i.	n.i.	Concentrate of “matrix pyrite” prepared by N. Waber.

TABLE 1:II (contd.)

Current no.	Sample location	Pyrite separates			Observations
		No.	size (#)	weight (g)	
15	S/N-24	15.1	≤ 3 mm	0.5	Pure concentrate of fresh pyrite from the silicate core of a massive U-nodule.
		15.2	+ 30	0.5	Pure concentrate of “pyrite layer” from the pitchblende zone of a massive U-nodule.
		15.3	30–48	0.5	Idem 15.2, finer grain-size.
		15.4	– 48	0.5	Idem 15.3, finer grain-size.
		15.5	≤ 1.5 mm	0.5	Pure concentrate of fresh pyrite from the external cover of a massive U-nodule.
16	KU-3	16.1	≤ 1.5 mm	0.3	Pure concentrate of fresh pyrite from the external cover of a massive U-nodule.
		16.2	≤ 1.5 mm	0.5	Pure concentrate of fresh pyrite from the pitchblende zone of a massive U-nodule.
17	KU-6	17.1	≤ 1.0 mm	0.5	Concentrate of pyrite from the pitchblende zone of a massive U-nodule containing impurities of U-oxides, silicates and minor (?) sulphates from incipient pyrite oxidation.
18	VII	18.1	≤ 0.5 mm	0.5	Pure concentrate of fresh pyrite from the silicate core of a massive U-nodule.
		18.2	≤ 1.5 mm	0.3	Pure concentrate of fresh pyrite from the external cover of a massive U-nodule.
		18.3	≤ 1.5 mm	0.5	Pure concentrate of fresh pyrite from the pitchblende zone of a massive U-nodule.
19	04/02	19.1	nat. size	1.0	Concentrate of recent sulphates (whitish-colourless flakes and needles) from the reduced side of a U-mineralised redox front.
20	M-1	20.1	nat. size	1.0	Concentrate of recent sulphates (bluish-coloured flakes and needles) from a fine-grained reduced phonolite.
21	U-1A	21.1	nat. size	1.0	Concentrate of recent, light-yellowish coloured botryoidal sulphates from a reduced breccia.

n.i. = not informed

TABLE 1-III
Results of sulphur isotopic analysis.

Current no.	Sample location	Pyrite no.	Separate size (#)	Analytical observations	$\delta^{34}\text{S}/\text{‰}$ CDT	Textural, genetic comments
1	F1(69.43-) F1(70-1C)	1.1	80–115	Pure pyrite concentrate	+1.24	Fresh pyrite from the conductive zone within a very porous hydrothermally altered phonolite
		1.2	80–115	Pyrite concentrate, minor silicate impurities	+0.80	Idem
		1.3	115–170	Pure pyrite concentrate	+1.04	Idem
2	F1(113.65-) F1(114-1A)	2.1	80–115	Pure pyrite concentrate	-2.30	Fresh pyrite from a hydrothermalised phonolite; “potassic rock” pyrite
		2.2	115–170	Pure pyrite concentrate	+0.36	Idem
3	F1(126-1A)	3.1	n.i.	Concentrate of “matrix pyrite” (by N. Waber)	-0.86	Idem
4	F4(242.57-) F4(243-1A)	4.1	-80	Impure concentrate, silicate and pitchblende impurities	in progress	Pyrite from a deep-seated hydrothermal U-mineralisation in breccia matrix; syn-breccia, syn-U-mineralisation pyrite
5	F4(276.15-) F4(277-1A)	5.1	-80	Pure pyrite concentrate	-14.77	Fresh, post-breccia(-fracture) pyrite associated with clays
6	F4(383-1A)	6.1	-16	Pure pyrite concentrate uncoated	-3.61	Fresh, post-breccia(-fracture) pyrite, uncoated
		6.2	-16	Mixed concentrate of coated < uncoated pyrite	-4.66	Dark coated, post-breccia (-fracture) pyrite

TABLE 1-III (contd.)

Current no.	Sample location	Pyrite no.	Separate size (#)	Analytical observations	$\delta^{34}\text{S}_{\text{CDT}}^{\text{‰}}$	Textural, genetic comments
7	F4(386-1A)	7.1	-16	Pyrite concentrate uncoated (386-1A-1), minor silicate impurities	+3.04	Fresh post-breccia (-fracture) pyrite, uncoated
		7.1.1	-16	Idem, re-run after cleaning	-2.18	Idem
		7.1.2	-16	Idem, re-run after cleaning	-2.38	Idem
		7.2	-16	Mixed concentrate of coated < uncoated pyrite (386-1A-2), minor silicate impurities	+4.60	Dark coated, post-breccia (-fracture) pyrite
		7.2.1	-16	Idem, re-run after cleaning	+0.46	Idem
		7.3	-16	Mixed concentrate of coated < uncoated pyrite	-2.29	Dark coated, post-breccia (-fracture) pyrite
		7.4	-16	Pure pyrite, concentrate uncoated	-1.80	Fresh, post-breccia (-fracture) pyrite, uncoated
8	F4(394-1A)	8.1	-16	Pure pyrite, concentrate uncoated	-2.29	Idem
		8.2	-16	Mixed concentrate of coated < uncoated pyrite	-3.31	Dark coated, post-breccia (-fracture) pyrite
9	F4(396.57-) F4(397-1A)	9.1	80-115	Pure pyrite concentrate	-0.57	Fresh pyrite from a weakly porous phonolite fragment; pre-breccia pyrite
		9.2	80-115	Pyrite concentrate, minor silicate impurities	-0.68	Idem
		9.3	115-170	Pure pyrite concentrate	-0.83	Idem
		9.4	115-170	Pyrite concentrate, minor silicate impurities	-0.74	Idem

TABLE 1-III (contd.)

Current no.	Sample location	Pyrite no.	Separate size (#)	Analytical observations	$\delta^{34}\text{S}^{\circ}/_{\text{oo}}$ CDT	Textural, genetic comments
10	F4(407.57-) F4(408-1A)	10.1	80–115	Pure pyrite concentrate	-1.67	Fresh pyrite from a strongly porous phonolite fragment; pre-breccia pyrite
		10.2	80–115	Pyrite concentrate, minor silicate impurities	-1.55	Idem
11	F4(414.10-) F4(414-1B)	11.1	60–80	Pure pyrite concentrate	-1.02	Fresh pyrite of breccia matrix; syn-breccia pyrite
		11.2	60–80	Pyrite concentrate, minor silicate impurities	-1.15	Idem
		11.3	80–115	Pure pyrite concentrate	-1.30	Idem
		11.4	80–115	Pyrite concentrate, minor silicate impurities	-0.95	Idem
		11.5	115–170	Pure pyrite concentrate	-1.27	Idem
		11.6	115–170	Pyrite concentrate, minor silicate impurities	-1.13	Idem
12	U-4(A)	12.1	≤ 0.5 mm	Pure pyrite concentrate	-0.49	Fresh fine-grained pyrite from a hydrothermally altered phonolite (“potassic rock”) with Mo-mineralisation; advanced argillic decomposition
	U-4(B)	12.2	1–3 mm	Pure pyrite concentrate	-2.40	Fresh medium-grained pyrite of hydrothermally altered phonolite (“potassic rock”); advanced argillic decomposition
	U-4(D)	12.3	≥ 8 mm	Pure pyrite concentrate	-2.05	Fresh coarse-grained pyrite of hydrothermally altered phonolite (“potassic rock”); advanced argillic decomposition with high kaolinite contents

TABLE 1-III (contd.)

Current no.	Sample location	Pyrite no.	Separate size (#)	Analytical observations	$\delta^{34}\text{S}/\text{‰}$ CDT	Textural, genetic comments
13	U-7(E)	13.1	115–170	Pyrite concentrate, minor silicate impurities	-0.54	Fresh fine-grained pyrite from the phonolite groundmass of a U-mineralised redox front
	U-7(G)	13.2	115–170	Pyrite concentrate, minor silicate impurities	-3.63	Idem
14	OUM-102	14.1	n.i.	Concentrate of “matrix pyrite” (by N. Waber)	-3.26	Fresh pyrite from a hydrothermally altered phonolite; “potassic rock” pyrite
15	S/N-24	15.1	≤ 3 mm	Pure pyrite concentrate	-8.85	Fresh pyrite from the silicate core of a massive U-nodule; mixture of two pyrite generations
		15.2	+ 30	Pure pyrite concentrate	-12.20	Fresh pyrite from a pre-pitchblende “pyrite layer” of a pitchblende zone within a massive U-nodule
		15.3	30–48	Pure pyrite concentrate	-13.31	Idem; 15.2 finer grain-size
		15.4	-48	Pure pyrite concentrate	-13.11	Idem; 15.3 finer grain-size
		15.5	≤ 1.5 mm	Pure pyrite concentrate	-8.13	Fresh pyrite from the external silicate cover of a massive U-nodule
16	KU-3	16.1	≤ 1.5 mm	Pure pyrite concentrate	-2.20	Fresh pyrite from the external silicate cover of a massive U-nodule
		16.2	≤ 1.5 mm	Pure pyrite concentrate	-2.40	Fresh pyrite from the pitchblende zone of a massive U-nodule

TABLE 1-III (contd.)

Current no.	Sample location	Pyrite no.	Separate size (mm)	Analytical observations	$\delta^{34}\text{S}/\text{‰}$ CDT	Textural, genetic comments
17	KU-6	17.1	≤ 1.0	Pyrite concentrate with impurities of silicates, pitchblende and possibly minor sulphates from pyrite oxidation	-3.14	Fresh and incipiently oxidised pyrite from the pitchblende zone of a massive U-nodule
		17.1.1	≤ 1.0	Idem; re-run after cleaning	-12.39	Fresh pyrite from the pitchblende zone of a massive U-nodule; syn-pitchblende pyrite
		17.1.2	≤ 1.0	Idem 17.1.1; re-run after cleaning	-11.83	Idem 17.1.1; syn-pitchblende pyrite
18	VII	18.1.1	≤ 0.5	Pure pyrite concentrate; 1st. run	-3.78	Fresh pyrite from the silicate core of a massive U-nodule
		18.1.2	≤ 0.5	Idem 18.1.1; 2nd. run	-3.81	Idem 18.1.1
		18.2	≤ 1.5	Pure pyrite concentrate	-5.16	Fresh pyrite from the pitchblende zone of a massive U-nodule
		18.3	≤ 1.5	Pure pyrite concentrate	-7.25	Fresh pyrite from the external cover of a massive U-nodule
19	04/02	19.1	nat. size	Concentrate of sulphates	in progress	Recent sulphates: whitish, colourless flakes and needles from a U-mineralised redox front in phonolite
20	M-1	20.1	nat. size	Concentrate of sulphates	in progress	Recent sulphates: bluish-coloured flakes and needles from a fine-grained phonolite with Mo-mineralisation
21	U-1A	21.1	nat. size	Concentrate of sulphates	in progress	Recent sulphates: light yellowish-coloured botryoidal masses of breccia

n.i. = not informed

microcavernous with macroscopically recognisable interconnected open pores (Plate 1:1-1) and is richer in total clay minerals than in alkali feldspars (60:35, in vol.% of total solids); samples (2) and (3) are massive, textured subvolcanic phonolites of only minor microporosity (Plates 1:1-2 and 1:1-3) and higher alkali feldspar than total clay mineral proportions (80:15, in vol.% of total solids).

The pyrites from sample (1) show somewhat larger grain-size variations, ranging from <0.1 to ≥ 0.5 mm, and there is a preferential occurrence of the larger pyrites in the open fabric of the sample. Microscopically, the pyrites consist of fresh idiomorphic grains, some intergrown, without any sign of corrosion surface alteration or coatings, indicating equilibrium conditions or perfect metastable preservation in the conductive zone. Geochemical data for sample (1) are lacking, although the general geochemical and mineralogical characteristics of the profile interval included have been established (Waber *et al.*, this report series; Rep. 2) and indicate the possibility of several phases of influence affecting the sample. These include: (1) hydrothermal Zr-REE-U mineralisation, (2) the nearby redox front III (at 66.20 m), and (3) the water-flow in the conductive zone. Three pyrite concentrates of two grain-size fractions and different degrees of purity were obtained from sample (1) (Table 1-II).

Pyrites from samples (2) and (3) are texturally very similar, although of a somewhat finer and more homogeneous grain-size (0.25 mm in diameter) than those of sample (1), and occur evenly disseminated throughout the rock and pore spaces. The pyrites comprise perfectly fresh and mainly idiomorphic grains devoid of any signs of surface alteration, corrosion or coatings. They represent a distinct genetic group formed during the reducing hydrothermal alteration phase of the “potassic rock”, which is not related to the uranium mineralisation. This is supported by radioactivity measurements and the chemistry of sample (3), which indicate uranium contents below detection level (Appendix 4). Two pyrite concentrates identified as “matrix pyrite” were obtained from sample (2) and one (by N. Waber) from sample (3) (Table 1-II).

Of more general interest is the occurrence of relict hematite in pyrite and the pyritisation of hematite in samples (2) and (3), indicating that the “potassic rocks” went through an oxidising, hydrothermal alteration phase prior to the reducing hydrothermal alteration and related pyritisation phase.

Samples 4 – 11 (Table 1-I) are drillcore samples from borehole F4 drilled to 415 m (350 m depth) for hydrothermal studies. The rocks intercepted include breccias, phonolites, nepheline syenites and post-breccia fracture mineralisations.

Sample (4) is a reduced breccia with a hydrothermal U-Zr-REE mineralised breccia matrix. In addition, the sample shows at least one event of post-brecciation that intersects the U-mineralisation. The silicate mineralogy of the breccia rock fragments consists mainly of K-rich alkali feldspars, illite/sericite, kaolinite, pyrite and zircon, and the mineralised matrix consists of pitchblende, pyrite, sphalerite, zircons and clay minerals. The post-breccia fractures carry minor pyrite and clay minerals. Ore microscopy indicated the presence of at least three distinct pyrite generations. The oldest are the pre-breccia pyrites that occur in variable amounts and textures in the different rock fragments of the breccia. Next in age are the syn-breccia pyrites (and marcasite) that occur in the breccia matrix and are intimately intergrown with pitchblende, sphalerite, zircon and clay minerals. The youngest are the post-breccia pyrites occurring along the fracture planes that crosscut the breccia matrix, i.e. those which intersect the U-mineralisation.

For the S-isotope studies, it was attempted to separate pyrite concentrates from the hydrothermal syn-breccia U-mineralisation type by selective preparation. However, only one impure concentrate could be obtained (Table 1-II) due to the very intimate intergrowth relationship with the ore. One XRF analysis of the highly mineralised part of the sample, consisting largely of fine-grained breccia and mineralised breccia matrix, is shown in Appendix 4.

Sample (5) contains an open fracture zone in reduced breccia. The fracture walls are argillised, covered by a continuous coating of white clays (mainly kaolinite) and pyritised with single medium-grained (1 – 2 mm sized) idiomorphic crystals. These post-breccia pyrites are fresh, showing no signs of alteration, surface coatings or inclusions. One pure concentrate was prepared (Table 1-II; Plate 1:1-5).

Samples (6), (7) and (8) are similar to sample (5), consisting of pyritised open fractures (of post-breccia origin) crosscutting reduced breccias (samples (6) and (7)) and a reduced nepheline syenite xenolith (sample (8)). In all three cases some mineralogical and textural characteristics of the pyrites differ from sample (5). The pyrites have not formed as individual crystals, but predominantly as a continuous aggregate of pyrite covering the non-argillised fracture planes. Macroscopically the most striking feature is the association of normal-coloured typical pyrites with others of silvery-white metallic appearance, very similar to galena. This abnormal colouration has been attributed to surface alteration or coatings of very fine films. From each of the three samples, two concentrates of coated and uncoated post-breccia (fracture) pyrites were prepared (Table 1-II).

The nature of the coatings and the reason for the abnormal colouration of the pyrite is not known. Even at highest magnifications, no distinct surface material covering or alteration of the pyrites could be recognised. However, some external intergrowths consisting of very fine irregular grains and discontinuous seams of stibnite (tentatively identified) do occur. In addition, all the fracture pyrites of the three samples (nos. 6, 7 and 8) show frequent but very fine inclusions of pyrrhotite (tentatively identified). The absence of such inclusions in any of the previously described samples characterises these fracture pyrites as being of true hydrothermal (mesothermal) origin, most probably belonging to an event different from the “potassic rock”-forming hydrothermal process.

Major and trace element XRF analysis (Appendix 4) of selected parts of the three samples (emphasising the pyritised fractures) failed to furnish any additional information about the nature of the pyrite coatings/surface alterations.

Samples (9), (10) and (11) are from nepheline syenite, phonolite xenoliths and breccia respectively (Plates 1:1-9, 1:1-10 and 1:1-11). Radioactivity measurements show background values (<20 ppm U) for the xenoliths and low values for the breccia (<150 ppm U). The xenoliths furnished concentrations of pre-breccia pyrites and the breccia provided syn-breccia (matrix) pyrites associated with weak hydrothermal U-mineralisation (Table 1-II). Ore microscopy indicated that all the rock samples contained pure pyrites devoid of inclusions and/or alterations.

Samples (12), (13) and (14) (Table 1-I) are from surface exposures. Sample (12) consists of a strongly hydrothermally altered, extremely porous/cavernous phonolite, partly argillised and non-mineralised. Pyrites range from very fine-grained to very coarse (from <0.1 to >15.0 mm); the finer-grained pyrites predominate in the rock, the coarse and very coarse are commonly found in the pores/caverns resulting from hydrothermal leaching/dissolution. Three pure concentrates were obtained: a) fine-grained pyrites (<0.5 mm), extracted from dark-grey, almost black-coloured phonolite (in argillic decomposition) with Mo-mineralisation, b) medium-grained pyrites (1-3 mm) from medium grey-coloured argillic phonolites, and c) very coarse-grained pyrites (>8 mm) from pores/caverns associated with white kaolinite clays (Table 1-II). All these pyrites comprise freshly preserved idiomorphic crystals microscopically free from inclusions and/or surface alterations.

Sample (13) is from a strongly U-mineralised redox front hosted by a fine-grained phonolite containing frequent pitchblende nodules measuring a few millimetres to about 1.5 cm in diameter (Plate 1:1-12). Sample separates were attempted of pyrite concentrates from the hydrothermally altered reduced rock matrix and from selectively

prepared/extracted pitchblende nodules. However, only the former was successful (Table 1-II). The redox front-related pitchblende nodules were too small and, in spite of their pyrite enrichment, were too poor to obtain reliable concentrates when compared to the enclosing reduced phonolite (Plate 1:1-13).

Sample (14) is a pyrite concentrate collected and prepared by N. Waber, Univ. Bern, and identified as “matrix pyrite” (Table 1-II), i.e. from a reduced non-U-mineralised “potassic rock” portion.

Samples (15), (16), (17) and (18) (Table 1-I) are massive pitchblende nodules from the Urânio do Brasil collections. Particular attention was given to them since they contain various pyrite generations with distinct growth and structural zones. Some information about the processes involved in the formation of the massive nodules was expected.

Sample (15) is a massive nodule about 10 cm in diameter (Plate 1:1-14). The form of the nodule is suboval-irregular and three major growth and structural zones can be distinguished: (1) a white silicate core, (2) the main black nodule-forming pitchblende zone, and (3) a fine external white silicate-rich shell. Pyrites were selectively extracted from all three zones.

The silicate core consists of common silicates and other minor minerals such as Ti-oxides and pyrite from the reduced phonolites and nepheline syenites of the mine (but in a somewhat more advanced stage of argillic alteration). Fluorite and carbonates were not observed. The silicate core of the nodule is interpreted as being a remnant of hydrothermally altered potassic country rock that was included, isolated and effectively protected from oxidation/dissolution by the surrounding nodule-forming massive pitchblende zone. Two pyrite generations could be distinguished in the core: a) fine-grained, older pyrites of idiomorphic and, in some cases, somewhat rounded forms due to incipient corrosion (of max. dimensions <0.4 mm), and b) younger medium- to coarse-grained pyrites (of dimensions ranging between 1-3 mm). The coarser pyrites occur preferentially as irregular aggregates and clusters near the interface of the core with the pitchblende zone and contain inclusions of the fine-grained pyrites. The fine-grained pyrites (first generation) are considered normal hydrothermal constituents of the silicate core-forming potassic rock; the coarser-grained younger pyrites also present in aggregates and clusters (second generation) are either reprecipitated minerals resulting from contractive growth of the nodule or products of a second post-hydrothermal, but pre-nodule-forming, pyritisation process. This is discussed later. Due to the separation techniques employed, only one mixed pyrite concentrate

(containing first and second generation pyrites) could be obtained from the silicate core (Table 1-II).

In the pitchblende nodule-forming main zone there occur three pyrite generations. The oldest consists, as in the silicate core, of fine-grained idiomorphic or slightly corroded grains (of max. dimensions <0.4 mm) which occur with similar random disseminated frequency throughout the pitchblende zone. These pyrites are older than the pitchblende and were incorporated from the rock in the course of the nodule growth and pitchblende precipitation, at the (partial) expense of silicate mineral replacement.

The next pyrite generation in age is fine- to medium-grained in the size range 0.5 – 2.0 mm. They occur concentrated in a layer parallel/subparallel to the first (fine-grained) pyrite generation, but are older than the pitchblende, as indicated by the inclusion of first generation pyrites and the lack of pitchblende inclusions. The textural evidence does not support a hydrothermal origin for these second generation pyrites, indicating instead formation in the reduced rock (post-hydrothermally) related to a water table, but earlier than the redox front-related U-mineralisation and the massive U-nodule formation. This pyrite generation was selectively extracted and prepared in three pure concentrates of different grain-sizes (Table 1-II).

The third pyrite generation from the massive pitchblende zone is less frequent and less well-defined. It is fine- to medium-grained and randomly disseminated throughout the pitchblende zone. Some of the coarser-grained varieties include fine-grained, partially corroded pyrites of the first generation, sometimes surrounded by fine pitchblende seams, whilst others may contain only fine pitchblende inclusions. Texturally, it becomes evident that the third pyrite generation is subsequent to the former two. It grew coevally with pitchblende precipitation, and was subsequently outlasted by the latter. However, this pyrite generation could not be separated due to low total contents in nodule S/N-24.

It is interesting to note that, in the massive pitchblende zone, greenockite (CdS) occurs as an additional trace constituent. Its mineralogical frequency (even if only a trace mineral), however, accounts for high Cd geochemical anomalies in the pitchblende zone of the nodule.

An external, fine silicate-rich shell coats the massive pitchblende zone. Microscopic and XRD studies have revealed the presence of all the main potassic rock-forming minerals in this shell, including quite an abundance of fine- to medium-grained pyrites. Quantitative mineralogical estimates were not possible, however, since only relicts of the silicate shell are preserved in the sample (Plate 1:1-14). Pyrites from the shell were extracted in one pure concentrate (Table 1-II) of original fine to medium grain-sizes

(<0.5 – 1.5 mm). This concentrate is interpreted genetically as most probably containing a mixture of all the pyrite generations existing in the pitchblende zone. They were enriched in the residual silicate shell due to the external selective dissolution of the massive pitchblende zone during the processes of contractive growth of the nodule.

Samples (16), (17) and (18) are also of massive pitchblende nodules and show, in general, similar growth zones, structuring, mineralogy and pyrite generations to sample (15). Differences concern the size dimensions of the nodules (Plate 1:1-15 and 1:1-16) and the fact that none show any sign of a layered pyrite concentration equivalent to the second pyrite generation of the massive pitchblende zone and sample (15). Various pyrite concentrates were obtained from these nodules (Table 1-II).

Samples (19), (20) and (21) (Table 1-I) are of recent sulphates formed by the oxidation of sulphides in the reduced hydrothermally altered rocks of the open pit since excavations exposed the fresh rock to the atmosphere. In the non- (or less) disturbed underground levels represented by the drillcores (unsaturated and saturated groundwater horizons), such sulphates were not found. Sulphates tend to form as acicular or platy crystals in clusters and coatings, or as dense botryoidal masses (Table 1-I; Plates 1:1-17 and 1:1-18) along rock fracture surfaces protected from water-flow. There exist different colour and textural varieties, mostly due to the presence of different minor elements (e.g. Mo, U etc). Three were sampled for XRD and S-isotope analysis (Tables 1-I, 1-II; Plates 1:1-17 and 1:1-18). These samples were included to obtain information about the character and possible influence of (incipient) stages of recent oxidic weathering on the reduced, hydrothermally altered rock of the mine, particularly with respect to the pyrites.

3.2. Sulphur isotopes

The sulphur isotopic signatures of the above-described pyrite and sulphate concentrates were analysed at SURRC. Some analyses (nos. 4, 19, 20 and 21) are still in progress and the details will be presented later. The isotopic data are presented in Table 1-III; the analytical error is $\pm 0.2\text{‰}$ (1).

The F1 samples/pyrite concentrates show no systematic variation with depth or with grain-size; they lie within a quite narrow compositional interval ranging from -2.30 to +1.24 $\delta^{34}\text{S}\text{‰}$ (Table 1-IV). Any major influence of the conductive zone upon the S-isotope compositions of the contained pyrites (concentrate nos. 1.1 – 1.3), when compared to their equivalents within the deep-seated hydrothermally altered (“potassic

rock”) phonolites (concentrate nos. 2.1, 2.2, 3.1), is not recognisable. However, a tendency to somewhat heavier S-compositions can be identified.

TABLE 1-IV
Isotope compositions of F1 pyrites.

Sample no.	Depth (m)	Separate		$\delta^{34}\text{S}^{\circ}/_{\infty}$ CDT	Observations
		no.	size (#)		
1	69.43- 69.63	1.1	80-115	+ 1.24	Pyrites from the conductive zone in hydrothermally altered phonolite
		1.2	80-115	+ 0.80	
		1.3	115-170	+ 1.04	
2	113.65- 113.79	2.1	80-115	-2.30	Deep hydrothermal pyrites
		2.2	115-170	+ 0.36	
3	125.30- 125.41	3.1	n.i.	-0.86	Idem

n.i. = not identified

The F4 samples/pyrite concentrates are shown in Table 1-V. No depth- or grain-size-dependence could be observed and the analytical data were therefore arranged according to the three textural/genetic groups of pre-breccia, syn-breccia and post-breccia (fracture pyrites).

The pre- and syn-breccia pyrites (Table 1-V, samples 9, 10, 11) all lie within a very narrow range of S-compositions (-1.67 to -0.57 $\delta^{34}\text{S}^{\circ}/_{\infty}$).

The post-breccia pyrites scatter considerably more (Table 1-V; samples 5 – 8) and can be subdivided into two paragenetic groups represented by samples (6), (7) and (8) and by sample (5). The first paragenetic group is characterised by the association of fresh and coated pyrites with post-breccia fractures devoid of any white (kaolinitic) clay cover. Macroscopically, the colour of the coated pyrites is dark-silver, very similar to galena which was recorded during drillcore logging and sampling of F4 (Plates 1:1-6, 1:1-7 and 1:1-8). During preparation of the pyrite separates it became clear that the minerals considered to be galena (of a hydrothermal pyrite-galena association, i.e. different from the common “potassic rock” hydrothermal association) were just surface-coated pyrites or, more generally, pyrites with surface alteration. Identification of these surface coatings and alterations was unsuccessful, although some other particularities became apparent, such as the occurrence of trace amounts of very fine-grained stibnite (intergrown with

TABLE 1-V
Isotope compositions of F4 pyrites.

Sample	Depth	Separate		$\delta^{34}\text{S}/\text{‰}$	
Current no.	(m)	no.	size (#)	CDT	Observations
9	396.57 – 396.83	9.1	80–115	-0.57	Pre-breccia pyrites
		9.2	80–115	-0.68	Idem
		9.3	115–170	-0.83	Idem
		9.4	115–170	-0.74	Idem
10	407.57 – 407.67	10.1	80–115	-1.67	Idem
		10.2	80–115	-1.55	Idem
11	414.10 – 414.24	11.1	60–80	-1.02	Syn-breccia pyrites
		11.2	60–80	-1.15	Idem
		11.3	80–115	-1.30	Idem
		11.4	80–115	-0.95	Idem
		11.5	115–170	-1.27	Idem
		11.6	115–170	-1.13	Idem
7	385.40 – 385.64	7.1	-16	+ 3.04	Post-breccia pyrite; fresh, impure concentrate
		7.1.1	-16	-2.18	Idem; cleaned concentrate
		7.1.2	-16	-2.38	Idem; cleaned concentrate
		7.2	-16	+ 4.60	Post-breccia pyrite; coated, impure concentrate
		7.2.1	-16	+ 0.46	Idem; cleaned concentrate
		7.3	-16	-2.29	Post-breccia pyrite; coated
		7.4	-16	-1.80	Post-breccia pyrite; fresh
8	394.42 – 394.60	8.1	-16	-2.29	Post-breccia pyrite; fresh
		8.2	-16	-3.31	Post-breccia pyrite; coated
6	382.49 – 382.63	6.1	-16	-3.61	Post-breccia pyrite; fresh
		6.2	-16	-4.66	Post-breccia pyrite; coated
5	276.15	5.1	-80	-14.77	Post-breccia pyrite; fresh associated with (kaolinite) clays

the pyrites) and of equally tiny, but quite frequent inclusions of pyrrhotite in the pyrites. Both observations set this group of pyrites distinctly apart from all the others.

The S-isotope compositions of most of the associated fresh and coated pyrites vary from -4.66 to -1.80 $\delta^{34}\text{S}/\text{‰}$ (Table 1-V; separate 6.1; 6.2; 7.3; 7.4; 8.1 and 8.2), with the coated pyrites always being lighter than their fresh associates; an exception is represented by separates 7.1 and 7.2 (Table 1-V). These were the first impure separates obtained, representing a pair of associated fresh and coated pyrites. Preliminary analysis of these resulted in the heaviest S-compositions of all, respectively +3.04 and +4.60 $\delta^{34}\text{S}/\text{‰}$, the heavier sulphur occurring in the coated pyrites. The analyses were re-run after additional cleaning of the remaining parts of the impure concentrates. This resulted in the extraction of pure pyrites of both fresh and coated original concentrates. The re-runs of the two cleaned fractions obtained from the original impure concentrate of fresh pyrites (Table 1-V; separate 7.1) yielded $\delta^{34}\text{S}$ values of 2.18 ‰ and -2.38 ‰ respectively (Table 1-V; separates 7.1.1 and 7.1.2), thus being in the range of the other fresh post-breccia pyrites of this paragenetic group. The cleaned fraction obtained from the original (impure) concentrate of coated pyrites (Table 1-V; separate 7.2), however, resulted in a $\delta^{34}\text{S}$ value of +0.46 ‰ (Table 1-V, separate 7.2.1), thus confirming a heavier S-composition than that of the fresh associates and the heaviest of all of the post-breccia pyrites of this paragenetic group.

The second paragenetic group of post-breccia pyrites is represented by only one fracture sample containing fresh pyrites associated with white (kaolinitic) clays (Plate 1:1-5). These are microscopically free of inclusions and are not intergrown with other ore minerals. Pure mineral separates were therefore easily obtained. These pyrites yielded $\delta^{34}\text{S}$ values of -14.77 ‰ , thus being of very light S-composition in the context of the previously discussed results.

The surface exposure specimens/pyrite concentrates are shown in Table 1-VI. They all lie within the range of -0.49 to -3.63 $\delta^{34}\text{S}/\text{‰}$ (CDT) compositions. No S-isotope fractionation related to primary grain-size variations could be observed (Table 1-VI; separates 12.1, 12.2 and 12.3), nor any influence of the mineralised redox fronts (Table 1-VI; separates 13.1 and 13.2). Paragenetic influences are also absent, as shown by local and regional comparisons (Table 1-III). Although pyrite separates 12.1, 12.2 and 12.3 are from closely sampled strongly hydrothermally altered phonolites with cavernous leaching and advanced argillic decomposition, local paragenetic (and grain-size) variations do, however, exist. Separates 13.1 and 13.2 comprise two continuous parts of one large sample of reduced phonolite from a mineralised redox front hosting pitchblende nodules. The pyrites are from the non-mineralised, reduced rock portions,

are similarly fine-grained, and paragenetic differences between the two rock portions are non-existent. Separate (14) was collected independently and prepared by N. Waber and consists of hydrothermal pyrites from an additional “potassic rock” surface exposure specimen. In spite of the local and regional paragenetic differences, the S-isotope variations fall within the same range (Table 1-VI).

TABLE 1-VI
Isotope compositions of hand specimen pyrites from surface exposures.

Sample no.	Sample		Separate		$\delta^{34}\text{S}_{\text{‰}}$ CDT	Observations
	code	location	no.	size		
12	U-4(A)	near 9-1RH	12.1	< 0.5 mm	-0.49	Hydrothermal fine-grained pyrite
	U-4(B)	idem	12.2	1-3 mm	-2.40	Hydrothermal medium-grained pyrite
	U-4(D)	idem	12.3	> 8 mm	-2.05	Hydrothermal coarse-grained pyrite
13	U-7(E)	near 8-1KK	13.1	115-170#	-0.54	Hydrothermal fine-grained pyrite
	U-7(G)	idem	13.2	115-170#	-3.63	Idem
14	OUM-102	n.i.	14.1	n.i.	-3.26	Hydrothermal pyrite of reduced phonolite (“matrix pyrite”)

n.i. = not identified

The pyrites extracted from massive pitchblende nodules are shown in Table 1-VII; these include zonal structures of the nodules and/or the paragenetic positions of the separated pyrite generations. The results are, in general, quite variable, not only within different zones of one individual nodule, but also for equivalent zones of different nodules. However, if one considers the mineralogical-textural evidence regarding formation of the nodules and their pyrite generations, some systematic variations can be established. First, only nodules (15), (17) and (18) will be discussed. The lightest S-isotope compositions occur in those pyrites from the nodule-forming pitchblende zones containing the three nodules. Exceptions are represented by the separates 17.1 and 18.2 (Table 1-VII). The former, however, was an impure concentrate and therefore only the two re-runs of its cleaned fractions (nos. 17.1.1 and 17.1.2) seem reliable. The second separate (no. 18.2; Table 1-VII) consists of a mixture of two pyrite generations: an older one of pre-pitchblende, hydrothermal origin (of heavier isotope composition),

TABLE 1-VII
Sulphur isotope compositions of pyrites from the massive pitchblende nodules.

Sample current no.	Sample code	S e p a r a t e		Z o n e s o f n o d u l e s					Observations
		no.	size	Silicate core	P i t c h b l e n d e z o n e			Silicate shell	
					pre-pitchblende	syn-pitchblende	undefined		
15	S/N-24	15.1	≤ 3 mm	-8.85					Mixture of two pyrite generations
		15.2	+ 30#		-12.20				“Pyrite layer”
		15.3	30–48#		-13.31				Idem 15.2, finer grain-size
		15.4	-48#		-13.11				Idem 15.3, finer grain-size
		15.5	≤ 1.5 mm					-8.13	–
16	KU-3	16.1	≤ 1.5 mm					-2.20	Pyrite poor, small nodule
		16.2	≤ 1.5 mm				-2.40		Idem 16.1
17	KU-6	17.1	≤ 1 mm			-3.14			Impure concentrate
		17.1.1	≤ 1 mm			-12.39			Idem 17.1, re-run after cleaning
		17.1.2	≤ 1 mm			-11.83			Idem 17.1.1
18	VII	18.1.1	≤ 0.5 mm	-3.78					–
		18.1.2	≤ 0.5 mm	-3.81					–
		18.2	≤ 1.5 mm				-5.16		Mixture of two pyrite generations
		18.3	≤ 1.5 mm					-7.25	–

and a younger one, syngenetic with the pitchblende nodule-forming processes (isotopically lighter). The two generations could be identified microscopically, but separation was not possible. Thus, the lightest S-isotope compositions seem restricted to low-temperature pyrites, independent of their origin, which can be either fossil water-table-related (i.e. pre-pitchblende, but distinctly post-hydrothermal as inferred in the case of the “pyrite layer” pyrites of separates 15.1, 15.3 and 15.4 (Table 1-VII)), or syn-pitchblende, related to the main nodule-forming process (separates 17.1.1 and 17.1.2; Table 1-VII).

Heaviest S-isotope compositions occur in those pyrites separated from the silicate core of nodule VII (18.1.1 and 18.1.2; Table 1-VII). These are typically fine-grained, sometimes slightly corroded hydrothermal pyrites. The composition of separate 15.1 pyrites from the silicate core of nodule S/N-24 (Table 1-VII; Plate 1:1-14) refers to a mixture of pre-pitchblende hydrothermal pyrite and of low-temperature post-hydrothermal pyrite.

The nature and genesis of the external silicate shell of the nodules could not be studied in greater detail, mainly for two reasons: a) nodules in their original genetic environment were not found, and b) the samples studied from the Urânio do Brasil collections contain only relict portions of the external silicate shells. Pyrite abundances in the silicate shell are similar to the inner pitchblende zones of the respective nodules (with the exception of the “pyrite layer” of sample S/N-24, Plate 1:1-14; Table 1-VII) and the major silicate composition is similar to the silicate cores of the nodules. These pyrites seem best explained as remnants from selective pitchblende dissolution during the processes of contractive growth of the nodules. In this case their isotope composition should be variable, depending on the relative proportions of hydrothermal and low-temperature pyrites present in the analysed mineral separate. This appears to be supported in the case of pyrites 15.5 and 18.3 (Table 1-VII).

Sample KU-3 (no. 16, Table 1-VII) does not conform to the above model. It is a generally small, pyrite-poor nodule that was selected for comparative studies because of its less well-developed character. The two analysed pyrite separates, from the external silicate shell and the pitchblende zone, yielded very similar S-isotope values (within the 1 analytical error limit), these being the heaviest of all compositions obtained from the massive nodule pyrites and indistinguishable from the main hydrothermal pyrites (Table 1-VII, no. 16, separates 16.1 and 16.2).

Analyses of *samples of (4), (19), (20) and (21)* (Tables 1-I, 1-II and 1-III) are still in progress. They refer to pyrites of deep-seated hydrothermal U-mineralisation origin (no. 4), and to sulphates resulting from recent sulphide oxidation (nos. 19-21).

4. Conclusions and summary

Pyrites from the reduced phonolites and nepheline syenites, breccias, redox front samples and massive pitchblende nodules can be classified mineralogically and texturally into hydrothermal (=high-temperature) and low-temperature pyrites. Hydrothermal pyrites occur in the F1 and F4 drillcore samples and in surface open pit hand specimens. The F4 samples can be subdivided into pre-breccia, syn-breccia and post-breccia (hydrothermal) pyrites. The S-isotope compositions of all the hydrothermal pyrites lie within a quite narrow interval ranging from +1.24 to -3.63 $\delta^{34}\text{S}_{\infty}$ (CDT), consistent with an origin from upper mantle-derived (mafic) magmas/rocks. Interestingly, this is also the typical compositional range of sulphides from porphyry copper deposits.

Most hydrothermal pyrites can, doubtlessly, be attributed to the “potassic rock”-forming hydrothermal process associated with Zr-REE-Mo-U – mineralisations that characterise the mine. However, some of the post-breccia hydrothermal pyrites in particular, for instance the association of fresh and dark coated pyrites (Tables 1-III, 1-V; samples 6, 7 and 8), may represent a distinct, younger hydrothermal event, as indicated by the mineralogical/paragenetic character of the pyrites.

Low-temperature (post-hydrothermal) pyrites occur only in the massive pitchblende nodules which could be separated from the pitchblende zones. These pyrites show the lightest S-isotope compositions (below -10 $\delta^{34}\text{S}_{\infty}$ (CDT)), probably suggesting biological reworking of sulphur during the development of pitchblende concentration related to water-table formation (Tables 1-III and 1-IV; pyrite separates 15.2 – 15.4; 17.1.1 and 17.1.2). The core and external silicate zones of the pitchblende nodules commonly contain non-separable associations of hydrothermal and low-temperature pyrites present in variable proportions, but always of heavier S-isotope compositions than the typical low-temperature pyrites.

The isotopically lightest pyrites, apart from the low-temperature pyrites from the pitchblende nodules, were found in one F4 sample from a deep-seated post-breccia fracture (Tables 1-III, 1-V; sample 5). The association of these pyrites with kaolinite, and the lack of other associated and included sulphides, distinguishes them paragenetically from the typical post-breccia hydrothermal pyrites (Tables 1-III, 1-V), indicating the possibility of a low-temperature origin together with deep fracture circulation and reprecipitation of biologically reworked sulphur. The influence of: a) a conductive zone (Tables 1-III, 1-IV; sample 1), and b) of a U-mineralised redox front at a few cm distance (Tables 1-III, sample 13) on the S-isotope composition of the pre-existent hydrothermal pyrites could not be characterised.

Analyses of pyrites from deep-seated, hydrothermal, higher U-grade mineralisations (Tables 1-I – 1-III, sample 4) and of recent sulphates (Tables 1-I – 1-III, samples 19-21) are still in progress and results will be forthcoming in due course.

Appendix 1:1

PLATES 1:1-1 – 1:1-18

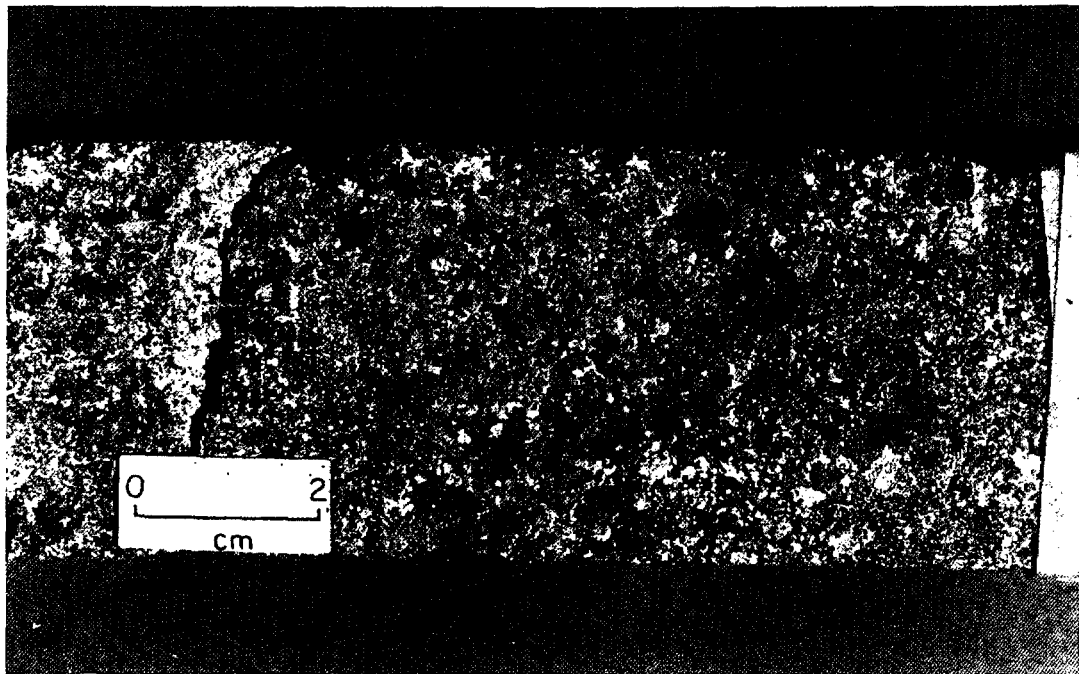


PLATE 1:1-1. Reduced medium- to coarse-grained hypabyssal phonolite from a conductive zone. Note open porosities and white clays. The rock is rich in pyrite. Pyrites are of max. grain-size ~0.5 mm and occur disseminated throughout the rocks and in the pores (sample 1; F1/69.43 – 69.63 m).

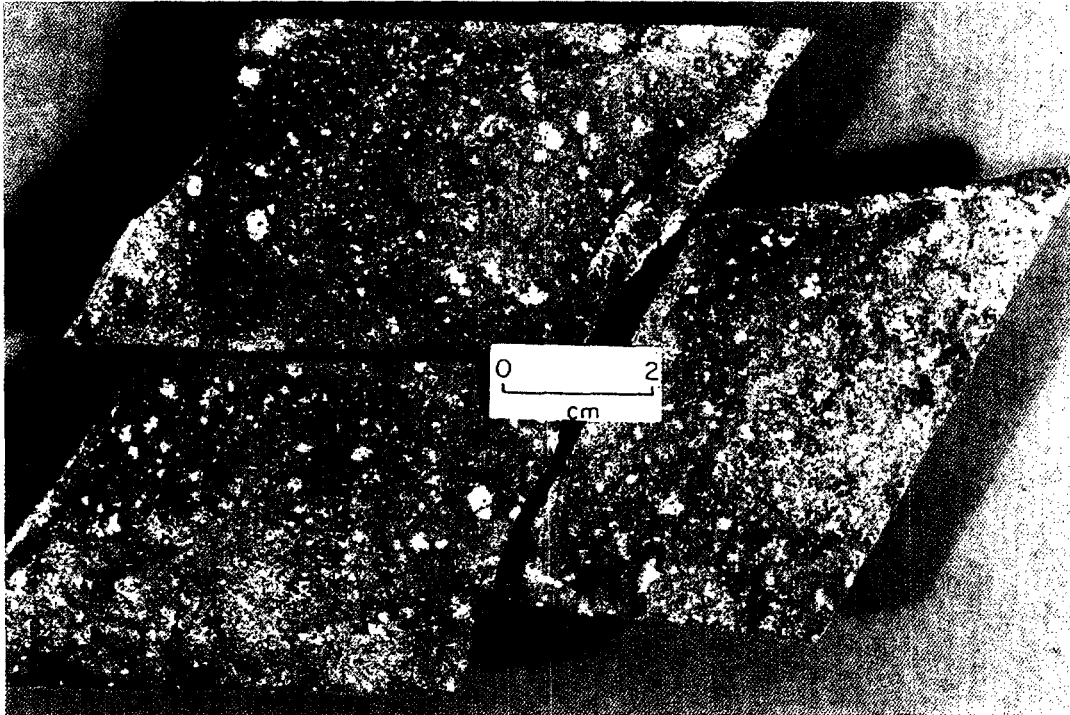


PLATE 1:1-2. Reduced porphyritic phonolite. Pyrites of mean grain-size ~ 0.25 mm occur finely disseminated throughout the rock and in the subordinate micropores (sample 2; F1/113.65 – 113.79 m).

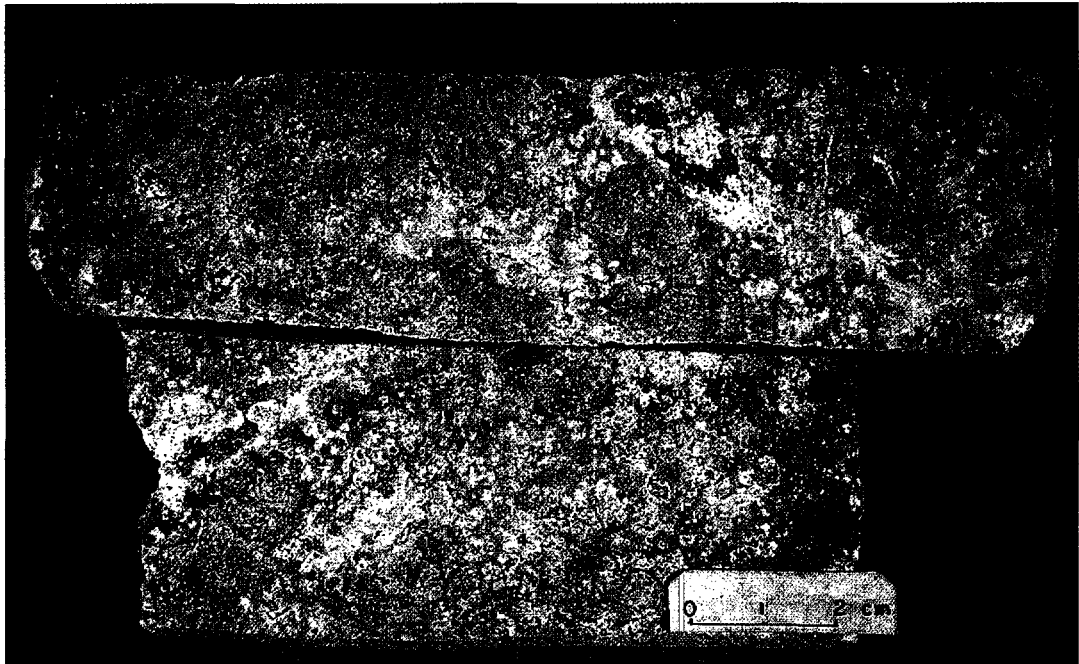


PLATE 1:1-3. Reduced subvolcanic phonolite with minor nepheline syenite pegmatoids of minor microporosity. Pyrites of mean grain-size ~ 0.25 mm are finely disseminated throughout the rock and in the pores. The analysed pyrite concentrate was separated by N. Waber (Univ. Bern) and identified as "matrix pyrite" (sample 3; F1/125.30 – 125.41 m).

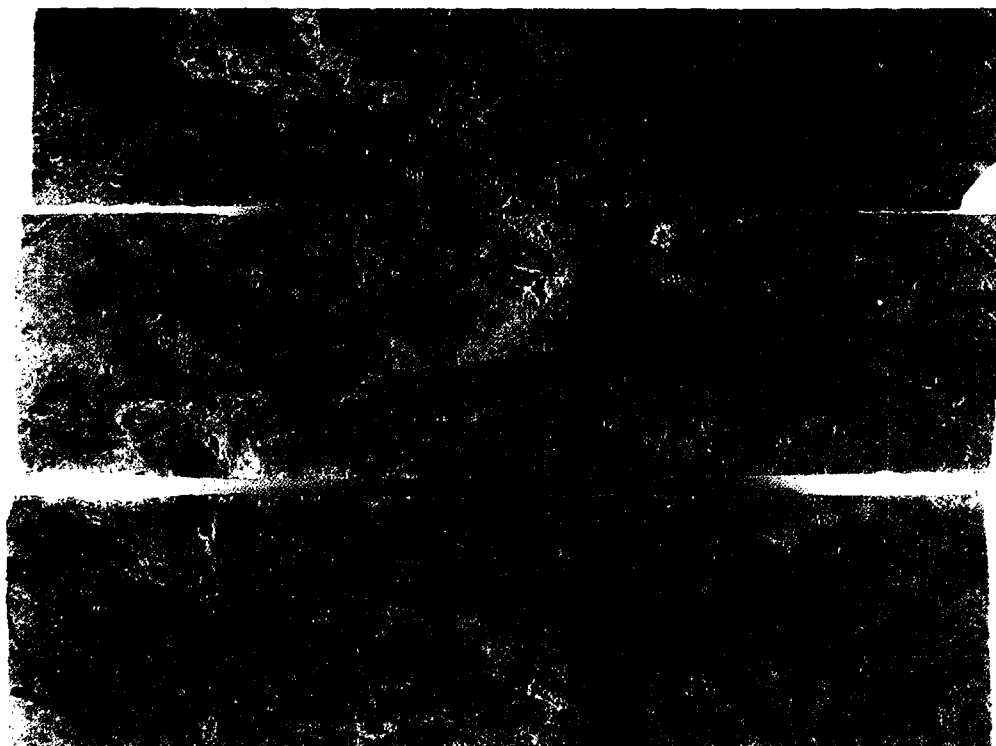


PLATE 1:1-4. Reduced breccia with hydrothermal Zr (-REE)-U-pyrite (-sulphides) mineralisation (black-coloured circles) disrupted by post-breccia fracturing. Pyrites are microcrystalline and aggregated with other ore minerals. Incipient recent light-grey sulphate and bluish secondary Mo-mineral/ilsemannite alteration products [e.g. enclosed by 50 cps-circles (sample 4; F4/242.57 – 242.95 m; 243-1A; scale: circle Ø = 27 mm)] are also present.



PLATE 1:1-5. Pyritised and argillised (white kaolinite clays) post-breccia fracture in reduced breccia (sample 5; F4/276.15 m).

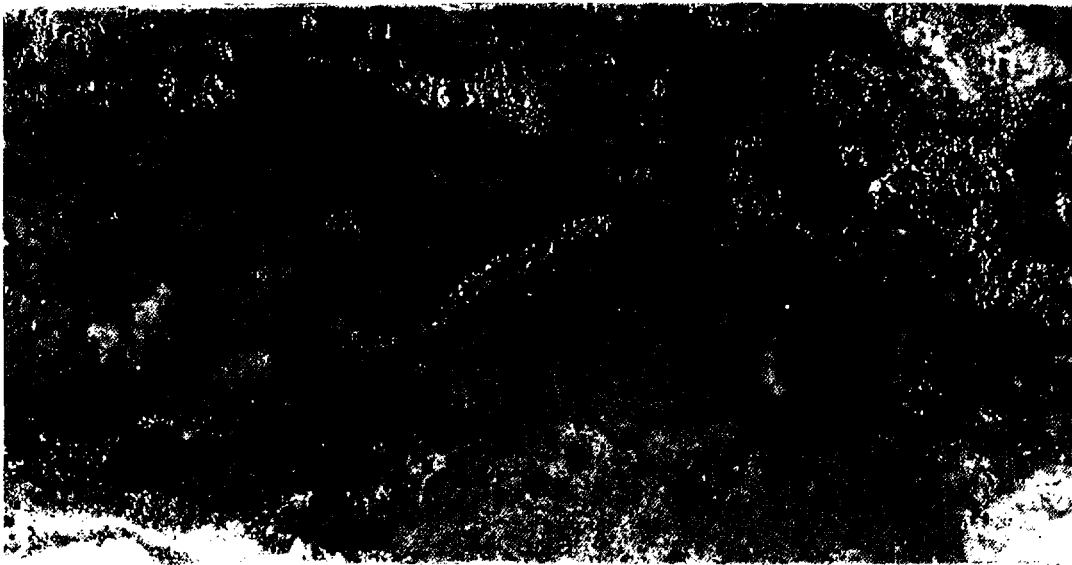


PLATE 1:1-6. Post-breccia fractures (circle) and pores from a nepheline syenite fragment in reduced breccia mineralised with fresh-yellow and silver-grey (galena-like material) coated pyrites (sample 6; F4/382.49 – 382.63 m; 383-1A; scale: circle \varnothing = 27 mm).



PLATE 1:1-7. Post-breccia fracture (in reduced breccia) mineralised with silvery-grey coated and uncoated pyrites and minor white clays (sample 7; F4/385.40 – 385.64 m; 386-1A; 2.5 x nat. size).



PLATE 1:1-8. Post-breccia fracture (in reduced nepheline syenite xenolith) mineralised with silvery-grey coated and uncoated pyrites (sample 8; F4/394.42 – 394.60 m; 394-1A (?); 2.5 x nat. size).

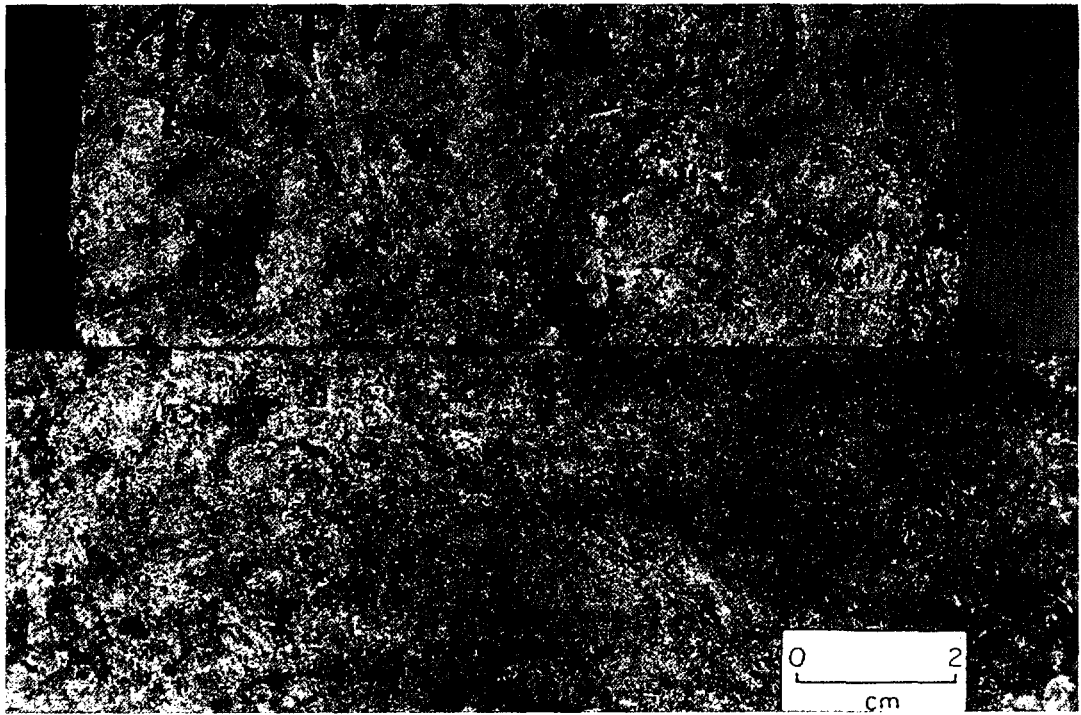


PLATE 1:1-9. Reduced transitional phonolite to nepheline syenite xenolith of breccia, very weakly microporous and non-fractured with finely disseminated pyritisation (max. dimensions of pyrites ≤ 0.3 mm) and argillised (sample 9; F4/396.57 – 396.83 m).

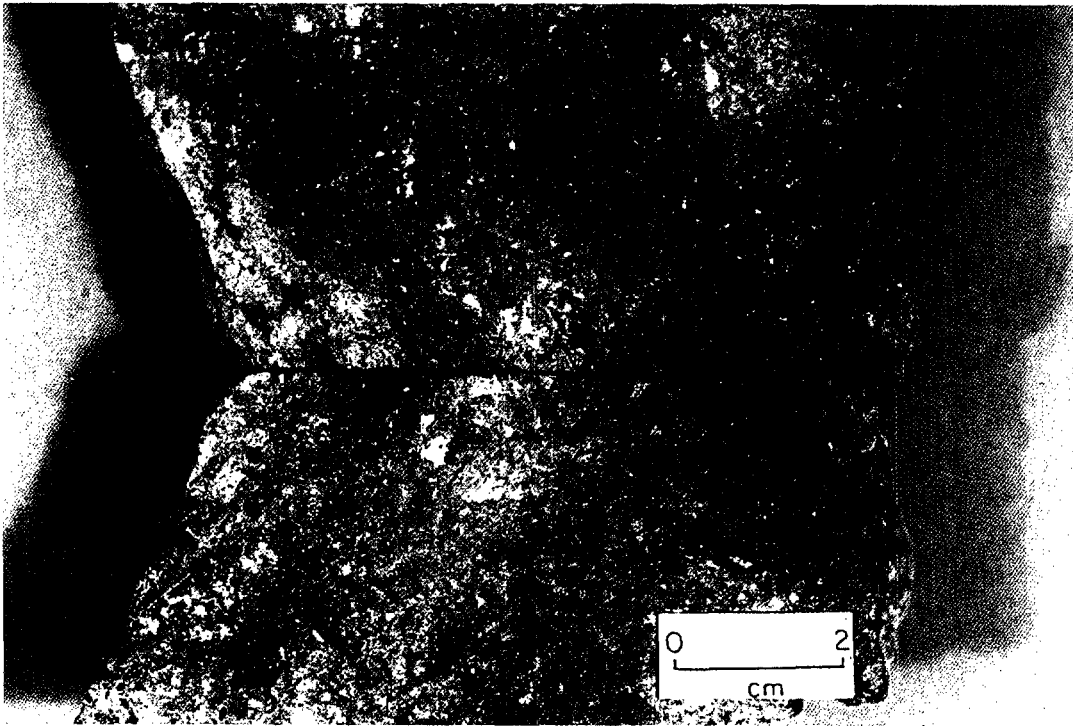


PLATE 1:1-10. Reduced, strongly porous and pyritised medium-grained phonolite xenolith (of breccia). Pyrite grain-sizes are around 1.0 mm (sample 10; F4/407.57 – 407.67 m).

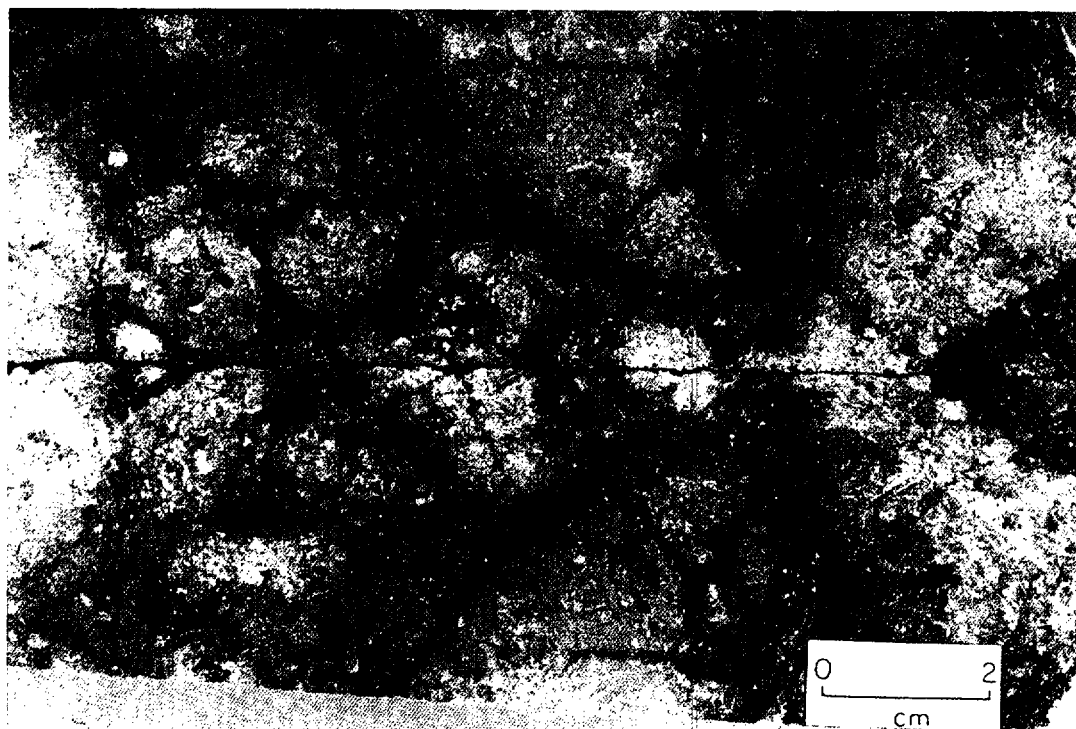


PLATE 1:1-11. Reduced, strongly pyritised breccia matrix in clast-supported breccia. Note microporosity of breccia matrix. The syn-breccia matrix pyrites are fine-grained and around 0.2 mm in size (sample 11; F4/414.10 – 414.24 m).

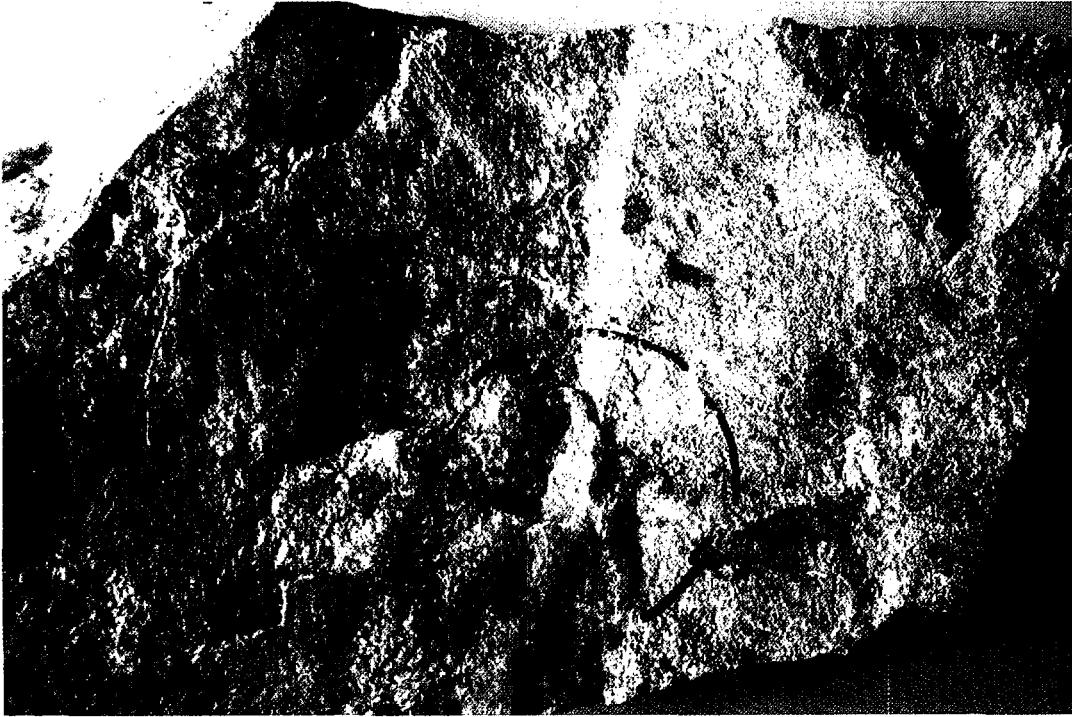


PLATE 1:1-12. Hand specimen of U-mineralised redox front in fine-grained phonolite. Note white versus light-grey (with darker nodules) coloured front of total pitchblende dissolution and white versus yellow-brown front of HFO (hydrous ferric oxides, mainly limonite) precipitation. Pyrites were selectively extracted from the fine-grained reduced phonolite avoiding the pitchblende nodules (sample 13; about 1.6 x nat. size).

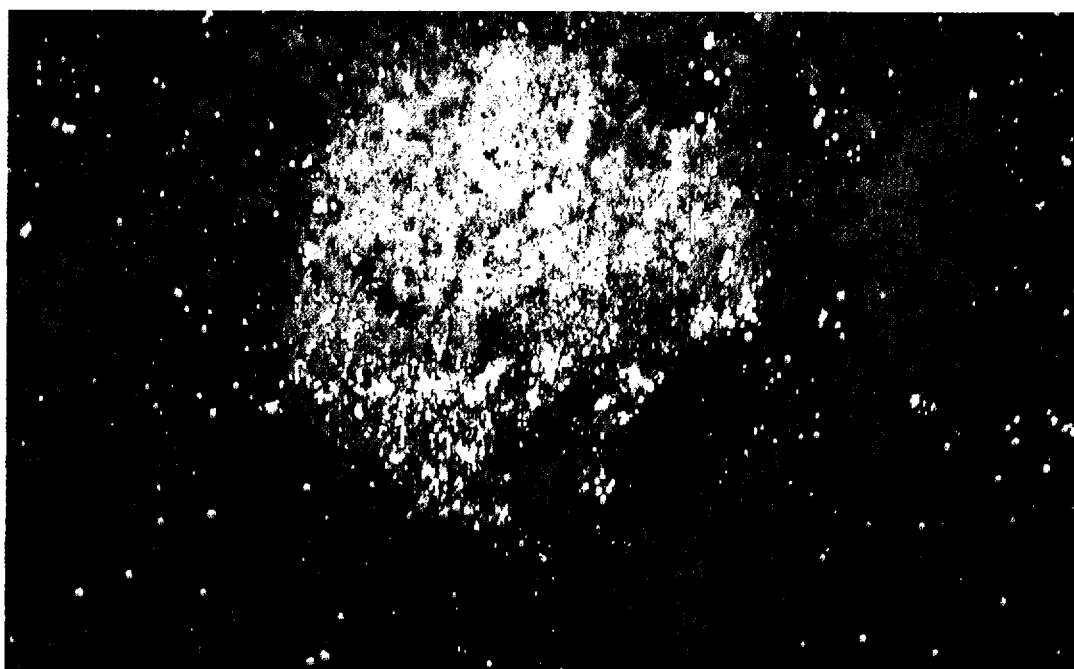


PLATE 1:1-13. Low magnification reflected light micro-photograph of a pitchblende nodule from a mineralised redox front in fine-grained (reduced) phonolite. The rounded nodule (light-grey; dense material in the centre) has a natural size \varnothing of around 2.5 mm and consists of cryptocrystalline pitchblende impregnated in the highly porous silicate rock matrix (silicates are medium-grey coloured; porosities almost black). Fine-grained pyrites (white coloured regular microcrystals of high reflectivity and natural grain-size between 0.01 – 0.05 mm) occur in small amounts regularly disseminated throughout the rock. In the pitchblende nodule the pyrites are highly concentrated and coarse in size when compared to the rock. This illustrates the presence of a second, additional pyrite generation, exclusively associated with the U-nodule formation.

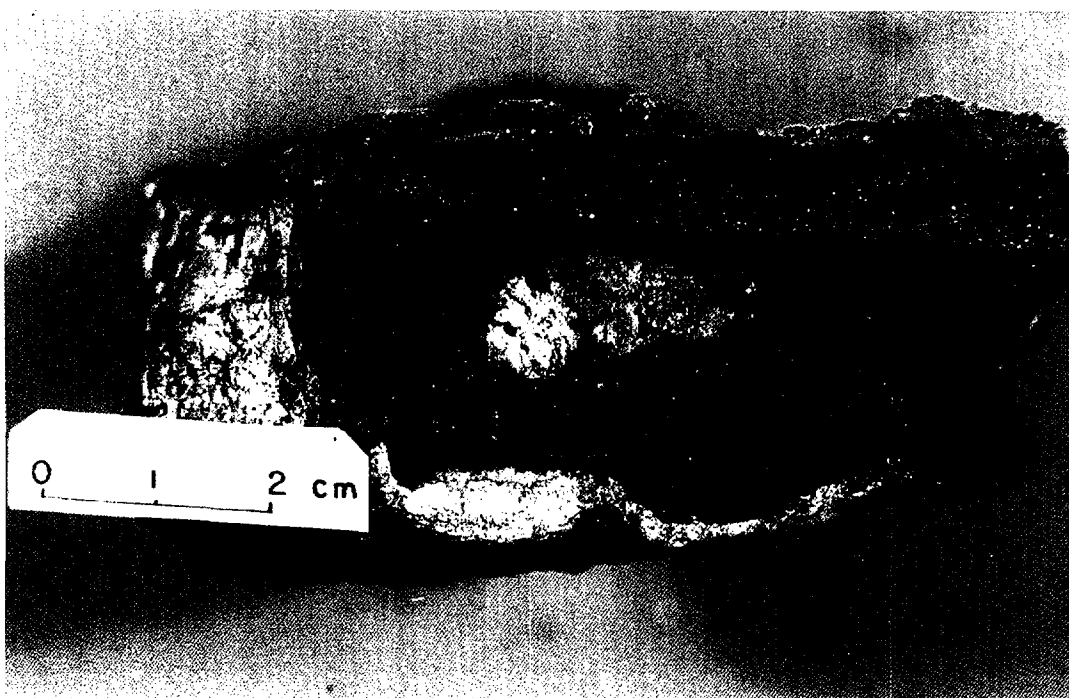


PLATE 1:1-14. Massive pitchblende nodule showing the silicate core (whitish) surrounded by the main pitchblende zone (black) and a discontinuous external silicate shell (whitish). The pitchblende zone contains, in the upper part of the photograph, a layer of pyrite (yellowish) of post-hydrothermal and pre-pitchblende origin. Coarse pyrites of syn- pitchblende origin (sample 15; S/N-24) are disseminated throughout the pitchblende zone.

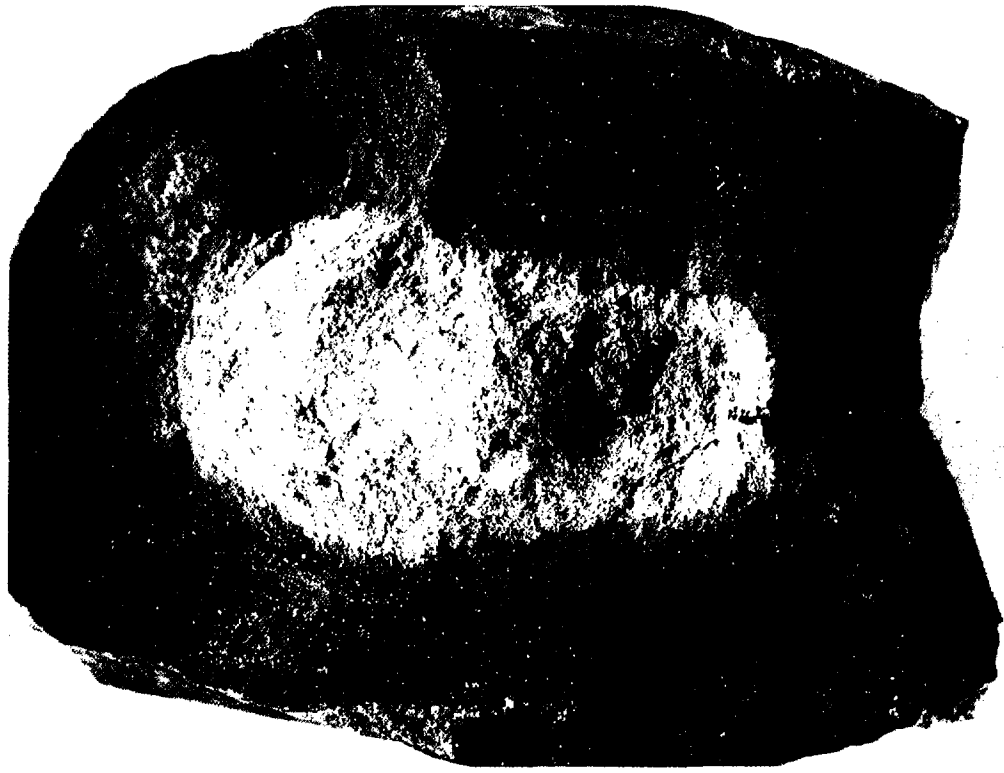


PLATE 1:1-15. Massive pitchblende nodule with silicate core (white) and massive pitchblende zone containing disseminated medium-grained pyrites (sizes Ø: 0.5 – 1.5 mm) of syn-pitchblende origin. Lower right-hand corner of nodule is shown in more detail in Plate 1:1-16 (sample 18; VII; about 1.7 x nat. size).

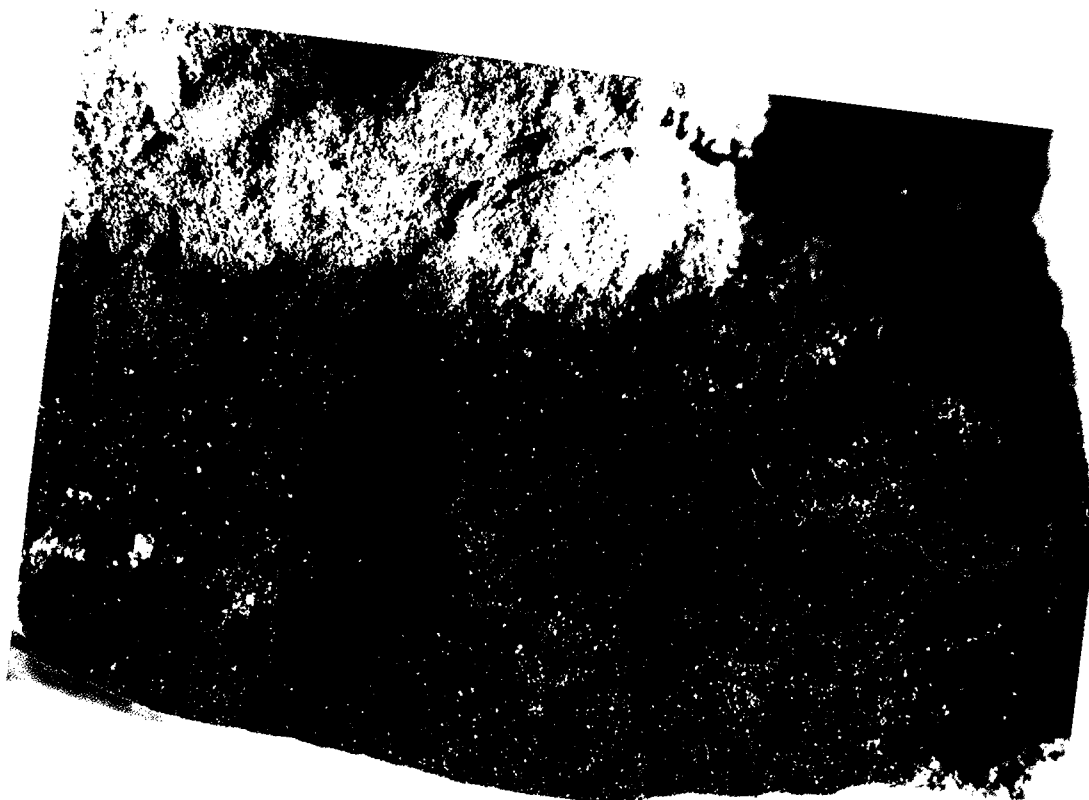


PLATE 1:1-16. Detail of massive pitchblende nodule VII (Plate 1:1-15) showing syn-pitchblende pyrites within the massive pitchblende zone (sample 18; VII; about 3.4 x nat. size).



PLATE 1:1-17. Recent sulphates (colourless-whitish needles) from the reduced side of the mineralised redox front hosted by pseudoleucite phonolite. Note parts of two pitchblende nodules (black) of \varnothing ~5 mm and ~12 mm respectively cut off by the lower limit of the photograph (sample 19; 04/02).



PLATE 1:1-18. Recent sulphates (bluish-whitish needles and dense mass) from a strongly pyritised phonolite (sample 20; M-1).

Appendix 2

**Selective phase extraction analyses on four rock samples
from the Osamu Utsumi mine site, Poços de Caldas,
Brazil.**

Contents

	page
1. Introduction	229
2. Method and materials	236
2.1. Samples and preparation	236
2.2. Extractions	236
2.2.1. Morgan's extraction	237
2.2.2. TAO	237
2.2.3. CDB	237
2.2.4. Total digestion	238
3. Results and samples	238
4. Conclusions	244
5. References	244

Appendix 2

Selective phase extraction analyses on four rock samples from the Osamu Utsumi mine site, Poços de Caldas, Brazil.

R. EDGHILL

Alligator Rivers Analogue Project, Australian Nuclear Science & Technology Organisation, Lucas Heights Research Laboratories, Australia.

1. Introduction

Four phase selective reagents were used to extract different adsorbed and mineral phases with associated radionuclides from four rock samples from the Poços de Caldas region. The four extractions undertaken were:

- Morgan’s sodium acetate reagent for the removal of species adsorbed onto solids or associated with carbonates.
- Tamm’s acid oxalate (TAO) for the extraction of amorphous phases of Si, Al and Fe (such as ferrihydrite).
- Citrate dithionite bicarbonate (CDB) for the extraction of crystalline iron oxides and contained elements.
- Total digestion.

The following are excerpts from Tim Nightingale’s MSc Thesis (Mobilisation and Redistribution of Radionuclides during Weathering of a Uranium Ore Body. University of Sydney, Australia (1988)), and explain some of the properties and effects of the phase selective reagents.

“2.7.1 Aims of selective phase extraction schemes

Many selective phase extraction schemes have been described in the literature, each one tailored to suit the particular requirements and constraints of the investigation. The diversity not only of schemes but also of different substrates makes intercomparison difficult. Although it is unlikely that any single extraction scheme could be universally accepted as a standard for use on all possible substrates, most schemes tend to concentrate on the distribution of metal species in five general forms:

- (a) Exchangeable metal species.
- (b) Metals associated with carbonates.
- (c) Metals associated with Fe and Mn oxides and oxyhydroxides.
- (d) Organically bound metals.
- (e) Metals in chemically resistant minerals.

2.7.3 Metals adsorbed or associated with carbonates

Most authors choose to follow an extraction of the exchangeable species with one by a reagent that is acidic enough to dissolve carbonate species yet mild enough in its action to leave slightly more acid-soluble minerals (such as amorphous ferric oxyhydroxides) intact. A 1 M sodium acetate solution buffered at pH 5.0 with acetic acid* is commonly employed for this purpose and was used as early as 1935 by Morgan (1935). Grossman and Millet (1961) reported no change in the organic carbon and free iron concentrations in non-calcareous soil samples after being in contact with this solution for nine weeks. Tessier *et al.* (1979) studied the effectiveness of this reagent in dissolving calcium from the carbonate fraction of marine sediments and found that dissolution was complete after a period of about 4 hours at room temperature. This treatment was also recommended by Nirel *et al.* (1985), Rapin *et al.* (1983) and Förstner *et al.* (1981). In each case it was used as a second treatment within a sequential extraction scheme for the specific purpose of dissolving the carbonate-bound fraction of heavy metal species occurring in polluted sediments. Schwertmann (1979) also recommended it for similar use with clay-containing substrates.

The fact that Morgan's reagent was used for the extraction of heavy metals warrants its possible application for substrates containing uranium, thorium and other actinides. In particular the fact that the solution is slightly acidic and contains acetate, a potentially complexing ion, suggests that it may be more effective in retaining these nuclides in solution than say magnesium chloride solution.

* For the sake of convenience this will be termed "Morgan's reagent" from hereon.

Tessier *et al.* (1979) reported that the apparent levels of Cu, Ni, Pb and Zn in the carbonate-bound fraction (i.e. in the extract of Morgan's reagent) were well in excess of what was expected for dolomite on the basis of available information on trace metal contents. They proposed that this was due to the incomplete (or negligible) dissolution of specifically adsorbed trace metals by the MgCl solution, the preceding reagent in the extraction scheme. The same considerations may well apply to uranium. Several authors have shown that uranium tends to adsorb very strongly onto the substrate at pH values above 5.0. For example Hsi and Langmuir (1985) demonstrated this using both ferrihydrite and goethite as the substrate. From this point of view Morgan's reagent, which is buffered at pH 5.0, would appear to be an excellent reagent for removing specifically adsorbed uranium, less so for thorium. Furthermore, the tendency of uranium and thorium to form complexes with organic ligands would tend to favour their retention in solution in the presence of acetate. In the present study the use of Morgan's reagent was investigated for the purpose of extracting both the loosely bound 'exchangeable' fraction, that associated with carbonates, and the specifically adsorbed fraction.

2.7.4 Metals associated with Fe and Mn oxides

Oxides of Fe and Mn are known to play an important part in the adsorption of metal species in both soils and sediments. Many authors have chosen to make a distinction between poorly crystalline iron III oxyhydroxides, which give only poorly defined X-ray diffraction (XRD) patterns, and more crystalline iron oxides such as hematite and goethite. The distinction is of particular importance with regard to the much greater surface area of the poorly crystalline oxide. This can impart a high adsorptive capacity and chemical activity to soils and sediments.

The differing effects of 'amorphous' and crystalline iron oxides on soil properties have long been recognised. To give three examples, Schwertmann (1959), Mackenzie (1949) and Taylor (1959) noted the occurrence of the amorphous form although extreme difficulty was encountered in characterising it due to its very low concentration in soils. Chukrov *et al.* (1972) studied a natural ferric oxide sample and were able to characterise it in terms of its X-ray reflections and infra-red adsorption. It was then considered to be an identifiable mineral and given the name 'ferrihydrite'. Schwertmann and Taylor (1977) published electron micrographs of specimens of natural ferrihydrite, showing it to consist of spheres with dimensions of less than 100 nm. Hematite consisted of better defined crystals of similar dimensions while goethite consisted of needles up to 50 nm long. Johnston and Lewis (1983) published a series of electron micrographs detailing the

transformation of synthetic ferrihydrite to hematite. The X-ray reflections corresponding to stages in the transformation were also shown. It could clearly be seen how poorly defined peaks of ferrihydrite gave way to sharp peaks of hematite.

The dissolution of ferrihydrite (this name will be used henceforth) is commonly achieved using a solution of ammonium oxalate buffered with oxalic acid. The use of such a method was reported by Tamm (1922 and 1934) and the reagent will be referred to as 'Tamm's reagent' from hereon. In order to make it more selective towards less crystalline iron oxides and oxyhydroxides, Schwertmann (1964) proposed a modification. It was found that in the absence of light at pH 3 the dissolution of the crystalline oxides was greatly reduced. McKeague and Day (1966) found that 0.2 M ammonium oxalate solution, buffered at pH 3.0 with oxalic acid and also used in the dark, was highly selective towards the 'amorphous' form. They proposed this extraction as an aid in differentiating various classes of soils in relation to their relative contents of 'amorphous' and crystalline iron oxides.

Pawluk (1971) used the same procedure, in the absence of light, to remove traces of 'amorphous' iron oxides for the purpose of enhancing the intensities of the XRD reflections of crystalline oxides. Conversely Pawluk (1972) tested the repeated effect of the Tamm's extraction and found that the second and third treatments were capable of completely dissolving the crystalline oxides goethite and lepidocrocite. Prolonged extraction could remove all traces of these reflections although the treatment decreased the relative intensities of hydrous micas and trioctahedral chlorite (a mineral that features in this study).

Both Chau and Zhou (1983) and Sondag (1981) employed the Tamm's reagent to extract 'amorphous iron oxides' within a sequential extraction scheme in the application of geochemical exploration. Chau and Zhou showed that up to 20% of a synthetically prepared magnetite was dissolved in the Tamm's treatment, demonstrating that the reagent is not entirely selective towards non-crystalline iron oxides. They proposed a 30 minute extraction with a solution of 0.25 M hydroxylamine hydrochloride and 0.24 M HCl at 70°C as the most efficient method of dissolving 'amorphous' iron oxides, showing that it dissolved far less magnetite than the Tamm's reagent.

Le Riche and Weir (1963) and de Endredy (1963) employed the Tamm's reagent in the presence of ultraviolet light to extract the total iron oxide content of soils. They also reported that this method dissolved part of the soil organic content. Sondag (1981) employed the standard Tamm's extraction (i.e. in the dark) to dissolve 'amorphous' iron oxides, then the same reagent in the presence of ultraviolet light to dissolve crystalline

oxides. Megumi and Mamuro (1976) used the same method to extract uranium and thorium associated with goethite.

2.7.5 Dissolution of crystalline iron oxides

Dissolution of crystalline iron oxides is normally achieved by a combination of a reducing agent and a complexing agent. The two most frequently used combinations are citrate/dithionite and hydroxylamine hydrochloride/acetic acid.

In early studies of iron oxides their dissolution was achieved by simply reducing the iron III with a solution of sodium dithionite, thereby liberating the more soluble iron II species. This technique was described by Mackenzie (1954) and was later employed by Taylor (1959) and Norrish and Taylor (1961) who used it to study the aluminium content of soil goethites.

Mehra and Jackson (1960) proposed a modification to this procedure whereby sodium citrate was added to the solution as a complexing agent and sodium bicarbonate was employed to buffer it at pH 7.3. Two extractions were performed at 80°C for 15 minutes. Coffin (1961) suggested a variation of this technique whereby the citrate-dithionite solution was buffered at pH 4.75 with citric acid and a single extraction performed at 50°C for 30 minutes. It was reported that no clay minerals other than nontronite (1 layer silicate mineral resembling smectite) were significantly affected by this procedure. It also showed good reproducibility with the Mehra and Jackson reagent with regard to the quantities of iron and aluminium extracted. Holmgren (1967) suggested that the extent of the extraction was dependent more on the amount of citrate present than the pH, and that the maintenance of a high pH helped to prevent the decomposition of dithionite. A single overnight extraction at room temperature was employed and the pH was maintained above 6. Above critical concentrations of dithionite and citrate, no additional iron was dissolved by further addition of these reagents.

2.7.6 Comparative dissolution of 'amorphous' and crystalline oxides

The Mehra and Jackson reagent, which will henceforth be referred to as the CDB reagent (short for citrate-dithionite-bicarbonate), was subsequently used in conjunction with the Tamm's reagent by several authors in order to differentiate between 'amorphous' and crystalline iron oxides in soils. For example Blume and Schwertmann (1969) used the ratio of 'amorphous' to crystalline iron, measured by sequential treatments with the Tamm's and CDB reagents, to study the genesis of soil profiles.

Included in this study was some interpretation of the extractability of both manganese oxides and aluminium.

Arshad *et al.* (1972) examined the effect of the Tamm's and CDB reagents on a selection of trioctahedral layer silicates and found that the release of cations from these minerals increased with decreasing particle size, becoming significant in the 2 μm fraction. This was attributed in part to the exposure of fresh surfaces during grinding. They concluded that the Tamm's extraction removed an appreciable amount of iron and aluminium from trioctahedral layer silicates while the CDB extraction removed a slightly smaller amount. They recommended caution when interpreting the results of extractions on soils containing these minerals.

Dudas and Harward (1971) investigated the effect of the Tamm's and CDB treatments on crystalline and clay mineral components and reported some structural alteration of nontronite but more by the Tamm's reagent than by the CDB. The Tamm's reagent was found to cause little or no structural alteration of biotite and interstratified vermiculite-mica. Pawluk (1972) compared the effects of repeated extractions with the Tamm's and CDB reagents. Crystalline iron oxides were found to be removed after several extractions with the Tamm's reagent. XRD reflections for goethite and lepidocrocite were found to be partially removed after the second Tamm's extraction and completely removed after the third. A single CDB extraction was found to remove nearly all reflections associated with crystalline oxides but they also showed some removal of iron that was more closely associated with clays. It was concluded that a double extraction with the Tamm's reagent and a separate, single extraction with CDB served as a reasonable indicator of the relative amounts of 'amorphous' and total 'free' iron oxide contents respectively. However, some misgivings were expressed regarding the use of the Tamm's reagent to measure absolute quantities of 'amorphous' iron. The method was suggested rather as a more general indicator of the 'amorphous' content.

Schwertmann (1973) commented on the findings of Arshad *et al.* (1972) and Pawluk (1972). It was pointed out that a single Tamm's extraction, rather than being a quantitative measure of 'amorphous' iron content, offered a general measure of the 'activity' of the iron oxides in a sample (the 'amorphous' oxides imparting a greater activity to the soil) and that it extracted a major part of the organically bound iron. Subsequent extractions would then highlight the 'less activity' component. It was pointed out that the occurrence of trioctahedral layer silicates in soils was the exception rather than the rule, but that the grinding of soils containing such minerals could increase the quantity of CDB-extractable iron due to the dissolution of iron on freshly exposed

surfaces. The important point was also made that the crystal structure of iron oxides comprises a continuum ranging from amorphous to highly crystalline.

Schwertmann (1979) recommended the CDB treatment for use within a sequential extraction scheme for samples containing clay minerals, proposing two successive extractions for samples containing 'well-crystallised' or greater amounts of iron oxides. It was pointed out that considerable amounts of aluminium were commonly found in the extract, which was attributed either to the dissolution of free alumina or to isomorphous substitution of aluminium within natural goethites. The latter was first proposed by Norrish and Taylor (1961).

More recently the CDB treatment has been used by several authors in the study of trace metal speciation in polluted sediments. In such a study the strict selectivity of reagents is generally considered less important than the measurement of a representative portion of the trace metals occurring within each fraction. If such trace metals are prone to adsorption then the ability of the extracting reagent to retain them in solution is also a major concern.

Gupta and Chen (1975) incorporated the CDB treatment within an extraction scheme for harbour sediments while Jenne *et al.* (1974) used it for the removal of metals present in hydrous manganese and iron oxides. Malo (1977) compared the action of the DB reagent on aquatic sediments with that of a half hour extraction with 0.3 M HCl. The HCl extraction produced very similar results with respect to the amounts of trace elements dissolved. It was therefore proposed, owing to its far greater simplicity, as an alternative to the CDB extraction in cases where a large number of analyses were required. Förstner *et al.* (1981) and Tessier *et al.* (1979) expressed some misgivings regarding the practicality of the CDB treatment, claiming that the dithionite reagent was normally contaminated with several common trace elements and that it was impractical for use in conjunction with absorption spectrometry (AAS), owing to the high salt content. Substantial precipitation of trace metals was observed and this was attributed to the formation of insoluble sulphides.

Rendell *et al.* (1980) expressed further caution regarding the CDB treatment, claiming that when applied to the study of sediments there was a misinterpretation of the data. To demonstrate this they measured adsorption of copper, lead and cadmium from 0.1 M sodium citrate solutions and found the degree of adsorption onto a sample of river sediment to be 33, 52 and 36% of total element respectively. This result clearly warranted caution when applying the CDB treatment to the study of samples containing uranium and thorium.

Lowson *et al.* (1986) employed both the Tamm's and CDB treatments within a sequential extraction scheme for the purpose of studying the distribution of uranium and thorium isotopes in mineral phases of a lateritic weathered zone. The Tamm's reagent was used to dissolve 'amorphous' Fe and Al oxides while the CDB treatment removed crystalline oxides. XRD analysis demonstrated that while the Tamm's treatment had no effect on goethite, the CDB treatment appeared to completely dissolve it. Quartz and clay mineral reflections were unaffected by either treatment.

Michel (1984) used a single CDB extraction to measure amount of uranium and thorium associated with secondary phases in isovolumetrically weathered granites. Up to 81% of the total thorium and 23% of total uranium were found to be dissolved in this treatment. Little attention, however, was paid to the selectivity of the extractant. These results, and those of Lowson *et al.*, demonstrated that both elements had appreciable solubility in the CDB reagent. The fact that thorium tends to form stable complexes with oxoligands would tend to favour the use of the Tamm's and CDB reagents. Langmuir and Herman (1980), who extensively reviewed data on thorium complexation behaviour, reported that it formed strong complexes with both oxalate and citrate."

2. Method and materials

2.1. Samples and preparation

Four samples were studied –

OUM 9-1A	Oxidised phonolite	1324 m a.s.l.
OUM 26-1A	Oxidised phonolite near RF	1356 m a.s.l.
OUM 35-1B	Oxidised argillic phonolite	1364 m a.s.l.
OUM 37-1A	Laterite	1372 m a.s.l.

Approximately 100 g of each was crushed in a tungsten ring grinder to a particle size of about <2 µm.

2.2. Extractions

Four extractions were done on each sample. The whole sample was used for the extractions, as opposed to using the residue from the previous extraction. This was to minimise the risk of contamination through frequent exposure and handling.

Uranium-236 and thorium-229 tracers were used, and were added during the extraction to minimise effects of readsorption of uranium and thorium after dissolution of the host phase.

In the case of the Morgan's, TAO and CDB extractions, the slurry resulting from the extraction period was centrifuged at about 3000 rpm for 10 minutes. The supernatant was then filtered through 0.45 μm and collected, while the pellet was washed once with the extraction reagent and twice with distilled water. The washings were collected and added to the supernatant.

2.2.1. Morgan's extraction

Reagent: 1 M sodium acetate, buffered at pH 5.0 with acetic acid.

40 mL of reagent was added to about 1 g (accurately weighed) of sample. The tracers were added and the slurry was shaken for 5 hours, then the solid and solution were separated as described above.

The supernatant was taken to dryness with 8 M nitric acid. The residue was taken up in a minimum volume of 9 M HCl, and put through the normal analytical procedure for uranium and thorium using α -spectrometry.

2.2.2. TAO

Reagent: 10.9 g/L oxalic acid + 16.1 g/L ammonium oxalate, adjusted to pH 3.0.

40 mL of reagent was added to an accurately weighed mass of about 1 g of sample, the tracers were added, and the slurry was shaken in darkness for 4 hours. The solid and liquid were then separated.

The supernatant was taken to dryness with nitric acid to destroy the oxalate. The residue was taken up in a minimum volume of 9 M HCl, and processed normally for thorium and uranium.

2.2.3. CDB

Reagent: Sodium dithionite 1 g, and a solution of trisodium citrate (0.3 M) and sodium hydrogen carbonate (0.2 M) at pH 7.2.

40 mL of reagent was added to about 1 g of sample; ^{229}Th and ^{236}U tracers were added. The mixture was heated to about 70°C and stirred for half an hour. The extraction was repeated at least once, until all the iron oxide colouration was removed. Previous attempts at digesting the resulting solution proved futile and resulted in a black tarry residue that was extremely difficult to redissolve. Instead, the solution was refluxed for about two hours in aqua regia by placing a watchglass over the beaker on a hotplate, then made up to an accurate volume with about 3 M HCl. Care was taken to avoid boiling the solution to dryness during the refluxing step and to prevent the tarry residue from forming. No precipitation was observed from the solution since any sulphur compounds arising from residual dithionite had presumably been oxidised to sulphates by the aqua regia.

The supernatant was taken to dryness with 8 M nitric acid. The residue was taken up in a minimum volume of 9 M HCl, and put through the normal analytical procedure for uranium and thorium using α -spectrometry.

2.2.4. Total digestion

About 0.5 g of sample was accurately weighed into a platinum beaker then HF (40%, 15 mL), perchloric acid (70%, 5 mL) and yield tracer were added. The mixture was evaporated slowly to dryness on a hotplate with extra heat being applied at the final stage to remove traces of perchloric acid. The residue was then dissolved in 6 M HCl. No further processes, such as alkaline fusion, were required to achieve complete dissolution of the samples.

3. Results and samples

The parameters considered here are the $^{234}\text{U}/^{238}\text{U}$ and $^{230}\text{Th}/^{234}\text{U}$ activity ratios and the concentrations of ^{238}U and ^{232}Th in the different phases. Table 2-I gives the data from each separate extraction of the whole sample. Table 2-II shows the same data converted to give the differences between one extraction and the previous one, which is similar to having extracted residues rather than the whole sample. Figures 2-1 to 2-4 show graphically the percentage of uranium extracted, the $^{234}\text{U}/^{238}\text{U}$ and $^{230}\text{Th}/^{234}\text{U}$ activity ratios, and the percentage of thorium extracted respectively for the four extractions of the four samples.

TABLE 2-I

Results from selective phase extraction analyses on whole-rock samples.

(Standard deviations in brackets include counting statistics and estimated 2% measurement errors)

	$^{234}\text{U}/^{238}\text{U}$	$^{230}\text{Th}/^{234}\text{U}$	^{238}U $\mu\text{g/g}$	^{232}Th $\mu\text{g/g}$	% Total ^{238}U	% Total ^{232}Th
OUM 9-1A						
Morgan's	0.758 (0.015)	0.641 (0.031)	8.15 (0.21)	6.28 (0.37)	10.3	6.8
TAO	0.785 (0.031)	0.998 (0.048)	29.4 (1.2)	25.3 (0.9)	37.2	27.4
CDB	1.028 (0.026)	1.104 (0.046)	49.7 (1.7)	49.1 (2.1)	62.9	53.2
Total Dig.	0.931 (0.042)	1.168 (0.063)	79 (4.0)	92.4 (3.1)	100.0	100.0
OUM 26-1A						
Morgan's	0.892 (0.006)	0.018 (0.002)	67.9 (2.0)	1.05 (0.16)	36.7	3.7
TAO	0.985 (0.028)	0.079 (0.004)	151.2 (7.4)	5.8 (0.4)	81.7	20.1
CDB	1.011 (0.016)	0.151 (0.006)	180.5 (5.9)	17.4 (1.0)	97.5	60.7
Total Dig.	1.045 (0.002)	0.195 (0.013)	184.9 (10.9)	28.6 (1.7)	100.0	100.0
OUM 35-1B						
Morgan's	1.154 (0.013)	0.278 (0.009)	110.6 (3.0)	2.75 (0.21)	9.6	3.1
TAO	0.987 (0.027)	0.996 (0.069)	354.0 (23.8)	16.3 (1.1)	30.8	18.1
CDB	1.218 (0.015)	1.111 (0.045)	485.0 (16.7)	25.6 (1.5)	42.2	28.7
Total Dig.	1.053 (0.016)	1.184 (0.056)	1150 (40)	89.8 (6.9)	100.0	100.0
OUM 37-1A						
Morgan's	0.987 (0.019)	0.193 (0.020)	8.4 (0.2)	6.64 (0.58)	13.5	5.1
TAO	1.028 (0.052)	0.553 (0.046)	16.5 (0.8)	27.0 (2.0)	26.5	20.8
CDB	1.143 (0.030)	1.012 (0.046)	24.7 (0.8)	70.9 (2.8)	39.7	54.5
Total Dig.	1.008 (0.055)	1.107 (0.065)	62.3 (3.4)	130.1 (4.2)	100.0	100.0

TABLE 2-II
 Results from selective phase extraction analyses, individual phases.
 (Values for each extraction minus the previous extraction, i.e. for the particular phase)

	²³⁴ U/ ²³⁸ U	²³⁰ Th/ ²³⁴ U	²³⁸ U μg/g	²³² Th μg/g	% Total ²³⁸ U	% Total ²³² Th
OUM 9-1A						
Morgan's	0.758	0.641	8.15	6.28	10.3	6.8
TAO	0.795	1.129	21.2	19.0	26.8	20.6
CDB	1.686	1.380	20.3	23.8	25.7	25.8
Total Dig.	0.767	1.313	29.3	43.3	37.1	46.9
OUM 26-1A						
Morgan's	0.892	0.018	67.9	1.05	36.7	3.7
TAO	1.061	0.120	83.2	4.7	45.0	16.4
CDB	1.145	0.471	29.3	11.6	15.8	40.6
Total Dig.	2.440	0.952	4.4	11.2	2.4	39.2
OUM 35-1B						
Morgan's	1.154	0.278	110.6	2.75	9.6	3.1
TAO	0.915	1.407	243.4	13.5	21.4	15.0
CDB	1.841	1.278	131.0	9.4	11.4	10.6
Total Dig.	0.934	1.171	655.5	64.1	57.8	71.4
OUM 37-1A						
Morgan's	0.986	0.193	8.4	6.64	13.5	5.1
TAO	1.070	0.898	8.1	20.4	13.0	15.7
CDB	1.374	2.339	8.2	43.9	13.2	33.7
Total Dig.	0.919	1.089	37.6	59.2	60.4	45.5

For sample 9-1A, 37% of the uranium was contained within the residual phases, 26% was contained within crystalline iron oxides, and 25% was either very strongly and very specifically adsorbed or entrapped by amorphous species of Si, Al and Fe (such as ferrihydrite). Only about 8% of the U was simply or specifically adsorbed onto the substrate.

The lower than unity activity ratio for the adsorbed phases suggest that ^{238}U has a greater activity than ^{234}U in the groundwater and is consequently being transported preferentially to ^{234}U . The greater than unity values for the amorphous crystalline iron and residual $^{230}\text{Th}/^{234}\text{U}$ activity ratios suggest a loss of uranium from these phases. The $^{234}\text{U}/^{238}\text{U}$ value for the TAO extract suggests preferential loss of ^{234}U (or gain of ^{238}U) from this phase. The very high $^{234}\text{U}/^{238}\text{U}$ ratio for the crystalline iron phases (CDB extracts) suggests a preferential emplacement process for ^{234}U . This may include a recoil effect of ^{234}Th from the amorphous surface sites into the crystalline iron phases. Differences in available sites and entrapment rates for ^{238}U and ^{234}Th may also play a role. The ratios for the residual phases also suggest a net leaching of U, with preferential loss of ^{234}U . Thorium-232 was found mostly in the residual phases, although significant quantities were also present in the amorphous material and crystalline iron oxide phases.

Sample 26-1A had most of its uranium associated with amorphous phases or adsorbed, with very little associated with residual phases (2-4%) and only 16% associated with crystalline iron oxides. The very low $^{230}\text{Th}/^{234}\text{U}$ ratios suggest a recent influx of uranium entering the region of the sample. The adsorbed material again seemed depleted in ^{234}U compared to ^{238}U . Thorium-232 was most concentrated in the crystalline iron oxides and residual phases.

In sample 35-1B most of the uranium was contained within the residual phases, with the amorphous phases being the next richest material. This sample contained by far the most uranium of the four samples in any of the four phases extracted. The activity ratios, especially $^{230}\text{Th}/^{234}\text{U}$, suggest that this sample had experienced net leaching of uranium. The crystalline iron oxides again appeared to be enriched in ^{234}U compared with ^{238}U . Thorium-232 was found mostly in the residual phases, with a quarter of the total in the crystalline iron oxides.

Sample 37-1A the least active of the four, had most of its uranium contained in residual phases. The $^{230}\text{Th}/^{234}\text{U}$ activity ratios of the residual material were close to unity, suggesting that very little leaching or accumulation of uranium in this phase had occurred. The very high $^{230}\text{Th}/^{234}\text{U}$ activity ratio for the crystalline iron oxides suggests that loss of uranium had occurred from these phases, although differences in entrapment

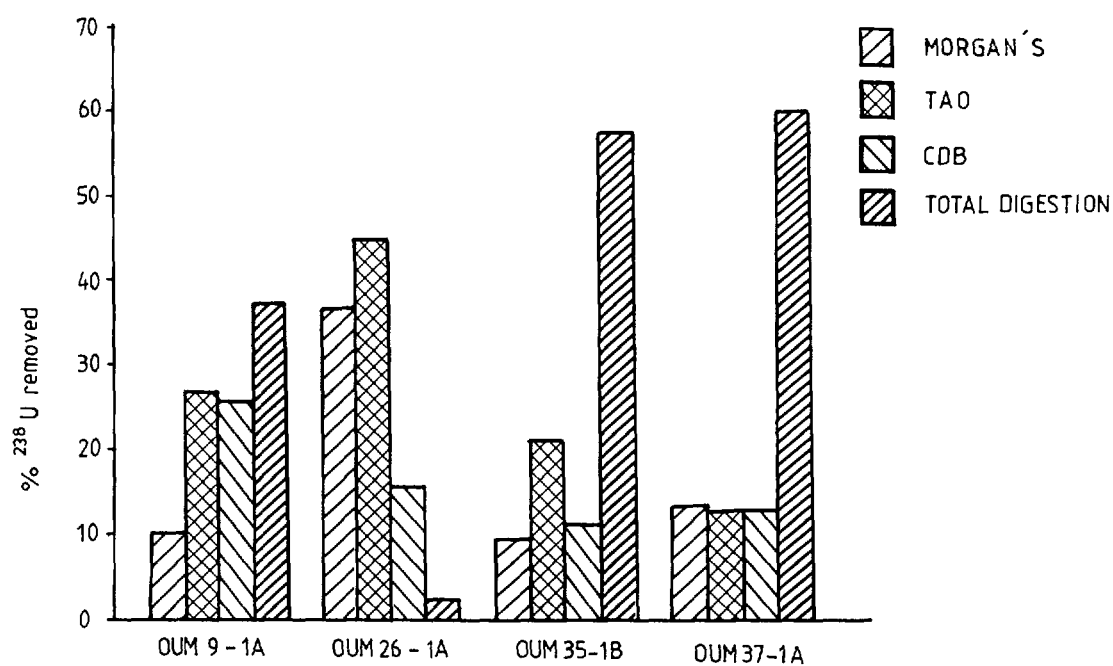


Figure 2-1. The percentage of total U removed by a particular extractant representing a particular phase(s), i.e. minus the uranium removed by the previous extractant.

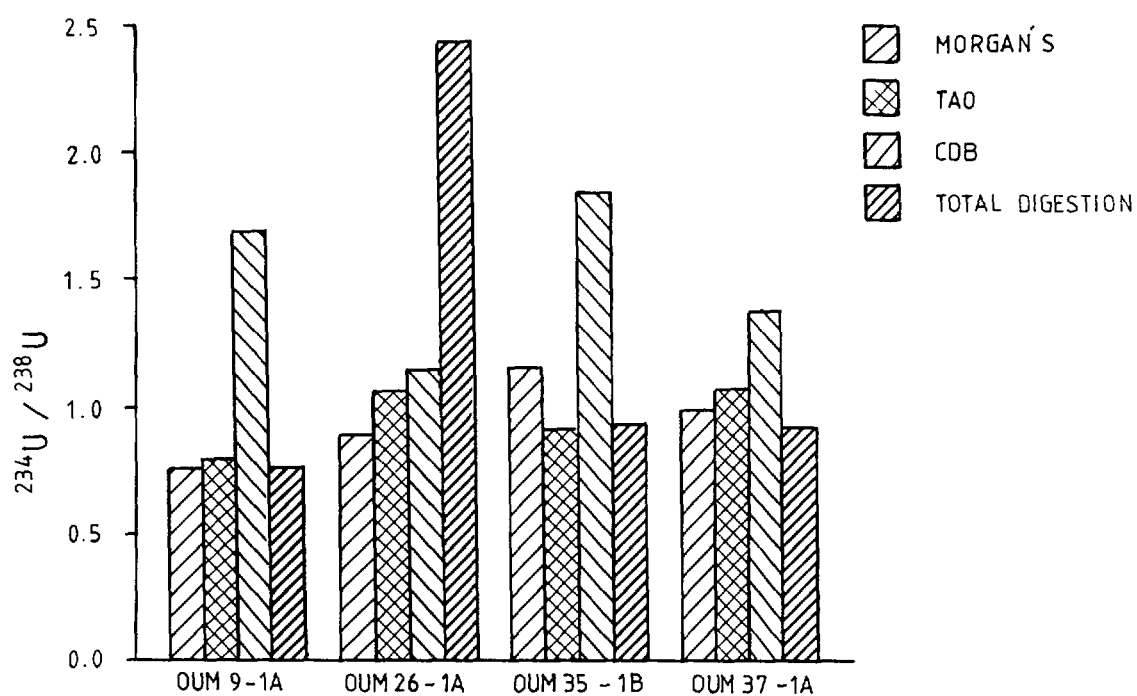


Figure 2-2. ²³⁴U/²³⁸U activity ratios for particular phases, characterised by extraction by particular reagents.

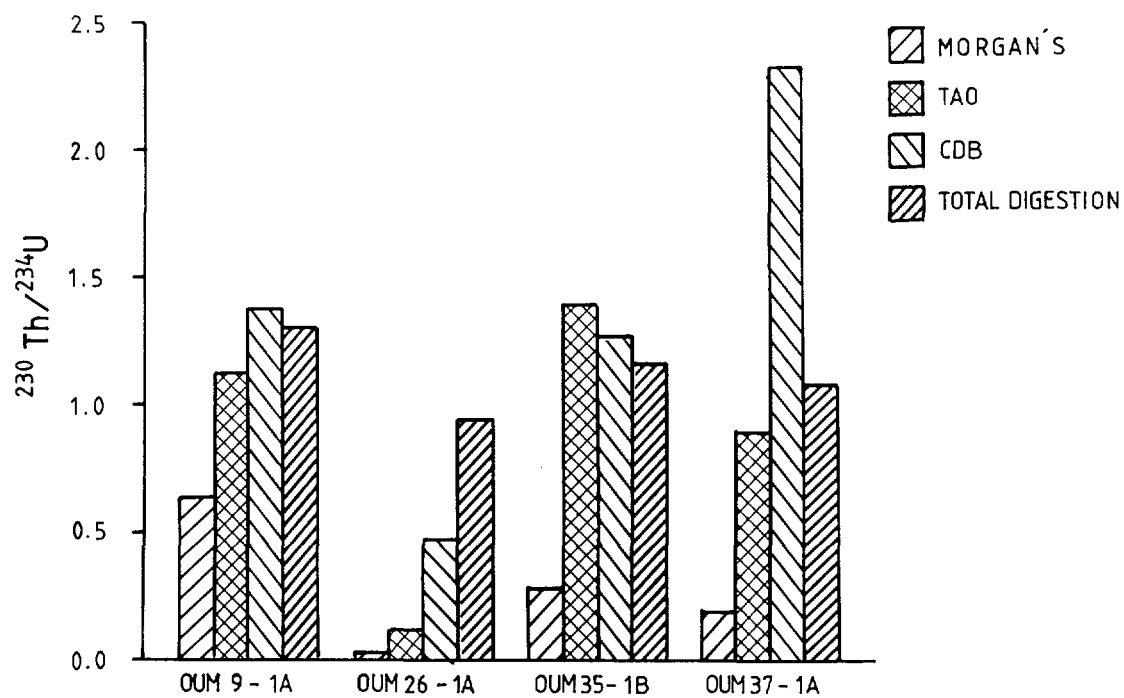


Figure 2-3. $^{230}\text{Th}/^{238}\text{U}$ activity ratios for particular phases, characterised by extraction by particular reagents.

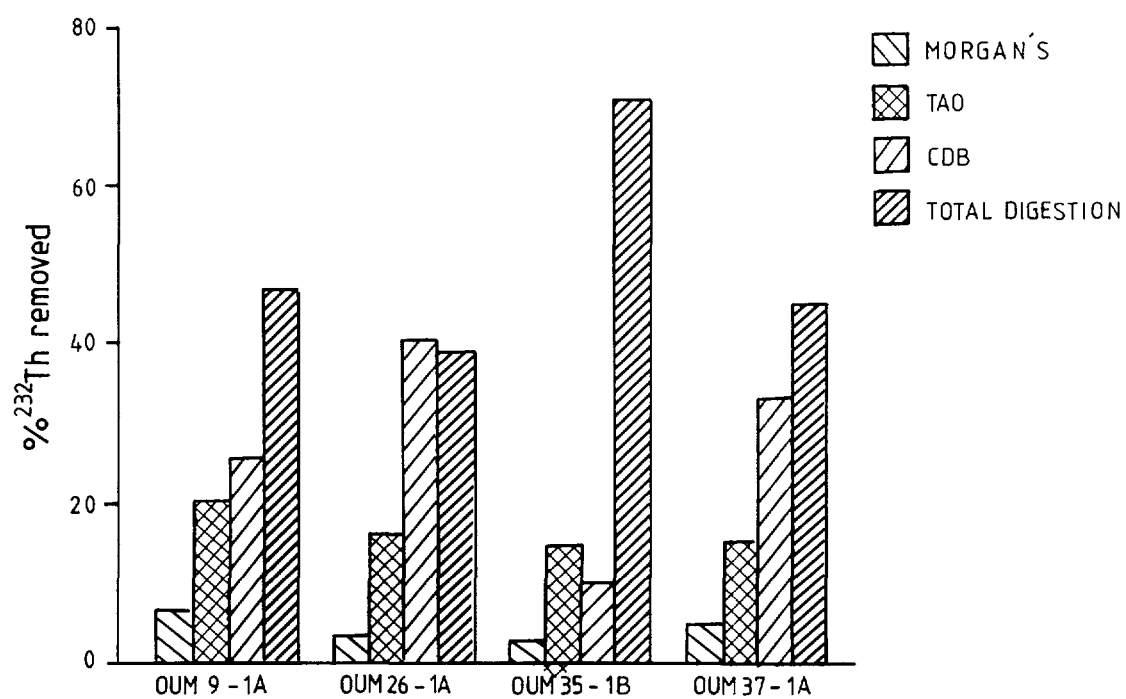


Figure 2-4. The percentage of total Th removed by a particular extractant representing a particular phase(s), i.e. minus the Th removed by the previous extractant.

between uranium and thorium may also be important. This sample contained the highest concentration of ^{232}Th of the four samples, with the residual phases containing the most.

4. Conclusions

The four samples appeared to be very different in terms of uranium series disequilibria and general concentrations of radionuclides. It is difficult to draw clear conclusions from this data without more knowledge of mineralogy and the sample positions. It does appear, however, that for samples 9-1A, 35-1B and 37-1A, the residual phases such as clays, feldspars, etc., contained the most uranium and thorium, and that net leaching of uranium has probably occurred from these areas. In sample 26-1A most of the uranium and thorium was associated with amorphous phases or carbonates. This, and the values of the activity ratios, suggest this sample has experienced an influx of uranium much more recently than the others. Crystalline iron oxides appear to be responsible for a significant amount of the disequilibria observed, especially in samples 9-1A, 35-1B and 37-1A. The iron oxides appear to have entrapped ^{234}U preferentially to ^{238}U . The processes that may have contributed to the phenomena include α -recoil, extremely strong and irreversible binding of ^{234}Th , and preferential inclusion of ^{234}Th into faults of the crystal structure during iron oxide transformations.

5. References

- Arshad, M.A., St. Arnaud, R.J. and Huang, P.M., 1972. Dissolution of trioctahedral layer silicates by ammonium oxalate, sodium dithionite-citrate-bicarbonate and potassium pyrophosphate. *Can. J. Soil Sci.*, 52, 19-26.
- Blume, H.P. and Schwertmann, U., 1969. Genetic evaluation of profile distribution of aluminium, iron and manganese oxides. *Soil Sci. Soc. Amer. Proc.*, 33, 438-444.
- Chukrov, F.V., Zvyagin, B.B., Ermilova, L.P. and Gorshkov, A.I., 1972. New data on iron oxides in the weathering zone. *Proc. Int. Clay Conf.*, Madrid, I. 397-404.
- Coffin, D.E, 1961. A method for the determination of free iron in soils. *Can. J. Soil Sci.*, 43, 7-17.
- de Endredy, A.S., 1963. Estimation of free iron oxides in soils and clays by photolytic method. *Clay Minerals*, 5, 218-226.

- Dudas, M.J. and Harward, M.E., 1971. Effect of dissolution treatments on standard soils and clays. *Soil Sci. Soc. Amer. Proc.*, 35, 134-140.
- Förstner, U., Calmano, W., Conradt, K., Jaksch, H., Schimkus, C. and Schoer, J., 1981. Chemical speciation of heavy metals in solid waste materials (sewage, mining wastes, dredged materials, polluted sediments) by sequential extraction. *Int. Conf. on heavy metals in the environment*, Amsterdam, September 1981, co-sponsored by CEC, WHO; pp. 698-704.
- Grossman, R.B. and Millet, J.C., 1961. Carbonate removal from soils by a modification of the acetate buffer method. *Soil Sci. Soc. Am. Proc.*, 25, 325-326.
- Gupta, S.K. and Chen, K.Y., 1975. Partitioning of trace metals in selective chemical fractions of nearshore sediments. *Environ. Lett.*, 10, 129-158.
- Holmgren, G.G.S., 1967. A rapid citrate-dithionite extractable iron procedure. *Soil Sci. Soc. Am. Proc.*, 31, 210-211.
- Hsi, C-K.D. and Langmuir, D., 1985. Adsorption of uranyl onto ferric oxohydroxides: application to the surface complexation site binding model. *Geochim. Cosmochim. Acta*, 49, 1931-1941.
- Jenne, E.A., Ball, J.W. and Simpson, C., 1974. Determination of trace metals in sodium dithionite-citrate extracts of soils and sediments by atomic adsorption. *J. Environ. Quality*, 3, 281-287.
- Johnston, J.H. and Lewis, D.G., 1983. A detailed study of the transformation of ferrihydrite to hematite in an aqueous medium at 92°C. *Geochim. Cosmochim. Acta*, 47, 1823-1831.
- Langmuir, D. and Herman, J.S., 1980. The mobility of thorium in natural waters at low temperatures. *Geochim. Cosmochim. Acta*, 44, 1753-1766.
- Le Riche, H.H. and Weir, A.H., 1963. A method of studying trace elements in soil fractions. *J. Soil Sci.*, 14, 229-239.
- Lowson, R.T., Short, S.A., Davey, B.G. and Gray, D.J., 1986. $^{234}\text{U}/^{238}\text{U}$ and $^{230}\text{Th}/^{234}\text{U}$ activity ratios in mineral phases of a lateritic zone. *Geochim. Cosmochim. Acta*, 50, 1697-1702.
- Mackenzie, R.C., 1949. The nature of free iron oxides in soil clays. *Nature*, 164, 244.
- Mackenzie, R.C., 1954. Free iron oxide removal from soils. *J. Soil. Sci.*, 5, 167-162.
- Malo, B.A., 1977. Partial extraction of metals from aquatic sediments. *Environ. Sci. Technol.*, 11(3), 277-292.

- McKeague, J.A. and Day, J.H., 1966. Dithionite-and oxalate-extractable Fe and Al as aids in differentiating various classes of solids. *Can. J. Soil Sci.*, 46, 13-22.
- Megumi, K. and Mamuro, T., 1976. The bearing of uranium series nuclides in soil. Annual report of the Radiation Centre of Osaka Prefecture, 17, 22-27.
- Mehra, O.P. and Jackson, M., 1960. Iron oxide removal from soils and clays by a dithionite-citrate system buffered with sodium bicarbonate. *Proceedings of 7th Int. Conf. on Clays and Clay Minerals*, 1958, Washington D.C., Monograph No. 5, 317-327.
- Michel, J., 1984. Redistribution of uranium and thorium series nuclides during isovolumetric weathering of granite. *Geochim. Cosmochim. Acta*, 48, 1249-1255.
- Morgan, M.F., 1935. The universal soil testing systems. *Connecticut Agricultural Experiment Station Bulletin*, 372.
- Nightingale, T., 1988. Mobilisation and Redistribution of Radionuclides during Weathering of a Uranium Ore Body. *Msc Thesis*, University of Sydney.
- Nirel, P., Thomas, A.J. and Martin, J.M., 1985. A critical evaluation of sequential extraction techniques. In "Seminar on Speciation of Fission and Activation Products in the Environment". Oxford, April 1985.
- Norrish, K. and Taylor, R.M., 1961. The isomorphous replacement of iron by aluminium in soil goethites. *J. Soil Sci.*, 12, 294-306.
- Pawluk, S., 1971. Characteristics of Ferra Elluviated Gleysols developed from acid shales in northwestern Alberta. *Can. J. Soil Sci.*, 51, 113-124.
- Pawluk, S., 1972. Measurement of crystalline and amorphous iron oxides. *Can. J. Soil Sci.*, 52, 119-123.
- Rapin, F., Nembrini, G.P., Förstner, U and Garcia, J.I., 1983. Heavy metals in marine sediment phases determined by sequential extraction and their interaction with interstitial water. *Environ. Tech. Lett.*, 4, 387-396.
- Rendell, P.S., Batley, G.E. and Cameron, A.J., 1980. Adsorption as a control of metal concentrations in sediment extracts. *Environ. Sci. Tech.*, 14, 314-318.
- Schwertmann, U., 1959. Die fractionierte Extraktion der freien Eisenoxide in Boden, ihre mineralogischen Formen und ihre Entstehungsweisen (the step-wise extraction of free iron oxide in soil, its mineralogical form and its mode of formation). *Z. Pflanzenernähr. Dung., Bodenk.*, 84, 194-204.

- Schwertmann, U., 1964. Differenzierung der Eisenoxide des Bodens durch Extraktion mit Ammonium-Oxalat-Lösung. (The differentiation of iron oxide in soils by a photochemical extraction with acid ammonium oxalate). *Z. Pflanzenernähr. Dung., Bodenk.*, 105, 194-202.
- Schwertmann, U. and Taylor, R.M., 1977. Iron Oxides. In: J.B. Dixon and S.B. Weed (Editors). Minerals in soil environments. *Soil Science Society of America*, Madison, Wisconsin, 145-180.
- Schwertmann, U., 1979. Dissolution Methods. In: H. Van Olphen and J.J. Fripiat (Editors), Data handbook for clay minerals and other non-metallic minerals, prepared under the auspices of the OECD and the Clay Minerals Society, 163-172. *Pergamon Press*, Oxford.
- Sondag, F., 1981. Selective extracting procedures applied to geochemical prospecting in an area contaminated by old mine workings. *J. Geochem. Explor.*, 15, 645-652.
- Tamm, O., 1922. Om bestämning av de oorganiska komponenterna i markens gelkomplex. *Medd. Statens Skogsförsökanst.*, 19, 384-404.
- Tamm, O., 1934. Über die Oxalatmethode in der chemischen Bodenanalyse (oxalate method in chemical extraction of soils). *Medd. Statens Skogsförsökanst.*, Stockholm, 27, 1-20.
- Taylor, R.M., 1959. Amorphous iron oxides in soils. *J. Soil Sci.*, 10, 309-315.
- Tessier, A., Campbell, P.G.C. and Bisson, M., 1979. Sequential extraction procedure for the speciation of particulate trace metals. *Anal. Chem.*, 51, 844-851.

Appendix 3

**Mineral chemistry studies of rocks from the Osamu
Utsumi uranium mine, Poços de Caldas, Brazil.**

Contents

	page
1. Introduction	253
2. Samples and analytical programme	253
3. Results	255
3.1. Alkali feldspar	255
3.2. Kaolinites	257
3.3. Illites/sericites	258
3.4. Zircon and ZrO ₂ -minerals	259
3.5. Fluorites	263
3.6. TiO ₂ -(rutile) minerals	263
3.7. U-minerals	264
3.8. Other minerals	265
4. References	267
APPENDICES:	
Appendix 3:1: K-feldspar	269
Textural and electron microprobe data	
Appendix 3:2: Kaolinite	277
Textural and electron microprobe data	
Appendix 3:3: Illite/sericite	283
Textural and electron microprobe data	
Appendix 3:4: Zircon	291
Textural and electron microprobe data	
Appendix 3:5: Fluorite	299
Textural and electron microprobe data	
Appendix 3:6: Rutile and Ti-oxides	303
Electron microprobe data	
Appendix 3:7: Pyrite	307
Electron microprobe data	
Appendix 3:8: Uranium-oxides	311
Electron microprobe data	
Appendix 3:9 PLATES 3:9-1 – 3:9-8	315

Appendix 3

Mineral chemistry studies of rocks from the Osamu Utsumi uranium mine, Poços de Caldas, Brazil.

H.D. SCHORSCHER¹

¹Universidade de São Paulo, Instituto de Geociências – DMP. C.P. 20 899, 014 98 São Paulo (Brazil).

1. Introduction

Microprobe – mineral chemistry studies were carried out during research visits to the Institute of Mineralogy and Petrography, University of Bern, using an automatic ARL-SEMQ microprobe equipped with 6 crystal spectrometers and an Energy Dispersive System (EDS). The raw data were corrected for drift, dead time and background with the aid of the COMIC-ED control program (Sommerauer, 1982), and the final complete ZAF corrections were carried out using the EMMA-5/1-86 program.

2. Samples and analytical programme

The studied samples include rocks of redox fronts collected in the Osamu Utsumi open mine pit, massive pitchblende nodules from earlier Urânio do Brasil (previously NUCLEBRÁS) collections, and from the F1 (9-1WC11) drillcore specimens. Table 3-I presents a list of the samples, their locations, and brief petrographic descriptions. The sample locations use the coordinate system of Urânio do Brasil completed, in the case of the drillcore specimens, with the borehole depth in metres. The sampling locations of the massive pitchblende nodules (from earlier Urânio do Brasil collections) are uncertain; these nodules occurred in the oxidised portions of the mine profile above zones of higher grade U-mineralisation which have been since removed during mining activities.

The analytical programme included the major and minor rock minerals and the uranium mineralisation-forming silicate and ore minerals; selection of these was based on detailed microscopic and bulk rock geochemical studies (Waber *et al.*, this report series; Rep. 2). Minerals included: alkali feldspar, kaolinite, illite/sericite, zircon, Ti-oxide, pyrite, U-oxide and Fe-oxyhydroxides (HFO). Fluorite was checked for possible contents of REEs, and the presence of greenockite (CdS) was confirmed in the massive pitchblende nodules.

TABLE 3-I

Samples selected for microprobe – mineral chemistry studies.

Curr. No.	Sample No.	Location (Depth in m)	Petrography
1	F1/67-1A	9-1WC11 (66.06 – 66.34)	Redox front in fine-grained pseudoleucite phonolite without U-mineralisation.
2	F1/68-1A	9-1WC11 (67.00 – 67.38)	Reduced, cataclastic phonolite.
3	F1/69-1A	9-1WC11 (67.99 – 68.07)	Reduced, porous (leached) phonolite, (Appendix 3:9; Plate 3:9-1).
4	F1/71-1B	9-1WC11 (70.44 – 70.76)	Reduced, very porous, “pegmatoid”, phonolite.
5	F1/75-1B1	9-1WC11 (74.79 – 74.93)	Reduced, medium-grained, compact (massive structure) phonolite (Appendix 3:9; Plate 3:9-2).
6	F1/75-1B	9-1WC11 (74.79 – 75.12)	Reduced, medium-grained, compact (massive structure) phonolite.
7	F1/78-1A	9-1WC11 (77.40 – 77.59)	Cataclastic zone in reduced phonolite.
8	F1/110-1A	8-1WC11 (109,44 – 109,53)	Reduced, porous, grey coloured phonolite of conductive zone.
9	S/N-18(05)	8-2 BI 33	Reduced fine-grained phonolite near redox front with pitchblende nodules (Appendix 3:9; Plates 3:9-3 and 3:9-4).
10	S/N-21(04)	8-2 AH 63	Redox front with pitchblende nodules, in fine-grained microxenolithic phonolite (Appendix 3:9; Plates 3:9-5 and 3:9-6).
11	S/N-24	Urânio do Brasil collection	Massive pitchblende nodule with two pyrite generations and argillised phonolite core (Appendix 3:9; Plates 3:9-7 and 3:9-8).

The minerals were analysed in three groups:

- alkali feldspar, kaolinite, illite/sericite, zircon, Fe-oxide/HFO and for the partial analysis of fluorite;
- Ti-Fe-U oxide ore minerals, and
- pyrite and eventually other sulphides.

Additionally it should be mentioned that the initial U-oxide measurements from a massive pitchblende nodule (S/N-24; Table 3-I) were carried out using a program developed for the measurement of U-silicates. Some measurements were later repeated, and these are discussed below.

3. Results

Emphasis of the microprobe analytical work was upon the reduced rock and redox front silicates, ore minerals and mineralisations. Oxidised rocks were included only for the tentative analysis of hydrous ferric oxides. These, together with other supergenic (weathering) silicates and oxide ore minerals (mainly Mo and Mn), usually prove too unstable under the electron beam.

The analysed minerals are discussed in groups according to the mineral species.

3.1 Alkali feldspar

More than 60 quantitative point analyses of alkaline feldspars were performed (Appendix 3:1), including all the microscopically distinguished types presented by Waber *et al.*, (this report series; Rep. 2). For example, structurally and chemically recrystallised phenocrysts and groundmass crystals with or without the exchange of former albitic exsolutions, and neoformed, hydrothermally precipitated alkali feldspars in rock voids, pores and leached caverns.

When possible, the central and intermediary portions, as well as borders of the alkali feldspars were analysed. Attention was given to the adjacent mineral types and to the emitted cathodoluminescence colours.

As stated above, the large majority of the analysed alkali feldspars were structurally and chemically modified from the magmatic parent minerals. Newly formed, hydrothermally precipitated alkali feldspars are quite rare. Microscopically, these two types are easily distinguished: the modified alkali feldspars substitute for their magmatic predecessors preserving the original igneous textures of the rocks. Besides, these feldspars are typically “clouded”, replete with myriads of tiny minerals. Inclusions consist of argillic components (mainly kaolinite), fluid and, as suspected, hydrous ferric oxides, resulting in a yellow-brown colouration under the microscope. The neoformed hydrothermal alkali feldspars are normally fine- to very fine-grained, idiomorphic, colourless to clear and, microscopically, fully transparent (without any significantly observable mineral or fluid inclusions).

Analytical results (Appendix 3:1) showed all of the analysed alkali feldspars to consist of almost pure K-feldspar. Na₂O contents, if present, remain below 0.5 wt.%. Detected impurities include Fe (as FeO_{tot}) in contents below 1 wt.% and sporadic Ce and Y. Significant variations between the replaced igneous and hydrothermally precipitated,

newly formed alkali feldspars, (i.e. zonation), could not be detected. Even preserved perthitic exsolutions proved to be alkali exchanged, composed of almost pure K-feldspar, although of different optical orientation from that of the hosting K-feldspar. The observed analytical variability of the “totals” and of the alkali/alumina ratios is due to the argillic alteration of the feldspar content.

The alkali feldspars are the major minerals of the studied rocks. Comparing the microscopic and microprobe results, and considering the texturally equivalent alkali feldspars of the regional rocks, it can be concluded that the hydrothermal event that affected the mine site and drillcore F1, resulting in the so-called “potassic rocks”, performed a very effective homogenisation of all the distinct primary magmatic feldspars (Ulbrich, M., 1983, 1986; Ulbrich, M. *et al.*, 1984), i.e. various types of orthoclase phenocrysts, groundmass sanidines, albite-rich plagioclases, alkali feldspars, in pseudoleucites etc., converting them into very pure K-feldspars. Primary magmatic Fe-contents (in trace amounts) may have been present, for example, Ulbrich, M. (1983) and Ulbrich, M. *et al.* (1984) measured and calculated Fe₂O₃-contents of 0.4 – 0.7 wt.% in alkali feldspars of regional nepheline syenites. However, the sporadically observed quite high Fe-contents of the analysed F1 feldspars described here are of different origin, resulting from inclusions of Fe-minerals, mainly pyrite.

Calcium, as expected from earlier mineralogical and bulk geochemical studies, which showed very low contents in alkali feldspars of the regional nepheline syenites of <0.1 wt.% (Ulbrich, M., 1983, 1986; Ulbrich, M. *et al.*, 1984), and also in drillcore F1 with a mean value of 0.07 wt.% of CaO (Waber *et al.*, this report series; Rep. 2), this element was not detected in any significant amount in the F1 alkali feldspars. It was therefore not included in the microanalytical programme.

Alkali feldspars of the oxidised rocks (Table 3-I; e.g. sample F1/67-1A, Appendix 3:9; Plates 3:9-5 and 3:9-6) were also analysed. They showed normal compositional variations (Appendix 3:1). However, the analytical uncertainties are greater due to the more pervasive argillisation/kaolinisation (2nd. generation, supergenic kaolinite formation) and the general pigmentation with HFO from the oxidation of pyrites.

Relict alkali feldspars occur in the silicate matrix of pitchblende nodules near redox fronts (Appendix 3:9; Plates 3:9-3 – 3:9-5) and even in the massive parts of massive pitchblende nodules that survived dissolution in the oxidised parts of the mine profile (Appendix 3:9; Plates 3:9-7 and 3:9-8). Their optical characteristics are indistinguishable from the analysed alkali feldspars, indicating similar compositions.

3.2 Kaolinites

Kaolinite, resulting from hydrothermal and supergene processes, is another important mineral of drillcore F1. In common with the feldspars, the existence of distinct generations of different origin is obvious, for example, by the systematically varying abundance of this mineral between the regional rocks and in the rocks of the mine (Waber *et al.*, op. cit.). In the former, kaolinite is present as a rare to trace constituent of “postmagmatic hydrothermal” origin. In the mine rocks, two generations of kaolinites can be distinguished and a possible third type of “postmagmatic hydrothermal” origin may also exist, as in the regional rocks. The two recognised kaolinite generations in the mine rocks are: a) in the reduced rocks the main hydrothermal “potassic rock”-related kaolinite generation, and b) in the oxidised rocks there occurs a secondary, additional generation of kaolinites, of supergenic (weathering) origin. Compared to the reduced rocks, the oxidised rocks show an increase in kaolinite (Waber *et al.*, op. cit.). Only the coarsest, flaky kaolinite individuals and booklets (max. Ø of about 15-30 μ) of the reduced F1 rocks were analysed. These tend to occur as hydrothermal substitution products of nephelines and as neoprecipitates in rock pores and interstices, intimately intergrown with similarly fine-grained pyrite, somewhat coarser illite/sericite and, in some cases, with zircon. These are the typical kaolinites of the main hydrothermalism that produced the “potassic rock” alteration and (hydrothermal) uranium mineralisation at the Osamu Utsumi site. They are texturally very characteristic and similar types were not observed in the regional rocks. Besides, they occur in the reduced F1 rocks, formed by the incipient kaolinisation of the alkali feldspars throughout the rocks, and others are associated with pyrite in fracture-hosted mineralisations. The former kaolinites are very fine-grained (of max. Ø <5 μ) and therefore not suitable for conventional microprobe analysis. In addition, these kaolinites are texturally indistinguishable from those of the regional rocks that resulted from the “postmagmatic-hydrothermal” stage, even though more abundant (i.e., of more general occurrence) than in the F1 rocks. The fracture kaolinites, despite their association with pyrite, are of uncertain origin, whether hydrothermal “potassic rock”-related or even supergene, as was indicated in one case by the S-isotope signature of the associated pyrites (see Appendix 1). The supergene kaolinite generation in the oxidised F1 rocks is post-hydrothermal; this continued kaolinisation, mainly of the alkali feldspars, resulted from weathering solutions and has resulted in neoprecipitates forming in pores and caverns from pyrite oxidation and dissolution.

More than 40 quantitative kaolinite analyses are contained in Appendix 3:2 which also lists brief textural descriptions and other chemical observations of the analysed phases.

Some analytical problems arose due to the instability of kaolinite under the electron beam; other more serious problems resulted from the contamination of the soft kaolinite aggregate with Pb from the polishing discs. The Pb-contamination (even weak) becomes quickly evident during analysis by high absorption losses (Appendix 3:2; analyses with “H₂O” > 18 wt.%). More frequently encountered chemical impurities include iron (expressed as total FeO), Na₂O and MgO (respectively < 0.7, < 0.1 and < 0.3 wt.%) and, sporadically, Ce and Y (trace amounts).

The kaolinites suffered partial substitution by illite/sericite in the course of the “potassic rock” hydrothermal alteration, probably under conditions of increasing temperature and potassium activity of the hydrothermal fluids.

3.3 Illites/sericites

These minerals are major characteristic constituents of the “potassic rock” hydrothermal alteration at the mine site. They occur as very fine-grained dense aggregates of microcrystalline individuals intergrown with pyrite and, in largely variable proportions, with kaolinite which pseudomorphs former nephelines. In rock voids, interstices and along fractures, the illite/sericite form as neoprecipitates associated frequently with zircon and/or fluorite.

The proportions of the illite/sericite-kaolinite aggregates vary over the whole range between the two almost monomineralic compositions. Textural observations show that the illites/sericites are always coarser grained when compared to the associated kaolinites. In absolute terms, they normally range from 30-60 μ (mean flake diameters) and not infrequently several tenths of mm (max. dimensions). The mean types are typical ‘sericites’, i.e., microcrystalline, colourless-white potassic micas devoid of any marked structural character. The coarsest types have been described in drillcore F4 as muscovite (Waber *et al.*, this report series; Rep. 2). X-ray diffraction data of the F1 rocks were also presented and showed, for the illites, high crystallinities in the order of 0.13 – 0.18 (after Kübler, 1968) interpreted as indicating relatively high hydrothermal temperatures) (above approx. 360°C) and/or very high K⁺-activity conditions.

The illite/sericite-kaolinite aggregates can exhibit homogeneous, random, or zoned intergrowth of the major minerals. The last-mentioned is by far the most frequent and the zoned aggregates may show regular textures of illite/sericite-rich border zones and kaolinite-rich centres or irregular ones, within domains where one or the other main mineral predominates. In both cases of zonation, the margins of the aggregates are more

illite/sericite-rich (even if not sufficiently to be characterised as an illite/sericite zone) and the transitions between the different domains are predominantly gradational.

Microscopically in all of the observed hydrothermal associations the illite/sericite-kaolinite relationships can be interpreted as a substitution of the kaolinite (as the earlier formed lower temperature mineral) by illite/sericite in the course of prograde hydrothermalism, i.e., rising temperatures and increasing K^+ -activities in the hydrothermal fluids.

Quantitative analyses of more than 40 illites/sericites are presented in Appendix 3:3 together with additional information on the textural and chemical character of the analysed points/crystals. Problems of Pb-contamination resulting from the polishing discs and residues still occurred, but were less significant than in the case of the kaolinite analyses. In general, the analysed K-mica minerals of the F1 samples are more similar to hydro-muscovites, as indicated by their major element Si:Al:K proportions, than to either illite or muscovite. Fe, Na and Mg are usually always present; Mg as a major element (calculated di-valent oxide of >1.0 – 3.0 wt.%) and Fe and Na as minor elements (both <0.5 wt.% of the respective oxides). In addition, Y (in a few cases) and Ce (in one case) were detected.

3.4 Zircon and ZrO_2 -minerals

Special attention was paid to this mineral group due to the relatively high Zr-contents of the “potassic rock” which characterise much of the Osamu Utsumi mine (Waber *et al.*, this report series; Rep. 2) and also to the very high contents (up to 15.000 ppm Zr) associated with the deep-seated hydrothermal uranium mineralisations in the area (Fränkel *et al.*, 1985).

Zircons and intergrown ZrO_2 -minerals are the only Zr- and other rare metal-bearing minerals that occur as regular constituents of the hydrothermally altered rock of the mine. They are variable in amount, and occur as traces in both minor and major minerals. Furthermore, it is interesting to note that this mineral, which normally occurs as a high temperature magmatic accessory in igneous rocks, is exclusively of hydrothermal origin at the mine site and totally absent from the studied regional (igneous) rocks of the Poços de Caldas complex (Schorscher and Shea, this report series; Rep. 1).

These rocks contain other Zr-rich rare metal silicates such as giannetite (in the studied regional rocks) and eudialite (in the case of most of the agpaitic rocks of the Poços de

Caldas complex) sometimes associated as minor amounts with other rare metal silicates; these are totally absent from the hydrothermally altered “potassic rocks” of the mine.

Table 3-II contains some comparative geochemical data of the mean Zr and U contents of the regional igneous rocks and the mine rocks, e.g. F1 rocks and the deep-seated hydrothermal U-mineralisations of the F4 reduced magmatic breccias respectively.

Three main morphological types of zircons/ ZrO_2 -minerals have been identified:

- a) fine-grained, granular, idiomorphic to hypidiomorphic zircons (of grain size < 1 mm) that occur as rare isolated grains in nepheline syenites and phonolites,
- b) idiomorphic to hypidiomorphic-zoned zircons of variable grain sizes (mainly fine- to medium-grained) that normally occur as aggregated individuals and clusters in rock voids, pores and interstices, and
- c) skeletal zircons occurring as intergranular mosaics within the hydrothermally altered rock matrices and along leached primary grain boundaries.

TABLE 3-II

Comparative Zr and U geochemistry (mean values) of regional alkaline igneous rocks of the Poços de Caldas complex and of rocks of the Osamu Utsumi uranium mine (F1 = potassic rocks and F4 = deep-seated hydrothermal U-mineralisations; n = number of analyses).

Rock types	Zr (ppm)	U (ppm)	n
Regional igneous rocks ¹⁾	965	0	10
F1-oxidised rocks ²⁾	826	48	10
F1-reduced rocks ²⁾	854	24	16
F1-total ²⁾	918	133	38
F4-hydrotherm. U-mineralis. ¹⁾	16.500	2.410	17

¹⁾Analytical data from Univ. Bern.

²⁾Data from Waber *et al.* (this report series; Rep. 2).

All the zircons/ ZrO_2 -minerals were heterogeneous with variations in colouration, metamictisation and zoning indicating compositional differences within single crystals and between crystals.

More than 140 analysis of zircons were carried out and different textural types were selected. Furthermore, observations of the cathodoluminescence colours emitted under the incidence of the electron beam during microprobe analysis were also registered, if

different from the normal bluish-white colouration. Appendix 3:4 lists the zircon/ ZrO_2 -mineral analyses and some additional diagnostic observations of the studied crystals.

The lack of an adequate zircon standard mineral gave rise to some problems; a synthetic ZrS_2 was used and proved to be very inhomogeneous. This problem, together with the strong natural variability of the minerals to be analysed, made accurate standardisation for Zr impossible. Even so, most of the “typical” zircons that proved to be stable under the electron beam, and were relatively poor in minor elements, resulted in “totals” summing near 100 wt.%. However, a systematic over-estimation of ZrO_2 to the extent of 3-6 wt.%, have still to be accounted for.

Despite of the problems of standardisation, it was possible to define the chemical variability of the analysed zircons, zircon intergrowths and alterations. As a result, five groups of zircons/ ZrO_2 -minerals were defined:

Common zircons. These are represented by 105 of the analyses and contain $\text{Y}_2\text{O}_3 < 1.0$ wt.%, $\text{ZrO}_2 < 74.0$ wt.% and “totals” differing by $< 5\%$ of the 100.0 wt.%. Of the analysed individuals/points, 11 show contents of ThO_2 (max. 0.41 wt.%); 93 of HfO_2 (max. 1.43 wt.%); 93 of Y_2O_3 (max. 0.88 wt.%); 83 of Ce_2O_3 (max. 0.56 wt.%), and 55 of Yb_2O_3 (max. 0.26 wt.%). Yb and Ce show, in most cases (but not always), relationships of mutual exclusion. The “totals” of most of these analyses are on the high side by a few wt.% and frequently show correlated contents of $\text{ZrO}_2 > 70.0$ wt.%, clearly indicating an overestimation of Zr.

High-Y zircons. These are represented by 13 of the analyses. This group contains $\text{Y}_2\text{O}_3 > 1.01$ wt.% and “totals” that lie within the absolute limits of the common zircons group; however, most of the analyses total to less than 100.0 wt.%. These zircons may or may not contain HfO_2 (max. 0.70 wt.%), i.e., they are generally Hf-poor. They show maximum contents of $\text{Y}_2\text{O}_3 > 6.0$ wt.% and are generally Yb- and Ce-bearing. One Yb-free (Ce-bearing) and one Ce-free (Yb-bearing) exception, however, do occur. The former also contains ThO_2 (0.82 wt.%). It is believed that the zircons of this group (Appendix 3:3, analyses nos. 20, 58, 61, 64, 65, 66, 77, 78, 79, 88, 89, 111 and 116) generally contain greater amounts of isomorphic xenotime.

High Zr-zircons/ ZrO_2 -minerals. These included 13 analyses that show contents of $\text{ZrO}_2 > 74.0$ wt.% and totals > 104.0 wt.%. In all cases the excess of the analytical totals above 100.0 wt.% corresponds almost entirely to an excess of $\text{ZrO}_2 (> 70.0$ wt.%). These minerals are moderately Y_2O_3 -bearing (max. 0.50 wt.%) and generally contain HfO_2 (2

exceptions; max. 0.70 wt.%), Ce_2O_3 (2 exceptions; max. 0.16 wt.%) and less frequently, Yb_2O_3 (6 exceptions; 0.21 wt.%).

The analytical and microscopical evidence (Appendix 3:3; analyses nos. 67, 69, 80, 81, 82, 83, 84, 85, 86, 90, 91, 92, 93) indicate that these compositions may represent zircon/ ZrO_2 intergrowths/transitions.

High Y-zircons and zircons characterised by low total contents. 10 analyses (Appendix 3:3; analyses nos. 52, 53, 54, 55, 56, 57, 59, 60, 94, 117) were included in this group characterised by Y_2O_3 contents >1.0 wt.% (max. 7.52 wt.%) and generally by the presence and quite high contents of both Yb and Ce (max. of the trivalent oxides: 0.66 and 0.56 wt.% respectively). In these zircons Hf was not detected and the analytical totals are low, ranging from ~80.0 to not more than 94.0 wt.%. It is considered that these compositions may represent REE- and H_2O^+ -containing amorphous structural sites in the analysed zircons.

There is also a small group of 3 analyses (Appendix 3:3, analyses nos. 62, 100, 101) of two zircons which contain ZrO_2 contents <60 wt.% and the analytical totals lie between 86 and 91 wt.%. Ce, Yb and Hf may be sporadically present in small amounts. It is considered that these analyses may represent metamict zones within the analysed grains.

General remarks

None of the analysed zircons/ ZrO_2 -minerals showed the presence of U and only a few showed Th. Contamination from other major silicate or sulphide mineral elements (Al, K, Si, Fe) are almost absent, although Na is probably present in several cases (Appendix 3:3). Moreover, it is of interest to note that the different zircon/ ZrO_2 -mineral compositions are dominantly heterogeneously intergrown within the individual crystals, for instance in skeletal zircons, and that they also substitute for each other, even within optically contiguous areas of zoned idiomorphic single crystals. However, the zircons/ ZrO_2 minerals appear to be stable throughout the lithological profile of the mine, from the deepest, reduced hydrothermally altered rocks up to the lateritic cover.

Correspondingly, they did not contribute much to the formation of the supergenic redox front-related U-mineralisations of the mine. The mineralogy of the zircon/ ZrO_2 species will be more important for estimations of P-T and the chemical conditions which resulted in the “potassic rock” and related deep-seated hydrothermal U-mineralisation forming processes.

3.5 Fluorites

Some fluorite crystals (Appendix 3:5) were included in the microanalytical work.

Petrographical studies of drillcores F1 and F4 and of the regional rocks (Schorscher and Shea and Waber *et al.*, this report series; Reps. 1 and 2) show that violet fluorite is present at the Osamu Utsumi mine in the deep-seated U-mineralised breccias related to the mineralising hydrothermal event. However, colourless or light yellowish and light greenish fluorites also occur at the mine and also regionally, without showing, at least in the regional case, any particular relation to the normal postmagmatic hydrothermal U-enrichment processes.

Examples containing homogeneous and inhomogeneous fluorite crystals of variable colours and colour intensities were chosen for analysis. However, both belong to the “potassic rock” and the U-mineralisation-related hydrothermal event that affected the mine site. The analytical data are presented in Appendix 3:5, together with some observations on colour and textures.

The analyses revealed compositions of quite pure fluorites: U and Th were not detected and only the strongly violet coloured varieties showed the correlated presence of Y, and in one case, additionally of Ce (in amounts higher than Y). K-contents ($K_2O < 1.0$ wt.%) were detected in all cases and Na ($Na_2O < 0.1$ wt.%) less regularly. The origin of the alkalis is uncertain, but some contribution from fluid inclusions seems possible.

3.6 TiO_2 -(rutile)-minerals

TiO_2 -minerals, probably rutiles, occur throughout the rocks and ores of the Osamu Utsumi mine. Their origin from the reducing “potassic rock”-related hydrothermal alteration of mainly aegirine-augites has been described in Schorscher and Shea, and Waber *et al.* (this report series; Reps. 1 and 2). The main processes include:

- removal into solution of Na, Ca and Mg from the sodic pyroxenes,
- reduction and reprecipitation of iron as pyrite,
- reprecipitation of Ti as TiO_2 -minerals, probably rutile, and
- clay mineral formation.

Once formed, the TiO_2 -minerals remained preserved throughout the supergene mineralisation and the redox front-forming processes. TiO_2 -mineral species from many

igneous, hydrothermal and even supergenic origins, are known to be very effective scavengers for elements such as Nb and Ta, but may also fix REEs, U and Th among others. Consequently these were also included in the microanalytical programme.

Most interesting from a crystal-chemical viewpoint are the HfO₂-contents. It seems that the tetravalent Hf substitutes preferentially for Ti in the analysed Ti-oxide species, without being accompanied, in spite of the hydrothermal activity, by Zr. Besides, there regularly occur small Fe- and Si-contents and irregularly minor Al-, K- and, in one case, Na-contents. Of the REEs only Ce was regularly detected.

Quantitative results are presented in Appendix 3:6. Mineralogical and textural descriptions of the analysed individuals/points are not presented. All the analysed grains show granular forms (individual dimensions of a few tens of microns in diameter) and occur frequently aggregated in clusters pseudomorphosing mostly former aegirine-augites.

The analyses confirmed the common presence of Fe, Si and Al, and further revealed the equally frequent presence of Nb and, less regularly, of Y; the presence of Ce was not confirmed.

The microanalytical data support the excellent correlation of Nb and TiO₂ shown by the drillcore F1 bulk rock geochemistry (Waber *et al.*, this report series; Rep. 2), and reveal some additional probable relationships of these mineral species with Hf and Y. The sporadically observed Th-contents of the TiO₂-minerals cannot be correlated with any other particular geochemical or mineralogical feature of the studied samples. The U-content observed in sample SN 24-2RU2, i.e., a massive pitchblende nodule, arose from contamination.

3.7 U-minerals

Among the previously described minerals, U determinations were limited by the detection level of conventional microprobe techniques.

The only U-minerals detected at Osamu Utsumi mine, associated with deep-seated hydrothermal and redox front mineralisations (including the massive nodules as particular cases; Appendix 3:9; Plates 3:9-3 – 3:9-8) are black coloured cryptocrystalline U-oxides, generally termed pitchblendes. Analysis were carried out on pitchblendes from redox fronts (Appendix 3:9; Plates 3:9-3 – 3:9-6) and of massive nodules (Appendix 3:9; Plates 3:9-7 and 3:9-8).

Transmitted light and ore reflectance studies showed that the redox front-related pitchblende nodules (Appendix 3:9; Plates 3:9-3 to 3:9-6) consist of cryptocrystalline U-oxide impregnations located along grain boundaries and micropores in the reduced hydrothermally altered rocks. Furthermore, in the pitchblende nodules there was always observed the precipitation of a younger, secondary pyrite generation of pre- to early syn-pitchblende origin. Pitchblende precipitation took place over a broader time interval exceeding the formation of the 2nd. generation pyrites and was accompanied by minor greenockite (CdS) formation. This is particularly exhibited in the massive pitchblende nodules (Appendix 3:9; Plates 3:9-7 and 3:9-8).

From the analytical viewpoint it must be stressed that only pitchblendes of the massive nodules furnished reasonably reliable analysis. The pitchblendes of the redox front-related nodules (Appendix 3:9; Plates 3:9-3 – 3:9-6) are more problematical because they occur in fine inter-silicate mineral seams with cryptocrystalline porous textures, thus preventing selective point analysis with conventional microprobe techniques. In the massive nodules the pitchblendes form both cryptocrystalline textures, finely intergrown with silicates, and more massive homogeneous ones. These latter types reveal beautiful botryoidal- drusy growth forms, as coatings and fillings of micropores within the massive nodules, and colloidal ore textures with typical shrinking cracks. These textures are characteristic of low-temperature chemical precipitation followed by partial dehydration during formation of the massive nodule.

The analyses of the massive pitchblendes show higher analytical “totals” (≥ 94 wt.%) than those of the cryptocrystalline intergrowth and porous varieties. In both cases the pitchblendes consist of quite pure U-oxides. Minor elements (not contaminations) always include SiO_2 (≥ 0.9 – ≥ 2.0 wt.%) and P_2O_5 (0.1 – 0.2 wt.%). K_2O was common (usually around 1.0 – 2.0 wt.%) and Al_2O_3 only in some cases (normally < 1 wt.%). The quite frequent Fe-contents (as FeO_{tot} : 0.0 – ≥ 0.3 wt.%) are considered due to slight contamination caused by subsurface pyrite inclusions. Thorium was not detected. Among the analysed trace and REEs, only Ce occurs with certain regularity (Ce_2O_3 : 0.00 – 0.25 wt.%; Y was observed rarely and Yb just in one case.

3.8 Other minerals

These included pyrites of drillcore F1 rock samples (110-1A; 78-1A and 75-1B) and Fe-oxyhydroxide (HFO) minerals from oxidised rocks adjacent to redox front samples.

Pyrite

More than 50 quantitative analysis of distinct textural generations of pyrites from drillcore F1 were made, and all revealed pure pyrite compositions devoid of any minor element content. Occasionally, some (minor) Pb-contamination was detected, invariably associated with traces of As, from the polishing discs. The presence of minor amounts of Mo in pyrite was not possible to establish because of the analytical interference of sulphur.

Oxidised rocks

Samples of oxidised rocks from U-mineralised redox fronts were included for two reasons: a) the occurrence and analysis of U-oxide minerals on the reduced side, and b) the occurrence of HFO-minerals, possibly co-precipitated with measurable concentrations of radionuclides, REEs and other elements of analogue interest, on the oxidised side of the front. Particular attention was paid to samples hosting sharp redox fronts (Appendix 3:9; Plates 3:9-5 and 3:9-6) that permitted all the zones and minerals intended for analysis to be contained within individual polished sections. The unsuccessful attempt to measure the pitchblendes of the redox front-related nodules has been already discussed above. Equally unsuccessful was the attempt to measure HFO-minerals of low crystallinity because of their instability under the electron beam. The more stable iron species proved to be pure Fe-oxides. Analysis of the HFO-minerals require additional specific analytical techniques (see Veiga *et al.*, 1989) that were not available.

The microprobe work also revealed the presence of hydrated Ti-oxides in the oxidised rocks near the redox fronts. They correspond to hydrated varieties of the analysed Nb-bearing Ti-oxides of the reduced rocks (see above). The number of analyses, however, were not enough to verify whether the hydrated Nb-bearing Ti-oxides are substitution/alteration products of the reduced equivalents, or if they occur as additional, more recent independent species of supergenic origin.

4. References

- Frænkel, M.O., Santos, R.C.d., Loureiro, F.E.d.L. and Muniz, W.d.S., 1985. Jazida de urânio do planalto de Poços de Caldas – Minas Gerais. Chap. V, 89-103. In: C. Schobbenhaus and C.E. Silva Coelho (Editors). Principais depósitos minerais do Brasil/Vol. 1 – Recursos minerais energéticos. *DNPM/MME – CVRD – CPRM*, Brasília, 187 pp.
- Kübler, B., 1968. Evaluation quantitative du métamorphisme par la cristallinité de l'illite. *Bull. Centre Rech. Pan.*, SNEAP, 1, 259-278.
- Sommerauer, J., 1982. COMIC-ED Manual; comic-ed version 2. EXT, June 1981/October 1982 (102 pp., 3 append. and Program Listing). *Inst. Krist. Petrog.*, ETH – Zürich.
- Ulbrich, M.N.C., 1983. Aspectos mineralógicos e petrológicos de nefelina sienitos do maciço alcalino de Poços de Caldas, MG-SP. *PhD. Thesis* (unpubl.). Inst. Geociências, Univ. São Paulo, USP, São Paulo, 369 pp.
- Ulbrich, M.N.C., 1986. K-feldspars from the Poços de Caldas nepheline syenites, Southern Brazil: chemical, optical and XRD studies. *Acad. Bras. Ciências, Anais*, 58(1), Rio de Janeiro, 166 pp.
- Ulbrich, M.N.C., Gomes, C.B. de and Ulbrich, H.H.G.J., 1984. Nefelina sienitos do maciço alcalino de Poços de Caldas, MG-SP. 33° *Cong. Bras. Geol., Anais*, IX, 4362-4376 (publ. Soc. Bras. Geol., SP), Rio de Janeiro.
- Veiga, M.M. (Paulo Abib Eng., São Paulo, Brazil), Nogueira, Francisco T., Schorscher, H.D. and Fyfe, W.S., 1989. Relationship of copper with hydrous ferric oxides: Salobo, Carajas, Pa., Brazil [abstr.]: Program with Abstracts – Geological Association of Canada; Mineralogical Association of Canada; Canadian Geophysical Union, Joint Annual Meeting, 14, p. 115, May 1989. Meeting: May 15-17, 1989, Montreal, PQ, Canada.

Appendix 3:1

K-feldspar

Textural and electron microprobe data

Sample	Rock type
WC-75-1B	Reduced, medium-grained leucocratic phonolite.
WC-78-1A	Cataclastic zone in reduced leucocratic phonolite.
WC-110-1A	Reduced porous leucocratic phonolite.

Textural and some chemical characteristics of the analysed alkali feldspars
(dimensions used are coarse-, medium- and fine-grained and microcrystals, i.e.
respectively >5mm, 1-5, 0,2-1 and <0,2 mm).

Anal. No.	Sample No.	Descriptions
1	75/1-KF11	Neoformed microcrystal -1, centre.
2	75/1-KF12	Neoformed microcrystal -1, border.
3	75/1-KF16	Neoformed microcrystal -2.
4	75/1-KF17	Neoformed microcrystal -2.
5	75/1-KF18	Neoformed microcrystal -3.
6	75/1-KF15	Neoformed fine-grained crystal -4, border.
7	75/1-KF13	Neoformed fine-grained crystal -4, centre.
8	75/1-KF14	Neoformed fine-grained crystal -4, intermediate zone.
9	75/3KF01	Fine-grained crystal -1, intermediate zone, poor in inclusions.
10	75/3-KF02	Fine-grained crystal -1, clear border – free of inclusions; Y-(trace) contents.
11	75/3-KF01A	Fine-grained crystal -1, centre very rich in kaolinite, fluid and (?)HFO inclusions.
12	75/3-KF01B	Fine-grained crystal -1, clouded centre (same as -01A).
13	75/3-KF03	Fine-grained crystal -2, clear border.
14	75/3-KF04	Fine-grained crystal -2, clouded centre (with inclusions).
15*	75/3-KF05	Fine-grained crystal -3, clear border.
16	75/3-KF05A	Fine-grained crystal -3, intermediate zone with inclusions.
17*	75/3-KF06	Fine-grained crystal -3, centre-rich in inclusions; weak Pb-contamination.
18	75/3-KF06A	Fine-grained crystal -3, centre (near point -06); very weak Pb-contamination.
19	75/4-KF01	Groundmass crystal -1, border with inclusions.
20	75/4-KF02	Groundmass crystal -1, centre with inclusions.
21	75/4-KF03	Groundmass crystal -1, intermediate zone with inclusions; Ce-, Y- (trace) contents.
22	78/2-KF28	Medium-grained crystal, border with inclusions.
23	78/2-KF26	Medium-grained crystal, border with inclusions.
24	78/2-KF27	Medium-grained crystal, border with inclusions; Fe-(minor) contents.
25	78/2-KF29	Medium-grained crystal, intermediate zone with inclusions.
26	78/2-KF30	Medium-grained crystal, centre with inclusions.
27	78/2-KF31	Medium-grained crystal, centre with inclusions.
28	78/3-KF12	Fine-grained groundmass crystal with inclusions; Y-(trace) contents.
29	78/3-KF13	Fine-grained groundmass crystal with inclusions; Fe-(minor) contents.
30	78/3-KF13B	Fine-grained groundmass crystal with inclusions; Fe-(minor) contents.

Anal. No.	Sample No.	Descriptions
31	78/3-KF11	Fine-grained groundmass crystal with inclusions.
32*	78/6-KF21	Fine-grained groundmass crystal -1, border with inclusions.
33*	78/6-KF22	Fine-grained groundmass crystal -1, intermediate zone with inclusions.
34*	78/6-KF23	Fine-grained groundmass crystal -2, border, in contact with fluorite.
35	78/6-KF24	Fine-grained groundmass crystal -3, border with inclusions; in contact with zircon.
36*	78/6-KF25	Fine-grained groundmass crystal -3, intermediate zone with inclusions.
37*	78/7-KF01	Fine-grained groundmass crystal, border with inclusions; in contact with zircon; Fe-(minor) contents.
38*	78/8-KF06	Neoformed microcrystal -1, grown into kaolinite; border free of inclusions.
39	78/8-KF07	Neoformed microcrystal -1, centre, free of inclusions.
40	78/8-KF08	Fine-grained groundmass crystal -2, intermediate zone with inclusions; Y-(trace) contents.
41	78/8-KF09	Fine-grained groundmass crystal -2, intermediate zone with inclusions.
42	78/8-KF09A	Fine-grained groundmass crystal -2, border with inclusions.
43	78/9-KF01	Microcrystal finely intergrown with illite/sericite.
44	110/1-KF66	Microcrystal -1, border with zircon; pale blue cathodoluminescence.
45	110/1-KF67	Microcrystal -1, centre, pale blue cathodoluminescence.
46*	110/1-KF68	Microcrystal -1, border with zircon; red cathodoluminescence; Fe-(minor) contents.
47	110/1-KF69	Microcrystal -1, centre; red cathodoluminescence; Fe-(minor) contents.
48	110/1-KF65	Microcrystal -1, intermediate zone; red cathodoluminescence; Fe-(minor) contents.
49	110/1-KF70	Microcrystal -2, intermediate zone.
50	110/1-KF71	Microcrystal -2, border with zircon, Y-(minor) contents.
51	110/3-KF01	Coarse-grained phenocryst -1, centre, very rich in inclusions.
52	110/3-KF02	Coarse phenocryst -1, intermediate zone, very rich in inclusions.
53	110/3-KF03	Coarse phenocryst -1, intermediate zone; very rich in inclusions.
54	110/3-KF04	Coarse phenocryst -1, border with illite/sericite; with inclusions.
55	110/3-KF04A	Coarse phenocryst -1, border with pyrite; with inclusions.
56	110/3-KFM22	Fine-grained groundmass crystal -2, centre with inclusions.

Anal. No.	Sample No.	Descriptions
57*	110/3-KFM20	Fine-grained groundmass crystal -2, border with inclusions.
58	110/3-KFM21	Fine-grained groundmass crystal -2, intermediate zone with inclusions.
59	110/3-KFM19	Fine-grained groundmass crystal -2, border with inclusions.
60	110/4-KF10	Coarse phenocryst -1, border with kaolinite; with inclusions.
61	110/4-KF11	Coarse phenocryst -1, border with kaolinite; with inclusions.
62*	110/4-KF12	Coarse phenocryst -1, intermediate zone with inclusions.
63	110/4-KF13	Coarse phenocryst -1, centre with inclusions.
64	110/4-KFM29	Fine-grained groundmass crystal, border with inclusions; Fe-(minor) contents.
65	110/4-KFM28	Fine-grained groundmass crystal with inclusions.
66*	110/4-KFM27	Fine-grained groundmass crystal with inclusions.
67	110/4-KFM26	Fine-grained groundmass crystal with inclusions.

*Analysis not reported.

Crystal matrix: fine-grained centre					Crystal matrix: fine-grained intermediate zone			Crystal matrix: fine-grained clear rim					
Sample	75/3-KF01A	75/3-KF01B	75/3-KF04	75/3-KF06A	75/3-KF01	75/3-KF05A		75/3-KF02	75/3-KF03				
SiO ₂	64.07	63.51	63.66	63.12	63.00	63.83		63.75	63.75				
FeO	0.00	0.00	0.00	0.00	0.00	0.00		0.00	0.00				
Na ₂ O	0.19	0.16	0.26	0.19	0.44	0.17		0.09	0.13				
MgO	0.00	0.00	0.00	0.00	0.00	0.00		0.00	0.00				
K ₂ O	16.02	16.16	15.84	15.77	15.89	16.18		16.33	16.08				
Al ₂ O ₃	18.11	17.62	17.54	18.06	17.68	18.27		17.64	18.02				
UO ₂	0.00	0.00	0.00	0.00	0.00	0.00		0.00	0.00				
ThO ₂	0.00	0.00	0.00	0.00	0.00	0.00		0.00	0.00				
Yb ₂ O ₃	0.00	0.00	0.00	0.00	0.00	0.00		0.00	0.00				
Ce ₂ O ₃	0.00	0.00	0.00	0.00	0.00	0.00		0.00	0.00				
Y ₂ O ₃	0.00	0.00	0.00	0.00	0.00	0.00		0.05	0.00				
La ₂ O ₃	0.00	0.00	0.00	0.00	0.00	0.00		0.00	0.00				
Total (wt.%)	98.39	97.44	97.29	97.14	97.01	98.44		97.86	97.98				
Or	97.94	98.94	97.85	97.85	95.79	97.96		98.99	98.97				
Ab	2.06	1.06	2.15	2.15	4.21	2.04		1.01	1.03				

Crystal matrix: medium-grained centre														
Sample	75/4-KF02	78/2-KF30	78/2-KF31	78/3-KF12	78/3-KF13	78/3-KF13B	78/3-KF11	78/9-KF01	110/1-KF67	110/1-KF69	110/3-KF22	110/4-KF26	110/4-KF27	110/4-KF28
SiO ₂	64.23	63.68	65.23	65.84	64.54	64.92	65.50	63.70	63.97	64.11	64.87	65.59	64.17	63.37
FeO	0.00	0.00	0.00	0.00	0.90	0.59	0.00	0.00	0.00	0.46	0.00	0.00	0.00	0.00
Na ₂ O	0.25	0.18	0.11	0.40	0.38	0.30	0.26	0.34	0.00	0.11	0.00	0.10	0.18	0.14
MgO	0.00	0.00	0.00	0.00	0.00	0.00	0.00	0.00	0.00	0.00	0.00	0.00	0.00	0.00
K ₂ O	15.71	15.88	16.42	16.10	16.41	16.15	16.33	15.94	16.24	16.29	16.83	16.89	16.35	15.98
Al ₂ O ₃	17.71	17.98	18.16	18.33	18.26	18.49	18.08	17.41	18.07	18.04	18.23	18.10	18.64	17.61
UO ₂	0.00	0.00	0.00	0.00	0.00	0.00	0.00	0.00	0.00	0.00	0.00	0.00	0.00	0.00
ThO ₂	0.00	0.00	0.00	0.00	0.00	0.00	0.00	0.00	0.00	0.00	0.00	0.00	0.00	0.00
Yb ₂ O ₃	0.00	0.00	0.00	0.00	0.00	0.00	0.00	0.00	0.00	0.00	0.00	0.00	0.00	0.00
Ce ₂ O ₃	0.00	0.00	0.00	0.00	0.00	0.00	0.00	0.00	0.00	0.00	0.00	0.00	0.00	0.00
Y ₂ O ₃	0.00	0.00	0.00	0.09	0.00	0.00	0.00	0.00	0.00	0.00	0.00	0.00	0.00	0.00
La ₂ O ₃	0.00	0.00	0.00	0.00	0.00	0.00	0.00	0.00	0.00	0.00	0.00	0.00	0.00	0.00
Total (wt.%)	97.90	97.72	99.93	100.75	100.49	100.45	100.18	97.39	98.28	99.01	99.93	100.69	99.33	97.11
Or	97.92	97.94	98.97	95.92	96.97	96.94	97.96	96.84	100.00	98.98	100.00	98.92	97.98	99.00
Ab	2.08	2.06	1.03	4.08	3.03	3.06	2.04	3.16	0.00	1.02	0.00	1.08	2.02	1.00

Crystal matrix: medium-grained intermediate zone							
Sample	75/4-KF03	78/2-KF29	78/8-KF08	78/8-KF09	110/1-KF65	110/1-KF70	110/3-KF21
SiO ₂	63.38	63.53	64.53	63.66	63.96	63.51	63.88
FeO	0.00	0.00	0.00	0.00	0.43	0.00	0.00
Na ₂ O	0.28	0.15	0.16	0.27	0.08	0.09	0.05
MgO	0.00	0.00	0.00	0.00	0.00	0.00	0.00
K ₂ O	15.52	16.59	15.81	16.06	15.95	16.05	16.86
Al ₂ O ₃	17.30	18.66	18.68	17.61	17.84	17.94	18.30
UO ₂	0.00	0.00	0.00	0.00	0.00	0.00	0.00
ThO ₂	0.00	0.00	0.00	0.00	0.00	0.00	0.00
Yb ₂ O ₃	0.00	0.00	0.00	0.00	0.00	0.00	0.00
Ce ₂ O ₃	0.18	0.00	0.00	0.00	0.00	0.00	0.00
Y ₂ O ₃	0.09	0.00	0.04	0.00	0.00	0.00	0.00
La ₂ O ₃	0.00	0.00	0.00	0.00	0.00	0.00	0.00
Total (wt.%)	96.75	98.92	99.22	97.61	98.26	97.59	99.09
Or	97.80	99.00	97.89	97.89	98.96	98.94	100.00
Ab	2.20	1.00	2.11	2.11	1.04	1.06	0.00

Crystal matrix: medium-grained rim										
Sample	75/4-KF01	78/2-KF28	78/2-KF26	78/2-KF27	78/6-KF24	78/8-KF09A	110/1-KF66	110/1-KF71	110/3-KF19	110/4-KF29
SiO ₂	64.37	64.42	63.40	64.93	64.55	64.55	63.64	63.73	64.09	64.77
FeO	0.00	0.00	0.00	0.59	0.00	0.00	0.00	0.00	0.00	0.56
Na ₂ O	0.32	0.06	0.13	0.09	0.18	0.17	0.00	0.00	0.00	0.18
MgO	0.00	0.00	0.00	0.00	0.00	0.00	0.00	0.00	0.00	0.00
K ₂ O	15.72	16.26	16.75	16.13	16.35	16.23	16.75	16.39	17.07	16.76
Al ₂ O ₃	17.82	18.71	18.03	18.63	18.11	18.34	17.70	18.41	17.82	17.58
UO ₂	0.00	0.00	0.00	0.00	0.00	0.00	0.00	0.00	0.00	0.00
ThO ₂	0.00	0.00	0.00	0.00	0.00	0.00	0.00	0.00	0.00	0.00
Yb ₂ O ₃	0.00	0.00	0.00	0.00	0.00	0.00	0.00	0.00	0.00	0.00
Ce ₂ O ₃	0.00	0.00	0.00	0.00	0.00	0.00	0.00	0.00	0.00	0.00
Y ₂ O ₃	0.00	0.00	0.00	0.00	0.00	0.00	0.00	0.20	0.00	0.00
La ₂ O ₃	0.00	0.00	0.00	0.00	0.00	0.00	0.00	0.00	0.00	0.00
Total (wt.%)	98.22	99.46	98.31	100.36	99.18	99.28	98.10	98.73	98.98	99.85
Or	96.91	98.97	90.91	98.95	97.98	97.96	100.00	100.00	100.00	98.02
Ab	3.09	1.03	9.09	1.05	2.02	2.04	0.00	0.00	0.00	1.98

Crystal matrix: phenocryst centre			Crystal matrix: phenocryst intermediate zone		Crystal matrix: phenocryst rim			
Sample	110/3-KF01	110/4-KF13	110/3-KF02	110/3-KF03	110/3-KF04	110/3-KF04A	110/4-KF10	110/4-KF11
SiO ₂	64.41	63.76	63.88	64.88	63.94	65.07	64.33	64.23
FeO	0.00	0.00	0.00	0.00	0.00	0.00	0.00	0.00
Na ₂ O	0.00	0.00	0.05	0.05	0.10	0.00	0.00	0.13
MgO	0.00	0.00	0.00	0.00	0.00	0.00	0.00	0.00
K ₂ O	15.62	16.88	16.04	16.59	17.09	16.38	16.70	16.89
Al ₂ O ₃	18.23	17.71	18.04	18.30	18.16	18.42	17.99	18.38
UO ₂	0.00	0.00	0.00	0.00	0.00	0.00	0.00	0.00
ThO ₂	0.00	0.00	0.00	0.00	0.00	0.00	0.00	0.00
Yb ₂ O ₃	0.00	0.00	0.00	0.00	0.00	0.00	0.00	0.00
Ce ₂ O ₃	0.00	0.00	0.00	0.00	0.00	0.00	0.00	0.00
Y ₂ O ₃	0.00	0.00	0.00	0.00	0.00	0.00	0.00	0.00
La ₂ O ₃	0.00	0.00	0.00	0.00	0.00	0.00	0.00	0.00
Total (wt.%)	98.26	98.35	98.01	99.82	99.29	99.87	99.03	99.63
Or	100.00	100.00	100.0	100.00	99.03	100.00	100.00	100.00
Ab	0.00	0.00	0.00	0.00	0.97	0.00	0.00	0.00

Crystal matrix: neoformed centre						Crystal matrix: neoformed clear rim			
Sample	75/1-KF11	75/1-KF16	75/1-KF17	75/1-KF18	75/1-KF13	78/8-KF07	75/1-KF12	75/1-KF14	75/1-KF15
SiO ₂	63.26	63.73	63.43	63.92	63.38	63.86	63.50	63.56	63.40
FeO	0.00	0.00	0.00	0.00	0.00	0.00	0.00	0.00	0.00
Na ₂ O	0.10	0.15	0.09	0.19	0.00	0.13	0.10	0.16	0.11
MgO	0.00	0.00	0.00	0.00	0.00	0.00	0.00	0.00	0.00
K ₂ O	15.63	16.39	15.85	15.70	16.75	15.81	16.20	16.69	16.35
Al ₂ O ₃	20.13	18.56	17.76	17.99	17.61	17.54	17.75	17.85	17.83
UO ₂	0.00	0.00	0.00	0.00	0.00	0.00	0.00	0.00	0.00
ThO ₂	0.00	0.00	0.00	0.00	0.00	0.00	0.00	0.00	0.00
Yb ₂ O ₃	0.00	0.00	0.00	0.00	0.00	0.00	0.00	0.00	0.00
Ce ₂ O ₃	0.00	0.00	0.00	0.00	0.00	0.00	0.00	0.00	0.00
Y ₂ O ₃	0.00	0.00	0.00	0.00	0.00	0.00	0.00	0.00	0.00
La ₂ O ₃	0.00	0.00	0.00	0.00	0.00	0.00	0.00	0.00	0.00
Total (wt.%)	99.11	98.82	97.14	97.80	97.74	97.34	97.55	98.26	97.68
Or	98.92	98.99	98.91	97.92	100.00	98.91	98.94	98.04	98.96
Ab	1.08	1.01	1.09	2.08	0.00	1.09	1.06	1.96	1.04

Appendix 3:2

Kaolinite

Textural and electron microprobe data

Sample	Rock type
WC-75-1B	Reduced, medium-grained leucocratic phonolite.
WC-78-1A	Cataclastic zone in reduced leucocratic phonolite.
WC-110-1A	Reduced porous leucocratic phonolite.

Textural and some chemical characteristics of the analysed kaolinites (minor element contents were considered to be <0.7 wt.% of the respective oxides).

Anal. No.	Sample No.	Description
1	78/5-KO00	Kaolinite-zircon-pyrite precipitate in a void.
2	78/8-KO01	Kaolinite-pyrite precipitate in a void, near pyrite; minor element contents of Na and Mg.
3	78/8-KO02	Idem, near pyrite; minor element contents of Fe, Na and Mg.
4	78/8-KO03	Idem, near pyrite; minor element contents of Na and Mg; weak Pb-contamination.
5	78/8-KO04	Idem, intermediate zone; minor element contents of Na and Mg; weak Pb-contamination.
6	75/5-KO01	Zoned kaolinite (centre)-sericite (border) pseudomorph of nepheline, near sericite border; weak Pb-contamination.
7	75/5-KO01A	Idem, near sericite border; minor element content of Na.
8	75/5-KO02	Idem, near sericite border; Pb-contamination!
9	75/5-KO02A	Idem, intermediate zone of kaolinite; Pb-contamination! Minor element contents of Fe and Na.
10	75/5-KO03	Idem, intermediate zone of kaolinite; Pb-contamination!
11	75/5-KO04	Idem, central part of kaolinite; K-(sericite) and Pb-contamination; minor element contents of Fe and Na.
12	75/5-KO05	Idem, central part of kaolinite; minor element contents of Fe and Na.
13	75/5-KO06	Idem, intermediate zone of kaolinite; Pb-contamination.
14	75/5-KO07	Idem, central part of kaolinite; minor element contents of Fe and Na.
15	78/2-KO00	Kaolinite-zircon-pyrite precipitate in a void centre.
16	78/2-KO19	As above, near zircon; minor element content of Mg.
17	78/2-KO20	Idem, near zircon.
18	78/2-KO21	Idem, intermediate zone.
19	78/2-KO22	Idem, intermediate zone; minor element content of Mg; Pb-contamination.
20	78/2-KO22A	Idem, intermediate zone.
21	78/2-KO23	Idem, intermediate zone; minor element content of Mg.
22	78/2-KO24	Idem, intermediate zone.
23	78/2-KO24A	Idem, intermediate zone.
24	78/2-KO25	Idem, near alkali feldspar; minor element content of Mg.
25*	110/5-KO03A	Mainly sericite pseudomorph of nepheline; minor element content of Ce.
26	110/5-KO02	As above, centre; K-(sericite) contamination; minor element content of Fe.
27	110/5-KO04	Idem, centre.
28	110/5-KO03	Idem, centre.
29	110/4-K01	Mainly kaolinite pseudomorph of nepheline; centre.
30	110/4-K02	As above, intermediate zone.

Anal. No.	Sample No.	Description
31	110/4-K03	Idem, centre; associated with pyrite.
32	110/4-K04	Idem, centre; associated with pyrite; minor content of Na; K-(sericite) contamination.
33	110/4-K05	Idem, centre; associated with pyrite.
34	110/4-K06	Idem, centre.
35	110/4-K07	Idem, border; K-(sericite) contamination.
36	110/4-K08A	Idem, intermediate zone; Pb contamination.
37	110/4-K09	Idem, intermediate zone; K-(sericite) and Pb-contamination.
38	78/5-KO19	Kaolinite-zircon-pyrite precipitate in a void, near zircon; Pb-contamination; minor element content of Mg.
40	78/5-KO18	Idem, near zircon; minor element content of Na.
41	78/5-KO18A	Idem, intermediate zone; Pb-contamination; minor element content of Y.
42	78/5-KO21	Idem, near pyrite.
43	78/5-KO22	Idem, intermediate zone; Pb-contamination; minor element contents of Na and Y.
44	78/5-KO20	Idem, intermediate zone.

*Analysis not reported.

Crystal matrix: kaolinites from nepheline pseudomorphs											
Sample	75/5-KO01	75/5-KO01A	75/5-KO02	75/5-KO02A	75/5-KO03	75/5-KO04	75/5-KO05	75/5-KO06	75/5-KO07	110/5-KO03	110/5-KO02
SiO ₂	43.88	47.12	45.20	48.05	47.59	47.96	47.99	47.50	47.48	47.16	46.73
FeO	0.00	0.00	0.00	0.68	0.00	0.64	0.44	0.00	0.51	0.00	0.47
Na ₂ O	0.00	0.06	0.00	0.05	0.00	0.05	0.06	0.00	0.09	0.00	0.00
MgO	0.00	0.00	0.00	0.00	0.00	0.00	0.00	0.00	0.00	0.00	0.00
K ₂ O	0.00	0.00	0.00	0.00	0.00	0.73	0.00	0.00	0.00	0.00	0.30
Al ₂ O ₃	36.54	39.00	37.87	39.43	39.32	39.37	40.17	39.86	39.00	38.38	38.14
UO ₂	0.00	0.00	0.00	0.00	0.00	0.00	0.00	0.00	0.00	0.00	0.00
ThO ₂	0.00	0.00	0.00	0.00	0.00	0.00	0.00	0.00	0.00	0.00	0.00
ZrO ₂	0.00	0.00	0.00	0.00	0.00	0.00	0.00	0.00	0.00	0.00	0.00
Ce ₂ O ₃	0.00	0.00	0.00	0.00	0.00	0.00	0.00	0.00	0.00	0.17	0.00
La ₂ O ₃	0.00	0.00	0.00	0.00	0.00	0.00	0.00	0.00	0.00	0.00	0.00
Y ₂ O ₃	0.00	0.00	0.00	0.00	0.00	0.00	0.00	0.00	0.00	0.00	0.00
Yb ₂ O ₃	0.00	0.00	0.00	0.00	0.00	0.00	0.00	0.00	0.00	0.00	0.00
HfO ₂	0.00	0.00	0.00	0.00	0.00	0.00	0.00	0.00	0.00	0.00	0.00
Total (wt.%)	80.42	86.17	83.07	88.21	86.91	88.75	88.65	87.36	87.09	85.71	85.64

Crystal matrix: kaolinites from nepheline pseudomorphs (contd.)											
Sample	110/5-KO04	110/5-KO03	110/4-K01	110/4-K02	110/4-K03	110/4-K04	110/4-K05	110/4-K06	110/4-K07	110/4-K08A	110/4-K09
SiO ₂	45.32	45.51	45.90	45.00	44.65	45.17	45.67	45.83	46.10	43.00	41.17
FeO	0.00	0.00	0.00	0.00	0.00	0.00	0.00	0.00	0.00	0.00	0.00
Na ₂ O	0.00	0.00	0.00	0.00	0.00	0.05	0.00	0.00	0.00	0.00	0.00
MgO	0.00	0.00	0.00	0.00	0.00	0.00	0.00	0.00	0.00	0.00	0.00
K ₂ O	0.00	0.00	0.00	0.00	0.00	1.73	0.00	0.00	0.71	0.00	0.45
Al ₂ O ₃	37.22	36.92	39.18	39.09	38.66	37.43	38.78	39.16	39.56	36.82	35.16
UO ₂	0.00	0.00	0.00	0.00	0.00	0.00	0.00	0.00	0.00	0.00	0.00
ThO ₂	0.00	0.00	0.00	0.00	0.00	0.00	0.00	0.00	0.00	0.00	0.00
ZrO ₂	0.00	0.00	0.00	0.00	0.00	0.00	0.00	0.00	0.00	0.00	0.00
Ce ₂ O ₃	0.00	0.00	0.00	0.00	0.00	0.00	0.00	0.00	0.00	0.00	0.00
La ₂ O ₃	0.00	0.00	0.00	0.00	0.00	0.00	0.00	0.00	0.00	0.00	0.00
Y ₂ O ₃	0.00	0.00	0.00	0.00	0.00	0.00	0.00	0.00	0.00	0.00	0.00
Yb ₂ O ₃	0.00	0.00	0.00	0.00	0.00	0.00	0.00	0.00	0.00	0.00	0.00
HfO ₂	0.00	0.00	0.00	0.00	0.00	0.00	0.00	0.00	0.00	0.00	0.00
Total (wt.%)	82.53	82.43	85.08	84.09	83.31	84.37	84.46	84.98	86.36	79.81	76.78

Crystal matrix: kaolinites from zircon-pyrite-clay precipitate in voids

Sample	78/5-KO00	78/8-KO01	78/8-KO02	78/8-KO03	78/8-KO04	78/5-KO19	78/5-KO19A	78/5-KO18	78/5-KO18A	78/5-KO21	78/5-KO22
SiO ₂	46.21	43.87	43.78	44.14	43.11	44.73	44.99	46.63	46.67	46.33	45.28
FeO	0.00	0.00	0.52	0.00	0.00	0.00	0.00	0.00	0.00	0.00	0.00
Na ₂ O	0.00	0.12	0.11	0.08	0.10	0.00	0.00	0.04	0.00	0.00	0.05
MgO	0.00	0.26	0.30	0.12	0.25	0.16	0.00	0.00	0.00	0.00	0.00
K ₂ O	0.00	0.00	0.00	0.00	0.00	0.00	0.00	0.00	0.00	0.00	0.00
Al ₂ O ₃	38.71	37.91	38.00	36.33	37.27	37.07	37.24	39.53	39.43	39.27	37.60
UO ₂	0.00	0.00	0.00	0.00	0.00	0.00	0.00	0.00	0.00	0.00	0.00
ThO ₂	0.00	0.00	0.00	0.00	0.00	0.00	0.00	0.00	0.00	0.00	0.00
ZrO ₂	0.00	0.00	0.00	0.00	0.00	0.00	0.00	0.00	0.00	0.00	0.00
Ce ₂ O ₃	0.00	0.00	0.00	0.00	0.00	0.00	0.00	0.00	0.00	0.00	0.00
La ₂ O ₃	0.00	0.00	0.00	0.00	0.00	0.00	0.00	0.00	0.00	0.00	0.00
Y ₂ O ₃	0.00	0.00	0.00	0.00	0.00	0.00	0.00	0.00	0.05	0.00	0.06
Yb ₂ O ₃	0.00	0.00	0.00	0.00	0.00	0.00	0.00	0.00	0.00	0.00	0.00
HfO ₂	0.00	0.00	0.00	0.00	0.00	0.00	0.00	0.00	0.00	0.00	0.00
Total (wt.%)	84.92	82.17	82.71	80.67	80.73	81.96	82.23	86.20	86.15	85.60	83.00

Crystal matrix: kaolinites from zircon-pyrite-clay precipitate in voids (contd.)

Sample	78/5-KO20	78/2-KO00	78/2-KO19	78/2-KO20	78/2-KO21	78/2-KO22	78/2-KO22A	78/2-KO23	78/2-KO24	78/2-KO24A	78/2-KO25
SiO ₂	43.70	46.60	45.98	45.38	45.64	43.25	46.79	46.92	44.23	44.37	44.58
FeO	0.00	0.00	0.00	0.00	0.00	0.00	0.00	0.00	0.00	0.00	0.00
Na ₂ O	0.00	0.00	0.00	0.00	0.00	0.00	0.00	0.00	0.00	0.00	0.00
MgO	0.00	0.00	0.09	0.00	0.00	0.07	0.00	0.11	0.00	0.00	0.06
K ₂ O	0.00	0.00	0.00	0.00	0.00	0.00	0.00	0.00	0.00	0.00	0.00
Al ₂ O ₃	37.45	38.85	38.41	38.56	38.60	36.24	39.14	38.18	36.96	37.44	37.59
UO ₂	0.00	0.00	0.00	0.00	0.00	0.00	0.00	0.00	0.00	0.00	0.00
ThO ₂	0.00	0.00	0.00	0.00	0.00	0.00	0.00	0.00	0.00	0.00	0.00
ZrO ₂	0.00	0.00	0.00	0.00	0.00	0.00	0.00	0.00	0.00	0.00	0.00
Ce ₂ O ₃	0.00	0.00	0.00	0.00	0.00	0.00	0.00	0.00	0.00	0.00	0.00
La ₂ O ₃	0.00	0.00	0.00	0.00	0.00	0.00	0.00	0.00	0.00	0.00	0.00
Y ₂ O ₃	0.00	0.00	0.00	0.00	0.00	0.00	0.00	0.00	0.00	0.00	0.00
Yb ₂ O ₃	0.00	0.00	0.00	0.00	0.00	0.00	0.00	0.00	0.00	0.00	0.00
HfO ₂	0.00	0.00	0.00	0.00	0.00	0.00	0.00	0.00	0.00	0.00	0.00
Total (wt.%)	81.15	85.45	84.48	83.94	84.25	79.56	85.93	85.21	81.19	81.81	82.24

Appendix 3:3

Illite/sericite

Textural and electron microprobe data

Sample	Rock type
WC-75-1B	Reduced, medium-grained leucocratic phonolite.
WC-78-1A	Cataclastic zone in reduced leucocratic phonolite.
WC-110-1A	Reduced porous leucocratic phonolite.

Textural and some chemical characteristics of the analysed illites/sericites (major element contents (M) were considered to be ≥ 1.0 wt.% and minor element contents (m) to be <1.0 wt.%, of the respective oxides).

Anal. No.	Sample No.	Description	Chemistry
1	78/9-S01	Almost monomineralic illite/sericite pseudomorph of nepheline	Fe - M; Na, Mg - m
2	78/9-S02	As above	Fe - M; Na, Mg - m; Pb-contamination!
3	78/9-S03	Idem	Fe - M; Na, Mg - m
4	78/9-S04	Idem	Fe - M; Na, Mg - m
5	78/9-S05	Idem	Fe, Na, Mg - m
6*	78/9-S06	Idem	Fe - M; Na, Mg, Y - m. Pb-contamination!
7	78/9-S07	Idem	Fe - M; Na, Mg - m; Pb-contamination!
8*	78/9-S08	Idem	Fe - M; Na, Mg, Y - m; Pb-contamination!
9*	78/9-S08A	Idem	Fe - M; Na, Mg - m; Pb-contamination!
10	75/2-S01	Almost monomineralic illite/sericite precipitate in a void	Fe - M; Na, Mg - m
11	75/2-S02	As above	Fe, Na, Mg, Y - m
12	75/2-S03	Idem	Fe, Na - m
13*	75/2-S05	Idem	Fe - M; Na, Mg - m; Pb-contamination!
14*	75/2-S06	Idem	Fe - M; Na, Mg - m; Pb-contamination!
15	75/2-S06A	Idem	Fe - M; Na, Mg - m
16	75/2-S06B	Idem	Fe-M; Na, Mg, Y - m
17	75/5-S08	Zoned illite/sericite-kaolinite aggregate, near border of kaolinite	Fe - M; Na, Mg, Ce - m
18	75/5-S10	As above, internal part of illite/sericite zone	Fe - M; Na, Mg - m
19	75/5-S11	Idem, internal part	Fe - M; Na, Mg - m
20	75/5-S12	Idem, internal part	Fe - M; Na, Mg - m
21	110/1-S72	Illite/sericite-zircon-pyrite precipitate in rock interstices, border of larger single crystal- 1	Fe, Mg - m
22	110/1-S73	As above, internal part of crystal - 1	Mg - m
23	110/1-S74	Idem, internal part of crystal - 1	Fe - m

Anal. No.	Sample No.	Description	Chemistry
24	110/1-S75	Idem, larger single crystal - 2, bordering pyrite	Fe, Mg - m
25	110/1-S76	Idem, larger crystal - 2, bordering zircon and pyrite	Fe - M; Na, Mg - m; Zr-contamination
26	110/1-S76	Idem, repeated analysis without Zr- contamination	Fe - M; Mg - m
27	110/1-S77	Idem, intermediate zone of crystal - 2	Fe, Mg - m
28	110/1-S78	Idem, internal part of crystal - 3	Fe, Na, Mg - m
29	110/1-S79	Idem, crystal - 3, border with pyrite	Fe, Mg - m
30	110/1-S80	Idem, internal part of crystal - 2	Fe, Na - m
31	110/3-S23	Centre of larger individual crystal -1	Fe - M; Mg - m
32*	110/3-S24	Internal part of larger crystal - 1;	Fe - M; Mg - m; Pb-contamination!
33	110/3-S25	Rim of larger crystal - 1	Fe - M; Mg - m
34*	110/3-S26	Rim of larger crystal - 1	Fe - M; Na, Mg - m; Pb-contamination!
35	110/5-SO05	Composed pseudomorph of ne, internal part of illite/sericite zone	Na - m
36	110/5-SO06	As above	Fe, Na, Mg, Y - m
37	110/5-SO07	Idem	Fe - M; Na - m
38	110/6-SO08	Idem	Fe - M; Na, Mg - m
39	110/5-SO09	Idem	Fe - M; Na, Mg - m
40	110/4-S21	Almost monomineralic illite/sericite domain of composed aggregate	Fe - M; Na - m
41	110/4-S22	As above	Fe, Mg - m
42	110/4-S23	Idem	Fe - M; Mg - m
43*	110/4-S24	Idem	Fe - M; Mg - m
44*	110/4-S25	Idem	Fe - M; Na, Mg - m

*Analysis not reported.

Crystal matrix: illite from nepheline pseudomorphs, central zone														
Sample	78/9-S01	78/9-S02	78/9-S03	78/9-S04	78/9-S05	78/9-S07	110/5-SO05	110/5-SO06	110/5-SO07	110/5-SO08	110/5-SO09	110/4-S21	110/4-S22	110/4-S23
SiO ₂	45.46	45.01	45.29	45.78	45.47	44.63	47.62	46.34	47.40	46.41	46.88	45.95	44.81	46.43
FeO	1.55	2.33	2.09	2.52	0.90	2.38	0.00	0.67	1.17	2.19	1.33	1.05	0.95	1.32
Na ₂ O	0.14	0.13	0.13	0.14	0.15	0.09	0.06	0.09	0.12	0.07	0.13	0.09	0.00	0.00
MgO	0.19	0.29	0.31	0.24	0.14	0.27	0.00	0.08	0.00	0.27	0.29	0.00	0.08	0.21
K ₂ O	9.91	9.60	9.73	9.37	9.81	9.34	10.87	11.13	11.37	10.60	10.84	10.84	10.38	10.40
Al ₂ O ₃	35.13	33.12	34.31	33.92	35.80	33.52	37.75	36.25	35.48	34.42	35.14	37.08	35.88	35.74
UO ₂	0.00	0.00	0.00	0.00	0.00	0.00	0.00	0.00	0.00	0.00	0.00	0.00	0.00	0.00
ThO ₂	0.00	0.00	0.00	0.00	0.00	0.00	0.00	0.00	0.00	0.00	0.00	0.00	0.00	0.00
Yb ₂ O ₃	0.00	0.00	0.00	0.00	0.00	0.00	0.00	0.00	0.00	0.00	0.00	0.00	0.00	0.00
Ce ₂ O ₃	0.00	0.00	0.00	0.00	0.00	0.00	0.00	0.00	0.00	0.00	0.00	0.00	0.00	0.00
Y ₂ O ₃	0.00	0.00	0.00	0.00	0.00	0.00	0.00	0.61	0.00	0.00	0.00	0.00	0.00	0.00
La ₂ O ₃	0.00	0.00	0.00	0.00	0.00	0.00	0.00	0.00	0.00	0.00	0.00	0.00	0.00	0.00
Total (wt.%)	92.39	90.48	91.85	91.97	92.26	90.23	96.31	95.16	95.54	93.96	94.61	95.00	92.09	94.09
Normalised on 22 O														
Si	6.21	6.30	6.24	6.29	6.19	6.26	6.20	6.17	6.22	6.27	6.27	6.11	6.14	6.23
Al IV	1.79	1.70	1.76	1.71	1.81	1.74	1.80	1.83	1.78	1.73	1.73	1.89	1.86	1.77
Al VI	3.86	3.76	3.81	3.78	3.93	3.80	3.99	3.86	3.86	3.75	3.81	3.93	3.93	3.88
Fe	0.18	0.27	0.24	0.29	0.10	0.28	0.00	0.07	0.13	0.25	0.15	0.12	0.11	0.15
Mg	0.04	0.06	0.06	0.05	0.03	0.06	0.00	0.02	0.00	0.06	0.06	0.00	0.02	0.04
K	1.73	1.71	1.71	1.64	1.70	1.67	1.81	1.89	1.90	1.83	1.85	1.84	1.81	1.78
Na	0.04	0.04	0.04	0.04	0.04	0.02	0.02	0.02	0.03	0.02	0.03	0.02	0.00	0.00

Sample	Crystal matrix: illite from nepheline pseudomorphs, central zone (contd.)		Crystal matrix: illite from nepheline pseudomorphs, border zone			
	110/4-S25	110/4-S24	75/5-S08	75/5-S10	75/5-S11	75/5-S12
SiO ₂	45.83	45.56	46.66	46.60	46.86	46.87
FeO	2.00	2.80	1.56	2.38	1.71	2.29
Na ₂ O	0.08	0.00	0.12	0.13	0.13	0.11
MgO	0.23	0.47	0.21	0.16	0.15	0.21
K ₂ O	10.83	10.37	8.34	8.80	8.36	8.69
Al ₂ O ₃	36.26	34.30	35.54	35.63	35.27	35.41
UO ₂	0.00	0.00	0.00	0.00	0.00	0.00
ThO ₂	0.00	0.00	0.00	0.00	0.00	0.00
Yb ₂ O ₃	0.00	0.00	0.00	0.00	0.00	0.00
Ce ₂ O ₃	0.00	0.00	0.33	0.00	0.00	0.00
Y ₂ O ₃	0.00	0.00	0.00	0.00	0.00	0.00
La ₂ O ₃	0.00	0.00	0.00	0.00	0.00	0.00
Total (wt.%)	95.24	93.50	92.76	93.70	92.48	93.58
Normalised on 22 O						
Si	6.12	6.21	6.28	6.25	6.32	6.28
Al IV	1.88	1.79	1.72	1.75	1.68	1.72
Al VI	3.83	3.72	3.92	3.88	3.92	3.87
Fe	0.22	0.32	0.18	0.27	0.19	0.26
Mg	0.05	0.10	0.04	0.03	0.03	0.04
K	1.84	1.80	1.43	1.50	1.44	1.49
Na	0.02	0.00	0.03	0.03	0.03	0.03

Crystal matrix: interstitial illite-zircon-pyrite assemblage												
Sample	110/1-S72	110/1-S73	110/1-S74	110/1-S75	110/1-S76	110/1-S76	110/1-S77	110/1-S78	110/1-S79	110/1-S80	110/3-S23	110/3-S25
SiO ₂	45.77	46.08	45.61	45.85	45.99	46.67	45.88	46.23	46.31	44.45	45.22	45.50
FeO	0.54	0.00	0.82	0.92	1.38	1.26	0.77	0.47	0.61	0.37	2.28	1.57
Na ₂ O	0.00	0.00	0.00	0.00	0.04	0.00	0.00	0.04	0.00	0.03	0.00	0.00
MgO	0.06	0.05	0.00	0.09	0.22	0.18	0.15	0.36	0.08	0.00	0.20	0.17
K ₂ O	9.92	10.25	10.43	7.82	9.41	8.24	10.36	10.28	10.11	10.65	9.71	8.94
Al ₂ O ₃	37.62	37.94	37.59	36.72	36.08	36.58	36.83	35.95	37.18	37.00	34.40	35.73
UO ₂	0.00	0.00	0.00	0.00	0.00	0.00	0.00	0.00	0.00	0.00	0.00	0.00
ThO ₂	0.00	0.00	0.00	0.00	0.00	0.00	0.00	0.00	0.00	0.00	0.00	0.00
Yb ₂ O ₃	0.00	0.00	0.00	0.00	0.00	0.00	0.00	0.00	0.00	0.00	0.00	0.00
Ce ₂ O ₃	0.00	0.00	0.00	0.00	0.00	0.00	0.00	0.00	0.00	0.00	0.00	0.00
Y ₂ O ₃	0.00	0.00	0.00	0.00	0.00	0.00	0.00	0.00	0.00	0.00	0.00	0.00
La ₂ O ₃	0.00	0.00	0.00	0.00	0.00	0.00	0.00	0.00	0.00	0.00	0.00	0.00
Total (wt.%)	93.89	94.32	94.45	91.39	93.23	92.93	93.99	93.33	94.29	92.51	91.81	91.92
Normalised on 22 O												
Si	6.11	6.11	6.08	6.21	6.19	6.24	6.14	6.22	6.16	6.06	6.23	6.20
Al IV	1.89	1.89	1.92	1.79	1.81	1.76	1.86	1.78	1.84	1.94	1.77	1.80
Al VI	4.03	4.04	3.99	4.07	3.92	4.00	3.95	3.92	3.99	4.00	3.82	3.94
Fe	0.06	0.00	0.09	0.10	0.15	0.14	0.09	0.05	0.07	0.04	0.26	0.18
Mg	0.01	0.01	0.00	0.02	0.04	0.04	0.03	0.07	0.02	0.00	0.04	0.04
K	1.69	1.73	1.77	1.35	1.62	1.40	1.77	1.76	1.72	1.85	1.71	1.55
Na	0.00	0.00	0.00	0.00	0.01	0.00	0.00	0.01	0.00	0.01	0.00	0.00

Crystal matrix: void infilling					
Sample	75/2-S01	75/2-S02	75/2-S03	75/2-S06A	75/2-S06B
SiO ₂	45.84	45.29	45.42	45.92	45.50
FeO	1.63	0.96	0.61	2.00	2.36
Na ₂ O	0.08	0.10	0.04	0.10	0.14
MgO	0.16	0.08	0.00	0.08	0.09
K ₂ O	9.37	9.73	9.52	8.11	9.49
Al ₂ O ₃	34.67	35.55	35.45	35.07	34.77
UO ₂	0.00	0.00	0.00	0.00	0.00
ThO ₂	0.00	0.00	0.00	0.00	0.00
Yb ₂ O ₃	0.00	0.00	0.00	0.00	0.00
Ce ₂ O ₃	0.00	0.00	0.00	0.00	0.00
Y ₂ O ₃	0.00	0.11	0.00	0.00	0.06
La ₂ O ₃	0.00	0.00	0.00	0.00	0.00
Total (wt.%)	91.74	91.83	91.05	91.29	92.42
Normalised on 22 O					
Si	6.28	6.20	6.24	6.28	6.22
Al IV	1.72	1.80	1.76	1.72	1.78
Al VI	3.88	3.93	3.98	3.93	3.83
Fe	0.19	0.11	0.07	0.23	0.27
Mg	0.03	0.02	0.00	0.02	0.02
K	1.64	1.70	1.67	1.41	1.66
Na	0.02	0.03	0.01	0.03	0.04

Appendix 3:4

Zircon

Textural and electron microprobe data

Sample	Rock type
WC-78-1A	Cataclastic zone in reduced leucocratic phonolite.

Characteristics of the analysed zircons/ ZrO_2 -minerals.

Anal. No.	Sample No.	Description	
1*	110/1-ZO15	Large sized (~6 mm) skeletal crystal - 1, population 1; border.	
2*	110/1-ZO16	Idem - 1, population 1; border.	
3*	110/1-ZO14	Idem - 1, population 1; internal part.	
4*	110/1-ZO13	Idem - 1, population 2; border(-1)	} profile across crystal
5*	110/1-ZO18	Idem - 1, population 2; centre	
6*	110/1-ZO12	Idem - 1, population 2; intermediate zone	
7*	110/1-ZO11	Idem - 1, population 2; border(-2)	
8*	110/1-ZO38	Idem - 1, population 3; border.	
9*	110/1-ZO37	Idem - 1, population 3; internal part	
10*	110/1-ZO36	Idem - 1, population 3; internal part, inclusions of higher reflectivity.	
11*	110/1-ZO41	Idem - 1, population 3; internal part, inclusions of higher reflectivity	
12*	110/1-ZO10	Idem - 1, population 4; internal border near K-feldspar inclusion.	
13*	110/1-ZO20	Idem - 1, population 4; internal border near K-feldspar inclusion.	
14*	110/1-ZO31	Idem - 1, population 4; internal part.	
15*	110/1-ZO30	Idem - 1, population 4; intermediate zone.	
16*	110/1-ZO09	Idem - 1, population 4; centre.	
17*	110/1-ZO29	Idem - 1, border.	
18*	110/1-ZO08	Idem - 1, population 5; intermediate zone.	
19*	110/1-ZO42	Medium sized skeletal crystal - 2, intermediate zone.	
20*	110/1-ZO43	Idem - 2, intermediate zone near TiO_2 -inclusion.	
21*	110/1-ZO48	Idem - 2, internal part, altered: higher reflectivity, strong anisotropy.	
22*	110/1-ZO49	Idem - 2, same as ZO48 – different analytical point.	
23*	110/1-ZO03	Idem - 2, centre.	
24*	110/1-ZO02	Idem - 2, border with K-feldspar, very strong blue cathodoluminescence; weak K-, Al-contamination!	
25*	110/1-ZO02	Repetition of analysis ZO02, without contamination.	
26*	110/1-ZO01	Idem - 2, intermediate zone; very strong yellow cathodoluminescence.	
27*	110/1-ZO45	Idem - 2, centre	
28*	110/1-ZO00	Idem - 2, centre.	
29*	110/1-ZO46	Idem - 2, intermediate zone.	
30*	110/1-ZO47	Idem - 2, border.	
31*	110/1-ZO07	Idem - 1, population 5; intermediate zone.	

Anal. No.	Sample No.	Description
32*	110/1-ZO06	Idem - 1, population 5; internal border near K-feldspar inclusion.
33*	110/1-ZO05	Idem - 1, population 5; internal part.
34*	110/1-ZO04	Idem - 1, population 5; border.
35*	110/2-Z00	Idem - 1, intermediate zone; very strong yellow cathodoluminescence.
36*	110/2-Z06	Idem - 1, intermediate zone.
37*	110/2-Z07	Idem - 1, border; very strong yellow cathodoluminescence.
38*	110/2-Z10	Skeletal crystal - 2, border
39*	110/2-Z09	Idem - 2, border; very strong yellow cathodoluminescence.
40*	110/2-Z08	Idem - 2, border
41*	110/2-Z16	Idem - 2, border; very strong yellow cathodoluminescence.
42*	110/2-Z11	Skeletal crystal - 3, border; very strong yellow cathodoluminescence.
43*	110/2-Z12	Idem - 3, border; very strong yellow cathodoluminescence.
44*	110/2-Z13	Idem - 3, centre.
45*	110/2-Z14	Idem - 3, intermediate zone.
46*	110/2-Z15	Idem - 3, border.
47*	110/2-Z02	Skeletal crystal - 1, border.
48*	110/2-Z01	Idem - 1, border.
49*	110/2-Z03	Idem - 1, centre.
50*	110/2-Z05	Idem - 1, centre.
51*	110/2-Z04	Idem - 1, intermediate zone.
52*	110/4-Z19	Zircon-ZrO ₂ -mineral intergrowth - 1, border.
53*	110/4-Z15	Idem - 1, border.
54*	110/4-Z17	Idem - 1, internal part.
55*	110/4-Z20	Idem - 1, border; Al-contamination!
56*	110/4-Z0	Idem - 1.
57*	110/4-Z16	Idem - 1, internal part.
58*	110/4-Z18	Idem - 1, internal part.
59*	110/4-Z19A	Idem - 1, border.
60*	110/4-Z14	Idem - 1, border.
61*	110/4-Z13	Idem - 1.
62*	78/2-Z15	Zoned crystal - 3, border.
63*	78/2-15A	Zoned crystal - 3, centre.
64*	78/2-15	Zoned crystal - 3, border.
65*	78/2-Z16	Idem - 3, centre.
66*	78/2-Z19	Idem - 3, border.
67*	78/2-Z15A	Idem - 3, centre.
68*	78/2-Z11	Idem - 3, border.
69*	78/2-Z17	Zoned crystal - 1, border.
70*	78/2-Z17A	Idem - 1, border ~ 20μ further towards the crystal centre than Z17.

Anal. No.	Sample No.	Description	
71*	78/2-Z18	Idem - 1, centre.	
72*	78/2-Z18A	Idem - 1, centre.	
73*	78/2-Z18B	Idem - 1, intermediate zone.	
74*	78/2-Z18C	Idem - 1, intermediate zone.	
75*	78/2-Z20	Idem - 1, about 40 μ from border.	
76*	78/2-Z21	Idem - 1, border.	
77*	78/2-Z01	Zoned crystal - 2, border zone - 1.	} Profile 1
78*	78/2-Z01A	Idem - 2, border zone - 1.	
79*	78/2-Z02	Idem - 2, border zone - 1.	
80*	78/2-Z03	Idem - 2, border zone - 1; alteration(?)	
81*	78/2-Z04	Idem - 2, intermediate zone - 2; alteration(?)	
82*	78/2-Z04A	Idem - 2, intermediate zone - 2; alteration(?)	
83*	78/2-Z04B	Idem - 2, intermediate zone - 2; alteration(?)	
84*	78/2-Z05	Idem - 2, intermediate zone - 3; alteration(?)	
85*	78/2-Z05A	Idem - 2, intermediate zone - 3; alteration(?)	} Profile 2
86*	78/2-Z06	Idem - 2, centre zone - 4; alteration(?)	
87*	78/2-Z08	Idem - 2, centre zone - 6; basis of crystal.	
88*	78/2-Z07	Idem - 2, centre zone - 5.	
89*	78/2-Z07A	Idem - 2, centre zone - 5.	
90*	78/2-Z14	Idem - 2, centre zone -4; alteration(?)	
91*	78/2-Z13A	Idem - 2, intermediate zone - 3; alteration(?)	
92*	78/2-Z13	Idem - 2, intermediate zone - 3; alteration(?)	
93*	78/2-Z12	Idem - 2, border zone - 1; alteration(?)	
94*	78/3-Z01	Skeletal crystal - 1, border.	
95	78/3-Z01A	Idem - 1, border.	
96	78/3-Z02	Idem - 1, border.	
97	78/3-Z03	Idem - 1, border.	
98*	78/3-Z04	Idem - 1, border.	
99	78/3-Z05	Idem - 1, border.	
100*	78/3-Z11	Idem - 1, intermediate zone; alteration(?)	} border to centre profile
101*	78/3-Z12	Idem - 1, intermediate zone; alteration(?)	
102	78/3-Z10A	Idem - 1, intermediate zone.	
103	78/3-Z10B	Idem - 1, intermediate zone.	
104*	78/3-Z10C	Idem - 1, intermediate zone.	
105	78/3-Z10	Idem - 1, centre.	
106*	78/3-Z09	Idem - 1, centre.	
107	78/3-Z08	Idem - 1, centre.	
108*	78/3-Z08A	Idem - 1, intermediate zone.	
109	78/3-Z07	Idem - 1, centre.	
110	78/3-Z06	Idem - 1, intermediate zone.	
111*	78/5-Z01	Zoned idiomorphic crystal - 1, border.	} border to centre profile
112*	78/5-Z02	Idem - 1, intermediate zone - 1.	
113*	78/5-Z03	Idem - 1, intermediate zone - 2.	
114*	78/5-Z04	Idem - 1, centre.	
115*	78/5-Z05	Idem - 1, intermediate zone.	
116*	78/5-Z06	Idem - 1, border.	
117*	78/5-Z07	Idem - 1, border.	

Anal. No.	Sample No.	Description
118*	78/5-Z17	Zoned idiomorphic crystal - 2, centre.
119*	78/5-Z16	Idem - 2, border; very strong yellow cathodoluminescence.
120*	78/5-Z13	Idem - 2, centre.
121*	78/5-Z14	Idem - 2, intermediate zone.
122*	78/6-Z01	Skeletal crystal - 1, border.
123*	78/6-Z02	Idem - 1, internal part.
124	78/6-Z03	Skeletal crystal - 1, border.
125*	78/6-Z05	Idem - 2, border.
126	78/6-Z04	Idem - 2, centre.
127*	78/6-Z06	Idem - 2, border; very strong yellow cathodoluminescence.
128	78/6-Z06A	Idem - 2, centre.
129*	78/6-Z07	Idem - 2, border; very strong yellow cathodoluminescence.
130	78/6-Z09	Idem - 2, border; very strong yellow cathodoluminescence.
131	78/6-Z08	Idem - 2, intermediate zone.
132*	78/6-Z10	Skeletal crystal - 3, centre.
133	78/6-Z10A	Idem - 3, border; very strong yellow cathodoluminescence.
134	78/6-Z11	Idem - 3, centre.
135	78/6-Z15	Idem - 3, sutured border; strong blue cathodoluminescence.
136	78/6-Z14	Idem - 3, border; very strong yellow cathodoluminescence.
137*	78/7-Z01	Skeletal crystal - 1, border; very strong yellow cathodoluminescence.
138*	78/7-Z01A	Idem - 1.
139	78/7-Z02	Idem - 1, intermediate zone; very strong yellow cathodoluminescence.
140*	78/7-Z03	Idem - 1, border.
141	78/7-Z04	Idem - 1, intermediate zone.
142	78/7-Z05	Idem - 1, centre.
143	78/7-Z06	Idem - 1, border.
144*	78/7-Z07	Idem - 1, internal part.

*Analysis not reported.

Crystal matrix: zircon														
Sample Location	78/6-Z04 Centre a	78/6-Z06A Centre a	78/6-Z08 Intermed. a	78/6-Z03 Rim a	78/6-Z09 Rim a	78/6-Z11 Centre b	78/6-Z10A Rim b	78/6-Z14 Rim b	78/6-Z15 Rim b	78/7-Z05 Centre	78/7-Z02 Intermed.	78/7-Z04 Intermed.	78/7-Z06 Rim	78/3-Z07 Centre
SiO ₂	32.77	33.34	33.23	32.90	33.57	33.20	32.33	31.87	33.74	33.13	32.43	32.89	33.11	33.06
FeO	0.00	0.00	0.00	0.00	0.00	0.00	0.00	0.00	0.00	0.00	0.00	0.00	0.00	0.00
Na ₂ O	0.10	0.10	0.11	0.15	0.07	0.08	0.13	0.11	0.09	0.18	0.07	0.08	0.12	0.06
MgO	0.00	0.00	0.00	0.00	0.00	0.00	0.00	0.00	0.00	0.00	0.00	0.00	0.00	0.00
UO ₂	0.00	0.00	0.00	0.00	0.00	0.00	0.00	0.00	0.00	0.00	0.00	0.00	0.00	0.00
ThO ₂	0.00	0.00	0.00	0.00	0.00	0.00	0.00	0.00	0.00	0.00	0.00	0.00	0.00	0.00
ZrO ₂	67.43	66.77	66.86	66.11	67.20	66.36	65.04	64.80	67.61	67.12	64.44	66.28	67.91	65.73
Yb ₂ O ₃	0.00	0.00	0.12	0.16	0.12	0.12	0.12	0.13	0.16	0.26	0.18	0.14	0.19	0.00
Ce ₂ O ₃	0.07	0.17	0.19	0.11	0.11	0.10	0.09	0.19	0.14	0.15	0.16	0.13	0.10	0.13
Y ₂ O ₃	0.39	0.23	0.36	0.29	0.33	0.62	0.68	0.33	0.46	0.20	0.06	0.31	0.39	0.16
K ₂ O	0.00	0.00	0.00	0.00	0.00	0.00	0.00	0.00	0.00	0.00	0.00	0.00	0.00	0.00
Al ₂ O ₃	0.00	0.00	0.00	0.00	0.00	0.00	0.00	0.00	0.00	0.00	0.00	0.00	0.00	0.00
La ₂ O ₃	0.00	0.00	0.00	0.00	0.00	0.00	0.00	0.00	0.00	0.00	0.00	0.00	0.00	0.00
HfO ₂	0.47	0.72	0.79	0.70	0.00	0.79	0.39	0.69	0.00	0.00	0.80	0.62	0.71	0.57
Total (wt.%)	101.22	101.33	101.66	100.40	101.40	101.28	98.77	98.13	102.21	101.03	98.14	100.46	102.53	99.71
Normalised to 16 O														
Si	3.97	4.02	4.01	4.01	4.04	4.02	4.01	3.99	4.03	4.01	4.04	4.01	3.97	4.04
Fe	0.00	0.00	0.00	0.00	0.00	0.00	0.00	0.00	0.00	0.00	0.00	0.00	0.00	0.00
Na	0.02	0.02	0.03	0.04	0.02	0.02	0.03	0.03	0.02	0.04	0.02	0.02	0.03	0.02
Mg	0.00	0.00	0.00	0.00	0.00	0.00	0.00	0.00	0.00	0.00	0.00	0.00	0.00	0.00
U	0.00	0.00	0.00	0.00	0.00	0.00	0.00	0.00	0.00	0.00	0.00	0.00	0.00	0.00
Th	0.00	0.00	0.00	0.00	0.00	0.00	0.00	0.00	0.00	0.00	0.00	0.00	0.00	0.00
Zr	3.98	3.93	3.93	3.93	3.94	3.91	3.93	3.95	3.94	3.96	3.91	3.94	3.97	3.92
Yb	0.00	0.00	0.00	0.01	0.00	0.00	0.00	0.01	0.01	0.01	0.01	0.01	0.01	0.00
Ce	0.00	0.01	0.01	0.00	0.01	0.00	0.00	0.01	0.01	0.01	0.01	0.01	0.00	0.01
Y	0.03	0.02	0.02	0.02	0.02	0.04	0.05	0.02	0.03	0.01	0.00	0.02	0.03	0.01
K	0.00	0.00	0.00	0.00	0.00	0.00	0.00	0.00	0.00	0.00	0.00	0.00	0.00	0.00
Al	0.00	0.00	0.00	0.00	0.00	0.00	0.00	0.00	0.00	0.00	0.00	0.00	0.00	0.00
La	0.00	0.00	0.00	0.00	0.00	0.00	0.00	0.00	0.00	0.00	0.00	0.00	0.00	0.00
Hf	0.02	0.03	0.03	0.02	0.00	0.03	0.01	0.03	0.00	0.00	0.03	0.02	0.02	0.02

Crystal matrix: zircon (contd.)								
Sample	78/3-Z10	78/3-Z01A	78/3-Z10A	78/3-Z10B	78/3-Z06	78/3-Z02	78/3-Z03	78/3-Z05
Location	Centre	Intermed.	Intermed.	Intermed.	Intermed.	Rim	Rim	Rim
SiO ₂	32.19	33.23	33.27	32.99	32.68	32.52	33.18	32.84
FeO	0.00	0.00	0.00	0.00	0.00	0.00	0.00	0.00
Na ₂ O	0.09	0.08	0.10	0.09	0.08	0.11	0.10	0.14
MgO	0.00	0.00	0.00	0.00	0.00	0.00	0.00	0.00
UO ₂	0.00	0.00	0.00	0.00	0.00	0.00	0.00	0.00
ThO ₂	0.00	0.00	0.00	0.00	0.00	0.00	0.00	0.00
ZrO ₂	65.95	66.60	67.77	65.86	64.92	66.64	66.82	65.64
Yb ₂ O ₃	0.00	0.00	0.19	0.00	0.13	0.20	0.13	0.00
Ce ₂ O ₃	0.08	0.18	0.37	0.16	0.08	0.11	0.09	0.29
Y ₂ O ₃	0.05	0.25	0.40	0.18	0.25	0.26	0.32	0.32
K ₂ O	0.00	0.00	0.00	0.00	0.00	0.00	0.00	0.00
Al ₂ O ₃	0.00	0.00	0.00	0.00	0.00	0.00	0.00	0.00
La ₂ O ₃	0.00	0.00	0.00	0.00	0.00	0.00	0.00	0.00
HfO ₂	0.00	0.00	0.00	0.48	0.58	0.41	0.00	0.52
Total (wt.%)	98.35	100.35	102.10	99.77	98.71	100.25	100.64	99.75
Normalised to 16 O								
Si	4.00	4.03	3.99	4.04	4.04	3.98	4.02	4.02
Fe	0.00	0.00	0.00	0.00	0.00	0.00	0.00	0.00
Na	0.02	0.02	0.02	0.02	0.02	0.03	0.02	0.03
Mg	0.00	0.00	0.00	0.00	0.00	0.00	0.00	0.00
U	0.00	0.00	0.00	0.00	0.00	0.00	0.00	0.00
Th	0.00	0.00	0.00	0.00	0.00	0.00	0.00	0.00
Zr	3.99	3.94	3.97	3.93	3.91	3.98	3.95	3.92
Yb	0.00	0.00	0.01	0.00	0.00	0.01	0.00	0.00
Ce	0.00	0.01	0.02	0.01	0.00	0.01	0.00	0.01
Y	0.00	0.02	0.03	0.01	0.02	0.02	0.02	0.02
K	0.00	0.00	0.00	0.00	0.00	0.00	0.00	0.00
Al	0.00	0.00	0.00	0.00	0.00	0.00	0.00	0.00
La	0.00	0.00	0.00	0.00	0.00	0.00	0.00	0.00
Hf	0.00	0.00	0.00	0.02	0.02	0.01	0.00	0.02

Appendix 3:5

Fluorite

Textural and electron microprobe data

Sample	Rock type
WC-78-1A	Cataclastic zone in reduced leucocratic phonolite.

Characteristics of the analysed fluorites.

Anal. No.	Sample No.	Description
1	78/6-F116	Colourless crystal - 1, intergrown with skeletal zircon.
2	78/6-F117	Colourless crystal - 2, intergrown with skeletal zircon.
3	78/6-F118	Colourless crystal - 3, intergrown with skeletal zircon.
4	78/6-F119	Light violet coloured crystal - 4, intergrown with skeletal zircon.
5	78/4-F101	Heterogeneously coloured crystal - 1, partly deep violet in colour.
6	78/4-F102	Idem 1, deep violet colour.
7	78/4-F103	Idem 1, light violet – almost colourless.
8	78/4-F104	Idem 1, light violet – almost colourless.
9	78/4-F106	Idem 1, violet colour, border of crystal.
10	78/4-F109	Idem 1, deep violet colour, internal part of the crystal.
11	78/4-F110	Idem 1, deep violet colour, intermediate zone of crystal.
12	78/4-F111	Idem 1, deep violet colour, border of crystal.

Crystal matrix: fluorite												
Sample	78/6-F116	78/6-F117	78/6-F118	78/6-F119	78/4-F101	78/4-F102	78/4-F103	78/4-F104	78/4-F106	78/4-F109	78/4-F110	78/4-F111
SiO ₂	0.00	0.00	0.00	0.00	0.00	0.00	0.00	0.00	0.00	0.00	0.00	0.00
FeO	0.00	0.00	0.00	0.00	0.00	0.00	0.00	0.00	0.00	0.00	0.00	0.00
Na ₂ O	0.06	0.07	0.09	0.06	0.00	0.00	0.00	0.08	0.00	0.00	0.09	0.00
MgO	0.00	0.00	0.00	0.00	0.00	0.00	0.00	0.00	0.00	0.00	0.00	0.00
UO ₂	0.00	0.00	0.00	0.00	0.00	0.00	0.00	0.00	0.00	0.00	0.00	0.00
ThO ₂	0.00	0.00	0.00	0.00	0.00	0.00	0.00	0.00	0.00	0.00	0.00	0.00
ZrO ₂	0.00	0.00	0.00	0.00	0.00	0.00	0.00	0.00	0.00	0.00	0.00	0.00
Yb ₂ O ₃	0.00	0.00	0.00	0.00	0.00	0.00	0.00	0.00	0.00	0.00	0.00	0.00
Ce ₂ O ₃	0.00	0.00	0.00	0.00	0.00	0.00	0.00	0.00	0.00	0.50	0.00	0.00
Y ₂ O ₃	0.00	0.00	0.00	0.07	0.12	0.15	0.00	0.00	0.07	0.15	0.20	0.10
K ₂ O	0.93	0.70	0.79	0.83	0.76	0.96	0.87	0.73	0.81	0.79	0.73	0.81
Al ₂ O ₃	0.00	0.00	0.00	0.00	0.00	0.00	0.00	0.00	0.00	0.00	0.00	0.00
La ₂ O ₃	0.00	0.00	0.00	0.00	0.00	0.00	0.00	0.00	0.00	0.00	0.00	0.00
Hf ₂ O ₃	0.00	0.00	0.00	0.00	0.00	0.00	0.00	0.00	0.00	0.00	0.00	0.00
F	48.67	48.67	48.67	48.67	48.67	48.67	48.67	48.67	48.67	48.67	48.67	48.67
CaO	50.51	50.70	50.62	50.54	50.60	50.42	50.61	50.66	50.61	50.12	50.50	50.58
Total (wt.%)	100.17	100.14	100.17	100.17	100.15	100.20	100.15	100.14	100.16	100.23	100.19	100.16

Appendix 3:6

Rutile and Ti-oxides

Electron microprobe data

Sample	Rock
S/N-24	Massive pitchblende nodule (Urânio do Brasil collection).
WC-75-1B	Reduced, medium-grained leucocratic phonolite.
WC-78-1A	Cataclastic zone in reduced leucocratic phonolite.
WC-110-1A	Reduced porous leucocratic phonolite.

Mineralogical characteristics of the analysed TiO₂-minerals (rutiles).

The presented analyses are of sample nos.; 110-1A, 78-1A, 75-1B and SN24 (see Table next page). All analysed grains are microgranular hydrothermal replacement products of aegirine-augites.

Crystal matrix: rutile and Ti-oxides

Sample	SN24-1RU5	SN24-1RU6	SN24-2RU2	SN24-2RU3	SN24-2RU4	SN24-2RU5	SN24-2RU7	110/1RU4	110/1RU5	110/1RU6	110/1RU7	110/1RU13A
TiO ₂	95.42	95.44	94.22	95.85	94.40	93.78	94.81	87.91	91.00	91.62	91.54	92.91
MnO	0.00	0.00	0.00	0.00	0.00	0.00	0.00	0.00	0.00	0.00	0.00	0.00
FeO	0.00	1.95	1.02	1.67	1.08	0.76	0.91	4.77	4.59	2.89	3.55	1.63
Al ₂ O ₃	0.76	0.81	1.10	0.68	0.93	0.94	1.07	0.68	0.64	0.66	0.70	0.98
SiO ₂	0.76	1.04	1.11	0.60	0.97	0.76	1.05	1.34	0.57	0.60	0.68	1.35
CaO	0.00	0.00	0.00	0.00	0.00	0.00	0.00	0.00	0.00	0.00	0.00	0.00
K ₂ O	0.00	0.00	0.00	0.00	0.00	0.00	0.00	0.38	0.00	0.00	0.00	0.00
Nb ₂ O ₃	0.50	0.00	0.47	0.24	0.36	0.30	0.50	2.07	1.08	1.96	0.87	1.06
UO ₂	0.00	0.00	0.00	0.00	0.00	0.65	0.00	0.00	0.00	0.00	0.00	0.00
ThO ₂	0.00	0.00	0.21	0.00	0.00	0.00	0.00	0.00	0.00	0.00	0.00	0.00
Y ₂ O ₃	0.00	0.10	0.15	0.31	0.07	0.00	0.06	0.46	0.00	0.00	0.21	0.00
Ce ₂ O ₃	0.00	0.00	0.00	0.00	0.00	0.00	0.00	0.00	0.00	0.00	0.00	0.00
La ₂ O ₃	0.00	0.00	0.00	0.00	0.00	0.00	0.00	0.00	0.00	0.00	0.00	0.00
Yb ₂ O ₃	0.00	0.00	0.00	0.00	0.00	0.00	0.00	0.00	0.00	0.00	0.00	0.00
Total (wt.%)	97.45	99.33	98.27	99.36	97.82	97.18	98.40	97.62	97.88	97.73	97.55	97.92

Crystal matrix: rutile and Ti-oxides

Sample	78/1RU18A	78/1RU18	78/1RU19	78/10RU7	78/10RU12A	78/10RU13	78/10RU17	75/1RU6	75/1RU5	75/1RU8	75/4RU4A
TiO ₂	90.65	95.01	97.74	92.60	94.87	93.90	92.36	93.55	94.27	93.64	91.66
MnO	0.00	0.00	0.00	0.00	0.00	0.00	0.00	0.00	0.00	0.00	0.00
FeO	1.51	0.86	0.00	1.97	1.16	1.72	2.83	1.49	1.30	1.76	2.21
Al ₂ O ₃	1.17	0.82	0.53	0.63	0.83	0.74	0.95	0.64	0.68	0.59	0.63
SiO ₂	1.95	0.65	0.00	0.81	0.81	0.00	0.83	0.53	0.68	0.00	0.63
CaO	0.00	0.00	0.00	0.00	0.00	0.00	0.00	0.00	0.00	0.00	0.00
K ₂ O	0.58	0.00	0.00	0.00	0.00	0.00	0.00	0.00	0.00	0.00	0.00
Nb ₂ O ₃	2.00	1.87	1.31	1.33	1.11	1.76	0.55	1.86	1.44	1.84	2.04
UO ₂	0.00	0.00	0.00	0.00	0.00	0.00	0.00	0.00	0.00	0.00	0.00
ThO ₂	0.00	0.00	0.00	0.00	0.00	0.00	0.00	0.00	0.00	0.00	0.00
Y ₂ O ₃	0.00	0.07	0.00	0.00	0.00	0.00	0.18	0.06	0.12	0.00	0.00
Ce ₂ O ₃	0.00	0.00	0.00	0.00	0.00	0.00	0.00	0.00	0.00	0.00	0.00
La ₂ O ₃	0.00	0.00	0.00	0.00	0.00	0.00	0.00	0.00	0.00	0.00	0.00
Yb ₂ O ₃	0.00	0.00	0.00	0.00	0.00	0.00	0.00	0.00	0.00	0.00	0.00
Total (wt.%)	97.86	99.28	99.58	97.34	98.78	98.11	97.68	98.13	98.49	97.83	97.18

Appendix 3:7

Pyrite

Electron microprobe data

Sample	Rock type
WC-78-1A	Cataclastic zone in reduced leucocratic phonolite.
WC-110-1A	Reduced porous leucocratic phonolite.

Crystal matrix: pyrite												
Sample	110/1-PY54	110/1-PY55	110/1-PY58	110/1-PY60	110/1-PY01	110/1-PY64	110/-PY	110/1-PY54	110/1-PY55	110/1-PY01	110/1-PY61	110/3-PY12
Fe	46.23	45.20	44.93	46.40	45.97	46.29	46.62	45.07	45.50	46.13	44.91	46.39
S	53.20	52.77	51.83	52.96	53.01	53.36	52.52	51.72	52.51	52.42	52.52	52.63
Pb	0.67	0.94	0.89	0.00	0.00	0.00	1.13	1.41	1.29	1.49	0.75	1.29
As	0.12	0.17	0.17	0.00	0.00	0.00	0.00	0.00	0.00	0.00	0.00	0.00
Mo	0.70	0.57	0.74	0.60	0.57	0.56	0.57	0.00	0.00	0.00	0.00	0.00
Ag	0.00	0.16	0.00	0.00	0.00	0.00	0.00	0.00	0.00	0.00	0.00	0.00
Total (wt.%)	100.91	99.81	98.56	99.96	99.56	100.20	100.84	98.19	99.30	100.04	98.18	100.31
S/Fe (atomic)	2.00	2.03	2.01	1.99	2.01	2.01	1.96	2.00	2.01	2.00	2.04	1.98

Crystal matrix: pyrite (contd.)								
Sample	110/3-PY13	110/5-PY09	78/1-PY15	78/1-PY13	78/1-PY14	78/1-PY10	78/1-PY04	78/2-PY34
Fe	45.69	46.85	45.54	46.31	45.69	45.57	44.48	45.34
S	53.18	52.64	52.92	53.05	52.83	50.97	51.76	52.77
Pb	0.80	0.93	0.00	0.51	0.75	3.73	2.84	0.86
As	0.00	0.00	0.00	0.00	0.00	0.17	0.00	0.00
Mo	0.00	0.00	0.00	0.00	0.00	0.00	0.00	0.00
Ag	0.00	0.00	0.00	0.00	0.00	0.00	0.00	0.00
Total (wt.%)	99.67	100.41	98.46	99.87	99.27	100.44	99.08	98.98
S/Fe (atomic)	1.97	1.96	2.02	2.00	2.01	1.95	2.04	2.03

Appendix 3:8

Uranium-oxides

Electron microprobe data

Sample	Rock
S/N-24	Massive pitchblende nodule with two pyrite generations and argillised phonolitic core (Urânio do Brasil collection, see Appendix 3:9; Plates 3:9-7 and 3:9-8).

Crystal matrix: uranium-oxides														
Sample	SN24-1U1	SN24-1U2	SN24-1U3	SN24-1U4	SN24-1U7	SN24-1U9	SN24-1U11	SN24-1U12	SN24-1U13	SN24-1U14	SN24-2U1	SN24-2U2	SN24-2U3	SN24-2U4
FeO	0.00	0.00	0.00	0.00	0.00	0.00	0.00	0.00	0.00	0.00	0.00	0.00	0.00	0.00
CaO	0.00	0.00	0.00	0.00	0.00	0.00	0.00	0.00	0.00	0.00	0.00	0.00	0.00	0.00
SiO ₂	2.42	2.15	2.23	2.09	2.13	2.96	2.59	2.52	2.13	2.87	2.99	2.14	2.88	2.72
Al ₂ O ₃	0.29	0.15	0.00	0.20	0.18	0.53	0.39	0.12	0.16	0.51	0.33	0.11	0.21	0.14
TiO ₂	0.00	0.00	0.00	0.00	0.00	0.00	0.00	0.00	0.00	0.00	0.00	0.00	0.00	0.00
MnO	0.00	0.00	0.00	0.00	0.00	0.00	0.00	0.00	0.00	0.00	0.00	0.00	0.00	0.00
K ₂ O	1.39	1.16	1.01	0.94	0.86	0.84	1.16	1.11	1.16	1.32	1.51	1.23	0.88	1.07
Nb ₂ O ₃	0.00	0.00	0.00	0.00	0.00	0.00	0.00	0.00	0.00	0.00	0.00	0.00	0.00	0.00
Yb ₂ O ₃	0.00	0.00	0.00	0.00	0.00	0.00	0.00	0.00	0.00	0.00	0.00	0.00	0.00	0.00
UO ₂	87.17	82.80	82.32	82.66	84.06	84.89	82.16	84.47	82.55	82.04	84.02	85.78	85.97	83.28
Y ₂ O ₃	0.42	0.00	0.30	0.07	0.00	0.14	0.00	0.00	0.00	0.11	0.09	0.13	0.62	0.00
Ce ₂ O ₃	0.32	0.00	0.00	0.00	0.00	0.30	0.00	0.16	0.14	0.12	0.13	0.14	0.00	0.00
La ₂ O ₃	0.00	0.00	0.00	0.00	0.00	0.00	0.00	0.00	0.00	0.00	0.00	0.00	0.00	0.00
ThO ₂	0.00	0.00	0.00	0.00	0.00	0.00	0.00	0.00	0.00	0.00	0.00	0.00	0.00	0.00
Total (wt.%)	92.01	86.26	85.86	85.97	87.23	89.66	86.30	88.39	86.13	86.98	89.08	89.53	90.56	87.21

Crystal matrix: uranium-oxides (contd.)														
Sample	SN24-2U5	SN24-2U6	SN24-3U1	SN24-3U2	SN24-3U3	SN24-3U4	SN24-3U5	SN24-3U6	SN24-3U7	SN24-3U8	SN24-3U9	SN24-3U10	SN24-4U2	SN24-4U3
FeO	0.00	0.00	0.00	0.00	0.98	0.00	0.00	0.00	1.19	0.00	0.00	0.00	0.00	0.00
CaO	0.00	0.00	0.00	0.00	0.00	0.00	0.00	0.00	0.00	0.00	0.00	0.00	0.00	0.00
SiO ₂	3.23	2.90	2.33	2.23	2.35	2.49	2.26	2.46	2.19	2.87	2.09	2.07	2.67	2.71
Al ₂ O ₃	0.38	0.43	0.00	0.00	0.00	0.00	0.00	0.00	0.00	0.00	0.12	0.31	0.88	0.62
TiO ₂	0.00	0.00	0.00	0.00	0.00	0.00	0.00	0.00	0.00	0.00	0.00	0.00	0.00	0.00
MnO	0.00	0.00	0.00	0.00	0.00	0.00	0.00	0.00	0.00	0.00	0.00	0.00	0.00	0.00
K ₂ O	1.52	1.39	1.22	1.51	1.20	1.40	1.01	1.95	1.08	0.00	0.90	1.36	0.84	0.92
Nb ₂ O ₃	0.00	0.00	0.00	0.00	0.00	0.00	0.00	0.00	0.00	0.00	0.00	0.00	0.00	0.00
Yb ₂ O ₃	0.00	0.00	0.00	0.00	0.00	0.00	0.00	0.00	0.00	0.00	0.00	0.00	0.00	0.00
UO ₂	84.75	84.80	81.53	81.26	79.94	80.84	79.78	81.92	79.16	81.97	82.71	81.18	79.06	78.62
Y ₂ O ₃	0.11	0.00	0.00	0.05	0.05	0.00	0.16	0.08	0.15	0.00	0.00	0.18	0.00	0.07
Ce ₂ O ₃	0.00	0.00	0.00	0.00	0.00	0.00	0.00	0.00	0.00	0.00	0.00	0.13	0.00	0.12
La ₂ O ₃	0.00	0.00	0.00	0.00	0.00	0.00	0.00	0.00	0.00	0.00	0.00	0.00	0.00	0.00
ThO ₂	0.00	0.00	0.00	0.00	0.00	0.00	0.00	0.00	0.00	0.00	0.00	0.00	0.00	0.00
Total (wt.%)	89.99	89.52	85.08	85.05	84.51	84.72	83.20	86.41	83.77	84.84	85.82	85.23	83.45	83.05

Crystal matrix: uranium-oxides (contd.)				
Sample	SN24-4U4	SN24-4U5	SN24-4U6	SN24-4U7
FeO	0.00	0.00	0.00	0.00
CaO	0.00	0.00	0.00	0.00
SiO ₂	1.67	1.83	4.52	2.38
Al ₂ O ₃	0.10	0.00	2.39	0.00
TiO ₂	0.00	0.00	0.00	0.00
MnO	0.00	0.00	0.00	0.00
K ₂ O	1.19	1.01	1.38	1.10
Nb ₂ O ₃	0.00	0.00	0.00	0.00
Yb ₂ O ₃	0.00	0.00	0.00	0.00
UO ₂	80.10	78.97	76.34	80.82
Y ₂ O ₃	0.00	0.00	0.06	0.00
Ce ₂ O ₃	0.00	0.00	0.00	0.00
La ₂ O ₃	0.00	0.00	0.00	0.00
ThO ₂	0.00	0.00	0.00	0.00
Total (wt.%)	83.06	81.81	84.69	84.29

Crystal matrix: uranium-oxides (contd.)															
Sample	2 1-15	3 1-15	4 1-15	5 1-15	6 1-15	7 1-15	8 1-15	9 1-15	10 1-15	11 1-15	12 1-15	13 1-15	14 1-15	15 1-15	16 1-15
SiO ₂	0.99	0.98	0.99	0.94	0.98	0.93	1.12	0.94	1.23	1.23	1.18	1.56	1.61	1.61	4.58
CaO	0.00	0.00	0.00	0.00	0.00	0.00	0.00	0.00	0.00	0.00	0.00	0.00	0.00	0.00	0.00
P ₂ O ₅	0.20	0.20	0.00	0.18	0.14	0.15	0.22	0.13	0.13	0.17	0.15	0.16	0.16	0.16	0.06
FeO	0.14	0.11	0.17	0.10	0.35	0.00	0.10	0.10	0.00	0.00	0.00	0.00	0.11	0.00	0.00
Na ₂ O	0.00	0.06	0.00	0.00	0.00	0.00	0.00	0.00	0.00	0.00	0.00	0.00	0.00	0.00	0.00
MgO	0.00	0.00	0.00	0.00	0.00	0.00	0.00	0.00	0.00	0.00	0.00	0.00	0.00	0.00	0.00
UO ₂	90.97	89.29	85.74	86.05	89.75	94.28	96.48	94.03	89.82	90.51	92.04	94.05	98.92	99.85	97.86
ThO ₂	0.00	0.00	0.00	0.00	0.00	0.00	0.00	0.00	0.00	0.00	0.00	0.00	0.00	0.00	0.00
TiO ₂	0.00	0.00	0.00	0.00	0.00	0.00	0.00	0.00	0.00	0.57	0.00	0.00	0.00	0.00	0.00
ZrO ₂	0.00	0.00	0.00	0.00	0.00	0.00	0.00	0.00	0.00	0.00	0.00	0.00	0.00	0.00	0.00
Yb ₂ O ₃	0.00	0.00	0.00	0.00	0.00	0.00	0.00	0.00	0.00	0.00	0.00	0.18	0.00	0.00	0.00
Nd ₂ O ₃	0.00	0.00	0.00	0.00	0.00	0.00	0.00	0.00	0.00	0.00	0.00	0.00	0.00	0.00	0.00
Ce ₂ O ₃	0.18	0.00	0.00	0.22	0.00	0.00	0.25	0.00	0.00	0.00	0.21	0.00	0.25	0.00	0.17
Y ₂ O ₃	0.00	0.09	0.00	0.00	0.00	0.00	0.00	0.00	0.00	0.00	0.09	0.00	0.00	0.00	0.00
Total (wt.%)	92.47	90.73	86.89	87.49	91.22	95.36	98.18	95.20	91.18	92.47	93.67	95.95	101.06	101.62	102.66